

UNCLASSIFIED

AD NUMBER

AD857473

LIMITATION CHANGES

TO:

Approved for public release; distribution is unlimited.

FROM:

Distribution authorized to U.S. Gov't. agencies and their contractors; Critical Technology; JUN 1969. Other requests shall be referred to Naval Weapons Center, China Lake, CA 93555. This document contains export-controlled technical data.

AUTHORITY

usnwc ltr, 30 aug 1974

THIS PAGE IS UNCLASSIFIED

UNCLASSIFIED

Security Classification

DOCUMENT CONTROL DATA - R & D		
(Security classification of title, body of abstract and indexing annotation must be entered when the overall report is classified)		
1. ORIGINATING ACTIVITY (Corporate author) Naval Weapons Center China Lake, California 93555		2a. REPORT SECURITY CLASSIFICATION UNCLASSIFIED
		2b. GROUP
3. REPORT TITLE  PROCEEDINGS OF THE 8TH NAVY SYMPOSIUM ON AEROBALLISTICS. VOLUME 1		
4. DESCRIPTIVE NOTES (Type of report and inclusive dates)		
5. AUTHOR(S) (First name, middle initial, last name)		
6. REPORT DATE June 1969	7a. TOTAL NO. OF PAGES 238	7b. NO. OF REFS 130
8a. CONTRACT OR GRANT NO.	9a. ORIGINATOR'S REPORT NUMBER(S)  TS 69-199	
b. PROJECT NO.		
c.	9b. OTHER REPORT NO(S) (Any other numbers that may be assigned this report)	
d.		
10. DISTRIBUTION STATEMENT  THIS DOCUMENT IS SUBJECT TO SPECIAL EXPORT CONTROLS AND EACH TRANSMITTAL TO FOREIGN GOVERNMENTS OR FOREIGN NATIONALS MAY BE MADE ONLY WITH PRIOR APPROVAL OF THE NAVAL WEAPONS CENTER.		
11. SUPPLEMENTARY NOTES	12. SPONSORING MILITARY ACTIVITY Naval Air Systems Command Naval Ordnance Systems Command Naval Material Command Washington, D.C. 20360	
13. ABSTRACT		

UNCLASSIFIED

Security Classification

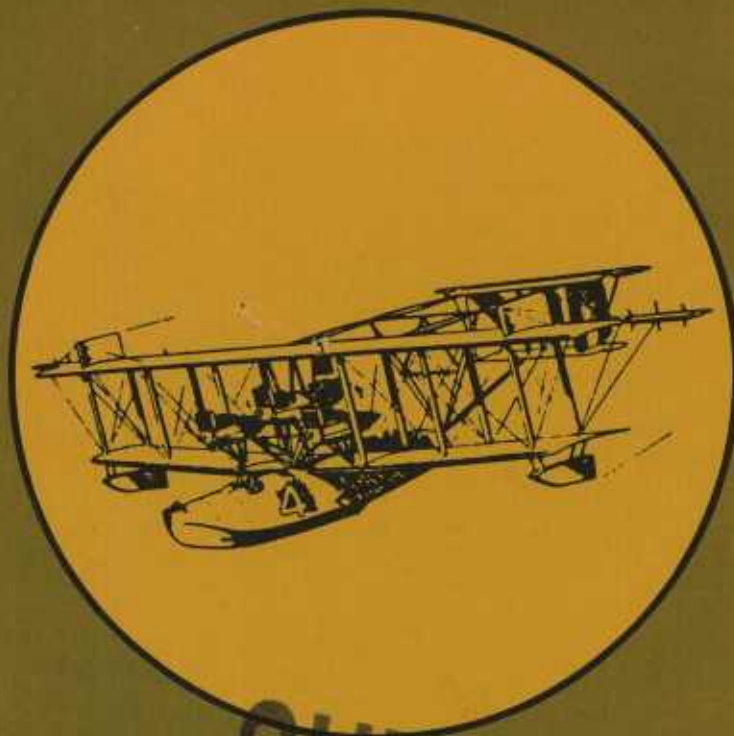
14. KEY WORDS	LINK A		LINK B		LINK C	
	ROLE	WT	ROLE	WT	ROLE	WT
Aeroballistics Navy Aeroballistics Symposium Aerodynamics Aerophysics Transpiration Cooling Boundary Layer Blunt Body Flows Heat Transfer Aerodynamic Heating Gas Dynamics						

AN (1) AD- 857 473  
 FG (2) 191000  
 FG (2) 200400  
 CI (3) (U)  
 CA (5) NAVAL WEAPONS CENTER CHINA LAKE CA  
 TI (6) Proceedings of the Navy Symposium on Aeroballistics (8th) 6, 7, 8 May 1969 Naval Weapons Center, Corona Laboratories, Corona, California. Volume I.  
 TC (8) (U)  
 RD (11) Jun 1969  
 PG (12) 258  
 RS (14) NWC-TS-69-199-Vol-1  
 RC (20) Unclassified report  
 NO (21) See also Volume 2, AD-857 474.  
 DE (23) \*SYMPOSIA), (\*AERODYNAMICS, (\*BALLISTICS, AERODYNAMICS), BASE FLOW, SLENDER BODIES, ANGLE OF ATTACK, BODIES OF REVOLUTION, LAMINAR FLOW, HEAT TRANSFER, HYPERSONIC CHARACTERISTICS, PRESSURE, CONICAL BODIES, EVAPOTRANSPIRATION, COOLING, STAGNATION POINT, BOUNDARY LAYER TRANSITION, REYNOLDS NUMBER.  
 DC (24) (U)  
 ID (25) \*aeroballistics.  
 IC (26) (U)  
 AB (27) Contents: Base and lee side flow studies of slender bodies at high angles of attack; An experimental investigation of the hypersonic aerodynamic characteristics of slender bodies of revolution at high angles of attack; Analytical investigation on laminar flow field and heat transfer on leeward side of a sharp nosed hypersonic cone at large angle of attack; Pressure distribution on bodies at large angle of attack; Compact gas-transpiration cooling system analysis; Experimental investigation of transpiration cooling near the stagnation point of a cylinder; Ballistics range experiments on the effect of unit Reynolds number on boundary-layer transition; Calculation of blunt body flows using Pade fractions and the method of characteristics.  
 AC (28) (U)  
 DL (33) 01  
 SE (34) 1  
 CC (35) 403019



NO FORN

NAVAL WEAPONS CENTER SECTION  
NAVAL AIR SYSTEMS COMMAND  
CORONA, CALIFORNIA 93940



# PROCEEDINGS OF THE 8TH NAVY SYMPOSIUM ON AEROBALLISTICS

VOLUME 1

6, 7, 8 MAY 1969

NAVAL WEAPONS CENTER • Corona Laboratories • Corona, California



SPONSORED BY THE NAVAL AEROBALLISTICS ADVISORY COMMITTEE  
FOR THE  
NAVAL AIR SYSTEMS COMMAND • NAVAL ORDNANCE SYSTEMS COMMAND

## DISTRIBUTION STATEMENT

THIS DOCUMENT IS SUBJECT TO SPECIAL EXPORT CONTROLS AND EACH TRANSMITTAL TO FOREIGN GOVERNMENTS OR FOREIGN NATIONALS MAY BE MADE ONLY WITH PRIOR APPROVAL OF THE NAVAL WEAPONS CENTER.

### 50TH ANNIVERSARY COMMEMORATED

Appropriately, the closing date of the Symposium marked the 50th anniversary of a significant milestone in aviation. On 8 May 1919, three naval aircraft left Long Island to attempt the first crossing of the Atlantic. Of the three Curtiss flying boats that started that historic 3,925-nautical-mile flight, the NC-4 (shown on cover), commanded by LCDR A. C. Read, was successful, making the first Atlantic crossing via Newfoundland, the Azores, and Portugal, finally arriving at Plymouth, England.

The Secretary of the Navy designated May 1969 a commemorative period, and it was especially appropriate that the Symposium salute the aeronautical pioneers who made history in May 1919.

# PROCEEDINGS OF THE 8TH NAVY SYMPOSIUM ON AEROBALLISTICS

## VOLUME 1

6, 7, 8 MAY 1969

NAVAL WEAPONS CENTER • Corona Laboratories • Corona, California



SPONSORED BY THE NAVAL AEROBALLISTICS ADVISORY COMMITTEE  
FOR THE  
NAVAL AIR SYSTEMS COMMAND • NAVAL ORDNANCE SYSTEMS COMMAND

### DISTRIBUTION STATEMENT

THIS DOCUMENT IS SUBJECT TO SPECIAL EXPORT CONTROLS  
AND EACH TRANSMITTAL TO FOREIGN GOVERNMENTS OR  
FOREIGN NATIONALS MAY BE MADE ONLY WITH PRIOR  
APPROVAL OF THE NAVAL WEAPONS CENTER.

NAVAL WEAPONS CENTER • CHINA LAKE, CALIFORNIA  
JUNE 1969

## FOREWORD

These *Proceedings*, published in five volumes, comprise the 49 papers presented at the Eighth Navy Symposium on Aeroballistics held at the Naval Weapons Center Corona Laboratories, Corona, Calif., 6, 7, and 8 May 1969.

This symposium was the eighth in a series begun in 1950 under the sponsorship of the then Bureau of Ordnance Committee on Aeroballistics, and currently conducted by the Naval Aeroballistics Advisory Committee as sponsoring committee for the Naval Air Systems Command and the Naval Ordnance Systems Command. The continuing purpose of the symposiums has been to disseminate the results of aeroballistics research and to bring the research findings of industry, the universities, and government laboratories to bear upon the Navy's aeroballistics research and development programs.

Over 200 research scientists representing more than 72 organizations attended this eighth symposium. Sessions 1 and 2 covered the subjects of heat transfer and aerophysics, nozzles and jet effects; Sessions 3 and 4 were concerned with aerodynamics and missile stability; and Session 5 dealt with structures and aeroelasticity, and external carriage and store separation.

The papers in these *Proceedings* have been reproduced in facsimile. They appear in the order of presentation except that all classified papers have been taken out of sequence and grouped together as Volume 5, a confidential volume. Volumes 1 through 4 are unclassified. This is Volume 1.

Requests for or comments on individual papers should be addressed to the respective authors.

RAY W. VAN AKEN  
*General Chairman*  
Symposium Committee

Published by the Publishing Division of the Technical Information Department, NWC; first printing, June 1969, 250 copies.

## CONTENTS

## Volume 1

Paper		Page
	Authors .....	viii
	Greetings .....	ix
	Welcome .....	x
	Introductory Remarks, Rear Admiral R. J. Schneider, USN .....	xi
	U.S. Navy Symposiums on Aeroballistics .....	xiii
	Naval Aeroballistics Advisory Committee .....	xiv
	Paper Selection Committee .....	xv
	Attendees .....	xvi
1	Base and Lee Side Flow Studies of Slender Bodies at High Angles of Attack by George S. Pick .....	1
2	An Experimental Investigation of the Hypersonic Aerodynamic Characteristics of Slender Bodies of Revolution at High Angles of Attack by Robert Feldhuhn, Allen Winkelmann and Lionel Pasiuk .....	29
3	Analytical Investigation on Laminar Flow Field and Heat Transfer on Leeward Side of a Sharp Nosed Hypersonic Cone at Large Angle of Attack by Paul K. Chang, Mario J. Casarella, and Russell A. Smith .....	95
4	Pressure Distribution on Bodies at Large Angle of Attack by Howard R. Kelly .....	129
5	Compact Gas-Transpiration Cooling System Analysis by R. W. Allen and R. W. Newman .....	153
6	Experimental Investigation of Transpiration Cooling Near the Stagnation Point of a Cylinder by Richard L. Humphrey .....	181
7	Ballistics Range Experiments on the Effect of Unit Reynolds Number on Boundary-Layer Transition by Norman W. Sheetz, Jr. ....	201
8	Calculation of Blunt Body Flows Using Pade' Fractions and the Method of Characteristics by Andrew H. Van Tuyl .....	215

## Volume 2

9	Applications of the Time-Dependent Technique for the Computation of Compressible Flows by John D. Anderson, Jr., Lorenzo M. Albacete and Allen E. Winkelmann ..	239
10	Nonequilibrium Flow Over Blunt Bodies Using Method of Integral Relations by T. C. Tai .....	267
11	Supersonic Laminar and Turbulent Ablation Studies With Teflon by E. M. Winkler, R. L. Humphrey, J. A. Koenig, and M. T. Madden .....	311
12	Recent Progress in the Calculation of Turbulent Boundary Layers by Tuncer Cebeci, A.M.O. Smith, and G. Mosinskis .....	351
13	An Experimental Investigation of the Compressible Turbulent Boundary Layer With a Favorable Pressure Gradient by William J. Yanta, David L. Brott, Robert L. Voisinet, and Roland E. Lee ..	389
14	An Experimental Reynolds Analogy for the Highly Cooled Turbulent Boundary Layer by Donald M. Wilson .....	411
15	The Effect of Flow Field Irregularities on Swept Leading Edge Heat Transfer by Albert F. Gollnick .....	441
16	An Experimental Study of Mass Addition Effects in the Near Wake by Norman G. Paul, H. J. Unger, F. K. Hill, and J. M. Cameron .....	473

## Vol. 1

Paper	Page
17 Isothermal Leading Edges by Bertram K. Ellis .....	507
18 Spikes as a Means of Reducing Drag and Rain Erosion of Blunt Bodies at Supersonic Speeds by Isidor C. Patapis .....	531

## Volume 3

21 Research on an Asymmetric Glide Reentry Vehicle by Herbert R. Little, Robert H. Burt, and Jerry Coble .....	545
24 An Analysis of a Slew-Launched Technique for Air-Launched Missiles by Eugene E. Kluth .....	587
26 Stabilization of a Liquid-Filled Shell by Inserting a Cylindrical Partition in the Liquid Cavity by John T. Frasier and William P. D'Amico .....	629
27 Effects of Roll on the Free-Flight Motion of Bodies by C. J. Welsh and R. M. Watt .....	651
28 Dynamic Stability of the 5-Inch/54 Rocket Assisted Projectile (The Influence of a Non-Linear Magnus Moment) for Eighth United States Navy Symposium on Aeroballistics by W. R. Chadwick .....	671
29 The University of Virginia Cold Magnetic Wind Tunnel Balance by Hermon M. Parker and Ricardo N. Zapata .....	695
30 Wind Tunnel Measurements of the Aerodynamic Characteristics of the 2.75 Wraparound Fin Rocket Using a Magnetic Suspension System by Milan Vlainac .....	717
31 Nonlinear Aerodynamic Stability Characteristics of the 2.75 Wrap-Around Fin Configuration by John D. Nicolaides, Charles W. Ingram, James M. Martin, and Alfred M. Morrison .....	751
32 A Study to Eliminate Flight Instabilities on a High-Drag Air Delivered Mine by Jack C. Hopps .....	833
34 Two-Dimensional Jet-Interaction Experiments Results of Flow-Field and Scale Effect Studies by Michael J. Werle, Richard T. Driftmyer, and David G. Shaffer .....	865
35 Interaction Between High Speed Flows and Transverse Jets: A Method for Predicting the Resultant Surface Pressure Distribution by Louis G. Kaufman II .....	885
36 Aerodynamic and Heat Transfer Effects of Saturn V Plume-Induced Flow Separation by Calvin L. Wilkinson .....	921

## Volume 4

38 Structural Qualification of the Low Speed FAE Weapon Dispenser by Jack D. Brannan and Wallace W. Parmenter .....	941
40 Stiffness Matrix for Missile Structures Using Thin Shell Theory by Pao C. Huang .....	981
41 An Experimental Investigation of Aircraft/Missile Interference Effects by C. Franklyn Markarian .....	1005
42 Store Separation From the McDonnell Douglas F-4 Aircraft by David L. Schoch .....	1025
43 Aircraft/Munitions Compatibility—U.S. Air Force Project "Seek Eagle" by Charles S. Epstein .....	1077
44 Prediction of Store Launch Characteristics Through Statistical Methods by Michael A. Sekellick .....	1103



Paper		Page
45	External Store Airloads Prediction by R. D. Gallagher and P. E. Browne .....	1131
46	Estimation of Aircraft Store Separation Behavior on the Basis of Captive Load Data by D. A. Jones .....	1159
47	Prediction of Store Separation Trajectories at the Naval Weapons Center by J. V. Netzer .....	1185
49	An Analytical, Numerical Program for Calculating the Aerodynamic Forces External to Aircraft by Hyman Serbin .....	1205

### Volume 5 (Classified Papers)

19	The Simulation of Ramjet Configurations With Pod Inlets for Stability and Control Wind Tunnel Testing by James C. Hagan .....	1213
20	Pitch Control Effectiveness of Flap Controls Mounted on a Body of Revolution by E. F. Lucero .....	1229
22	Wing-Tail Interference in Hypersonic Missile Configurations by H. H. Hart .....	1243
23	An Investigation of the Aerodynamic Behavior of Submissiles During Ejection from a High-Speed Rocket by Chris A. Kalivretenos and David N. Bixler .....	1257
25	Feasibility of Increasing Sidewinder Maneuverability by Means of Enlarged Canards by R. E. Meeker .....	1277
33	A Summary of the Sonic Lateral Jet Studies With 9-Degree Cones at Mach Numbers 6 to 20 by W. T. Strike .....	1297
37	Aerodynamic Design of Reaction Jet Controlled Tactical Missiles by L. A. Cassel, D. P. Engh and L. Y. Lam .....	1337
39	Evaluation of Radomes for Hypersonic Flight by L. B. Weckesser and R. K. Frazer .....	1371
48	Weapon-Aircraft Separation: A Review of a Particular Weapon Problem by R. E. Smith .....	1401

## WELCOME

### To conference attendees:

On behalf of the military and civilian personnel of the Naval Weapons Center we extend a hearty "welcome aboard". It is an honor for the Naval Weapons Center to be the host organization for this Symposium, which is sponsored by the Naval Aeroballistics Advisory Committee on behalf of the Naval Air Systems Command and Naval Ordnance Systems Command. We have been pleased by the interest shown in the meeting and hope that it will be a profitable one.



Dr. Thomas S. Amlie  
*Technical Director, NWC*



CAPT M. R. Etheridge, USN  
*Commander, NWC*



CDR R. E. Forbis, USN  
*Commanding Officer*  
NWC Corona Laboratories



## INTRODUCTORY REMARKS

Rear Admiral R. J. Schneider, USN

The charter of the Naval Aeroballistics Advisory Committee (NAAC) assigns it the responsibility to review, at least annually, the current and projected Navy research and development effort in aeroballistics and to make recommendations to the joint-sponsoring commands, NAVAIR and NAVORD, for the support of important and/or critical work areas.

It is encouraging to note that almost half of the papers being presented at this symposium result from studies prompted by your recommendations of recent years. The wide variety of the subject matter attests to the broad interests of the two command sponsors and is a testimonial to the broad base of knowledge which our joint aero research and development programs are generating. The wide representation you draw from Air Force, Army, universities and industry is further indication of the cross fertilization which exists and in large part must be credited to the aeroballistics committee activity.

The flexibility of the NAAC organization in addressing Navy's needs has again been demonstrated by the organization of a panel on separation of stores from aircraft. You will note heavy emphasis on store carriage and separation problems in this symposium agenda. With the assistance of this panel we are embarked upon a strong program seeking solutions to these problems, striving for significant improvements in weapon delivery, safety, and accuracy. Such coordinated effort brought to bear on this complex aircraft/missile interface problem will produce results and drive home recognition that aircraft weapon delivery systems are *systems*, not separate development programs of aircraft, launchers, and weapons, simply glued together in production as a package.

While it is necessary to find solutions to current problems, it is equally important that we maintain long range research and exploratory development programs, looking well ahead for the advanced technology which will be needed in future defense developments. For example, the series of papers concerning jet-interaction control fall in this category and point to attaining technical feasibility of a finless missile, with its promise of tactical and logistical advantages.

Much of the remainder of the program illustrates the increasing improvements in experimental techniques and the ever increasing utilization of high speed computer technology. These combined advances should go a long way in improving the analytical and theoretical background to understand the behavior of fluid systems, where presently we depend so heavily on an empirical approach.

It may be desirable to point out that in the May 1966 reorganization of the Navy Department, within the Navy Material Command management of research and the early stages of development has been placed on an organizational par with the hardware engineering development effort. The technology funding and budget items no longer fall easy prey to every disaster or over-run in current acquisition programs.

### Vol. 1

There is a busy and attractive future ahead in aerodynamic science and technology. As scientific fields and disciplines go, this one, despite remarkable progress of the past 50 years, is still in its infancy. There is room for youth, new uninhibited approaches, innovations, and I'm sure there are great surprises of discovery and invention ahead. As scientific men might be measured, this science is really just leaving the first generation—the second generation is now well established—and the future belongs to those now maturing from their apprenticeship. I suspect we are just beginning the period where some of the science is *old enough to be forgotten* and that needs careful watch in this arrogant age.

This is a complex physical field—the mathematics is tortuous—the equations massive and complicated, because of very real first, second and third order interactions. In the past this has forced empiricism to a high degree—skillful guess work and lucky estimations have been necessary—but with the mathematical flexibility and near omnipotence of the massive digital computers now available, the theory, the mathematics, and the tedium of nonlinear coefficients can be properly assailed. This will open new horizons in every direction.

Symposia are the hallmark of our scientific and engineering community. We must love them. They proliferate at an astounding rate. Often they seem to be drawn to lovely location spots, "The high rent districts attract them." Now managers, as distinct from the scientist/engineer class, tend to live in a world of cost-consciousness. Time and again I note instructions, policies and the like setting restrictions, limitations on attendance, etc.

Yet we need this communication. The body of knowledge is rapidly enhanced by communication and the sharing it engenders. As we get better educated we need more and more of this communication—and despite the miracles of printing, data transmission, telephone, radio, and even the modern copying machines, face to face human communication hasn't been beat.

So I exhort each of you, to give something, to take something, or both, from your friends at this meeting. Make it profitable for yourself and for someone else. And that in itself advances the so-called "state of the art."

In conclusion let me suggest the strength of the program for this symposium is an excellent indication that the Naval Aeroballistics Advisory Committee remains a strong and responsive organization, and will continue to exercise a great influence on the aeroballistics research and development programs of the Navy and the nation. Both NAVAIR and NAVORD, integrated organizationally under the Chief of Naval Material, intend to maintain support and attain progress in this vital scientific area and discipline.

## U.S. NAVY SYMPOSIUMS ON AEROBALLISTICS

**FIRST SYMPOSIUM—NOVEMBER 1950**

Hosted by ..... Defense Research Laboratory  
Held at ..... University of Texas  
Austin, Tex.

**SECOND SYMPOSIUM—MAY 1952**

Hosted by ..... Naval Weapons Center  
Held at ..... Huntington Hotel  
Pasadena, Calif.

**THIRD SYMPOSIUM—OCTOBER 1954**

Hosted by ..... Applied Physics Laboratory  
The Johns Hopkins University  
Held at ..... Applied Physics Laboratory  
The Johns Hopkins University  
Silver Spring, Md.

**FOURTH SYMPOSIUM—NOVEMBER 1957**

Hosted by ..... Naval Weapons Laboratory  
Held at ..... Department of Commerce Auditorium  
Washington, D.C.

**FIFTH SYMPOSIUM—OCTOBER 1961**

Hosted by ..... Naval Ordnance Laboratory  
Held at ..... Naval Ordnance Laboratory  
White Oak, Md.

**SIXTH SYMPOSIUM—OCTOBER-NOVEMBER 1963**

Hosted by ..... Naval Ship Research and Development Center  
Held at ..... National War College  
Fort McNair, Washington, D.C.

**SEVENTH SYMPOSIUM—JUNE 1966**

Hosted by ..... Naval Missile Center  
Held at ..... Naval Missile Center  
Point Mugu, Calif.

**EIGHTH SYMPOSIUM—MAY 1969**

Hosted by ..... Naval Weapons Center  
Held at ..... NWC Corona Laboratory  
Corona, Calif.

ATTENDEES  
EIGHTH NAVY SYMPOSIUM ON AEROBALLISTICS

**Aberdeen Research and Development Center  
Aberdeen Proving Ground, Md.**

D'Amico, W. P., 1LT, USN  
Murphy, Dr. C. H.  
Nielsen, G. I.

**Aerojet General Corp.  
Sacramento, Calif.**

Demuth, O. J.

**Aerospace Corp.  
San Bernardino, Calif.**

Nowlan, D. T.  
Ross, R. F.  
Steiger, M. H.

**Air Force Armament Laboratory  
Eglin Air Force Base, Fla.**

Sears, E. S.

**Air Force Flight Dynamics Laboratory  
Wright-Patterson Air Force Base, Ohio**

Zonars, Dr. D.

**Air Force Special Weapons Center  
Kirtland Air Force Base, N. Mex.**

Luke, D. C., CAPT, USAF

**Air Force Weapons Laboratory  
Kirtland Air Force Base, N. Mex.**

Aungier, R., CAPT, USAF  
Fogarty, J. J., MAJ, USAF

**Applied Physics Laboratory, Johns Hopkins University  
Silver Spring, Md.**

Allen, R. W.  
Caywood, W. C.  
Cronvich, Dr. L. L.  
Hagan, J. C.  
Hart, H. H.  
Hill, Dr. F. K.  
Lucero, E. F.  
Marley, E. T.

Pace, N. G.

Paul, N. G.

Weckesser, L. B.

**Armament Development and Test Center  
Eglin Air Force Base, Fla.**

Bowers, B. R.

Butler, C. B.

Epstein, C. S.

**Army Ballistics Research Laboratories  
Aberdeen Proving Ground, Md.**

Frasier, J. T.

**Army Missile Command  
Redstone Arsenal, Ala.**

Henderson, J. H.

**Arnold Air Force Base, Tenn.**

Maderia, P. F., Jr., CAPT, USAF

**Arnold Research Organization Inc.  
Arnold Air Force Station, Tenn.**

Little, H. R.

Strike, W. T., Jr.

Welsh, C. J.

**Atlantic Research Corp.  
Costa Mesa, Calif.**

Baipsys, V. J.

**AVCO**

Wilmington, Mass.

Buss, H. M.

**Douglas Aircraft Co.  
Long Beach, Calif.**

Cebeci, T.

Kaups, K.

Keltner, G. L.

Kyle, R. L.

**Edgewood Arsenal  
Edgewood Arsenal, Md.**

Flatau, A.

Federal Aviation Administration  
Los Angeles, Calif.  
Hilton, J. H.

Fleet Missile Systems Analysis & Evaluation Group  
Corona, Calif.  
Betzer, W. E., CAPT, USN

FluiDyne Engineering Corp.  
Minneapolis, Minn.  
Casey, J. J.

General Dynamics, Corp.  
Pomona, Calif.  
Bird, L. R.  
Niemeier, B. M.  
Rimer, J. P.

General Dynamics Corp.  
San Diego, Calif.  
Butsko, J. E.  
D'Annunzio, M. G.

General Electric Co.  
Philadelphia, Pa.  
Kyriss, C. L.

Grumman Aircraft Engineering Corp.  
Bethpage, Long Island, N.Y.  
Cook, C. B.  
Kaufman, Dr. L. G. II  
Lu, H. R.

G.V.R. RAO Associates  
Sherman Oaks, Calif.  
Pursel, G. T.  
Rao, G. V. R.

Hercules Inc.  
Cumberland, Md.  
Freeman, W. T.

Hercules Inc.  
Magna, Utah  
Berhold, G. H.  
Scott, L. R.  
Zeamer, R. J.

Honeywell Inc.  
St. Louis Park, Minn.  
Brannan, J. D.  
Chase, T. W.  
Hopps, J. C.

Hughes Aircraft Corp.  
Canoga Park, Calif.  
Crowell, W. E.  
La Flash, J. C.  
O'Malley, T. P.  
Oswald, T. W.  
Stephenson, J. W.  
Williams, B. H.

Hughes Aircraft Corp.  
Culver City, Calif.  
Amano, M. R.

Lockheed Aircraft Corp.  
Burbank, Calif.  
Miller, L. D.

Lockheed Missiles and Space Co.  
Sunnyvale, Calif.  
Ericsson, L. E.  
McAlexander, R. L.

LTV, Aerospace Corp.  
Dallas, Tex.  
Browne, P. E.  
Gallagher, R. D.  
McWherter, R.

Martin Marietta Corp.  
Baltimore, Md.  
Delaney, Dr. L. J.

Martin Marietta Corp.  
Orlando, Fla.  
Gebhard, J. G.  
Hall, J. F.  
Sprague, G. H.

Massachusetts Institute of Technology  
Cambridge, Mass.  
Finston, M.  
Gollnick, A. F.  
Vlajinac, M.

**Vol. 1**

**McDonnell Douglas Astronautics Co.  
Santa Monica, Calif.**

Barnes, J. W.  
Beckwith, J. L.  
Cassel, L. A.  
Harvey, D. W.  
Hopkins, D. F., Jr.  
Maddox, A. W.  
Tang, Dr. H. H.  
Wright, John

**McDonnell Douglas Corp.  
St. Louis, Mo.**  
Bledsoe, J. L.

**National Aeronautics and Space Administration  
Ames Research Center  
Moffett Field, Calif.**  
Chapman, G. T.  
Peterson, V. L.

**National Aeronautics and Space Administration  
Langley Research Center  
Hampton, Va.**  
Spearman, M. L.  
Stainback, P. C.

**Naval Air Development Center  
Johnsville-Warminster, Pa.**  
Adams, F. T.  
Cavallo, B. L.  
Hess, J. R.

**Naval Air Systems Command  
Washington, D.C.**  
Belding, J. A., Jr.  
Dellinger, C. Y., Jr., CDR, USN  
Desmond, G. L.  
Ornoff, H.  
Pierce, F. S.  
Riley, J. B.  
Schneider, R. J., RADM, USN  
Volz, W. C.  
Williams, G. A., LTCOL, USAF

**Naval Air Test Center  
Patuxent River, Md.**  
Maughlin, R., LCDR, USN

**Naval Missile Center  
Point Mugu, Calif.**  
Beanfield, B. F.  
Cooper, G. F.  
Elliott, T. W.  
Gardner, C. A.  
Gnagy, J. R.  
Ingalls, R.  
Kopan, E. L.  
Larsen, K. A.  
Peterson, R. H.  
Stork, F. D.

**Naval Ordnance Laboratory  
White Oak, Md.**  
Anderson, J. D., Jr.  
Bixler, D. N.  
Dengel, Dr. O. H.  
Feldhuhn, R. H.  
Harris, Dr. E. L.  
Hastings, S. M.  
Huang, Dr. P. C.  
Humphrey, R. L.  
Kluth, E. E.  
Lee, R. E.  
Lobb, Dr. R. K.  
Madden, M. T.  
Schindel, Dr. L. H.  
Sheetz, N. W.  
Van Tuyl, Dr. A. H.  
Werle, Dr. M. J.  
Wilson, D. M.  
Wilson, Dr. R. E.

**Naval Ordnance Systems Command  
Washington, D.C.**  
Drimmer, B. E.  
Pasiuk, L.  
Seidman, O.

**Naval Postgraduate School  
Monterey, Calif.**  
Nunn, Dr. R. H.

**Naval Ship Missile Systems Engineering Station  
Port Hueneme, Calif.**  
Shao, E. A.

**Naval Ship Research and Development Center  
Washington, D.C.**

Anderson, Dr. A. W.  
De los Santos, Dr. S.  
Ellis, B. K.  
Patapis, I. C.  
Pick, G. S.  
Sekellick, M. A.  
Tai, T. C.  
Thompson, R. H.

**Naval Weapons Center  
China Lake and Corona, Calif.**

Amlie, Dr. T. S.  
Anderson, C. H.  
Carter, S. K.  
Cunningham, L. M.  
Etheridge, M. R., CAPT, USN  
Forbis, R. E., CDR, USN  
Freeman, J. V.  
Haseltine, Dr. W. R.  
Johnson, C. H.  
Kelly, Dr. H. R.  
Maddox, A. R.  
Markarian, C. F.  
Meeker, R. E.  
Myers, W. A.  
Netzer, J. V.  
Newkirk, H. L.  
Ohleyer, G. J.  
Okauchi, K.  
Oliver, D. W.  
Parmenter, W. W. E.  
Peoples, J. R.  
Premselaar, T. B.  
Riggs, L.  
Ryan, B. M.  
Schultz, L. D.  
Seeley, L. W.  
Serpanos, J. E.  
Smith, R. E.  
Thielbahr, W. H.  
Thomas, L. P.  
Thomas, R. W.  
Van Aken, R. W.  
Werback, W. J.  
West, W. W.

**Naval Weapons Laboratory  
Dahlgren, Va.**

Brown, D. R.  
Caster, H. P.

Chadwick, W. R.  
Frick, Dr. C. H.  
Gros, J. R.  
Jones, D. A.  
Kemper, Dr. W. A.

**Norden Division, United Aircraft Corp.  
Norwalk, Conn.**  
Simpson, J. A.

**North American Rockwell Corp.  
Columbus, Ohio**  
Davison, P. H.

**Northrop Corp.  
Hawthorne, Calif.**  
McNally, D. J.  
Wheldon, W. G.

**Pacific Missile Range  
Point Mugu, Calif.**  
Stearns, W., CAPT, USN

**Picatinny Arsenal  
Dover, N. J.**  
Mertz, D. H.  
Wasserman, S.

**Raytheon Co.  
Bedford, Mass.**  
Casazza, S. A.  
Filbin, R. F.  
Kent, K. E.  
Morse, D. S.  
Rapp, G. H.  
Sanders, D. H.

**Sandia Corp.  
Albuquerque, N. Mex.**  
Bustamante, A. C.  
Curry, W. H.  
Hartley, D. L.  
Kelsey, J. R.  
Millard, W. A.

**The Boeing Company  
New Orleans, La.**  
Wilkinson, C. L.

**The Boeing Company  
Seattle, Wash.**  
Giese, D. J.



## INTRODUCTION

The base and lee side flows of slender bodies represent fundamental fluid mechanics problems which derive their basic features from the fact that flow separation exists. The necessity of studying these regions in detail has been dictated by the effect of their local flow properties on guidance, maneuverability, communication and identification of high speed vehicles. Design of vehicles or components that will function in the separated flow regimes is only possible if a reasonably complete picture of the flow field is available. Due to the extreme complexity of the flow, which at the present is not completely understood physically, there are formidable difficulties in the analytical solution of the problem.

A configuration that demands considerable attention is the slender body at angle attack. This problem is of extreme practical importance since a maneuverable missile will not be at zero attitude throughout its entire flight trajectory. In fact, in such vehicles, the angle of attack can be quite large.

Fig. 1 illustrates a tentative picture of the flow field around a slender body at angle of attack in super/hypersonic speeds. Experimental measurements in Ref. 1 indicate that some features of this model might be correct, others (such as the mixing of the lee side flow with the base flow and the shape and characteristics of the base flow), however, are based on intuition. The flow field shows the presence of shock waves (besides the primary shock there are imbedded secondary shocks on the lee side). These are associated with strong pressure gradients which give rise to interactions between boundary layers and shock waves. These interactions lead to flow separation. The incidence of the slender body to the primary flow causes vortex generation which results in rolled up vortex sheets in the flow. Recently there were indications that these vortex sheets might cause the reattachment of the flow at the leeward meridian.

It is obvious from the aforesaid that analysis dealing with first principles only will not yield results, and a great deal of empiricism must be employed to obtain engineering solutions which can be used to predict pressure and heat transfer in the leeward and base regions of a general body of revolution.

A comprehensive review of the available base flow theories in supersonic flow was recently presented in Ref. 2, where some 175 papers and articles were reviewed. Base flow theories may be divided into



four main groups, namely semiempirical theories, those based on the Chapman-Korst model, integral methods, and multimethod base flow theories which attempt to take the dynamics of the recirculating flow into account.

The overwhelming majority of the experimental information reported in the literature (in the form of pressure and heat transfer data in the base region) deals with either two-dimensional or zero angle of attack axisymmetric geometries. A comprehensive summary of the experimental reports issued over the past several years on this subject has been presented in Ref. 3, and includes near wake data for a variety of vehicle configurations, free stream Mach numbers, Reynolds numbers, wall temperature ratios, etc.

The the past few years a few investigators obtained some data in the base region of slender cones at angles of attack up to  $10^\circ$ . Schlesinger and Martelluci (Ref. 4) tested a  $10^\circ$  half angle cone at  $M_\infty = 6.0$  and at a  $10^\circ$  angle of attack. The free stream Reynolds number is sufficiently large so that fully turbulent flow was achieved both on the cone surface and in the near wake. Significant changes in the flow field were observed due to the angle of attack of the body compared to the zero angle of attack configuration.

Schmidt and Cresci (Ref. 5) examined the flow characteristics in the near wake, a  $10^\circ$  half angle cone at  $M = 7.7$  and at  $10^\circ$  angle of attack for laminar flow. They obtained radial variations of pitot and static pressures at selected axial location in the near wake. Their measurements indicated that the angle of attack produced a region on the leeward side of the cone surface wherein the boundary layer which was originally laminar on the windward side became transitional or turbulent at lower Reynolds numbers than expected from the axisymmetric flow case. This effected the mixing processes and therefore the behavior of the local flow conditions in the wake. In addition, it appeared that for the angle of attack configuration there was a large scale mixing caused by the vertical inviscid flow above the cone surface. Pitot pressure profiles showed that the symmetry axis in the viscous core was displaced toward the leeward side of the cone by about one tenth of the base diameter. The stagnation pressure ratio increased by a factor of five above the laminar axisymmetric flow conditions.

Much of the published experimental information concerning base flow has been clouded by the uncertainty introduced by model support interference. The sting model support system, in common usage in wind tunnel measurements, is bound to distort the flow field to some degree; consequently, the reliability of the resulting data might be questionable.

It is the objective of the experimental program currently in progress in the Aerodynamics Laboratory of NSRDC to obtain reliable, interference-free data of separated flow regimes surrounding slender

### Vol. 1

bodies at angles of attack for a wide range of speeds (subsonic to hypersonic) and angles of attack (up to  $60^\circ$ ). These data would facilitate engineering solutions which can be used to predict fluid flow properties in the leeward and near wake regions. Furthermore, it is hoped that the final outcome of the program would contribute to the basic understanding of the physical mechanisms which govern the fluid dynamic behavior in the separated flow regimes.

To date, the major emphasis has been placed on establishing the basic parameters of the problem, developing and testing methods of model support in the wind tunnel which would have only a small effect on the separated flow, and evaluating suitable instrumentation for the final experiments. To this end a series of preliminary experiments were carried out at  $M = 6.22$  and  $9.89$ , and unit Reynolds number of  $1 \times 10^6/\text{ft.}$ , for angles of attack up to  $60^\circ$  using sting mounted, band supported, and free drop models. In these experiments surface and base heat transfer, base pressure and wake survey tests were conducted together with oil flow, schlieren, and high-speed motion picture visualization techniques. The results of these tests are outlined in the present report.

A considerable amount of work was done on the development of a direction insensitive miniature total pressure probe, to be used in subsequent surveys of separated flow regions, and on the evaluation of a multi-channel pressure telemetry system installed in the base of a small model. The results of this work are reported in Ref. 20.

## TEST APPARATUS AND EXPERIMENTAL TECHNIQUES

### WIND TUNNEL FACILITY AND DATA ACQUISITION SYSTEM

All of the experiments described herein were conducted in the NSRDC hypersonic facility. High speed acquisition of all test data is provided by a high-speed fifty-channel Beckman Model 210 data acquisition system. Details of the facility can be found in Ref. 6.

### MODELS AND MODEL MOUNTING SYSTEMS

Several models with identical outside dimensions were used in the test program. The basic model configuration consisted of a  $9^\circ$  half angle, six inches long, sharp cone. All the models were fabricated from type 416 stainless steel with mirror surface finishes and geometric tolerances of  $\pm 0.001$  inch.

#### Sting Mounted Model

This configuration was used to obtain heat transfer and base pressure data. Some wake and lee side surveys and oil flow information

relating to separation lines were also performed with this model.

Four Chromel-Alumel thermocouples were installed on the surface of the  $9^\circ$  cone three inches from the tip and  $90^\circ$  apart to measure surface heat transfer. In addition, one chromel-alumel thermocouple was mounted in the base of the model.

Base pressures were measured at two locations,  $180^\circ$  apart at 0.612 inches from the model axis. The model support assembly was attached to the sector at the base of the sting. Fig. 2 shows the sting mounted cone assembly in the test section.

#### Band Supported Models

In order to accommodate a model support with minimal effect on the separated flow regimes, a horizontal carriage system was designed and installed in the hypersonic tunnel.

The model support itself consisted of two 7-inches long, 0.029 inch thick, and 0.50 inches wide bands constructed of a special steel alloy (uniloy A-286) which did not lose its tension strength at high temperatures (higher than 90,000 psi at  $1500^\circ$  F). Fig. 3 shows a photograph of the band support system.

### PRESSURE INSTRUMENTATION

#### Total Pressure Transducers

Two calibrated Statham pressure transducers 0-2 and 0-5 psia were used for the Mach and various wake surveys. These were accurate and repeatable to within  $\pm 0.5\%$  full scale.

#### Base Pressure Transducers

Because base pressure values at hypersonic speeds are quite low, conventional pressure transducers would be inadequate. Therefore two low pressure, Datametrics type 1014 Electronic Manometer and type 511-3 Barocel pressure sensor systems were used for these measurements. These systems were capable of measuring pressures between 0 and 1 psia on seven consecutive scales from 0.001 to 1.0 psi full scale with accuracy and linearity of  $\pm 0.1\%$  of full scale in each range. The National Bureau of Standards calibrated both systems to  $\pm 0.05\%$  full scale accuracy.

### Vol. 1

interference in supersonic speeds. It has been confirmed that the base pressure is strongly influenced by sting interference. Based on Refs. 8 to 12 the measured critical sting-to-base diameter and sting length-to-base diameter ratios for laminar flow were plotted and faired in Figs. 5 and 6 as functions of the Mach number. In the present experiments structural considerations limited the maximum sting length-to-base diameter ratio to 9.3, and the minimum sting diameter-to-base diameter ratio to 0.32. These were used in both tested Mach numbers. At  $M = 6.22$  the sting geometry is not too far from the extrapolated values of about 9.7 and 0.20. At  $M = 9.89$  the data of Figs. 5 and 6 will not yield meaningful results, and therefore the zero angle of attack base pressure measurement is compared with free flight model tests under similar conditions. This comparison with references shows that the measured data in the present experiments are in fair agreement with the reported data values.

There is no information in the literature about sting effects at angle of attack and therefore the data presented here should only be regarded as preliminary.

#### Pressure-Time Response

Since the measured base pressure values were quite low, considerable time was required to reach steady state. Computations, based on Ref. 13, showed that in the present apparatus, depending on the measured pressure, the time response ranges from 20 to 45 seconds for 1 percent accuracy. Subsequent measurements showed these time estimates to be within  $\pm 8\%$  of experimental value.

#### Pressure-Error Due to High Temperature

Model surface pressure measurements leeward side, and base pressure readings are subject to error due to a gaseous flow phenomenon which occurs at the boundary of a surface and a gas at low pressure and high temperature. Ref. 14 presents a computational procedure for the error estimation. According to this calculation, the maximum error at  $M = 9.89$  is around 2.5%, the average error however is less than 1%. The data are not corrected for this error.

#### ACCURACY ESTIMATES

Due to slight instrumentation inaccuracy certain errors exist. It is estimated that quantities which are computed on the basis of pitot pressure measurements, such as Mach number and wake surveys, have a probable error of  $\pm 1\%$ . The individual temperature measurements have a probable error of  $\pm 2\%$ . The error of base pressure measurements below  $\alpha = 20^\circ$  is tentatively estimated at  $\pm 25\%$ , this increases to  $\pm 50\%$  at  $\alpha = 40^\circ$ . Beyond this pitch angle the sting effects completely

invalidate the base pressure data.

## RESULTS AND DISCUSSION

### SURFACE TEMPERATURE DISTRIBUTION

A sample of the measured temperature-time data is presented in Fig. 7. The time history shows that the initial transient after model injection die out in about 4 seconds and thereafter the slopes are nearly constant. The highest heating rate occurs at the most windward side which is signified by the highest temperature-time slope. The temperature-time rate  $90^\circ$  from the windward meridian is equal on each side throughout the angle of attack range showing that the flow is symmetrical about the meridian plane. The heating rate on the lee side apparently is higher than in the base region.

Fig. 8 shows the temperature-time slopes on the windward, leeward meridians and at two locations on the base region for  $M = 9.89$ . The slopes in the meridian planes stay relatively constant below an angle of attack of  $10^\circ$ ; however, beyond that angle they increase rapidly. It is interesting to note the nonuniformity of the base temperature distribution beyond  $10^\circ$  angle of attack. As the angle of attack increases the wrapped shock heats up the near wake and base region in the windward half of the base while the temperature-time rate is relatively low in the base area far from the shock. In this area the base temperature slope is nearly constant up to  $27^\circ$  of angle of attack and beyond this the increase is still moderate.

Another significant point is the large difference in the temperature slope between the base region and the leeward meridian. Recent tests at NOL indicated that the rolled up vortex sheets generated at angles of attack might be reattaching close to the leeward meridian thereby causing a local peak in heat transfer. This could then be the reason for the large temperature slope difference. The results were similar in the  $M = 6.22$  speed range.

### BASE PRESSURE MEASUREMENTS

Base pressure measurements were made with the sting mounted model at several angles of attack between  $0$  and  $60^\circ$  for both  $M = 6.22$  and  $9.89$ . A sample of the base pressure-time history data is presented in Fig. 9. The settle-out time in that particular run was about 20 seconds. The base pressures at both locations at  $\alpha = 0$  were nearly the same. Furthermore, this is true even at angles of attack as shown in Figs. 10 and 11, where the base pressure ratios (nondimensionalized by the free stream static pressure) are presented as functions of the angle of attack for  $M = 6.22$  and  $9.89$ . This observation, at least for



## Vol. 1

$\alpha = 0$ , was confirmed by other investigators who demonstrated that the base pressure distribution on blunt based axisymmetric bodies exhibited a slight maximum in the geometric center with an axially symmetric decrease toward the edge of the base.

In view of the axial symmetry of the base pressure distribution, it is not unreasonable that the obtained data at zero angle of attack show similar values, particularly since the sensing orifices were located at  $180^\circ$  apart and equi-distant from the center axis.

As shown in Figs. 10 and 11, the base pressure ratio is nearly constant below about  $15^\circ$  angle of attack and then increases. This was also confirmed, Ref. 15, for a  $5^\circ$  cone angle. Beyond about  $40^\circ$ , because of the sting effects, no steady base pressure value could be reached.

A fair amount of confidence in the data obtained here may be gained by comparing it to the work of other investigators. Based on a large number of experimental measurements conducted in the  $M = 7.7$  to  $19.0$  speed range, both for laminar and turbulent flows, an empirical base pressure correlation was developed recently for a  $10^\circ$  half angle sharp cone at zero angle of attack. Fig. 12 shows the base-to-freestream static pressure ratio as a function of both the freestream Mach and Reynolds numbers. The correlation equation may be expressed as:

$$P_B/P_\infty = 0.33 \left[ M_\infty^3 / \sqrt{\text{Re}_d} \right]^{0.75} \quad (5)$$

where the base diameter is the characteristic length in the Reynolds number computation. The measured base pressure ratios at  $M = 6.22$  and zero angle of attack are apparently close to the predicted value of Equation (5). In our case  $M_\infty^3 / \sqrt{\text{Re}_d} = 0.53$  and consequently from Fig. 12  $P_B/P_\infty \approx 0.21$ . This is shown in Fig. 10.

Theoretical calculation in Ref. 16 (showing the effect of cone angle bluntness ratio and Mach number on the base pressure ratio) predicts base pressure ratio values of 0.17 for  $M = 6.22$  and 0.19 for  $M = 9.89$ . Both are in good agreement with the measured values at  $\alpha = 0$  considering all the uncertainties. These values are shown in Figs. 10 and 11.

## CONE SHOULDER AND NEAR WAKE SURVEY

The data from this survey has not been completely analyzed yet but preliminary indications are that the band support does not disturb the near wake significantly. However, a more thorough examination of the data and some additional measurements are forthcoming.

## TWO-DIMENSIONAL WAKE SURVEY

The objectives of this part of the investigation were to determine the effect of the band support on the flow field and demonstrate that it is smaller than the effect of the wire support which was claimed to have no interference with the near wake flow. According to Ref. 17, a critical wire diameter-to-base diameter ratio range exists below which there is no interference due to the wire support. They found that this critical diameter ratio is in between 0.0031 and 0.0062. In the present case the critical wire size would be 0.012 inches in diameter. To begin with, this wire would support only about 0.5 lb. and in the present configuration the maximum load is on the order of 15 lbs. This would necessitate the use of 30 wires which is unfeasible. A more realistic wire size would be the 0.02 inch diameter which would exceed the prescribed size but which would have the load bearing capacity of about 5 lbs. Both of these sizes were tested together with the band support and indeed it turned out that the band support has the smallest disturbing effect on the flow; its shock strength is lower than either of the wires. The schlieren picture of the wake of the band support is shown in Fig. 13 at  $M = 6.22$ , while for the same Mach number the wake shock for the 0.02 inch diameter wire is shown in Fig. 14. The quantitative results of the wake survey at  $M = 6.22$  are shown in Figs. 15 to 17. The data are presented in terms of nondimensionalized quantities. The vertical distance is nondimensionalized by the thickness of the band or the wire diameters respectively, and the pitot pressure is divided by the freestream pitot pressure. At freestream conditions,  $P_{T_2}/P_{T_2\infty}$  is unity. When the value is larger the probe encounters a shock region, conversely where it is smaller the wake region is traversed. Fig. 15 shows the vertical wake traverses of the band support at six horizontal locations behind the trailing edge of the band. Fig. 16 shows six traverses for the 0.02 wire and Fig. 17 gives three wake traverses for the 0.01 wire. In all three cases, the wake widens downstream. The shock locations closely correspond to the locations in the schlieren photographs.

## FLOW VISUALIZATION

Oil Flow

The surface streamlines appear to indicate a strong cross flow at angle of attack which was also noted by several authors (see Refs. 1 and 15 for example). They seem to form an inflection line at the azimuthal angle corresponding to the minimum surface pressure and then became tangent to the separation line a few degrees behind the minimum pressure line. Fig. 18 illustrates the oil flow patterns in this experiment. Protractor measurements indicated that beyond  $20^\circ$  angle of attack at both tested Mach numbers, flow separation occurs at

### Vol. 1

approximately  $142^\circ$  as shown in Fig. 19. To within the accuracy of the present data, flow separation appears to occur along a conical generator. The appearance of a separation line very close to a local minimum in pressure is consistent with the data presented in Ref. 18 and Ref. 1. The oil flow pattern exhibited the same behavior for both the sting and band supported models.

### Schlieren Photos

Schlieren photos indicated that the incipient shock on the windward side of the body becomes highly curved downstream of the model at high angles of attack. The shock strength is very small on the leeward side shock and approximates a shock wave. A shock is visible on the underside of the sting at high angles of attack as shown in Fig. 20. This shock interacts with the incipient shock on the windward side. The appearance of the shock wave on the sting indicates that the near wake flow is supersonic.

### High Speed Motion Pictures

High speed movies were taken of the motion of the band supported model. Analysis of these motion pictures indicated that the natural frequency of yawing oscillation of the band supported model was about 5 cps, and no asymmetric forces acted on the band supported model at angle of attack and consequently it was stable and at zero degree yaw angle in the yaw plane.

## CONCLUSIONS

A preliminary experimental investigation, concerning the aerothermodynamic characteristics of hypersonic flows around a highly inclined  $9^\circ$  half angle sharp cone at Mach numbers of 6.22 and 9.89, has been conducted. In addition, some work was performed in developing suitable instrumentation for a detailed investigation of separated flow regimes in all speed ranges around highly inclined axisymmetric bodies. From this investigation the following conclusions are made:

1. The base pressure measurements showed an increase with angle of attack. The zero angle of attack base pressure values agree well with those reported in the literature.
2. The base temperature distribution and slopes are effected by the angle of attack, but they are lower than the surface temperatures around the model.
3. The two-dimensional wake survey showed that the band support has a smaller effect on the flow field than even thin wires.



4. The location of the measured separation line is in good agreement with the reported values of other investigators.

5. No significant forces act in the yaw plane of angle of attack.

#### FUTURE PLANS

A detailed investigation of the leeward side and near wake regions of slender bodies at high angles of attack in the super/hypersonic speed range is planned in the near future. The support system (discussed in the present paper) and the advanced instrumentation developed (see Ref. 20) will be utilized in the program.

#### REFERENCES

1. California Institute of Technology. Hypersonic Flow over a Yawed Circular Cone (U), by Richard R. Tracy. Pasadena, Calif., August 1963. 135 pp. (Memorandum No. 69, publication UNCLASSIFIED)
2. University of Cincinnati. Survey and Evaluation of Supersonic Base Flow Theories (U), by P. W. Carpenter and W. Tabakoff. Cincinnati, Ohio, October 1968. 196 pp. (NASA CR-97129, publication UNCLASSIFIED)
3. AVCO. Measurements of Laminar and Turbulent Near Wakes (U), by A. Todisco and A. Pallone. Everett, Mass., January 1967. 18 pp. (AIAA Paper No. 67-30, publication UNCLASSIFIED)
4. General Applied Sciences Laboratory. Wind Tunnel Investigation of the Turbulent Near Wake of a Cone at Angle of Attack (U), by A. T. Schlesinger and A. Martellucci. Long Island, N. Y., March 1966. 55 pp. (Tech. Rpt. 581, publication UNCLASSIFIED)
5. Polytechnic Institute of Brooklyn. Near Wake of a Slender Cone in Hypersonic Flow (U), by E. M. Schmidt and R. J. Cresci. Brooklyn, N. Y., May 1967. 23 pp. (AGARD Conference on Fluid Physics of Hypersonic Wakes, Vol. I, publication UNCLASSIFIED)
6. David Taylor Model Basin. The David Taylor Model Basin Gas Dynamics Wind Tunnel Facility (U), by Norman G. Ziegler. Carderock, Md., TMB, July 1963. 20 pp. (Aero Rpt. 1027, publication UNCLASSIFIED)
7. Langley Aeronautical Laboratory. Aerodynamic Characteristics at a Mach Number of 6.77 of a  $9^\circ$  Cone Configuration, with and without Spherical Afterbodies, at Angles of Attack up to  $180^\circ$  with Various Degrees of Nose Blunting (U), by Luther Neal, Jr. Langley Field,

Vol. 1

- Va., NASA, May 1962. 19 pp. (NASA TN D-1606, publication UNCLASSIFIED)
8. Ames Aeronautical Laboratory. An Experimental Investigation of the Base Pressure Characteristics of Nonlifting Bodies of Revolution at Mach Numbers from 2.73 to 4.98(U), by J. O. Riller and F. M. Hamaker, Moffett Field, Calif., NACA, March 1955. 45 pp. (NASA TN 3393, publication UNCLASSIFIED)
  9. University of California. Results of Some Base Pressure Experiments at Intermediate Reynolds Numbers with  $M = 2.84$  (U), by Leslie L. Kavanau, Berkeley, Calif., April 1954. 3 pp. (Journal of Aeronautical Sciences, Vol. 21, No. 4, publication UNCLASSIFIED)
  10. Langley Aeronautical Laboratory. A Summary of Information on Support Interference at Transonic and Supersonic Speeds (U), by Eugene S. Love. Langley Field, Va. NACA, January 1954. 28 pp. (NACA RM L53K12, publication UNCLASSIFIED)
  11. Determination of Base Pressure from Free-Flight Data (U), by A. C. Charters and A. Turetsky. June 1948. 55 pp. (APG Rpt. No. 653, publication UNCLASSIFIED)
  12. Ames Aeronautical Laboratory. Experimental Investigation of the Effects of Viscosity on the Drag and Base Pressure of Bodies of Revolution at a Mach Number of 1.5 (U), by D. R. Chapman and E. W. Perkins. Moffett Field, Calif., NACA, January 1951, 36 pp. (NACA Rpt. 1036, publication UNCLASSIFIED)
  13. Arnold Engineering Development Center. A Method of Calculating the Response Time of Pressure Measuring Systems (U), by Robert C. Bauer. Tullahoma, Tenn., Arnold AFS, November 1956. 33 pp. (Arnold AFS TR-56-7, publication UNCLASSIFIED)
  14. California Institute of Technology. An Experimental Investigation of Pressure Gradients in Small Diameter Tubes (U), by William M. Howard. Pasadena, Calif., June 1955 (Ph. D. Thesis, publication UNCLASSIFIED)
  15. Naval Ordnance Laboratory. An Experimental Investigation of the Aerodynamic Characteristics of Slender Hypersonic Vehicles at High Angles of Attack (U), by R. H. Feldhuhn and L. Pasiuk. White Oak, Md., NOL, May 1968. 95 pp. (NOL TR 68-52, publication UNCLASSIFIED)
  16. General Electric Company. Ratio on Base Pressure (U), by John M. Cassanto. King of Prussia, Pa., December 1965. 2 pp. (AIAA Journal, Vol. 3, No. 12, publication UNCLASSIFIED)
  17. Polytechnic Institute of Brooklyn. An Experimental Investigation of the Near Wake of a Slender Cone at  $M_{\infty} = 8$  and 12 (U), by V. Zakkay and R. J. Cresci. Brooklyn, N. Y., PIBAL, January 1966. 5 pp. (AIAA Journal, Vol. 4, No. 1, publication UNCLASSIFIED)

18. Academy of Sciences, USSR. Investigation of the Laminar Flow Separation on a Cone at Angles of Attack (U), by V. A. Avduevsky and K. I. Medvedev. Moscow, USSR, March 1966. 2 pp. (Izvestia ANSSSR Fluid and Gas Mechanics, No. 3, publication UNCLASSIFIED)
19. Langley Aeronautical Laboratory. Wind Tunnel Investigation of a Number of Total Pressure Tubes at High Angles of Attack (U), by William Gracey. Langley Field, Va., NACA, June 1957. 18 pp. (NACA R-1303, publication UNCLASSIFIED)
20. Naval Ship Research and Development Center. Multi-Channel Pressure Telemetry System for Base Pressure Measurements on Small Models (U), by G. S. Pick and S. E. Dawson. Carderock, Md., NSRDC, May 1969. 12 pp. (IEEE 3rd International Congress on Instrumentation in Aerospace Facilities, publication UNCLASSIFIED)

TABLE I  
Tunnel Free Stream Conditions

Mach Number	6.22 $\pm 0.13$	9.89 $\pm 0.15$
Stagnation Pressure (psia)	148.5 $\pm 2$	511 $\pm 6$
Stagnation Temperature ( $^{\circ}$ F)	1129 $\pm 45$	1314 $\pm 50$
Stagnation Temperature Drop Through the Nozzle ( $^{\circ}$ F)	41 $\pm 4$	37 $\pm 7$
Run Time (seconds)	70	70
Increase in Stagnation Temperature During Run ( $^{\circ}$ F)	235 $\pm 45$	115 $\pm 55$
Reynolds Number/ft.	$1 \times 10^6 \pm 2\%$	$1 \times 10^6 \pm 3\%$

TABLE II  
OUTLINE OF TEST PROGRAM

Type of Test	Nominal angle of attack	$M_{\infty}$	$Re_{\infty}/ft$	Model 9° Cone	Remarks
Surface Temperature	0° - 60°	6.22, 9.89	$1 \times 10^6$	Sting mounted	Base Temperature also measured. Rolled 45 & 90°.
Base Pressure	0° - 60°	6.22, 9.89	$1 \times 10^6$	Sting mounted	Measured in two locations. Rolled 45 & 90°.
Cone Shoulder and Near Wake Survey	0°, 30°	6.22, 9.89	$1 \times 10^6$	Sting mounted. Band supported.	
2-Dimensional Wake Survey	--	6.22, 9.89	$1 \times 10^6$		Band, 0.01 in. and 0.02 in. dia. wire.
Flow Visualization	0° - 60°	6.22, 9.89	$1 \times 10^6$	Sting mounted. Band supported.	Schlieren.
	0°, 30°	6.22, 9.89	$1 \times 10^6$	Sting mounted. Band supported.	Oil flow. Oil Flow.

## APPENDIX

## DERIVATION OF ANGLE OF ATTACK CORRECTION

Using the equation of a simply supported cantilevered beam with a concentrated load on its free end, the maximum deflection angle can be expressed in the present conditions as:

$$\Delta\alpha = 5.68 \times 10^{-4} P \quad (1)$$

where  $P$  = concentrated load (lbs).

Since the model is a  $9^\circ$  half angle cone, the concentrated load acting at the end of the sting (which coincides with the center of the model) may be expressed as the normal component of the aerodynamic force on the cone or

$$P = C_N qS \quad (2)$$

where

$q$  = dynamic pressure (psi)

$S = 2.84 \text{ in}^2$

$C_N$  = the normal force coefficient and according to Ref. 7 it is a linear function of the angle of attack ( $\alpha$ ). For a sharp  $9^\circ$  cone this function may be expressed up to  $\alpha = 60^\circ$  as:

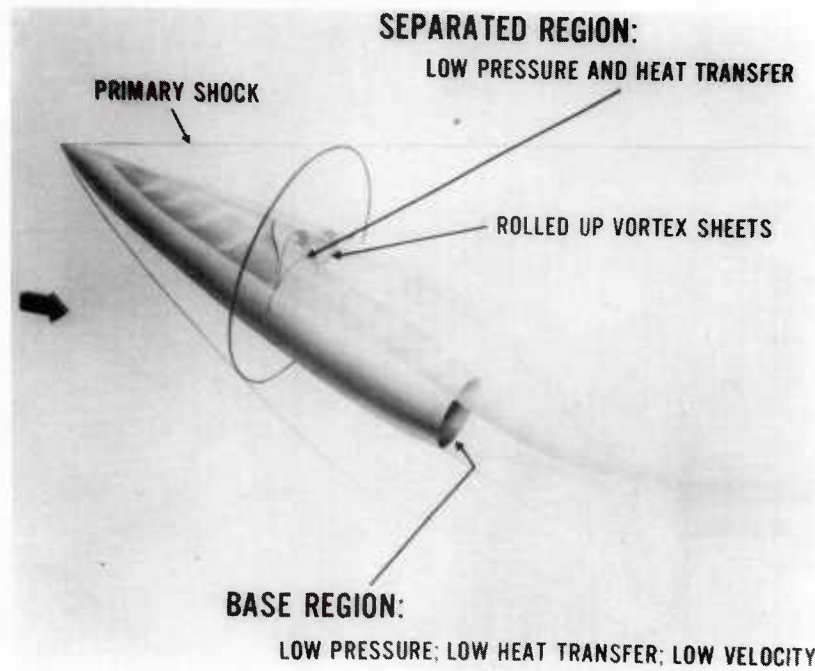
$$C_N = 0.04\alpha \quad (3)$$

where  $\alpha$  is in degrees.

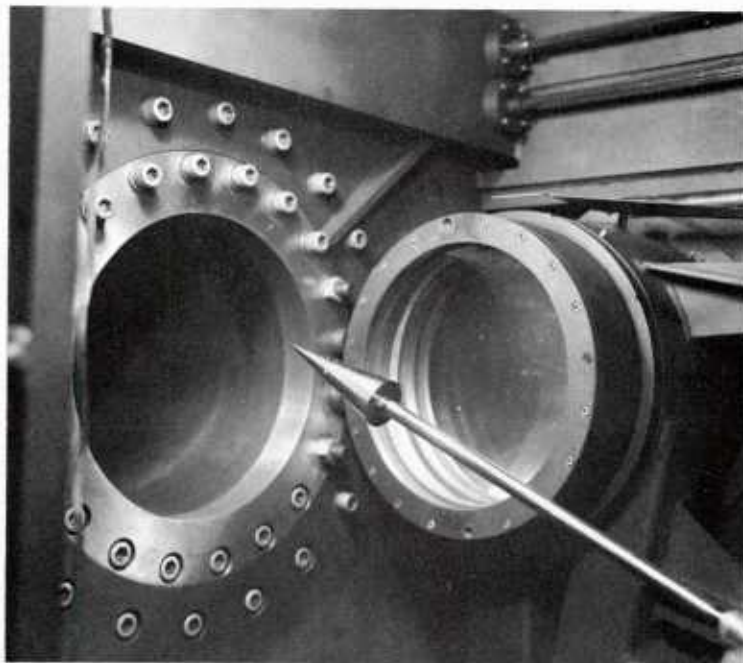
Combining Equations (5) and (7) and rewriting it in a more convenient form gives:

$$\Delta\alpha = 0.00372 \alpha \frac{q}{P_{to}} P_{to} \quad (4)$$

This equation was used in the data reduction program to correct for sting deflection.

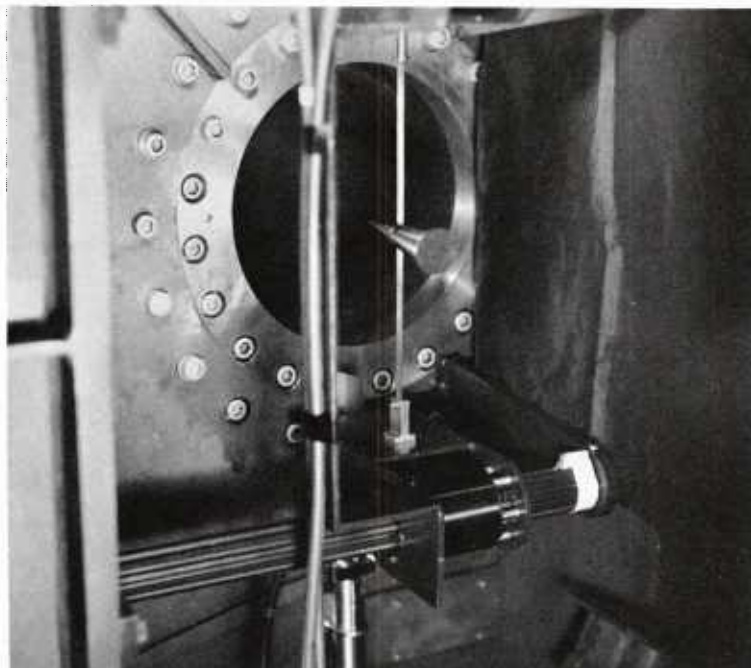


(U) Fig. 1. Flow Field of a Slender Body at Angle of Attack in Super/Hypersonic Flow

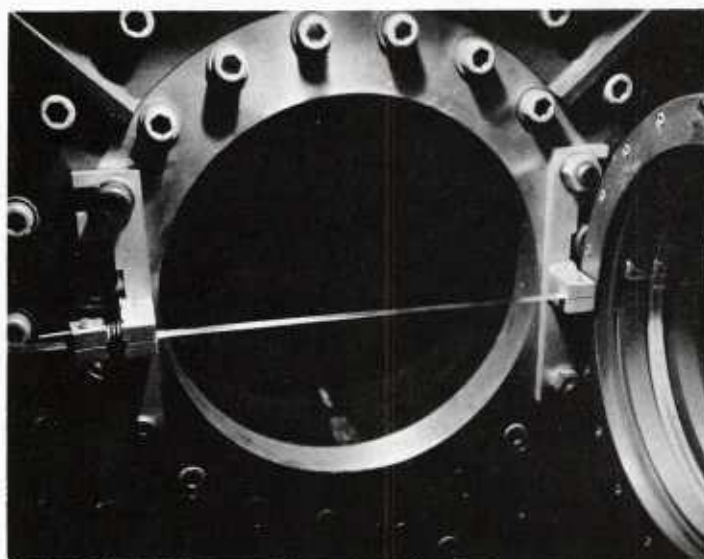


(U) Fig. 2. Sting Mounted Model in the Test Section



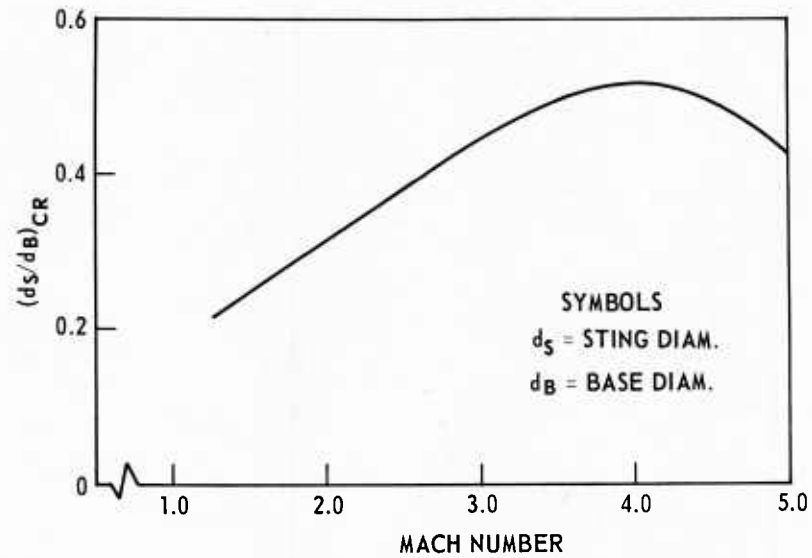


(U) Fig. 3. Band Supported Model in the Test Section

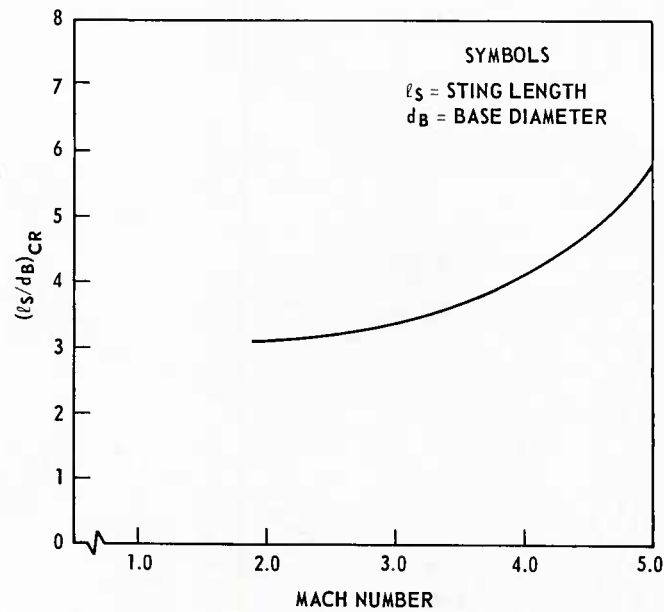


(U) Fig. 4. Band Support Installed at Nozzle Exit

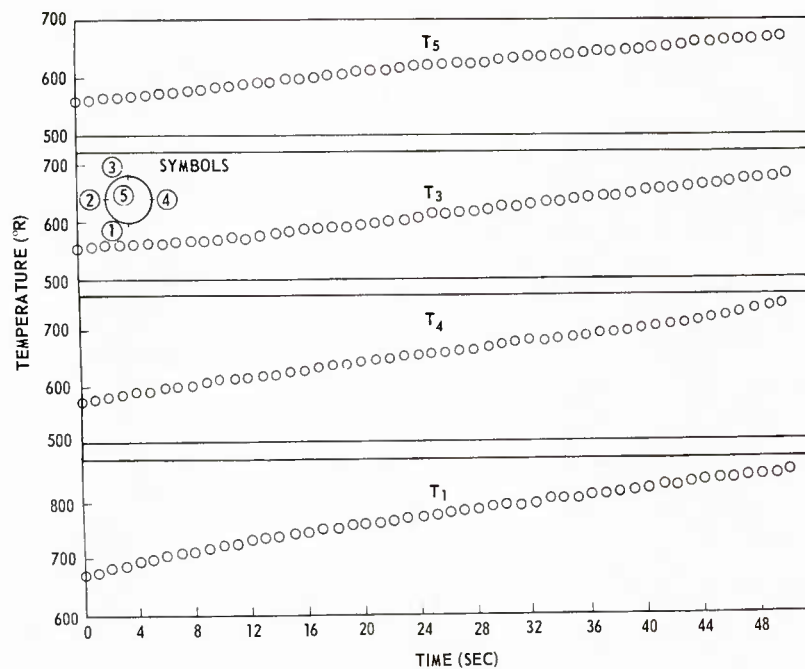




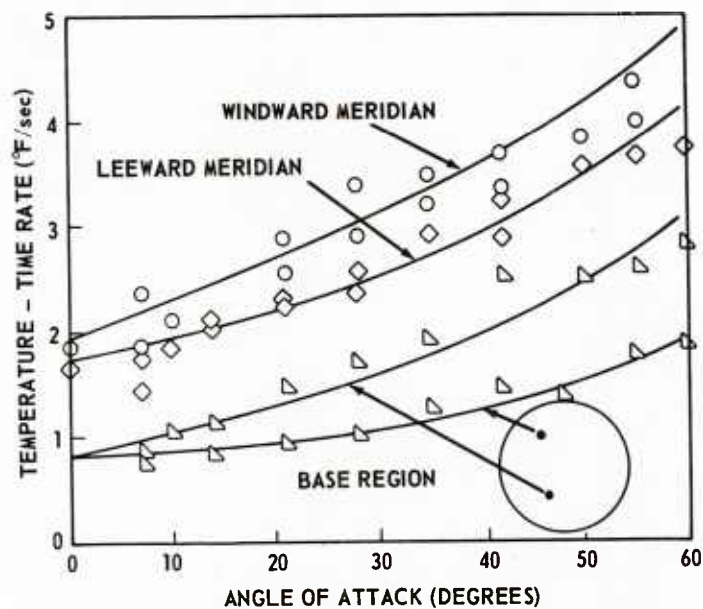
(U) Fig. 5. Critical Sting-to-Base Diameter Ratio as Function of Mach Number in Laminar Flow



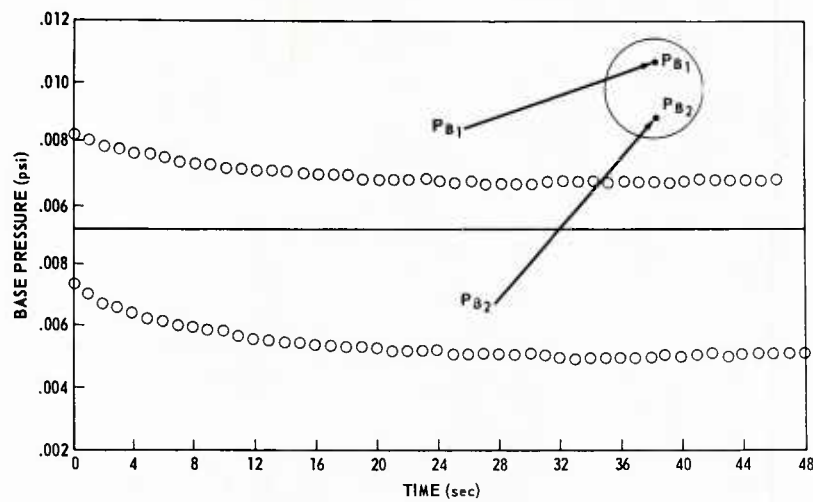
(U) Fig. 6. Critical Sting Length-to-Base Diameter Ratio as Function of Mach Number in Laminar Flow



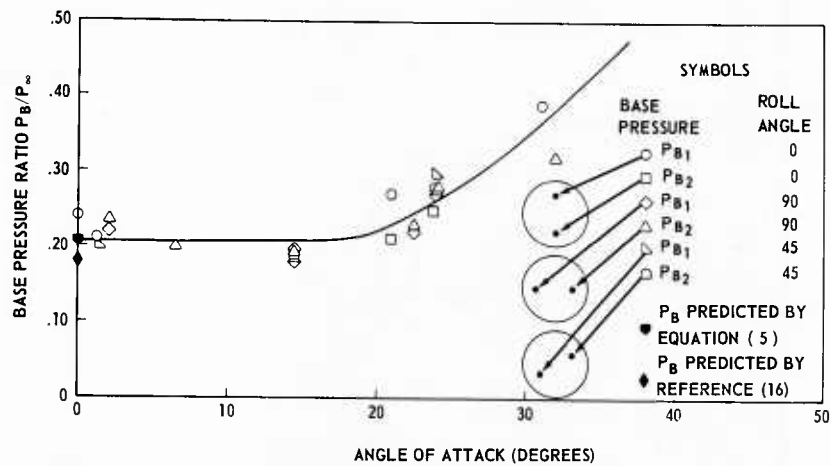
(U) Fig. 7. Temperature-Time History at  $\alpha = 35^\circ$  and  $M = 9.89$



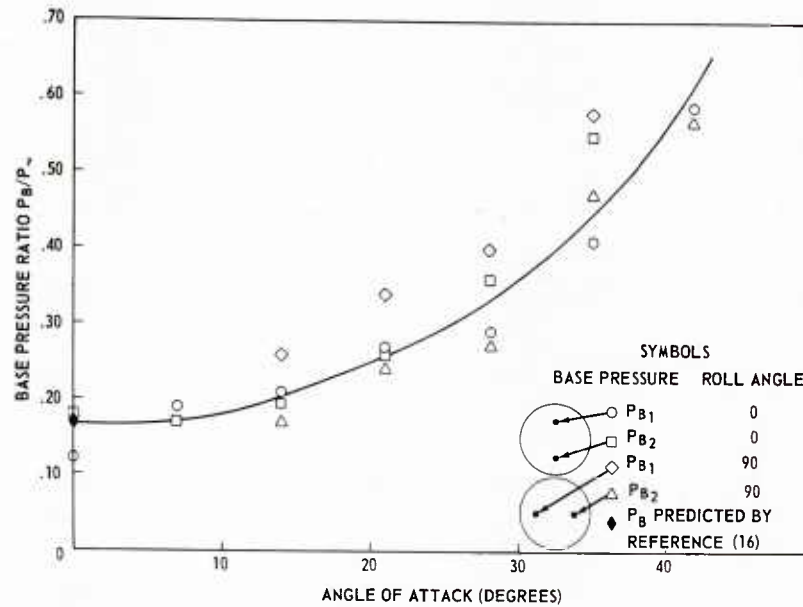
(U) Fig. 8. Temperature-Time Rate as Function of Angle of Attack at  $M = 9.89$



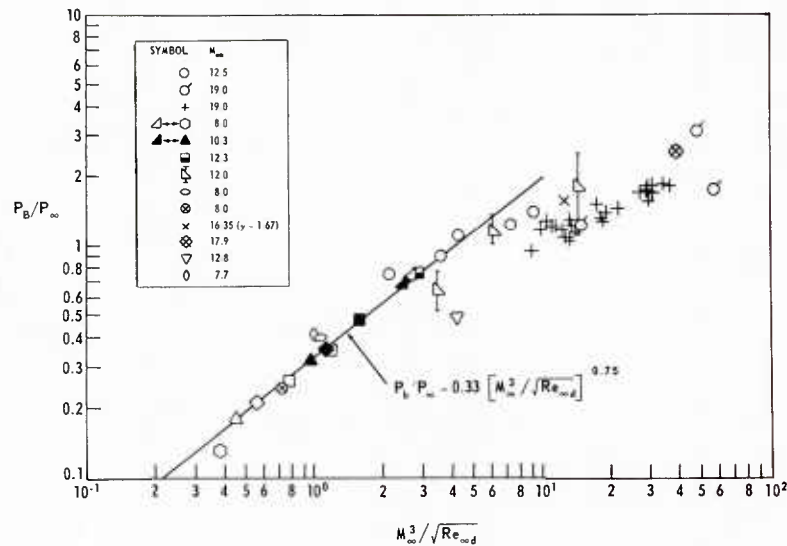
(U) Fig. 9. Base Pressure-Time History at  $\alpha = 28^\circ$  and  $M = 9.89$



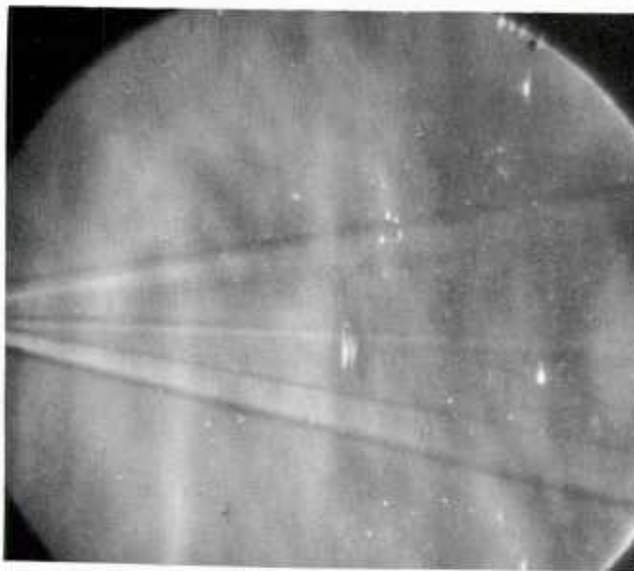
(U) Fig. 10. Base Pressure Ratio as Function of Angle of Attack at  $M = 6.22$



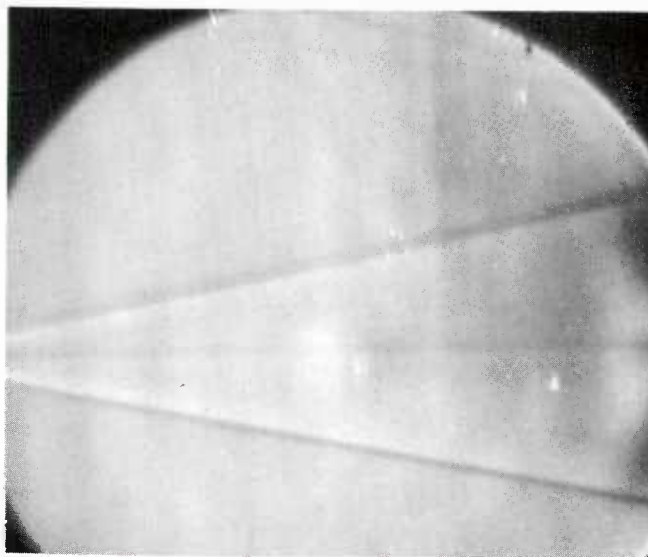
(U) Fig. 11. Base Pressure Ratio as Function of Angle of Attack at  $M = 9.89$



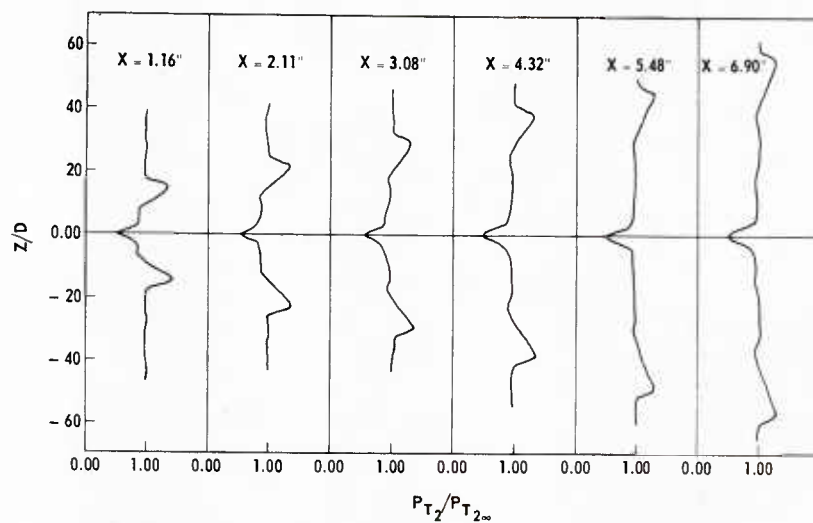
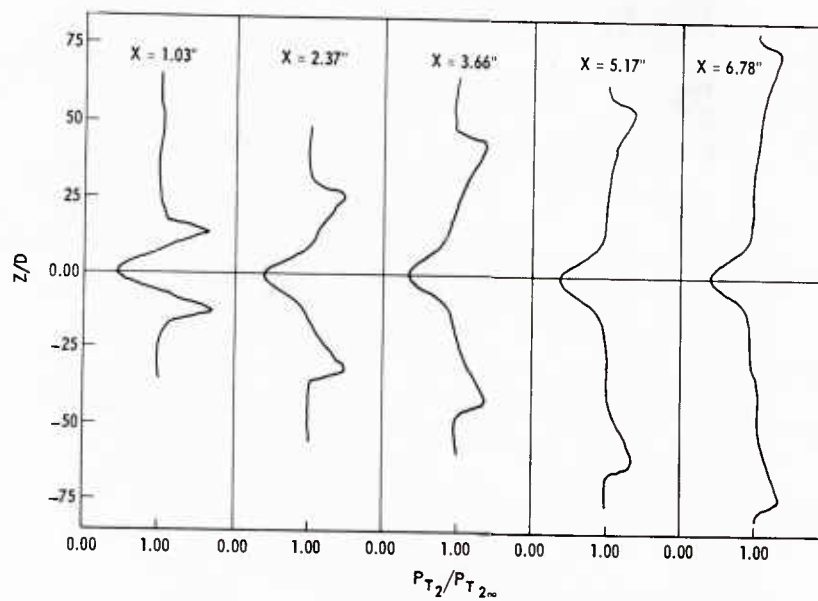
(U) Fig. 12. Base Pressure Correlation for 10° Half Angle Sharp Cone

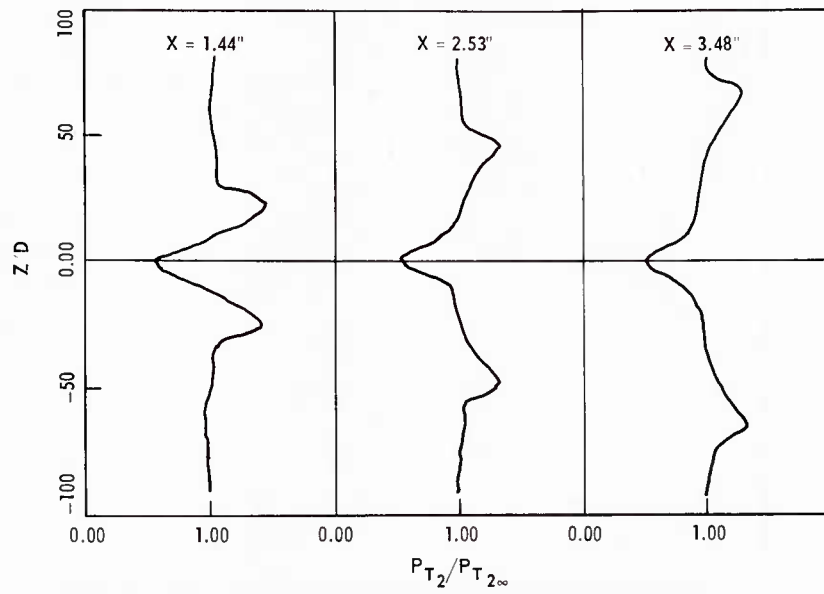


(U) Fig. 13. Wake of Band Support at  $M = 6.22$

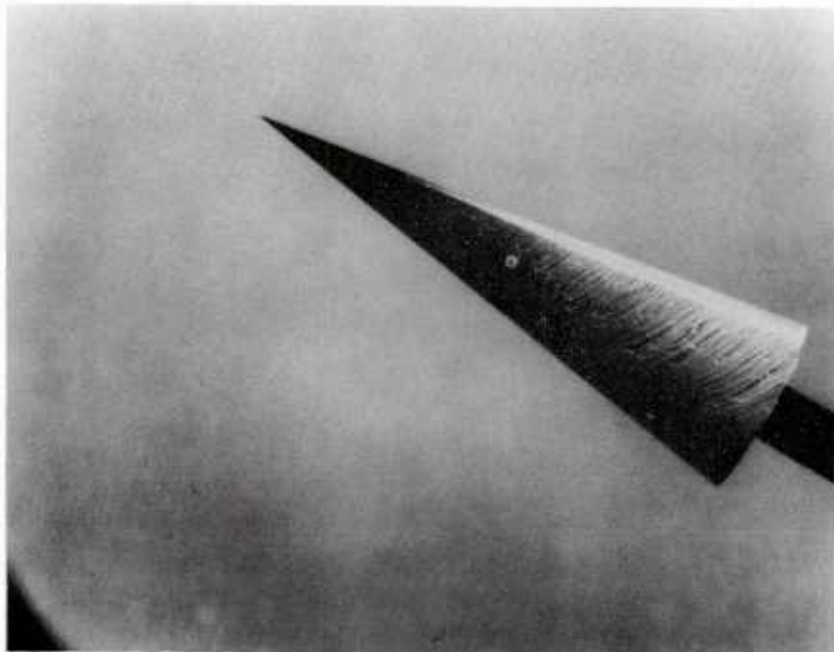


(U) Fig. 14. Wake of a 0.02" Dia. Wire at  $M = 6.22$

(U) Fig. 15. Wake Survey of the Band Support at  $M = 6.22$ (U) Fig. 16. Wake Survey Behind a 0.02" Dia. Wire at  $M = 6.22$

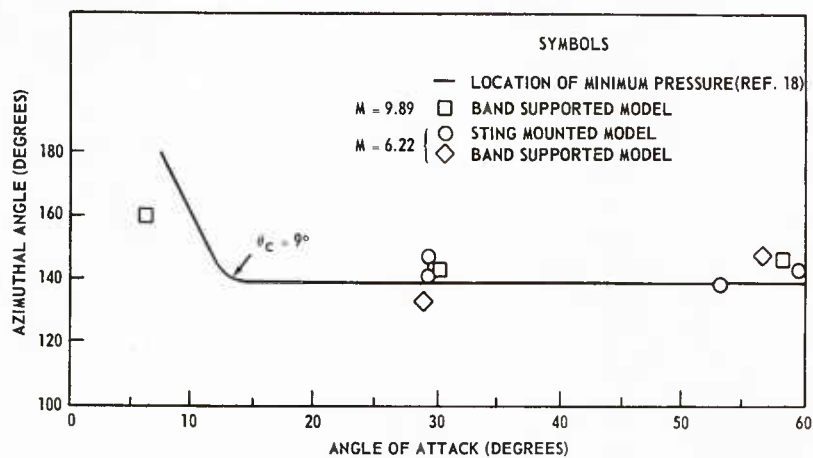


(U) Fig. 17. Wake Survey Behind a 0.01" Dia. Wire at  $M = 6.22$

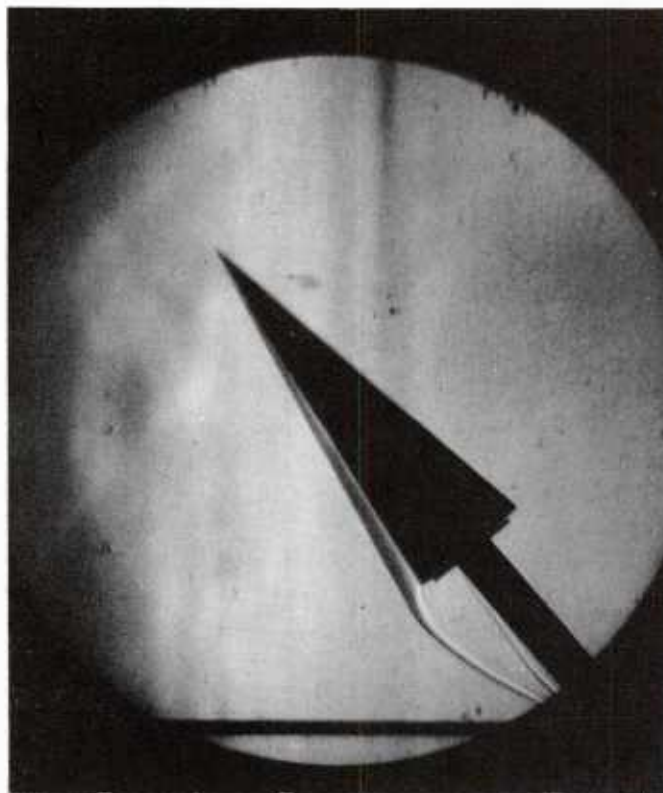


(U) Fig. 18. Oil Flow Pattern at  $\alpha = 28^\circ$  and  $M = 6.22$





(U) Fig. 19. Flow Separation Angle as Function of Angle of Attack



(U) Fig. 20. Schlieren Photograph of Cone at  $\alpha = 49^\circ$  and  $M = 6.22$

Paper No. 2

AN EXPERIMENTAL INVESTIGATION OF THE HYPERSONIC  
AERODYNAMIC CHARACTERISTICS OF SLENDER BODIES  
OF REVOLUTION AT HIGH ANGLES OF ATTACK\*

(U)

(Paper UNCLASSIFIED)

by

Robert Feldhuhn, Allen Winkelmann  
and Lionel Pasiuk\*\*

U.S. Naval Ordnance Laboratory  
White Oak, Silver Spring, Md. 20910

ABSTRACT. (U) An experimental investigation of the aerothermodynamic properties associated with axisymmetric bodies at large angles of incidence has been conducted in two of the wind tunnels at the Naval Ordnance Laboratory (NOL). During this study, surface pressure, heat transfer and static force measurements were obtained with a slender  $5^\circ$  half-angle cone. Static force measurements were also obtained with a  $2/3$  power-law body and two ducted cone configurations. In addition, flow visualization experiments and a limited series of Pitot-tube surveys provided some information concerning the separated flow field on the leeward side of a yawed cone.

\* The work described herein has been sponsored by the Advanced Research Projects Agency under ARPA order number 905, Program Code No. 6E30, as part of Project Defender.

\*\*Aerospace Engineer, Weapon Dynamics Division, Naval Ordnance Systems Command

## NOMENCLATURE

A	= maximum cross-sectional area of center-body (reference area for force measurements)
$C_D$	= drag coefficient - Drag/qA
$C_L$	= lift coefficient - Lift/qA
$C_P$	= specific heat of air at constant pressure
h	= heat transfer coefficient $\frac{\dot{q}}{T_O - T_W}$
L	= configuration length
M	= Mach number
$P_C$	= static pressure on surface of cone
$P_O$	= stagnation pressure
$P_{t_2}$	= Pitot pressure
$P_\infty$	= free-stream static pressure
q	= free-stream dynamic pressure
$\dot{q}$	= heat-transfer rate per unit area
Re	= Reynolds number: $Re_{\infty, L} = \frac{\rho_\infty U_\infty L}{\mu_\infty}$ ; $Re_{\infty, S} = \frac{\rho_\infty U_\infty S}{\mu_\infty}$
	$Re_{e, S} = \frac{\rho_e U_e S}{\mu_e}$ ; $Re_{e, \theta} = \frac{\rho_e U_e \theta}{\mu_e}$
	$Re_{r_n, \infty} = \frac{\rho_\infty U_\infty R_n}{\mu_\infty}$ ; $Re_{\infty, X} = \frac{\rho_\infty U_\infty X}{\mu_\infty}$

- $R_b$  = base radius
- $R_n$  = tip radius of curvature
- $S$  = distance from the tip measured along the surface of the cone
- $S_t$  = Stanton number  $\frac{h}{\rho U C_p}$
- $\overline{S}_{t_{\phi=0}}$  = calculated stagnation-streamline Stanton number for a yawed cylinder
- $T_o$  = free-stream stagnation temperature
- $T_w$  = wall temperature
- $U$  = velocity
- $X$  = distance from tip of model measured along the axis of symmetry
- $X_{cp}$  = distance of the center of pressure from tip of model measured along axis of symmetry
- $\alpha$  = angle of attack
- $\gamma$  = ratio of specific heats
- $\theta$  = boundary-layer momentum thickness
- $\theta_c$  = cone half-angle
- $\rho$  = density of gas
- $\tau$  = time
- $\phi$  = azimuthal angle measured from most windward meridian plane

#### Subscripts

- $e$  = local conditions at the outer edge of the boundary layer
- $\infty$  = free-stream conditions

## INTRODUCTION

(U) Increased interest in the development of maneuverable hypersonic vehicles has provided the impetus for the present investigation. Slender axisymmetric conical shapes and slender power-law shapes are of interest from this standpoint as center of pressure variation and aerodynamic drag, respectively, can be minimized with these configurations (refs. 1-4). However, if a body is required to achieve large lateral accelerations, axisymmetric configurations must sustain a large angle of attack and maintain a very high velocity in order to compensate for their low lift effectiveness characteristics. Both of these alternatives lead to rather substantial increases in convective heat transfer. Furthermore the possibility of sustaining large angles of attack immediately confronts the aerodynamicist with the fact that there will be large regions of separated flow on the leeward side of the vehicle. A description of the detailed characteristics of the leeward flow field is necessary in order to evaluate the control effectiveness and wake flow-field characteristics associated with inclined bodies of revolution.

(U) It is the purpose of this investigation to provide some fundamental experimental measurements concerning aerothermodynamic properties of flow fields around highly inclined bodies of revolution at hypersonic speeds. The study is intended to provide data in the following areas pertinent to the design of an axisymmetric maneuverable hypersonic vehicle.

- (1) heat transfer
- (2) performance and stability
- (3) separated flow-field phenomena

(U) The present paper summarizes the results that we have obtained and described in detail in references 5 and 6. Our investigation of separated flow phenomena is continuing and we are presently planning to conduct a series of detailed flow-field surveys in the flow field on the leeward side of an inclined cone.

## EXPERIMENTAL CONSIDERATIONS

Test Facilities

(U) Two facilities at NOL were utilized during the course of the experimental investigation. Force, pressure, heat-transfer and flow-visualization experiments were performed in the Hypersonic Tunnel at a Mach number of 6. These experiments were conducted over a range of Reynolds numbers that was large enough to ensure that data was obtained for laminar and turbulent flow conditions, respectively. An investigation of phenomena associated with the separated flow field on the leeward side of an inclined cone was conducted in the Supersonic Tunnel No. 2 at a free-stream Mach number of 5 and a nominal free-stream Reynolds number per foot of  $5 \times 10^6$ .

(U) An outline of the test program is given in Table I.

Model Descriptions and Instrumentation(1) Conical Configurations

(U) Individual force, pressure and heat-transfer models whose exterior geometry was a  $5^\circ$  half-angle cone with a 2.5-inch base diameter were fabricated from stainless steel. Interchangeable sharp and slightly blunted nose tips ( $R_n = 0.031$  inch) were constructed for these models. A sketch giving the dimensions of this configuration is shown in Figure 1. The distance of the pressure orifices and thermocouple junctions from the tip is also tabulated in Figure 1. The static force-measurements were carried out with a slightly blunted cone with the same exterior dimensions as the model shown in Figure 1. The force model, designated henceforth as configuration 6FN, was mounted on an internal water-cooled multi-component balance.

(2) 2/3 Power-Law Configuration (6FX-1)

(U) A model of a slightly blunted axisymmetric body whose outside radius varies essentially with the axial coordinate raised to the  $2/3$  power was constructed and mounted on an internal balance. A sketch of this configuration is shown in Figure 2.



Vol. 1

(3) Ducted-Cone Configurations (6FX-2-1 and 6FX-2-2)

(U) Two ducted cone force models were also constructed to investigate the possibility of substantially increasing the lateral maneuverability of bodies of revolution. Sketches of these configurations are shown in Figures 3a and 3b.

(4) Data Recording

(U) The outputs of the transducers (i.e., pressure transducers, thermocouples, and force balances) were recorded on multi-channel magnetic tape data recording systems. Individual channels were monitored on X-Y plotters during the experiments.

Testing Techniques and Data Reduction

(U) Each model employed in these experiments was supported on a sting whose axis was coincident with the axis of the model. During most of the experiments, the model sting assembly was attached to a pitch sector that oriented the model at the desired angle of attack. Pressure and heat transfer distributions in the circumferential direction were obtained by employing a remote control roll-indexing device in conjunction with the pitch sector. Models mounted on a dog-leg sting roll-indexing device assembly (Fig. 4) were used for some flow visualization experiments. This mounting arrangement facilitated photographic recording of the phenomena from different orientations with respect to the model while the model maintained a constant angle of attack.

(U) Stagnation pressure and temperature were measured in the plenum chamber upstream of the nozzle throat. Free-stream conditions were calculated from the measured stagnation conditions by assuming that the flow within the nozzle behaves as a calorically perfect gas experiencing an isentropic expansion. The Mach number in the test section was determined from the measured ratio of the Pitot pressure to the stagnation pressure.

(1) Surface Pressure Measurements

(U) Surface pressure distributions were obtained in the Hypersonic Tunnel with the slightly blunted 5° half-angle cone pressure model mounted in a roll-indexing device.



The cone was pitched to the desired angle of attack after flow was established in the tunnel and then rolled about its axis in order to obtain data in the circumferential direction. The outputs from pressure transducers that were connected with one windward and one leeward pressure tap, respectively, were monitored on an X-Y plotter in order to minimize measurement errors associated with the time response of the pressure measurement system.

(U) Pressure distributions along the most windward and most leeward meridian generators were obtained with a sharp  $5^\circ$  half-angle cone in the Supersonic Tunnel No. 2. Data was obtained at different angles of attack by pitching the model and waiting until the measured pressure reached its steady value.

(U) Testing times for these experiments were of the order of minutes. The pressure transducers were calibrated just before or just after each test.

## (2) Heat Transfer Experiments

(U) Heat-transfer measurements were made by the transient calorimeter technique. In these experiments the model was positioned in the test section of the Hypersonic Tunnel at the desired orientation and then covered with a retractable cooling shield. The model was cooled by spraying liquid nitrogen over its surface until the wall temperature reached some predetermined level. Data at two initial average wall to total temperature ratios ( $T_w/T_o \sim 0.35$  and  $0.55$ ) were obtained in this manner during the high Reynolds number experiments ( $M = 6$ ,  $Re_\infty/FT = 21 \times 10^6$ ), while data at one average wall temperature ratio ( $T_w/T_o \sim 0.55$ ) were obtained during the low Reynolds number experiments ( $M_\infty = 5.93$ ,  $Re_\infty/FT = 2.4 \times 10^6$ ). Flow was established in the wind tunnel with the model within the cooling shield. The shield was retracted after steady flow was established, at the desired supply pressure, and the temperature variation with time was recorded. The heat-transfer coefficient was calculated at a time  $\bar{\tau} = \tau_1 + \tau_2/2$  from the following relationship:

$$h = \frac{\rho_w C_{wo} d}{\tau_2 - \tau_1} \left[ 1 - \frac{d}{2 s \tan \theta_c} \right] \left\{ (1 + \epsilon T_o) \ln \frac{T_1 - T_o}{T_2 - T_o} - \epsilon (T_2 - T_1) \right\} \quad (1)$$

Vol. 1

where:  $T_O$  = stagnation temperature

$$C_w = C_{wO}(1 + \epsilon T) = \text{specific heat of 17-4PH stainless steel}$$

Values of  $C_{wO}$  and  $\epsilon$  for each interval of time were determined from curve fits to available measurements of the specific heat of 17-4PH stainless steel.

(3) Force and Moment Measurement

(U) Static force and moment measurements were obtained in the Hypersonic Tunnel with models mounted on water-cooled, multi-component, internal strain-gage balances. The balances were calibrated before the experiments by placing weights at different positions along the balance. A calibration was also made to account for the angular deflection of the balance and the apparent weight of the model.

(U) The deduced lift and drag data presented herein include the drag associated with the base pressure.

(U) The volume, reference areas, and reference lengths of the configurations used for the data reduction are tabulated in Table II.

(4) Pitot-Tube Surveys

(U) Pitot-tube surveys were obtained on the leeward side of a yawed cone by traversing a Pitot tube perpendicular to the free-stream direction. The axis of the probe was aligned with the flow direction in the undisturbed free stream.

(5) Flow Visualization Techniques

(U) During the course of these experiments, several standard wind-tunnel flow-visualization techniques were employed to illustrate phenomena associated with inclined bodies of revolution.

(U) (a) Schlieren Photography - Schlieren photographs were taken throughout the course of the experiments (knife edge horizontal). A series of photographs were obtained with the sharp conical model mounted on a dog-leg sting. The dog-leg sting was affixed to a roll-indexing device. Once the axis of the roll-indexing device was

aligned with the flow direction in the undisturbed free stream, the model could be rolled about this axis while maintaining a constant angle of attack (Fig. 4).

(U) (b) Surface Oil Flow Pattern - A qualitative measure of the direction of the shear stress at the surface of the cone was determined in the Hypersonic Tunnel by observing the oil pattern that was formed after the surface was exposed to the incident stream. A mixture of lampblack and silicone oil was applied to the surface at random points. The shield used in the heat-transfer experiments was placed over the model so that the starting procedure in the wind tunnel did not disturb the flow pattern. Once flow was established, the shield was withdrawn for approximately 25 seconds. Prior to the shut down of the tunnel, the shield was replaced in order to preserve the pattern.

(U) Measurements of separation points were made at three stations along the model with protractors.

(U) (c) Surface Sublimation Experiments - A qualitative measurement of the surface shear stress and heat transfer on the leeward side of a sharp cone was provided by the surface sublimation experiments conducted in the Supersonic Tunnel No. 2. A sharp teflon cone ( $\theta_c = 5^\circ$ , base diameter = 2.5 inches) was painted black and then coated with azobenzene. Azobenzene is an orange colored, low melting point ( $\leq 200^\circ\text{F}$ ) organic compound which is suitable for illustrating regions of high shear and heat transfer in supersonic tunnels that are operated at stagnation temperatures above  $150^\circ\text{F}$ .

(U) The coated model was mounted in the wind tunnel on the offset-sting assembly (Fig. 4) and exposed to the incident stream for approximately five minutes. The transient start-up and shut-down periods did not alter the pattern.

(U) (d) Vapor-Screen Photographs - A qualitative indication of the aerothermodynamic properties within the flow field on the leeward side was provided by the vapor-screen photographs. A sharp  $5^\circ$  half-angle cone was mounted on the dog-leg sting roll device assembly in the Supersonic Tunnel No. 2 (Fig. 4). Flow was established at the desired stagnation pressure without heating the air to prevent air liquefaction. A thin slit of light was passed across the test section and the resultant pattern was photographed.

## RESULTS AND DISCUSSION

Pressure Experiments

(U) Some typical surface pressure distributions recorded on the slender cones during these experiments are shown in Figures 5, 6 and 7. The circumferential pressure distribution shown in Figure 5 was obtained in the Hypersonic Tunnel at angles of attack up to approximately  $55^\circ$ . The data were fairly well predicted by the Newtonian relationship,  $C_p = 2\cos^2\delta$  (where  $\delta$  is the angle between the local unit normal and the free-stream velocity vector), on the windward side of the cone. The data illustrate the fact that the pressure distribution on the leeward side of a  $5^\circ$  half-angle cone is rather insensitive to angle of attack once the angle of attack exceeds  $20^\circ$ . The data also illustrate the existence of a relative minimum in the pressure distribution at an azimuthal angle of approximately  $125^\circ$ .

(U) An examination of this pressure data along with the results of flow-visualization experiments indicates that at large angles of attack, flow separation occurs in a region of adverse pressure gradient at an azimuthal angle of approximately  $132^\circ$ .

(U) The data measured in the Hypersonic Tunnel were recorded at nominal free-stream Reynolds numbers per foot of  $2 \times 10^6$  and  $20 \times 10^6$ . While data on the windward side showed very little dependence upon Reynolds number, the data obtained on the leeward side of a slender slightly blunted cone did indicate a consistent dependence upon the Reynolds number. This dependence is illustrated in Figure 6. In order to demonstrate conclusively the conical nature of the flow field on the windward side and the existence of a pressure gradient on the leeward side, the pressure distribution along the most windward and the most leeward generators of an inclined sharp cone ( $\theta_c = 5^\circ$ ) were measured in the Supersonic Tunnel No. 2. The results of these experiments, presented in Figure 7, illustrate these facts.

(U) The observation of a constant pressure along the most windward meridian generator is a manifestation of the conical nature of the inviscid flow field on the windward side. The flow field on the leeward side shows a dependence upon the free-stream Reynolds number based upon distance from tip. The results of our measurements were fairly well correlated with those of other experiments by plotting the static-pressure ratio ( $P/P_\infty$ ) as a function of the viscous

interaction parameter ( $M_\infty^3 / \sqrt{Re_{\infty,x}}$ ) (Fig. 8). At the present time there are no analytical treatments which adequately predict the leeward flow field of a conical body at large angles of attack.

### Heat Transfer Experiments

(U) The heat-transfer measurements were obtained on a slightly blunted ( $R_n/R_b = 0.025$ ) slender cone ( $\theta_c = 5^\circ$ ) in the Hypersonic Tunnel at a nominal number of 6.0. Some typical data obtained in these experiments are presented in Figures 9 thru 13.

#### (1) Zero Angle of Attack

(U) The data obtained at zero angle of attack with the slightly blunted cone are presented in Figure 9. All of the data obtained at the lower unit Reynolds number indicated that the boundary layer was laminar. The data obtained at the higher unit Reynolds number indicate that boundary-layer transition occurs for these conditions at free-stream Reynolds numbers between  $10 \times 10^6$  and  $14 \times 10^6$ .

(U) Since the tip of the cone was slightly blunted in these experiments, the local flow properties can no longer be determined from solutions to the inviscid flow over a sharp circular cone. A calculation of the laminar boundary-layer growth on a slightly blunted cone was accomplished using the integral method proposed by Wilson (ref. 8) to account for variable Mach number conditions external to the boundary layer. The variations of local momentum-thickness Reynolds number, local Reynolds number based upon distance from the tip and local Mach number along the cone as calculated by Wilson's method are presented in Figures 14, 15 and 16. At zero angle of attack, the conditions over which transition occurred in our experiments are tabulated below:

$$10 \times 10^6 < Re_{\infty,s} < 14 \times 10^6$$

$$4.45 < Me < 4.7$$

$$5.4 \times 10^6 < Re_{e,s} < 9.5 \times 10^6$$

$$950 < Re_{e,\theta} < 1250$$



Vol. 1

(U) A calculation of the turbulent heat transfer to a sharp cone as calculated by the Spalding-Chi method (ref. 9) is shown for the purposes of comparison. Our measurements of turbulent heating rates are approximately 10-20 percent higher than those predicted by this method.

(2) Cone at Angle of Attack

(U) Typical heat-transfer distributions along the most windward streamline at angles of attack of  $15^\circ$ ,  $20^\circ$ ,  $30^\circ$ ,  $45^\circ$  and  $54^\circ$  are illustrated in Figures 10a and 10b. A comparison of these measurements with those obtained at zero angle of attack (Fig. 9) indicates that boundary layer transition occurs on the stagnation streamline closer to the tip of a highly yawed cone than it does on an unyawed cone. The variation of transition Reynolds number (i.e., based upon free-stream properties) with angle of attack is shown in Figure 17 for one wall temperature ratio and one unit Reynolds number.

(U) Most available data concerning the variation of boundary-layer transition along the windward streamline with angle of attack have been limited to small angles of attack (references 10, 11 and 12). The data presented in references 10 and 11 indicate that transition moves rearward on the windward meridian of a cone for small angles of attack while the data presented in reference 12 indicate that transition moves forward along the windward meridian of a sharp cone for small angles of attack. A method which predicts the location of transition on simple shapes is not available at the present time. For a yawed cone, the problem is complicated by the presence of cross-flow and varying Mach number and unit Reynolds number conditions at the edge of the boundary layer.

(U) The measured laminar heat-transfer distributions along the stagnation streamline compare favorably with those predicted from calculations of the laminar heat-transfer distribution on the stagnation streamline of a yawed cylinder whose axis is parallel to the most windward generator of the cone (ref. 13)

(U) Some representative heat-transfer distributions in the circumferential direction are shown in Figures 11, 12 and 13. For the purposes of presentation, the data are normalized by the calculated laminar heat transfer coefficient at the stagnation streamline of a yawed cylinder (ref. 13). The data shown in Figure 11 are



representative of the laminar heat-transfer distribution on the windward side of a yawed circular cone. The peak heat transfer rates occur along the stagnation streamline. A second local maximum in the heat transfer rate occurs along the most leeward meridian generator of the cone. This observation is probably related to the fact that the most leeward generator acts like a rear stagnation point to the separated flow. At the present time there is no adequate method of predicting this increase of heat transfer on the leeward generator. Pitot surveys, surface oil-flow patterns, surface-sublimation experiments and schlieren photographs all provide information which indicate that there are regions of attached flow near the most leeward meridian generator of the cone. These results will be presented in a later section where separated flow phenomena will be discussed.

(U) The heat-transfer data shown in Figure 12, beyond  $x = 1$  inch, are representative of data that were obtained where the boundary layer on the windward side was turbulent. Heat-transfer coefficients are maximum along the stagnation streamline and decrease in magnitude around the periphery of the cone.

(U) Data shown in Figure 13 were obtained in a region on the cone where boundary-layer transition occurred. These results indicate maxima in the heat transfer distribution approximately  $15^\circ$  from the most windward generator. One explanation for this observation is that transition can occur closer to the tip on generators that are displaced from the most windward generator.

#### Force and Moment Measurements

(U) In order to provide an indication of the performance and stability characteristics of axisymmetric maneuverable hypersonic vehicles, a series of static-force tests were conducted with a slightly blunted cone (configuration 6FN), a slightly blunted  $2/3$  power-law body (configuration 6FX-1), and two ducted cone configurations (6FX-2-1 and 6FX-2-2) in the Hypersonic Tunnel. The measured lift and drag data along with the lift to drag ratios for these configurations are shown in Figures 18 thru 21. These results indicate that the maximum lift to drag ratio of the ducted conical configurations are as much as 20 to 50 percent larger than the maximum lift to drag ratios of the simple bodies of revolution.

## Vol. 1

(U) The measured distance between the center of pressure and the tip for each of these configurations, normalized by the length of the body, is shown in Figure 22. The slightly blunted cone (configuration 6FN) exhibited the smallest variation in the location of the center of pressure. Our measurements indicated that the center of pressure of a slightly blunted cone varied by less than 0.3 percent of the body length over an angle of attack variation from 2 degrees to 54 degrees. Furthermore, measurements which we have made indicate that the center of pressure location of a slightly blunted cone can be predicted by the following relationship:

$$\frac{x_{cp}}{L} = \frac{\frac{2}{3\cos^2\theta_c} \frac{[1 - (\frac{R_n}{R_b})^3 \cos^3\theta_c]}{[1 - (\frac{R_n}{R_b})^2 \cos^2\theta_c]} - \frac{R_n}{R_b} \frac{(1-\sin\theta_c)}{\cos\theta_c}}{1 - \frac{R_n}{R_b} \frac{(1-\sin\theta_c)}{\cos\theta_c}} \quad (2)$$

The value computed from this formula is illustrated in Figure 22 for the purposes of comparison.

(U) When assessing the presented lift and drag data, it is important to note that lift to drag ratio is not the only figure of merit for a maneuverable hypersonic vehicle. An examination of the equations of motion for an unpowered vehicle indicate that two additional dimensional figures of merit are the ballistic coefficient,  $w/C_D A$ , and the wing-loading parameter  $C_L A/w$ . For a given altitude and velocity, the longitudinal and lateral accelerations are proportional to the ballistic coefficient and the wing-loading parameter, respectively. In order to calculate these parameters, a preliminary design analysis must be conducted to obtain some estimate of the weight of the vehicle. Since this is beyond the scope of the present investigation, the only attempt to compare the maneuverability characteristics will be made by showing the drag factor at zero lift ( $\text{Volume}/C_D A$ ), the lift factor ( $C_L A/\text{Volume}$ ) and the lift-to-drag ratios. The ballistic coefficient and the wing loading parameter can be found from these factors once the packaging density ( $\bar{p}^* = \frac{\text{weight}}{\text{volume}}$ ) is determined.

(U) The drag factors at zero lift for these configurations are shown in Figure 23. Configurations 6FN and 6FX-1 have essentially the same length, base radius and drag coefficient. The larger volume afforded by the power-law body accounts for the 30 percent increase of the drag factor of this body beyond that of a cone (see Table II). The drag coefficients at zero lift of configurations 6FX-2-1 and 6FX-2-2 are 2 to 2-1/2 times that of the simple conical body (Figs. 18, 20 and 21). These increases are not proportionately reflected in the drag factor at zero lift because the volumes of configurations 6FX-2-1 and 6FX-2-2 are between 1-1/2 to 2 times that of the simple conical body (see Table II). In calculating the drag factor of configuration 6FX-2-1 one notes that the increase in drag coefficient was more than offset by the increase in volume.

(U) A comparison of the lateral maneuverability characteristics of these configurations is shown in Figure 24. The results indicate that the ducted conical configurations can sustain at least twice the lift factor and a considerably larger lift-to-drag ratio than the simple bodies of revolution can maintain at a given angle of attack. The ducted conical configurations achieve a given lift factor at a smaller angle of attack than the simple bodies of revolution. Furthermore, for a given lift factor, the lift-to-drag ratio of the ducted configurations is generally as large or larger than the lift-to-drag ratio of the simple bodies of revolution. For the conditions of our experiments, these results indicate that the maneuverability characteristics of bodies of revolution can be augmented by the addition of a duct. A decision, concerning whether or not such configurations are practical from the standpoint of a maneuverable hypersonic vehicle, requires an understanding of design trade-offs which was beyond the scope of our investigation.

#### Separated Flow Phenomana on a Yawed Cone

(U) A complete understanding of the flow field on the leeward side of a yawed cone is not presently available. Uncertainties concerning the boundaries between viscous and inviscid regions of the flow and the entropy distribution on the leeward side prevent one from constructing a valid flow-field model. It is our intention to perform a detailed series of flow-field surveys which will provide some useful information concerning these problems. However, some of the data which we have already obtained do provide information relevant to the construction of a valid flow-field model. This information was obtained from surface-pressure distributions, flow-visualization experiments, and Pitot-tube surveys.

(1) Surface Pressure

(U) It was previously noted that the pressure distribution along the most leeward generator of a highly yawed cone is dependent upon the viscous interaction parameter ( $M_\infty^3/\sqrt{Re_{\infty, x}}$ ) (Fig. 8). A satisfactory explanation of this observation is not presently available. However, this result does cause one to question previous observations which indicate that the flow field on a highly yawed conical configuration is "essentially conical" (References 14, 15 and 16). If the flow on the leeward side of a yawed cone is determined by the interaction between a viscous flow and an inviscid flow, as this correlation seems to suggest, the assumption that the flow field is conical appears to be unjustifiable.

(U) A second indication of non-conical flow characteristics is illustrated by a schlieren photograph that was obtained with a sharp  $5^\circ$  half-angle cone at angle of attack of  $20^\circ$  (Fig. 25). The photograph indicates non-conical flow phenomena as the density gradients do not exist along straight lines emanating from the vertex.

(2) Flow-Visualization Experiments

(U) In order to demonstrate some separated flow phenomena on a highly yawed cone some standard flow-visualization experiments were conducted.

(U) Oil-flow and surface-sublimation experiments enabled us to locate flow separation lines on the surface of the cone. To within the accuracy of the experiments ( $\Delta\phi = \pm 5^\circ$ ), the measured separation lines were found to be along conical generators. The primary separation line is shown in the photograph obtained during the surface sublimation experiment (Fig. 26). The appearance of regions of large shear and heat transfer on the leeward side of a yawed cone was also illustrated in a surface-sublimation experiment (Fig. 27). This observation is consistent with the heat-transfer measurements presented previously and the experiments of Tracy (ref. 14) and Rainbird (refs. 15 and 17). The direction of the shear near the most leeward meridian was illustrated in a surface oil flow experiment (Fig. 28). Measured azimuthal location of the separation lines are shown in Figure 29.

(U) An attempt was made to illustrate some properties of the separated flow field between the surface and the shock wave on the leeward side of the yawed cone. Schlieren photographs and vapor screen photographs were utilized in this regard. Conventional schlieren photographs did illustrate the attached flow on the leeward side



of the cone at an angle of attack of  $15^\circ$  (Fig. 30). This is indicated by the appearance of a density gradient near the base which appears like a Prandtl-Meyer expansion fan that one observes on flat-based bodies in a supersonic flow.

(U) At larger angles of attack (Fig. 31), schlieren photographs indicate the existence of two density gradients on the leeward side of a cone. Pitot-tube surveys (Fig. 39) indicate that gradients do exist on the leeward side of a yawed cone in the plane of symmetry. From these measurements we conclude that there are apparently three distinct regions within the flow field on the leeward side of a highly yawed cone.

(U) Schlieren photographs obtained with the cone mounted on a dog-sting assembly offered views from different orientations with the model mounted at a fixed angle of attack. A typical photograph obtained with this arrangement is shown in Figure 32. By analyzing a series of photographs obtained from different orientations, we were able to define the shockwave in the cross-flow plane (Fig. 33 and 34). The analysis employed to define a 3-dimensional disturbance from a conventional schlieren photograph is described in reference 18. While our attempts to define the leeward flow field solely from such schlieren photos were not entirely successful, large density gradients were found to exist in the plane of symmetry and off the plane of symmetry. We believe that the gradients that exist off the plane of symmetry are associated with the existence of imbedded shock waves in the flow field which we observed with vapor screen techniques.

(U) Photographs of the vapor screen pattern obtained using the set-up illustrated in Figure 4 are shown in Figures 35 thru 37. The enveloping bow shock wave is illustrated in all of the photographs. Imbedded shock waves are discernible in the photograph shown in Figure 37. Furthermore, the absence of crystallized particles near the body in Figures 36 and 37 suggest the existence of a closed region on the leeward side of a yawed cone which is characterized by a high temperature.

### (3) Pitot-Tube Surveys

(U) Additional information concerning the leeward flow was obtained from Pitot-tube surveys. Two Pitot surveys that were obtained in the plane of symmetry on the leeward side of a yawed cone are shown in Figures 38 and 39.

Vol. 1

The pressure measured at the surface is shown for the purposes of comparison. In the survey recorded with the model at an angle of attack of  $15^\circ$ , one notes that the Pitot pressure at a point 0.134 inch above the surface is approximately 10 times the pressure measured by the static tap at the surface. This result should be compared with the survey taken at  $30^\circ$  angle of attack. For the latter condition the surface pressure is in close agreement with the Pitot pressure. The apparent difference between the Pitot pressure and the surface pressure at  $15^\circ$  angle of attack is associated with the presence of an energetic attached flow near the leeward meridian generator. One might speculate that the attached flow is actually a reattached flow. The reattachment might be the result of a pair of vortices formed from the flow which separates along the primary separation line (ref. 17).

(U) At the present time, no attempt has been made to distinguish between viscous and inviscid regions of the flow. Our experiments have neither confirmed nor negated the existence of a vortical singularity within the flow field. A determination of the existence or non-existence of the vortical singularity as well as a mapping of the velocity and thermodynamic properties in the flow field on the leeward side of a yawed cone are two specific objectives of our forthcoming flow-field experiments.

#### CONCLUSION

(U) An experimental investigation concerning the aerothermodynamic characteristics of flows around highly inclined bodies of revolution has been conducted in the wind tunnels at NOL. From this investigation, the following conclusions concerning hypersonic flow around inclined axisymmetric bodies are made:

(1) (U) At large angles of attack, boundary-layer transition on the windward streamline occurs closer to the tip than at zero angle of attack.

(2) (U) The measured static longitudinal aerodynamic characteristics indicate that significant increases in maneuverability can be achieved by the addition of a duct around a slender cone. The measured lift-to-drag ratio of the ducted conical bodies was as much as 50 percent greater than the maximum lift-to-drag ratio of the simple bodies of revolution for the specific Mach number and Reynolds number conditions of the present tests. The increase in the lift-



to-drag ratio is realized solely because of the increase in lift effectiveness of these configurations.

(3) (U) The location of the center of pressure of a slightly blunted cone exhibited a variation of less than 0.3 percent of the body length over an angle of attack variation from 2 degrees to 54 degrees.

(4) (U) Schlieren photographs and pressure distributions along the most leeward meridian generator demonstrated the existence of non-conical regions on the leeward side of a yawed cone. The measured pressure distribution has been correlated with other data by plotting the data as a function of the viscous interaction parameter ( $M_\infty^3 / \sqrt{Re_{\infty, x}}$ )

(5) (U) Flow-visualization techniques, Pitot-tube surveys and heat-transfer measurements indicate that there are regions of attached flow on the leeward side of a yawed cone ( $\theta_c = 5^\circ$  and  $\alpha < 20^\circ$ ). These regions are characterized by local maximum values of heat transfer and surface shear stress.

(6) (U) Vapor-screen photographs indicate the existence of imbedded shock waves on the leeward side of the yawed cone.

(U) TABLE I. Hypersonic Tunnel Experiments

Type of Test	Nominal Angle of Attack	$M_\infty$	$Re_\infty/ft$	Remarks	$R_n/R_b$
Surface Pressure	0°, 10°, 20°, 30°, 45°, 54°	5.93	$2.4 \times 10^6$	0° ≤ φ ≤ 180°	0.02
	0°, 20°, 30°, 45°, 54°	6.00	$21 \times 10^6$	0° ≤ φ ≤ 180°	0.02
Heat Transfer	0°, 15°, 30°, 54°	5.93	$2.4 \times 10^6$	0° ≤ φ ≤ 180° Δφ = 15° $T_w/T_o \sim 0.5$	0.02
	0°, 20°, 30°, 45°, 54°	6.00	$21 \times 10^6$	Δφ = 15° $T_w/T_o \sim 0.5$ $T_w/T_o \sim 0.3$	0.02
Force	0° - 54°	5.96	$4.4 \times 10^6$	Config. 6FN	0.02
	0° - 54°	6.00	$21 \times 10^6$	Config. 6FN	0.02
	0° - 54°	6.00	$21 \times 10^6$	Config. 6FX-1	0.02
	0° - 15°	6.00	$21 \times 10^6$	Config. 6FX-2-1	0.00
	0° - 15°	6.00	$21 \times 10^6$	Config. 6FX-2-2	0.00
Flow Visualization	10°, 15°, 20°, 30°, 40°	5.93	$2.4 \times 10^6$	Oil Flow Experiments	0.02
Pitot Survey	15°, 30°, 45°	5.93	$2.4 \times 10^6$	Leeward Meridian Plane	0.02

## (U) Supersonic Tunnel No. 2 Experiments

Type of Test	Nominal Angle of Attack	$M_\infty$	$Re_\infty/ft$	Remarks	$R_n/R_b$
Surface Pressure	$0^\circ, 10^\circ, 15^\circ, 20^\circ, 30^\circ, 40^\circ$	5.07	$4.8 \times 10^6$	$\phi = 0^\circ$ $\phi = 180^\circ$	0.00
Pitot Surveys	$15^\circ, 30^\circ$	5.07	$4.8 \times 10^6$	Leeward Side	0.00
Schlieren Photographs	$0^\circ, 10^\circ, 15^\circ, 20^\circ, 30^\circ, 40^\circ$	5.07	$4.8 \times 10^6$	Offset Sting @ $\alpha = 15^\circ$ and $\alpha = 40^\circ$	0.00
Surface Sublimation	$15^\circ, 40^\circ$	5.07	$4.8 \times 10^6$		0.00
Vapor Screen	$0^\circ, 15^\circ, 40^\circ$	5.05	$6.5 \times 10^6$		0.00

Vol. 1

(U) TABLE. II

Configuration	Reference Length	Reference Area	Volume
6FN	13.967 in.	4.91 sq.in.	23.38 cu.in.
6FX-1	14.027 in.	4.91 sq.in.	29.57 cu.in.
6FX-2-1	16.800 in.	4.26 sq.in.	47.81 cu.in.
6FX-2-2	16.800 in.	4.26 sq.in.	36.36 cu.in.

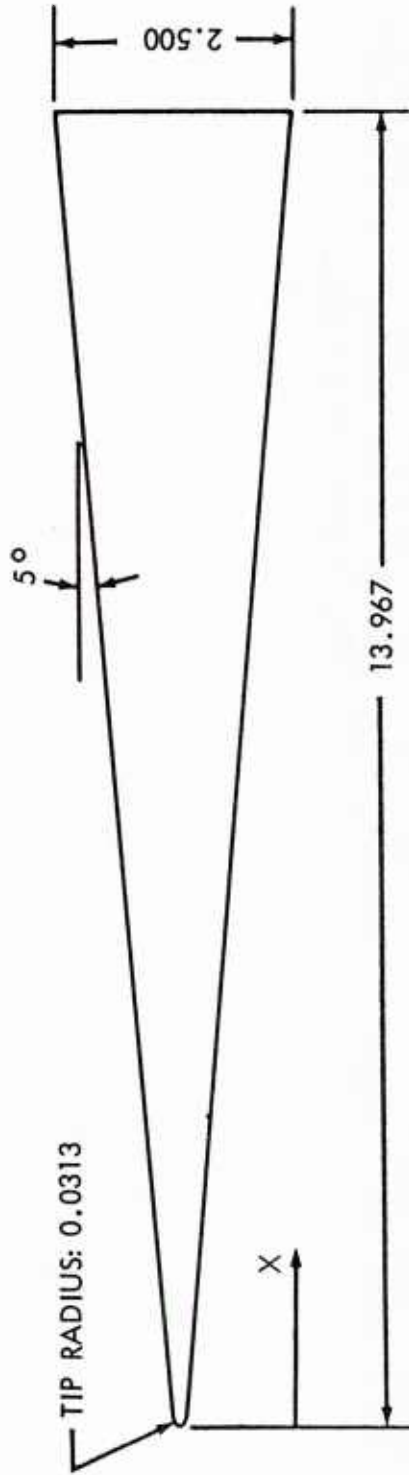
## REFERENCES

1. Spencer, B., Jr. and Fox, C. H., Jr., "Hypersonic Aerodynamic Performance of Minimum-Wave-Drag Bodies," NASA TR R 250, 1966
2. Berman, R. J., "Ballistic Coefficients for Power Law Bodies," AIAA Journal, Vol. 5, No. 1, January 1967
3. Penland, J. A., "A Study of the Stability and Location of the Center of Pressure on Sharp, Right Circular Cones at Hypersonic Speeds," NASA TN-D-2283, 1964
4. Maddalon, D. V., "Aerodynamic Characteristics of the Sharp Right Circular Cone at Mach 20.3 and Angles of Attack to  $110^\circ$  in Helium," NASA TN-D-3201, 1966
5. Feldhuhn, R. H., and Pasiuk, L., "An Experimental Investigation of the Aerodynamic Characteristics of Slender Hypersonic Vehicles at Large Angles of Attack," NOLTR 68-52, 1968
6. Feldhuhn, R. H. and Winkelmann- A. E., "Separated Flow Phenomena on a Slender Cone at Mach 5," NOLTR 69-36, 1969
7. Reshotko, E., "Laminar Boundary Layer With Heat Transfer on a Cone at Angle of Attack in a Supersonic Stream," NACA TN 4152, 1957
8. Wilson, R. E., "Laminar and Turbulent Boundary Layers on Slightly Blunted Cones at Hypersonic Speeds," NOLTR 66-54, 1966
9. Wilson, D., "A Digital Computer for Making Comparative Aerodynamic Heat Transfer and Skin Friction Drag Calculations," NOLTR 67-137, 1967
10. Stetson, K. and Rushton, G., "A Shock Tunnel Investigation of the Effects of Nose Bluntness, Angle of Attack and Boundary Layer Cooling on Boundary Layer Transition at a Mach Number of 5.5," AIAA Paper No. 66-495, June 1966
11. Stainback, P. C., "Effect of Unit Reynolds Number, Nose Bluntness, Angle of Attack, and Roughness on Transition on a  $5^\circ$  Half-Angle Cone at Mach 8," NASA TN-D-4961, January 1969

Vol. 1

12. Maddalon, D. V. and Henderson, A., Jr., "Hypersonic Transition Studies on a Slender Cone at Small Angles of Attack," AIAA Technical Note, Vol. 6, No. 1, January 1968, p. 176
13. Reshotko, E. and Beckwith, I. E., "Compressible Laminar Boundary Layer Over a Yawed Infinite Cylinder With Heat Transfer Arbitrary Prandtl Number," NACA Report 1379, 1953
14. Tracy, R. R., "Hypersonic Flow Over a Yawed Circular Cone," GALCIT Hypersonic Research Project Memorandum No. 69, 1963
15. Rainbird, W. J., "Turbulent Boundary Layer Growth and Separation on a Yawed Cone at Mach Numbers 1.8 and 4.25," Preprint No. 68-98, AIAA 6th Aerospace Sciences Meeting, New York, January 1968
16. Cross, E. J., Jr. and Hankey, W. L., "Investigation of the Leeward Side of a Delta Wing at Hypersonic Speeds," Preprint No. 68-675, AIAA Fluid and Plasma Dynamics Conference, Los Angeles, Calif., June 1968
17. Rainbird, W. J., Crable, R. S., Peake, D. J. and Meyer, R. F., "Some Examples of Separation in Three-Dimensional Flows," Canadian Aeronautics and Space Journal, Vol. 12, No. 10, December 1966, p. 409-423
18. Winkelmann, A. E. and Feldhuhn, R. H., "How to Analyze 2-D Schlieren Photographs to Obtain the Density Gradient Structure of 3-D Flow Fields," NOLTR, to be published

MATERIAL: ARMCO 17-4 PH  
STAINLESS STEEL



#### PRESSURE MODEL

WALL THICKNESS: 0.063

4 ALIGNMENT ORIFICES AT  $X = 4.00$  AND  $13.25$

#### HEAT TRANSFER MODEL

WALL THICKNESS: 0.020

4 ALIGNMENT ORIFICES  $X = 13.217$

#### DISTANCE (X) FROM TIP TO PRESSURE ORIFICES:

1.00, 1.75, 2.50, 3.75, 4.00, 4.75, 5.50, 6.25, 7.00,  
7.75, 8.50, 9.25, 10.00, 10.75, 11.50, 12.25, 13.25

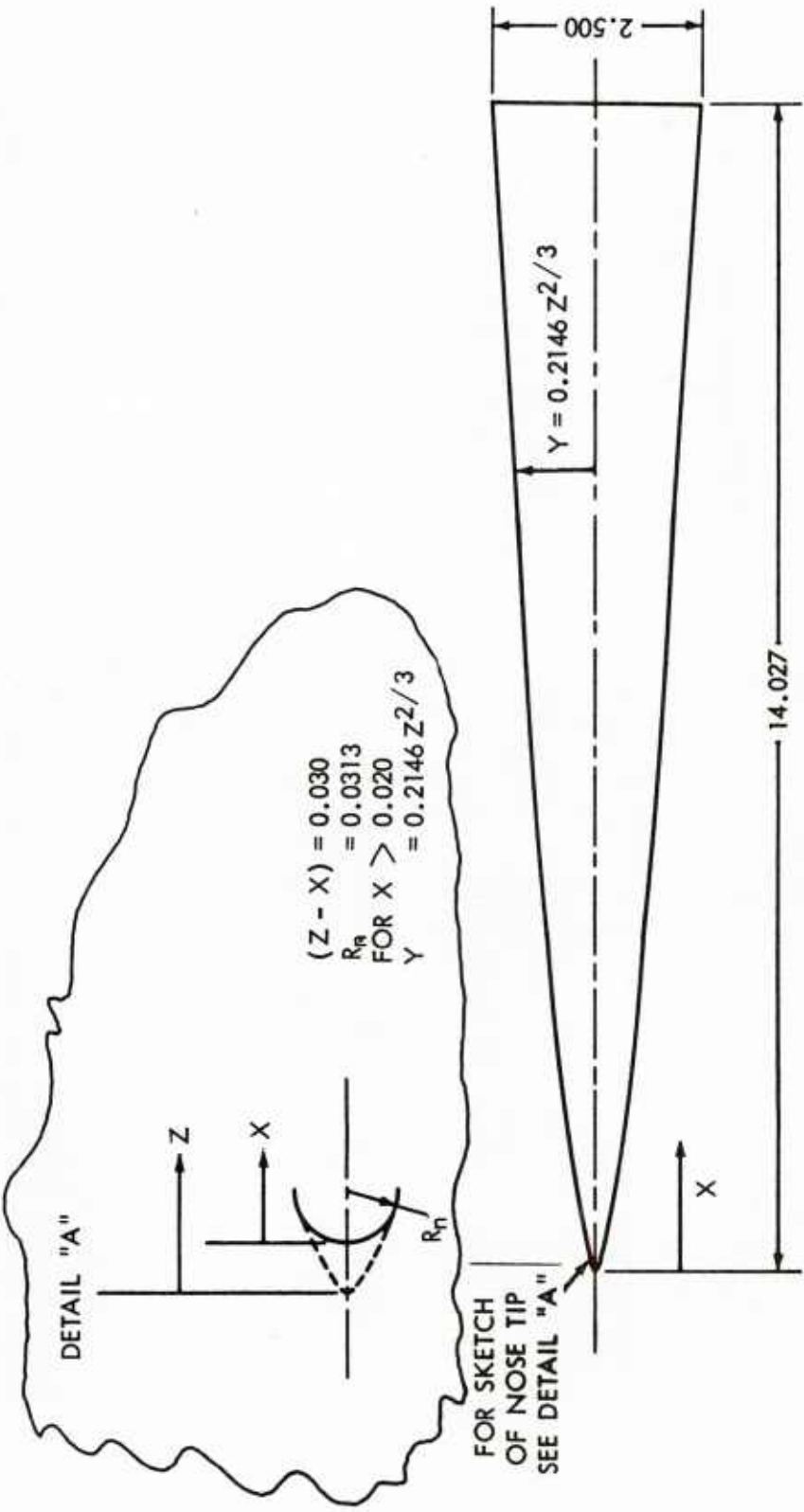
#### DISTANCE (X) FROM TIP TO THERMOCOUPLE JUNCTIONS:

1.00, 1.75, 2.50, 3.25, 4.00, 6.25, 7.75, 9.25, 10.75

NOTE: ALL LENGTH DIMENSIONS ARE IN INCHES

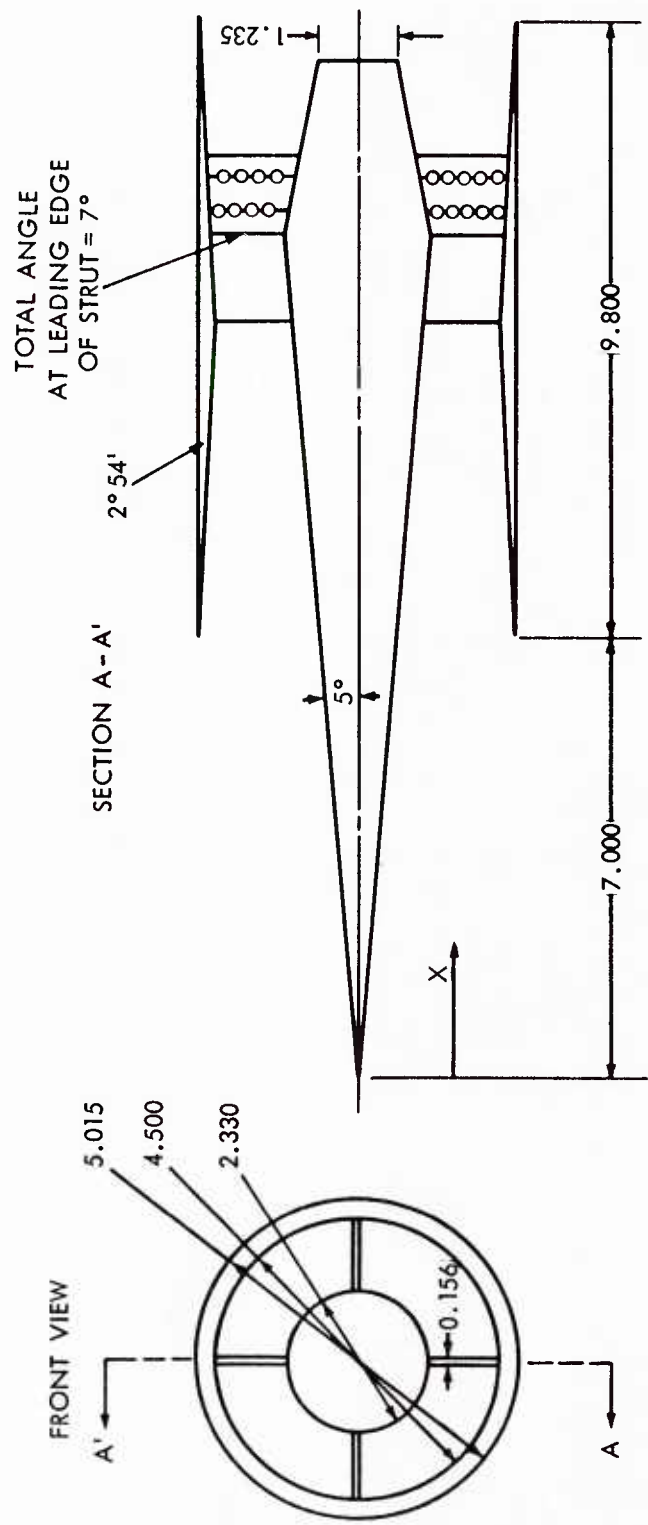
(U) Fig. 1 Slightly Blunted Conical Pressure and Heat Transfer Models





NOTE: ALL LENGTH DIMENSIONS ARE IN INCHES

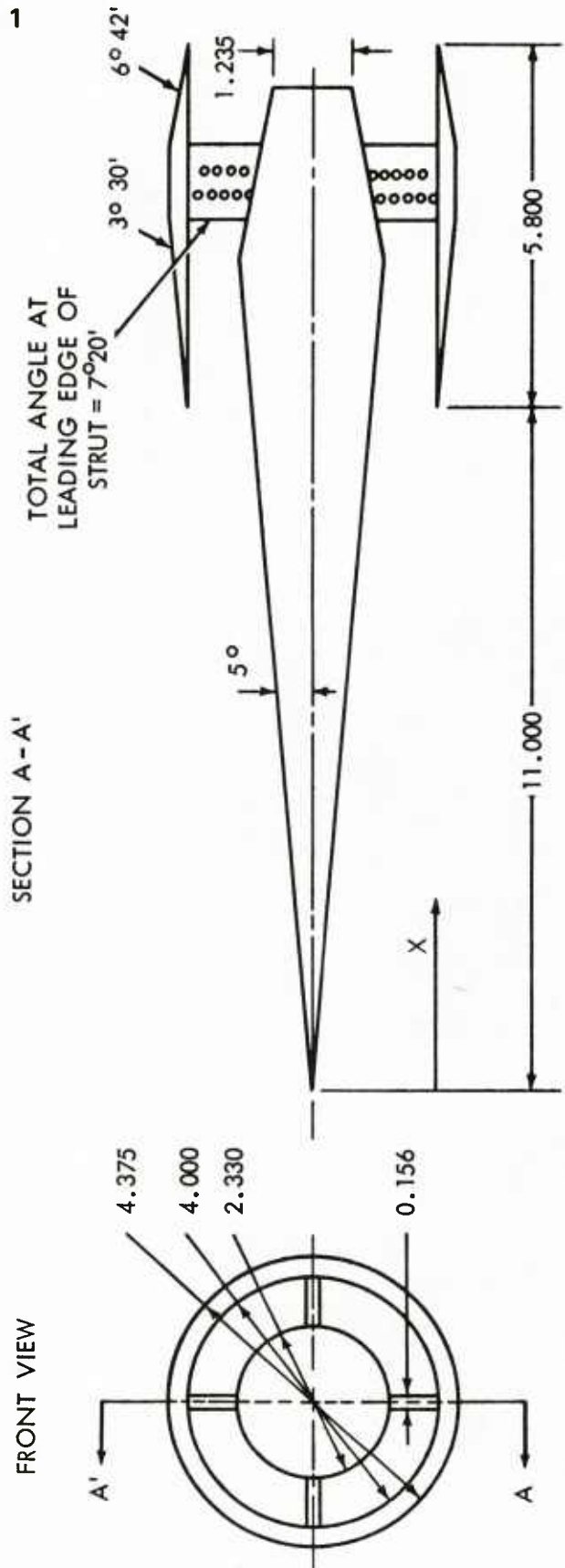
(U) Fig. 2 Slightly Blunted  $2/3$  Power Law Body of Revolution-Configuration 6 FX-1



REFERENCE AREA: A = 4.26 SQUARE INCHES  
REFERENCE LENGTH: L = 16.800 INCHES

NOTE: ALL LENGTH DIMENSIONS ARE IN INCHES

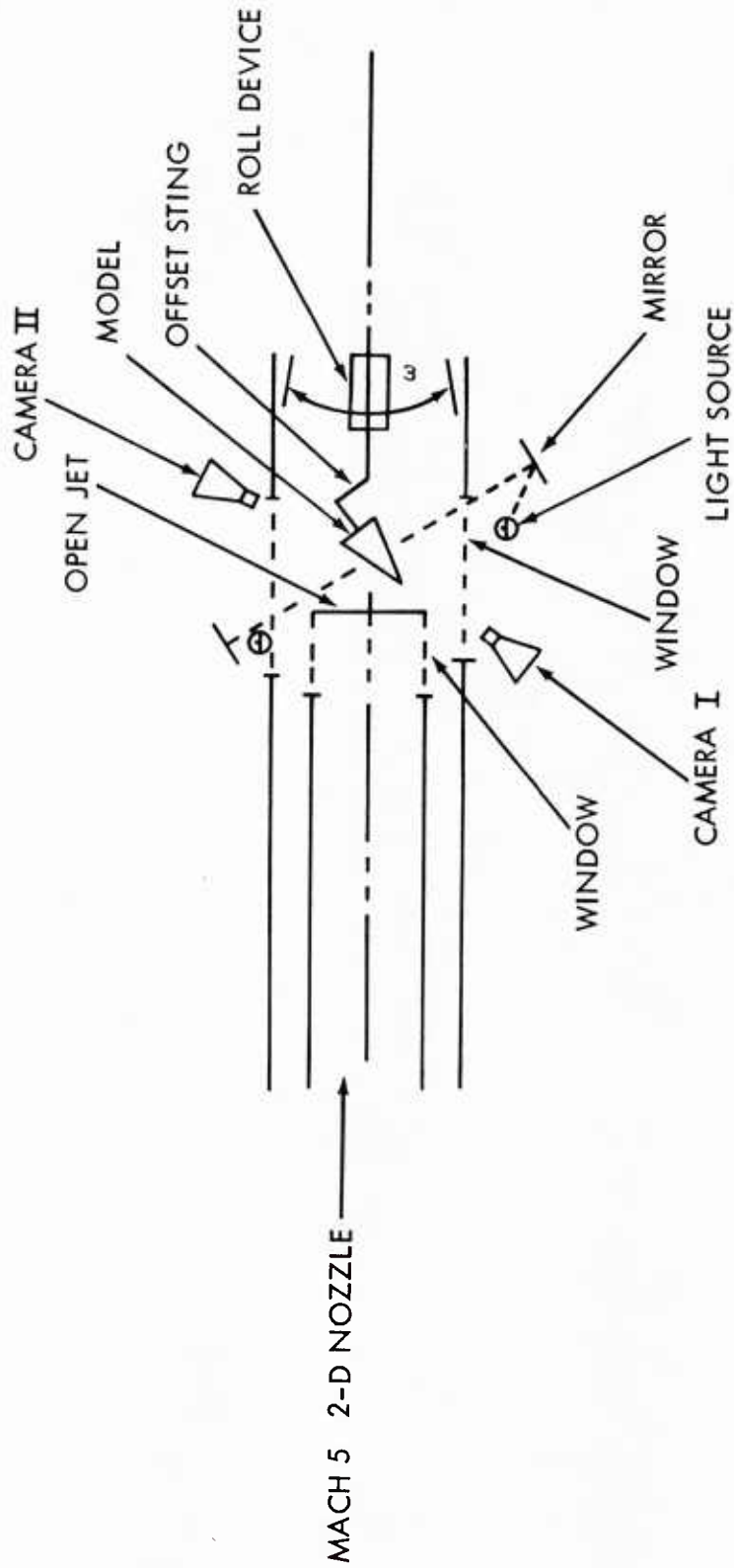
(U) Fig. 3a Ducted Cone - Configuration 6FX-2-1



REFERENCE AREA: A = 4.26 SQUARE INCHES  
REFERENCE LENGTH: L = 16.800 INCHES

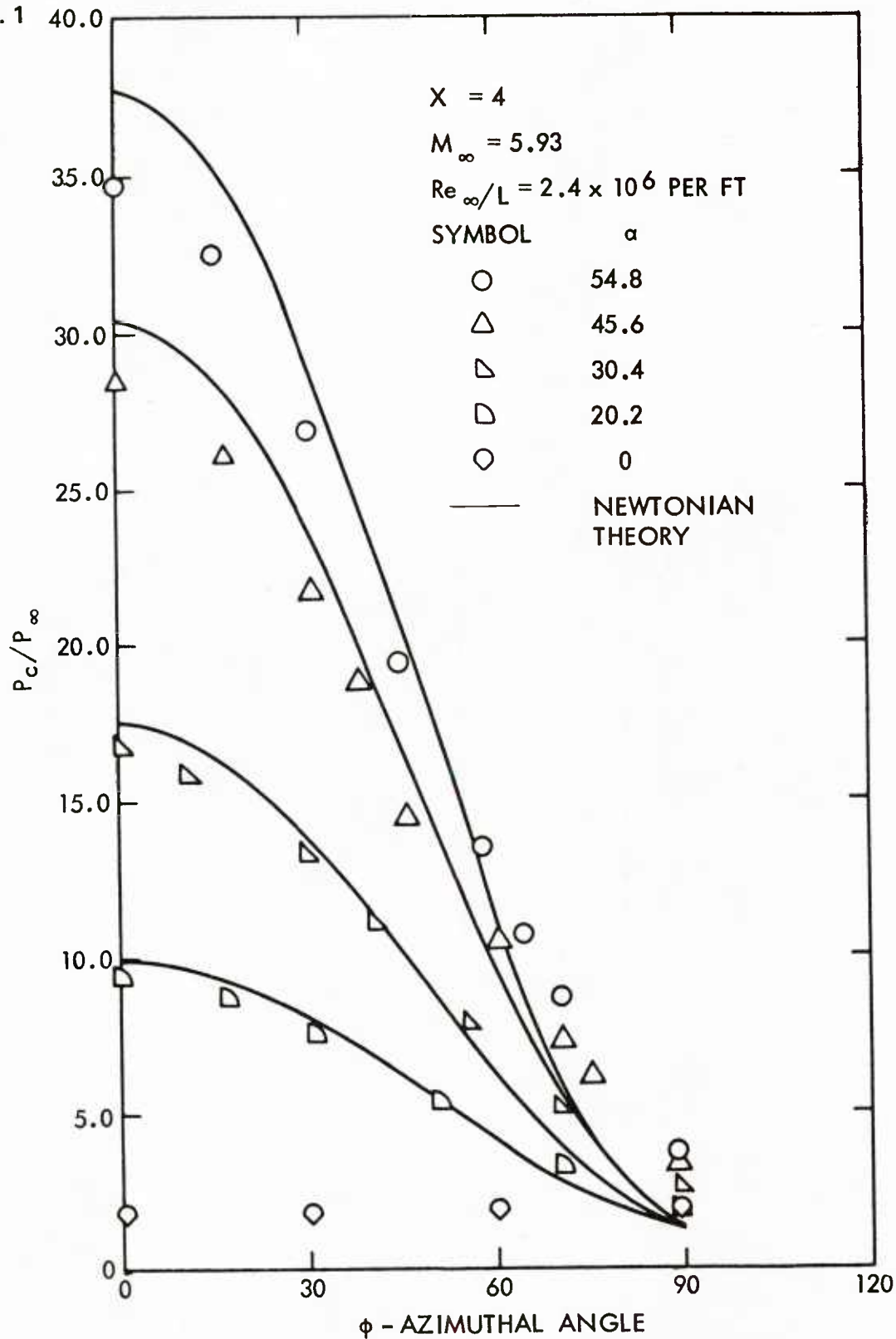
NOTE: ALL LENGTH DIMENSIONS ARE IN INCHES

(U) Fig. 3b Ducted Cone - Configuration 6FX-2-2

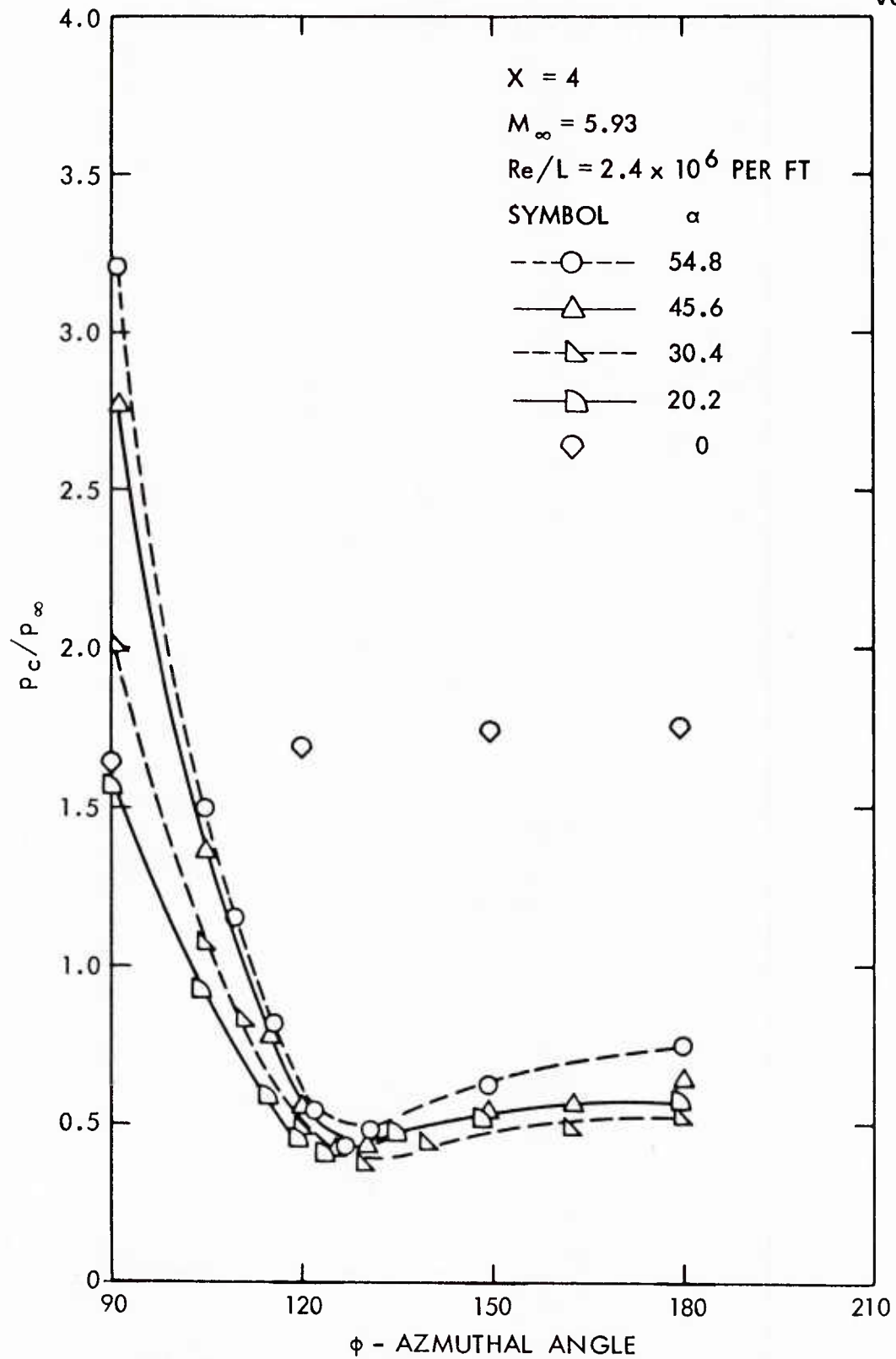


(U) Fig. 4 Vapor Screen Set-up (Top View)

Vol. 1 40.0

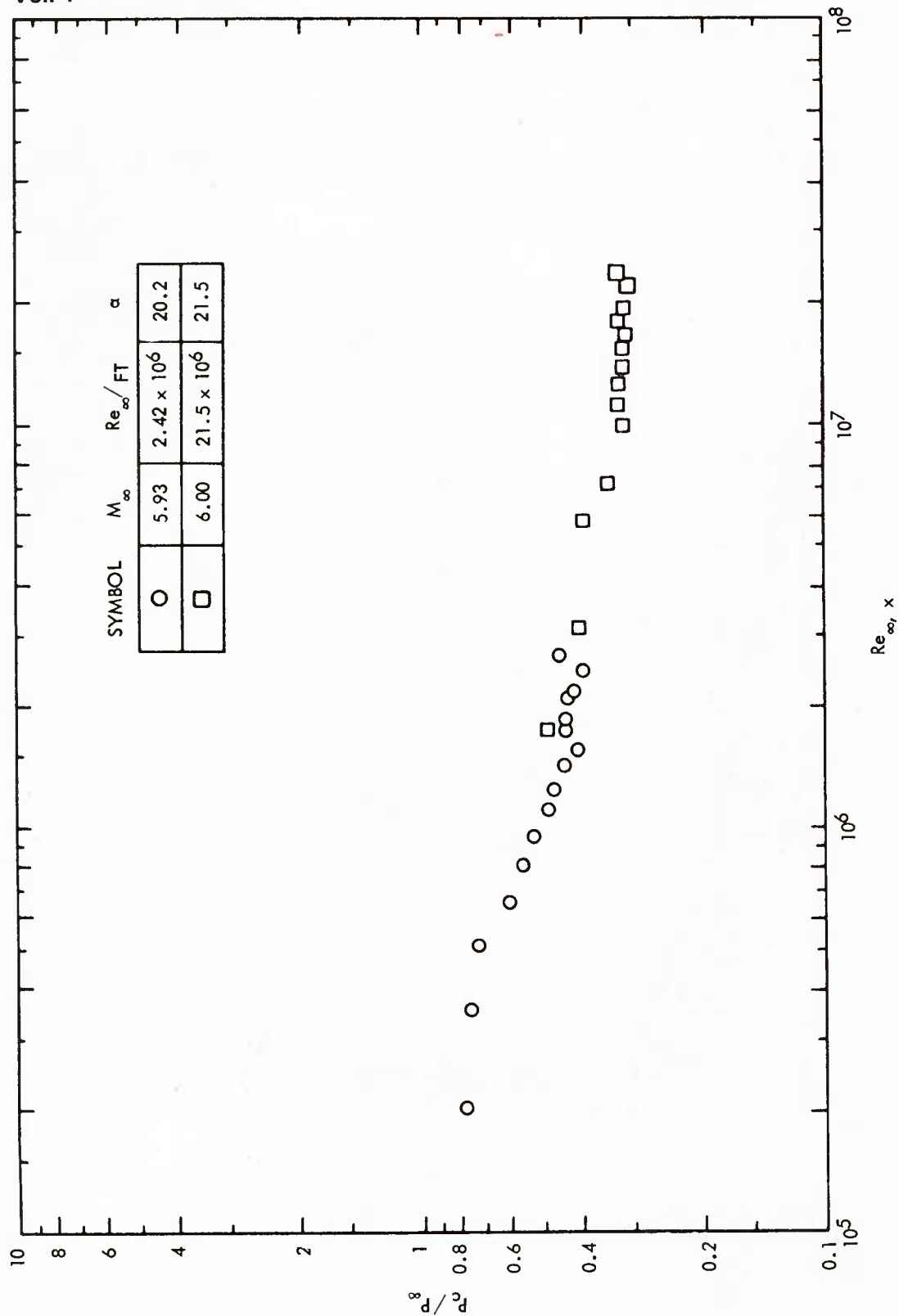


(U) Fig. 5a Circumferential Pressure Distribution

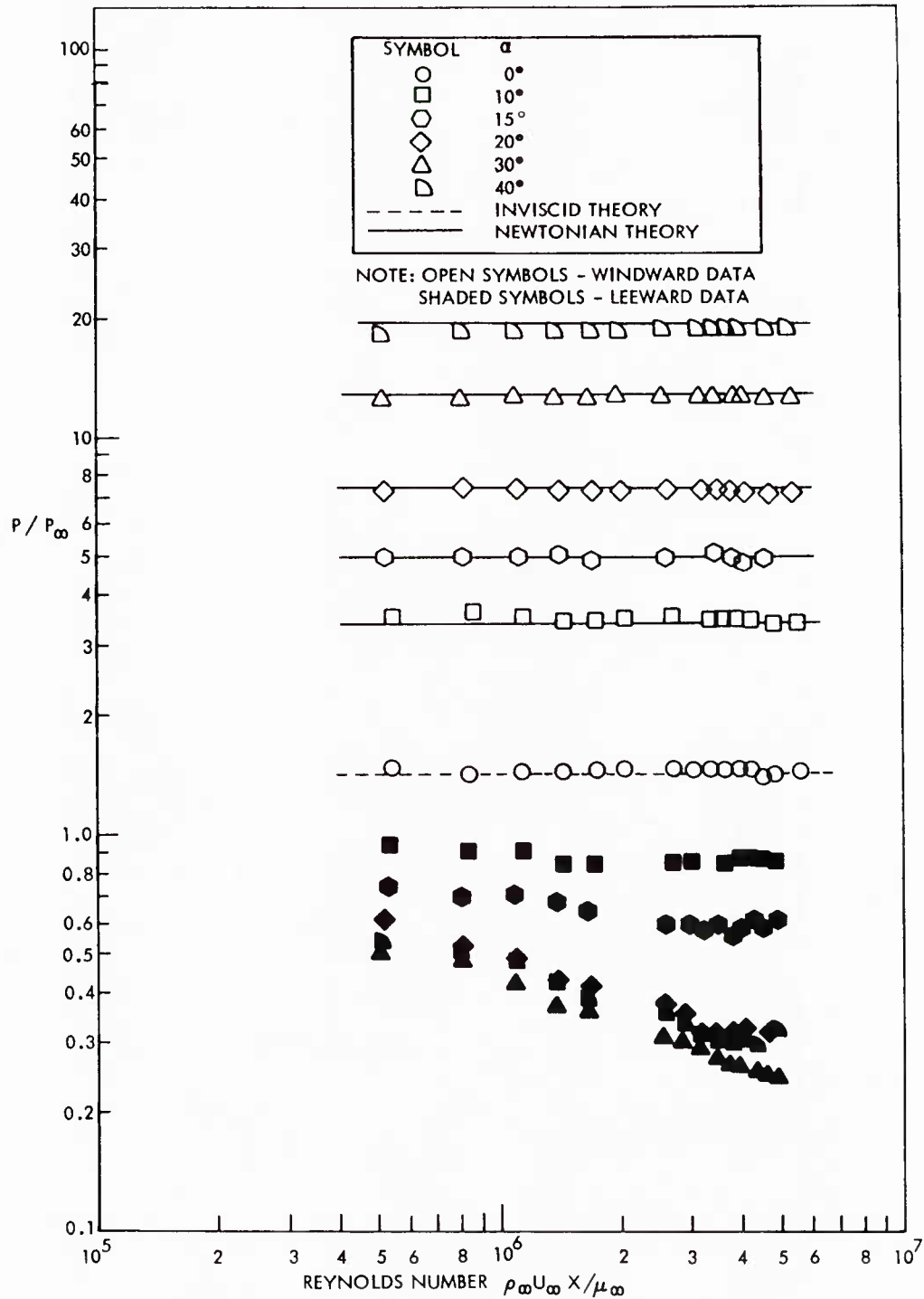


(U) Fig. 5b Circumferential Pressure Distribution

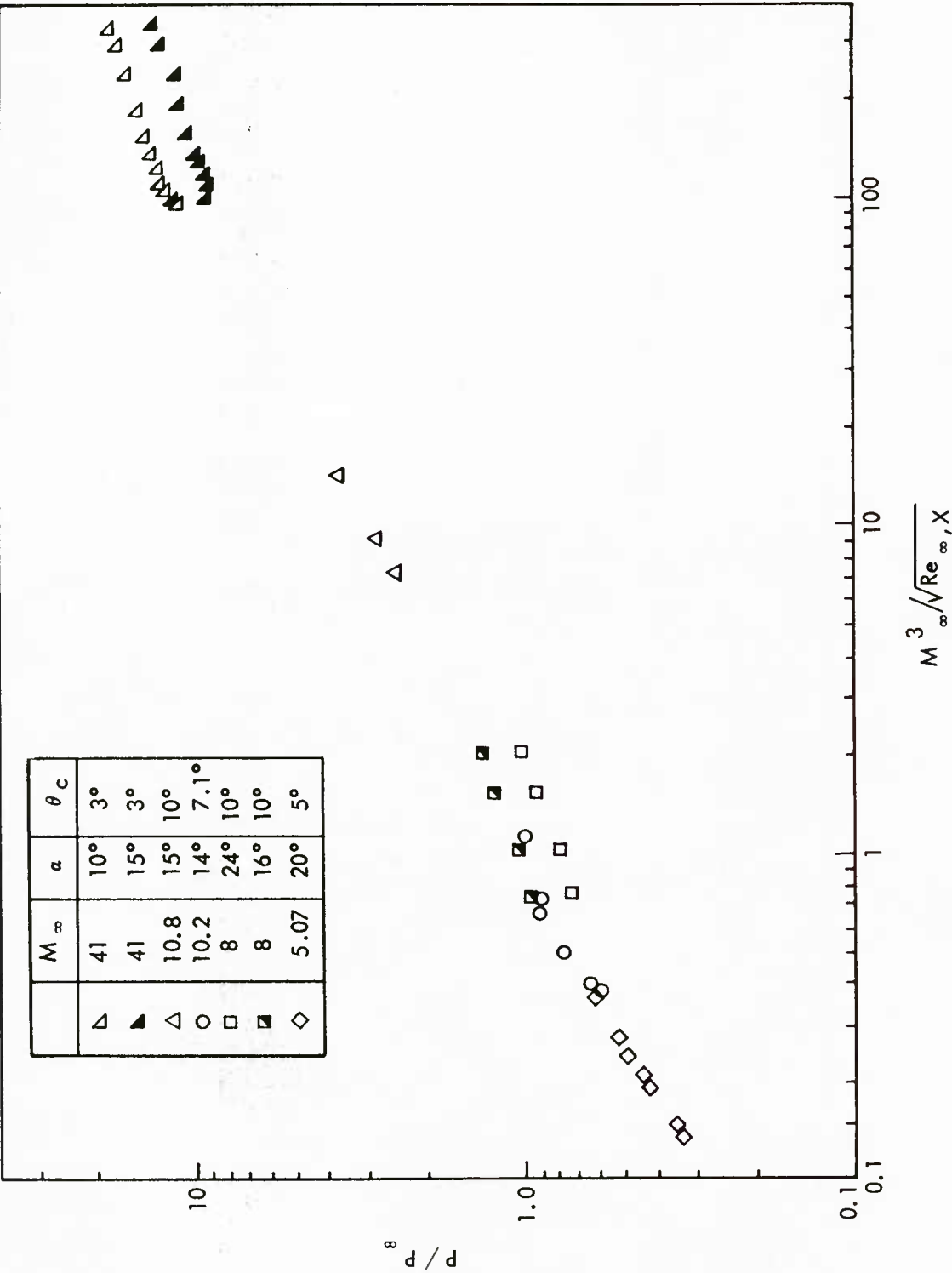




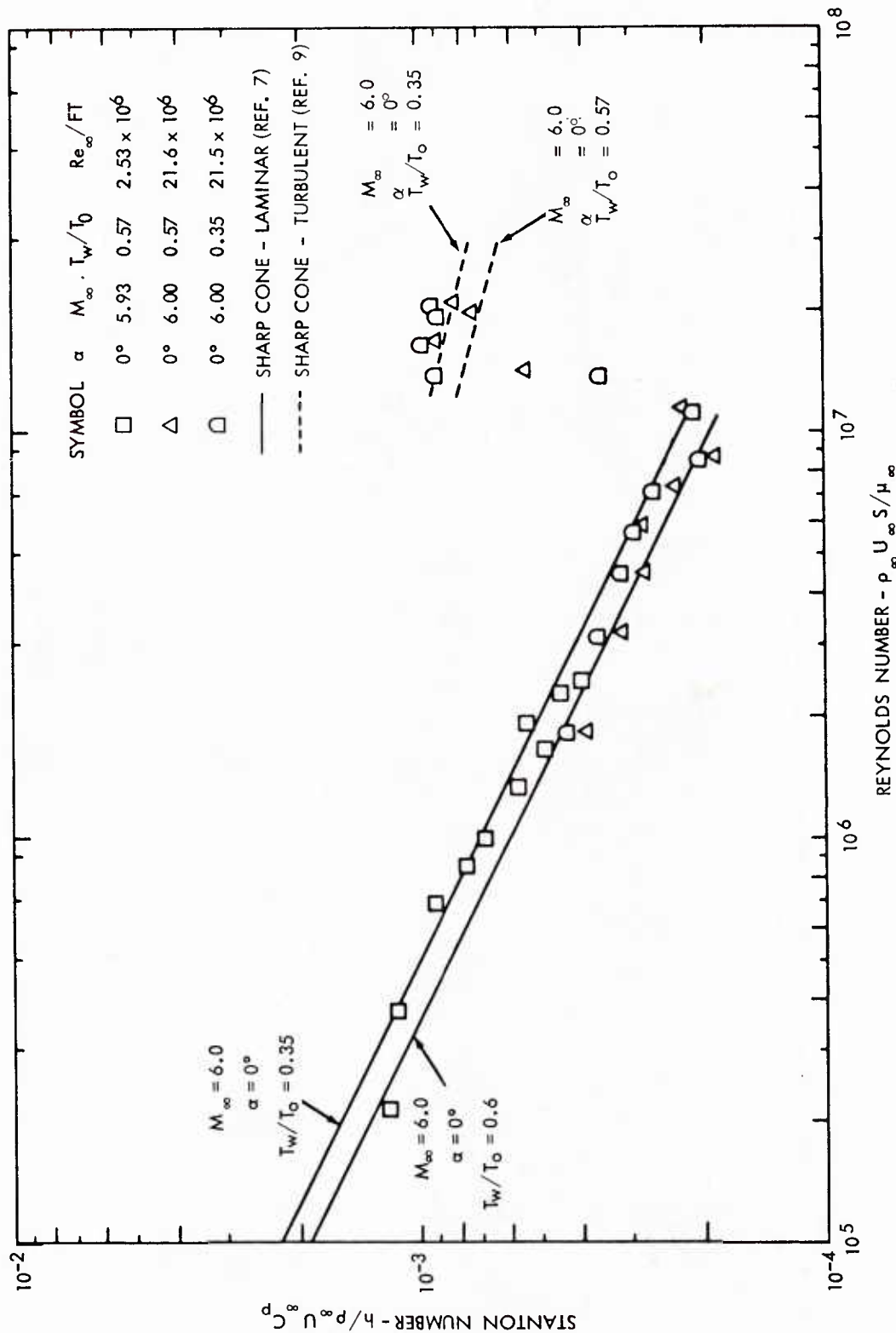
(U) Fig. 6 Static Pressure Variation Along the Most Leeward Meridian Plane-  $\alpha = 20^\circ$



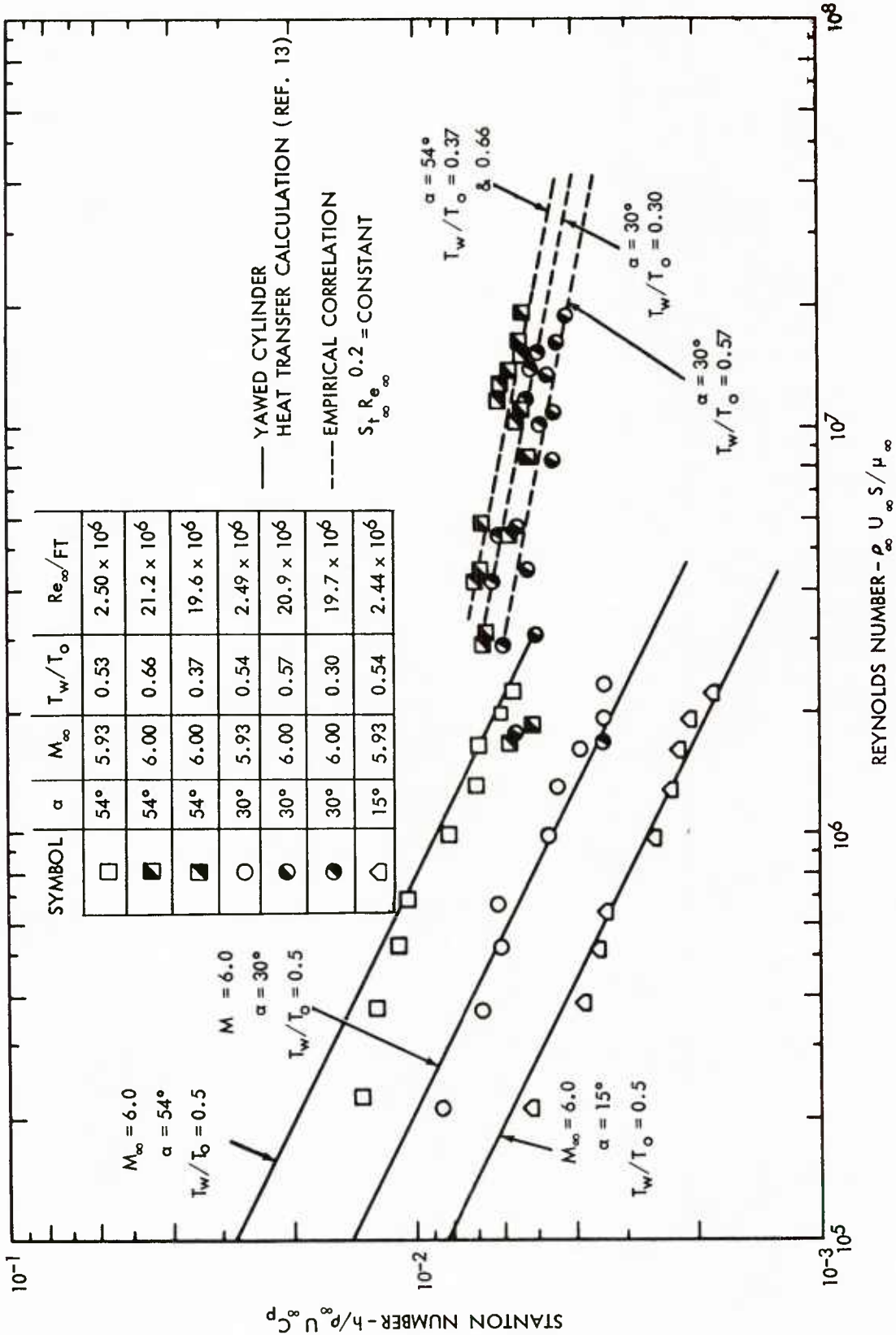
(U) Fig. 7 Surface Pressure Distribution Along 5-Degree Cone  
( $M_\infty = 5.07$ ,  $Re_\infty / FT = 4.8 \times 10^6$ )



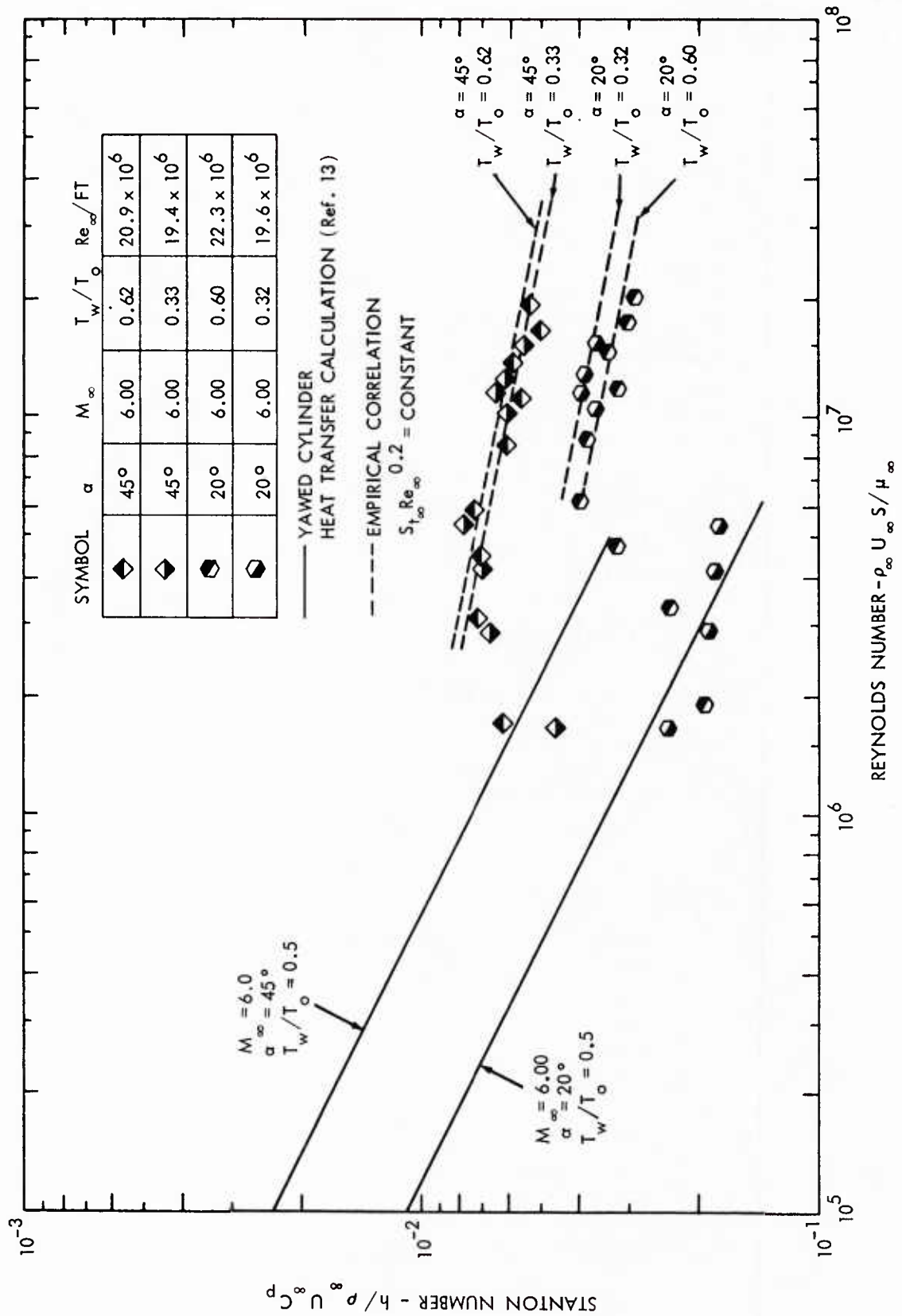
(U) Fig. 8 Correlation of Pressure Distribution Along Leeward Meridian Generator



(U) Fig. 9 Zero Angle of Attack Heat Transfer Distribution

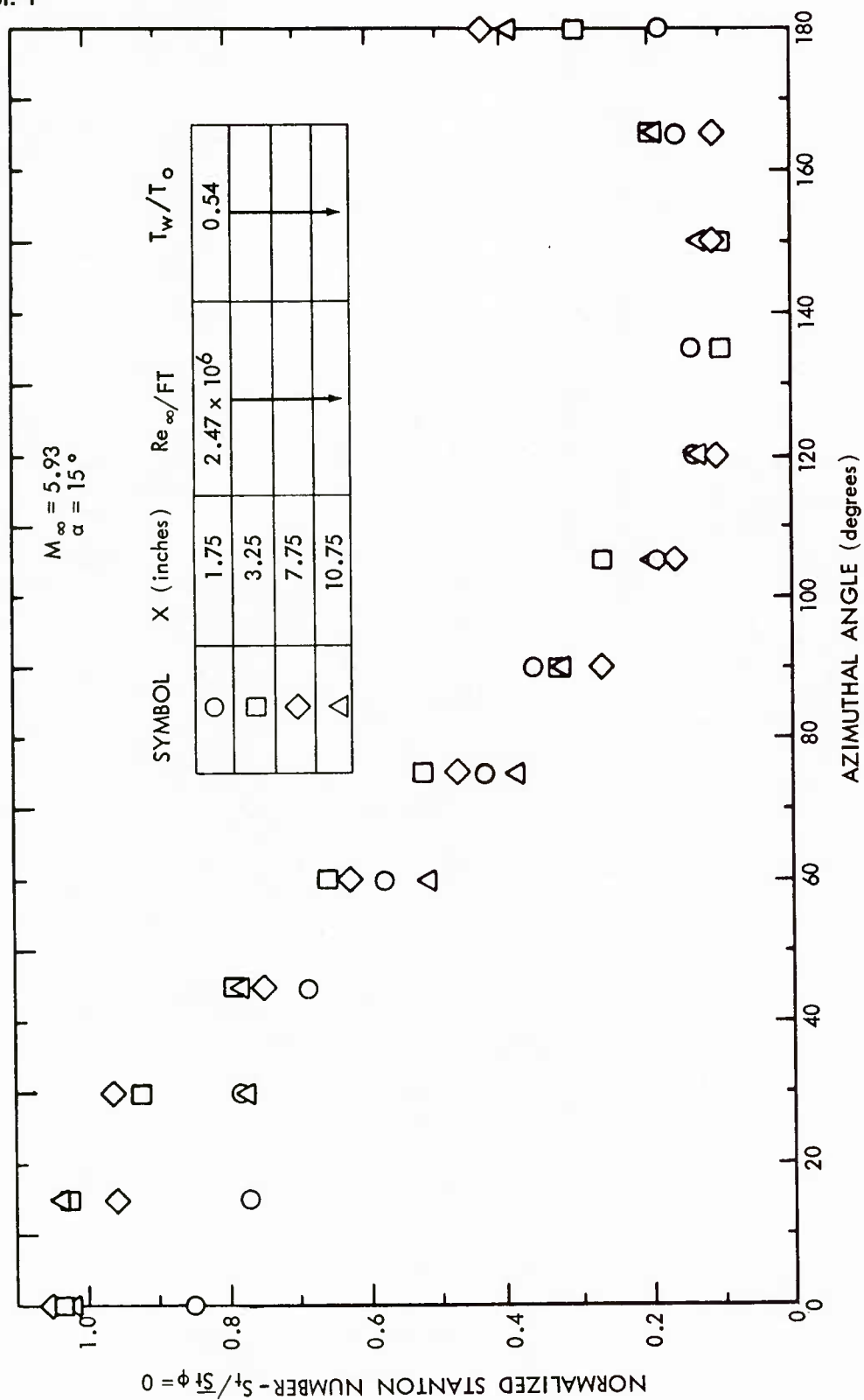


(U) Fig. 10a Heat Transfer Distribution Along Stagnation Streamline

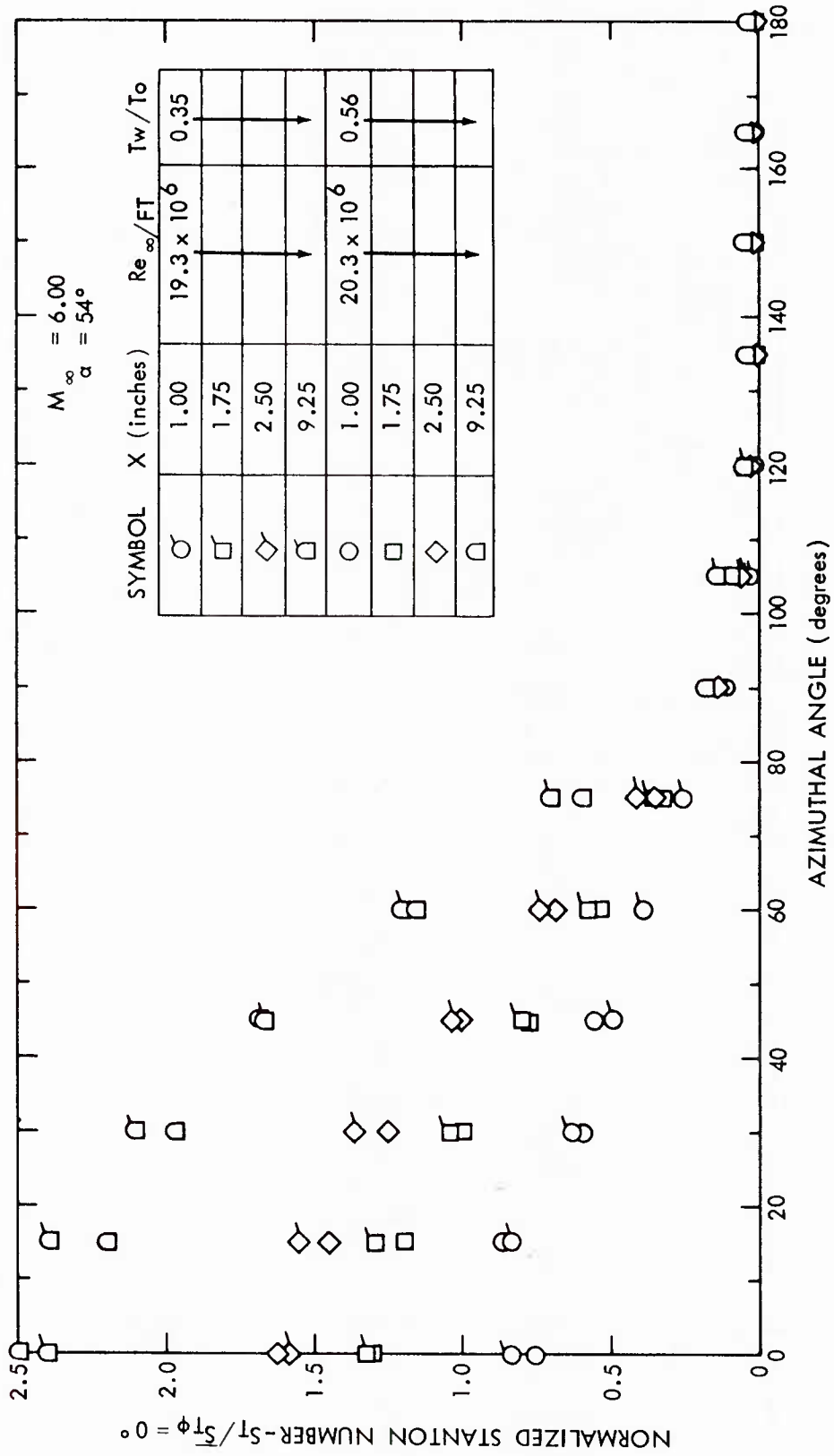


(U) Fig. 10b Heat Transfer Distribution Along Stagnation Streamline

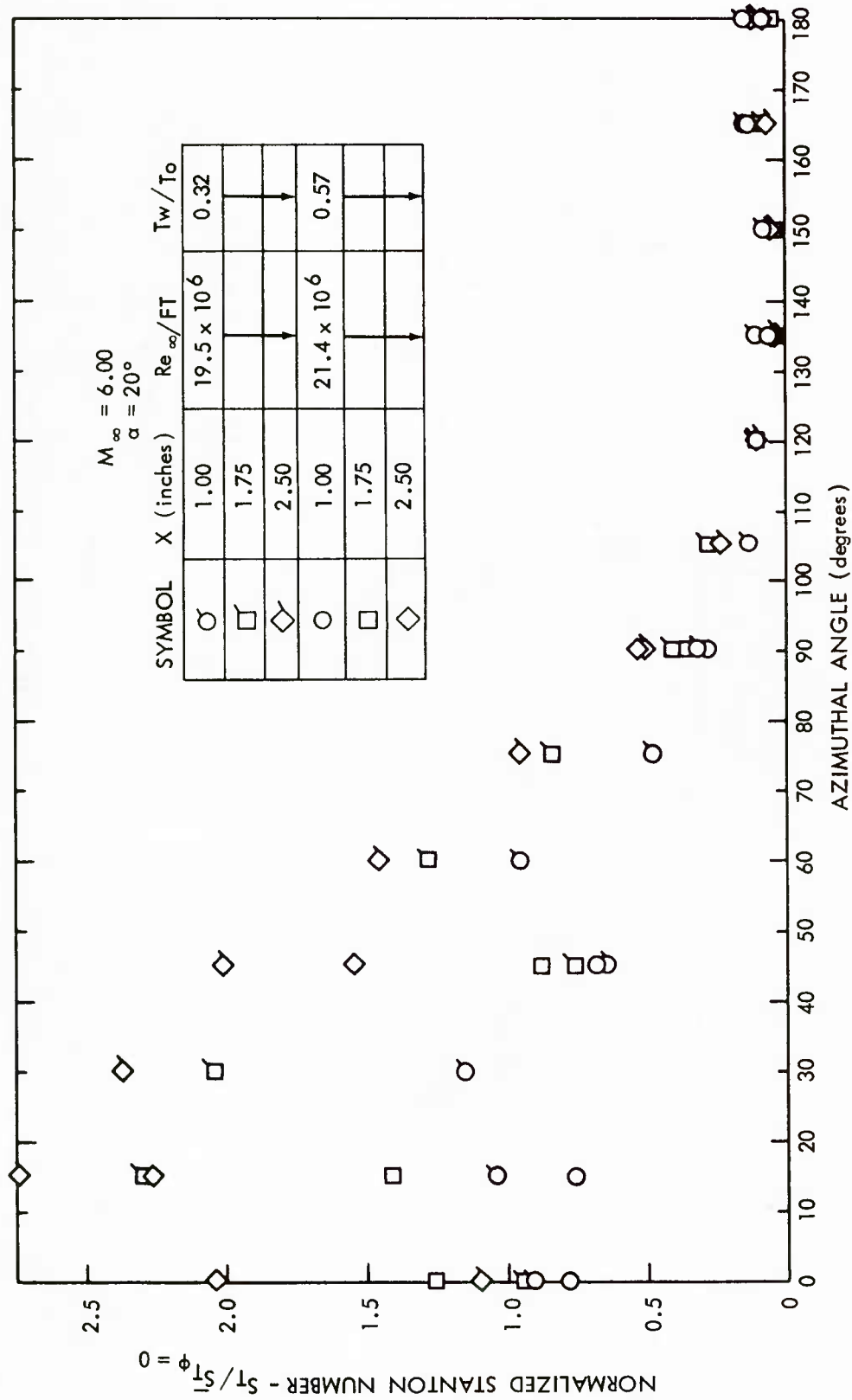




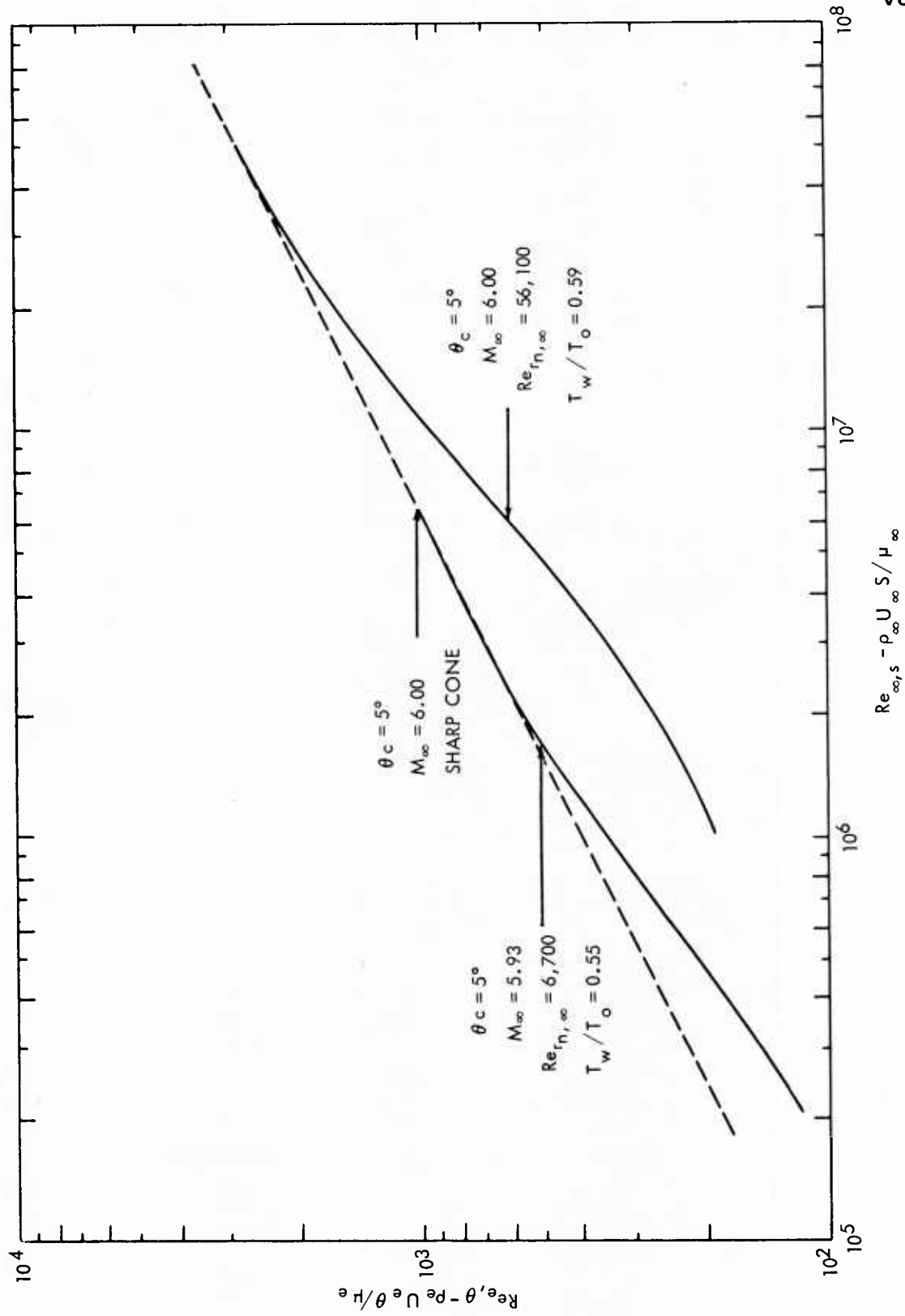
(U) Fig. 11 Circumferential Heat Transfer Distributions



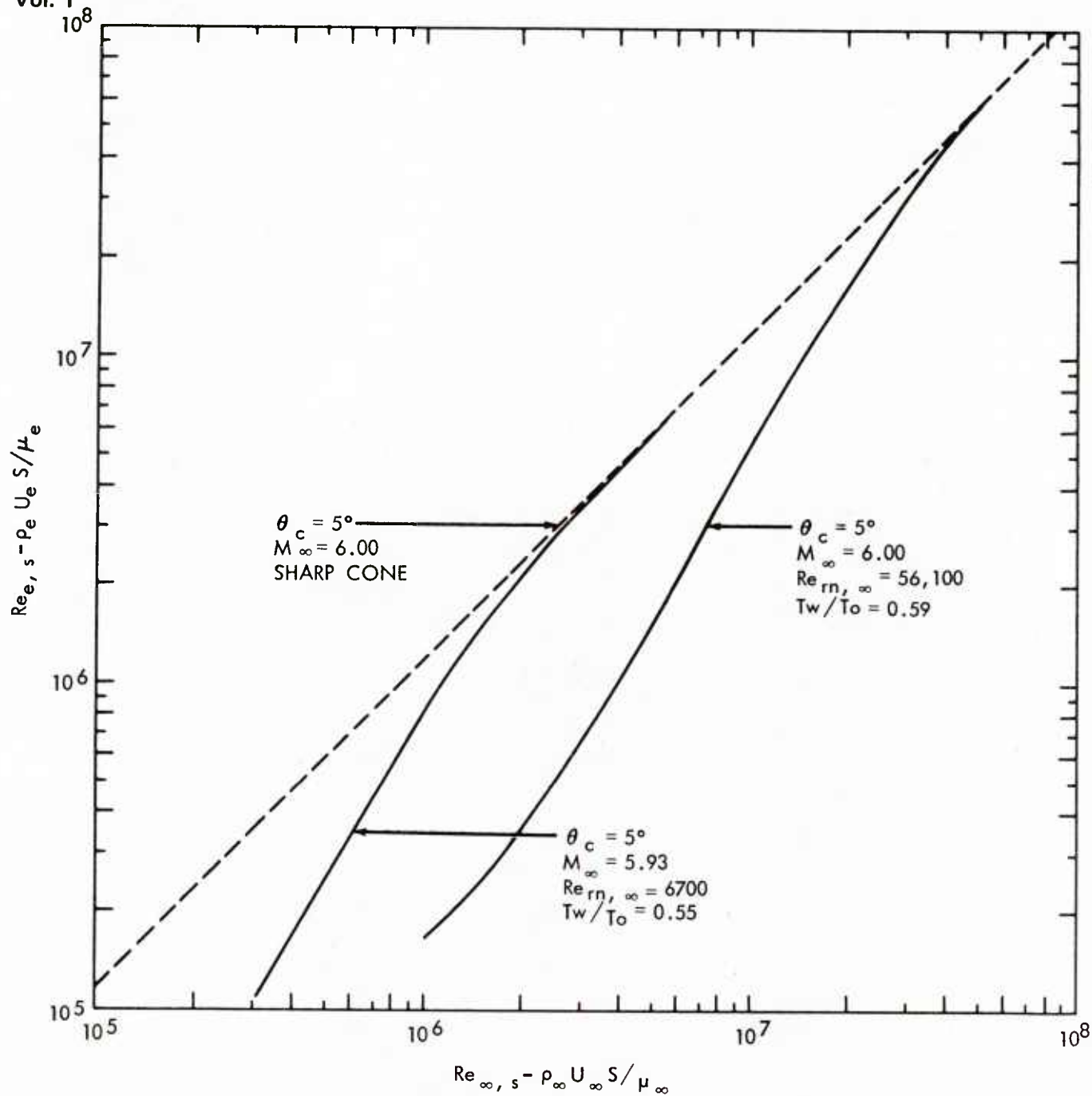
(U) Fig. 12 Circumferential Heat Transfer Distributions



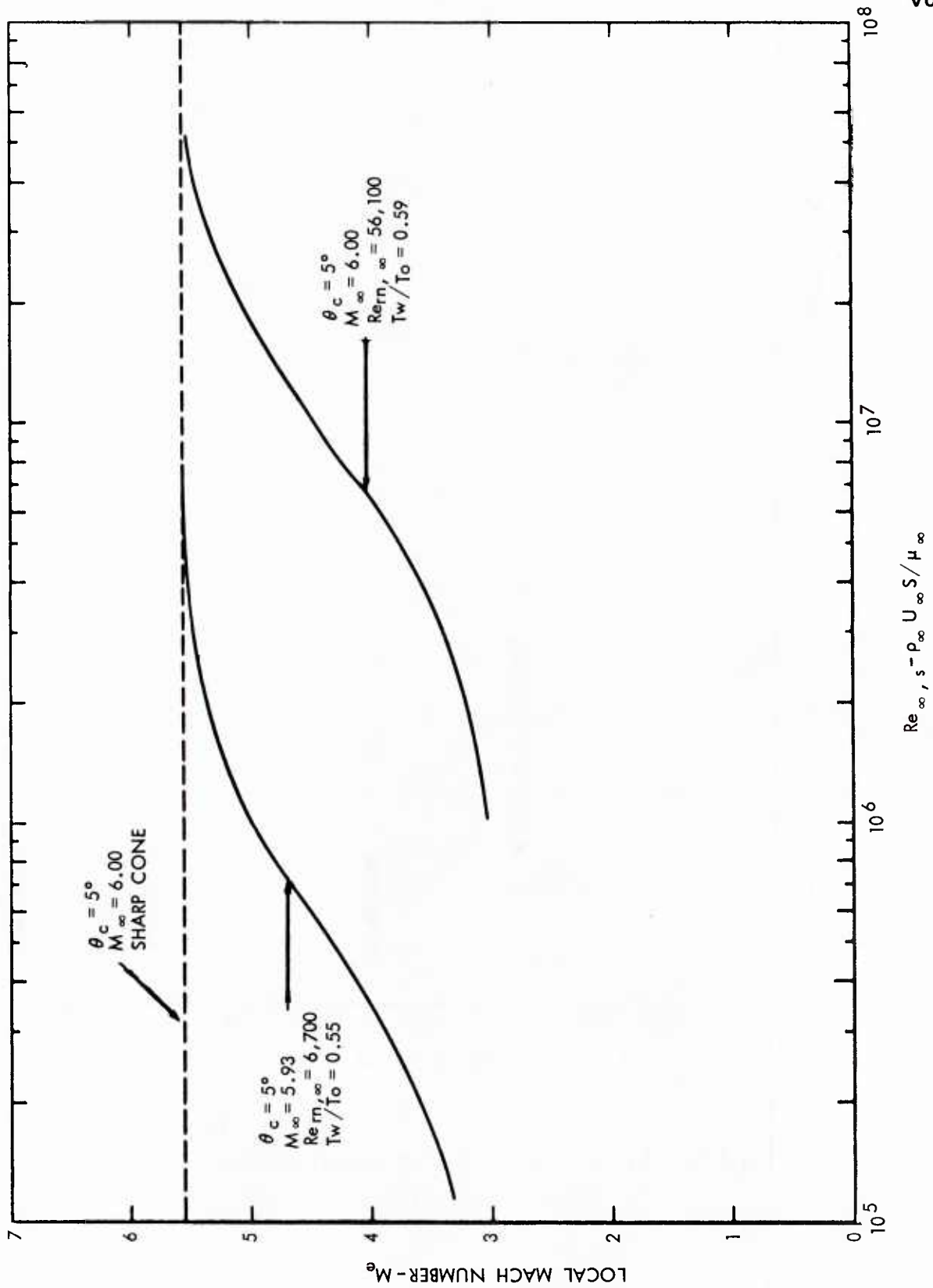
(U) Fig. 13 Circumferential Heat Transfer Distributions



(U) Fig. 14 Effect of Bluntness on Momentum Thickness Reynolds Number

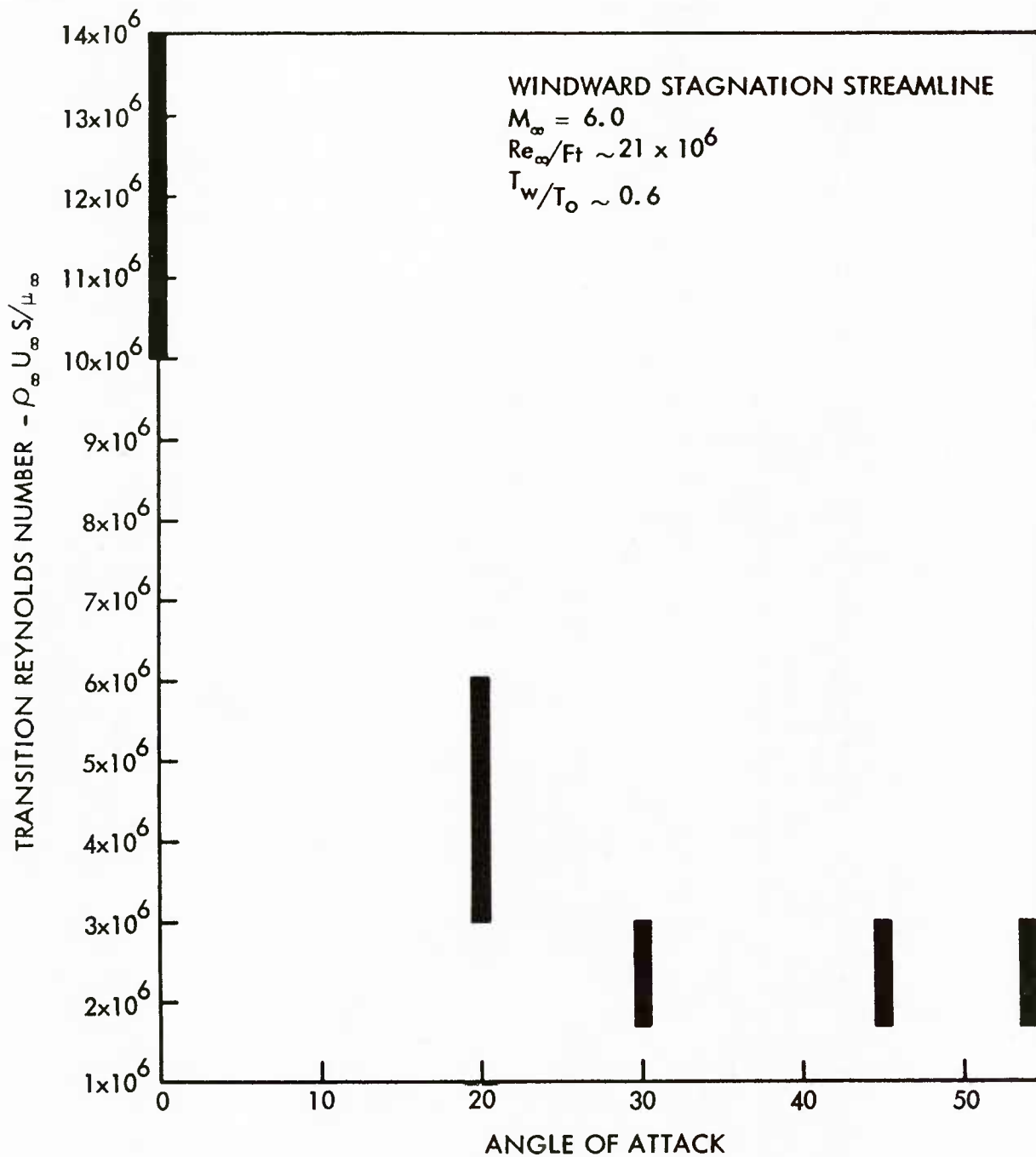


(U) Fig. 15 Effect of Bluntness on Local Reynolds Number

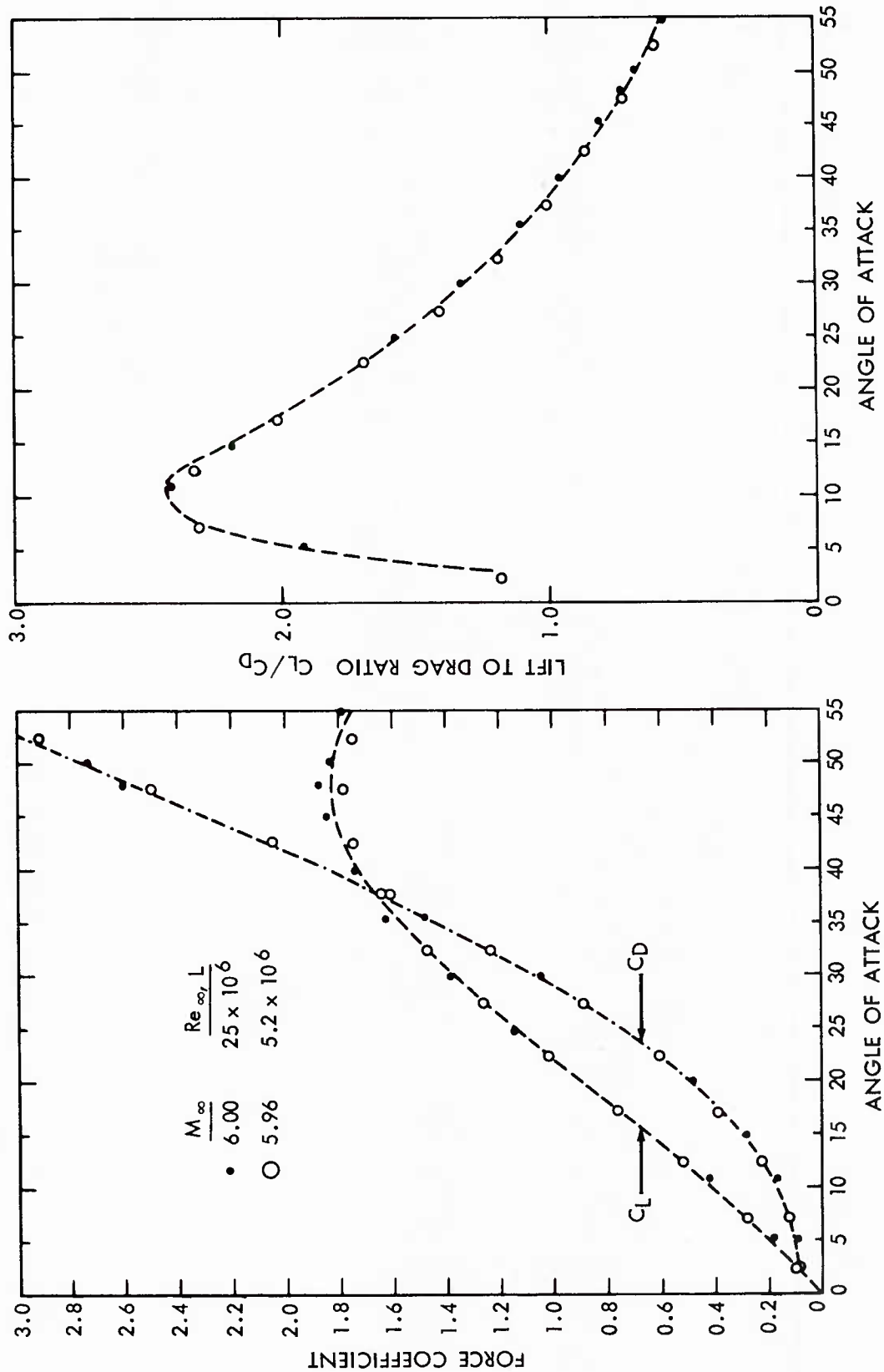


(U) Fig. 16 Effect of Bluntness on Local Mach Number

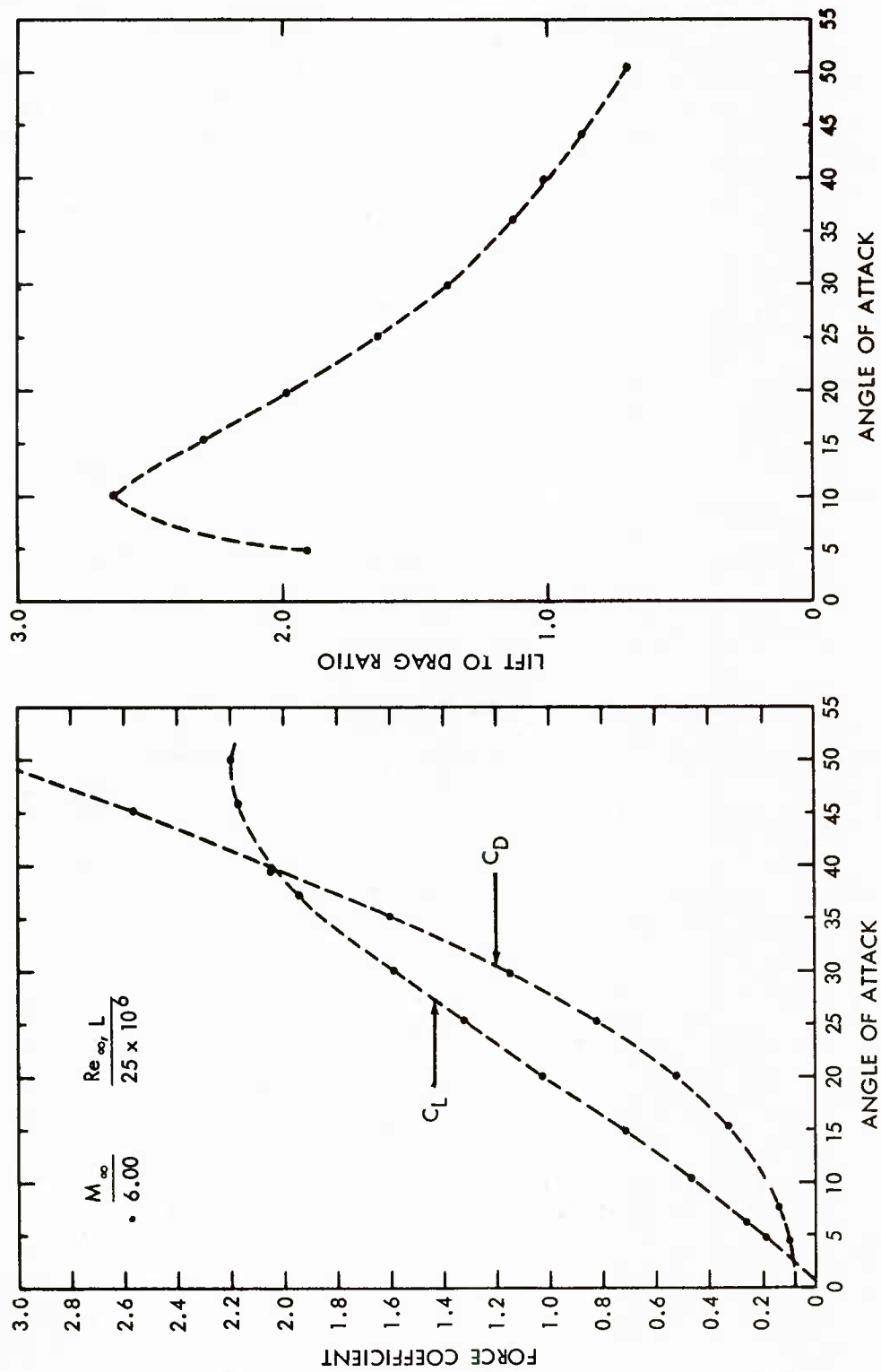




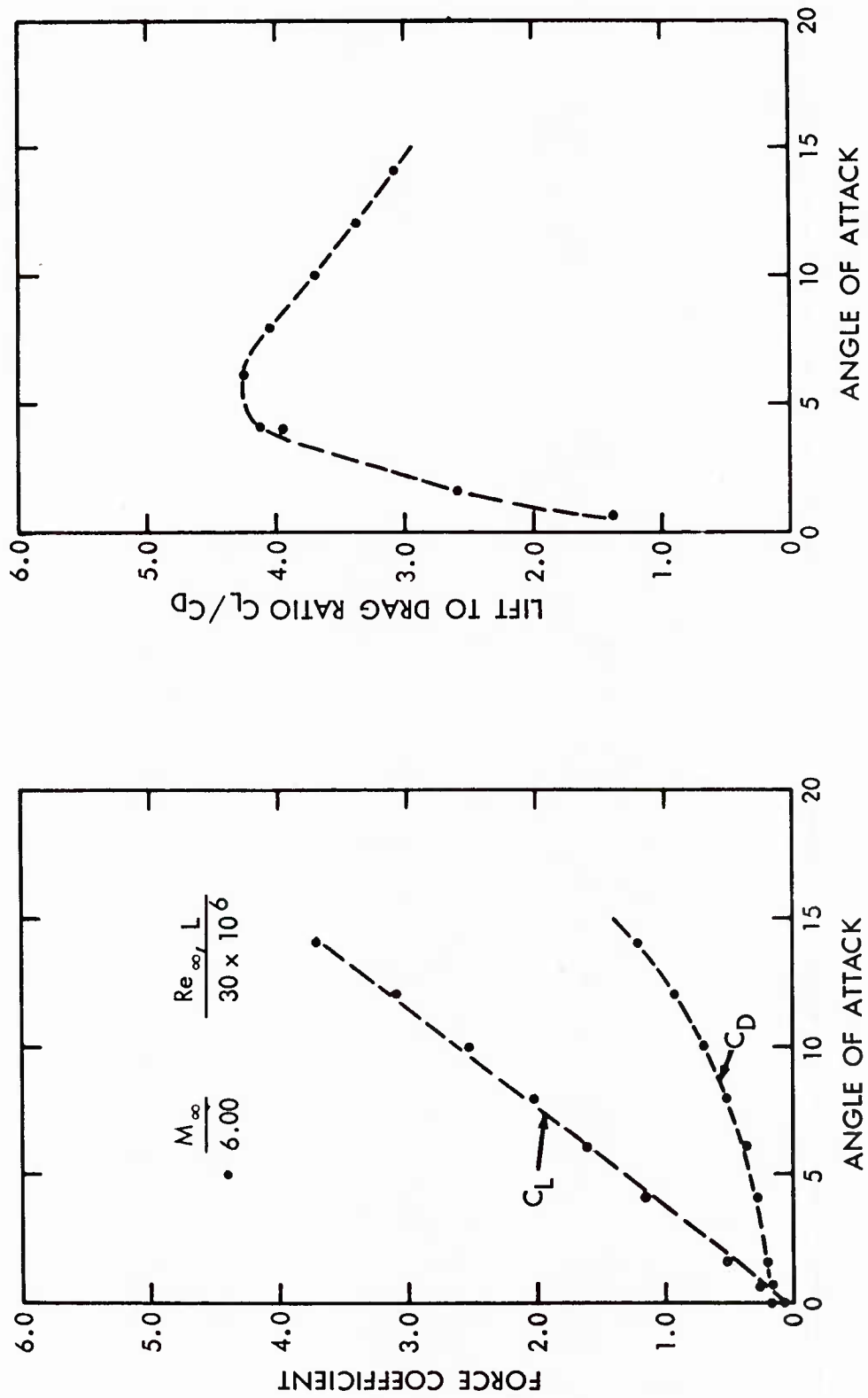
(U) Fig. 17 Variation of Transition Reynolds Number with Angle of Attack



(U) Fig. 18 Lift and Drag Coefficients and Lift to Drag Ratio-Configuration 6 FN

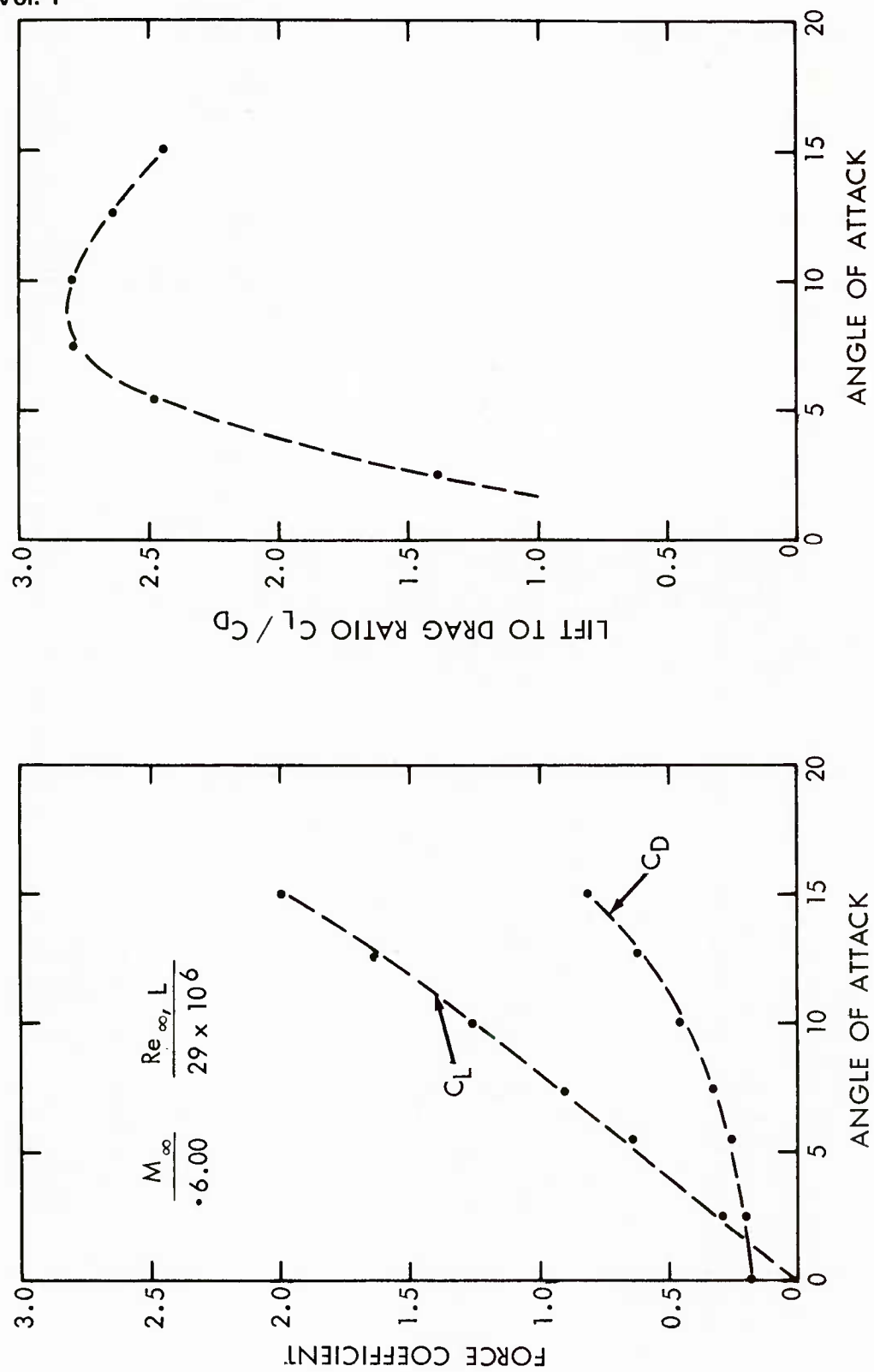


(U) Fig. 19 Lift and Drag Coefficients and Lift to Drag Ratio-Configuration 6FX-1

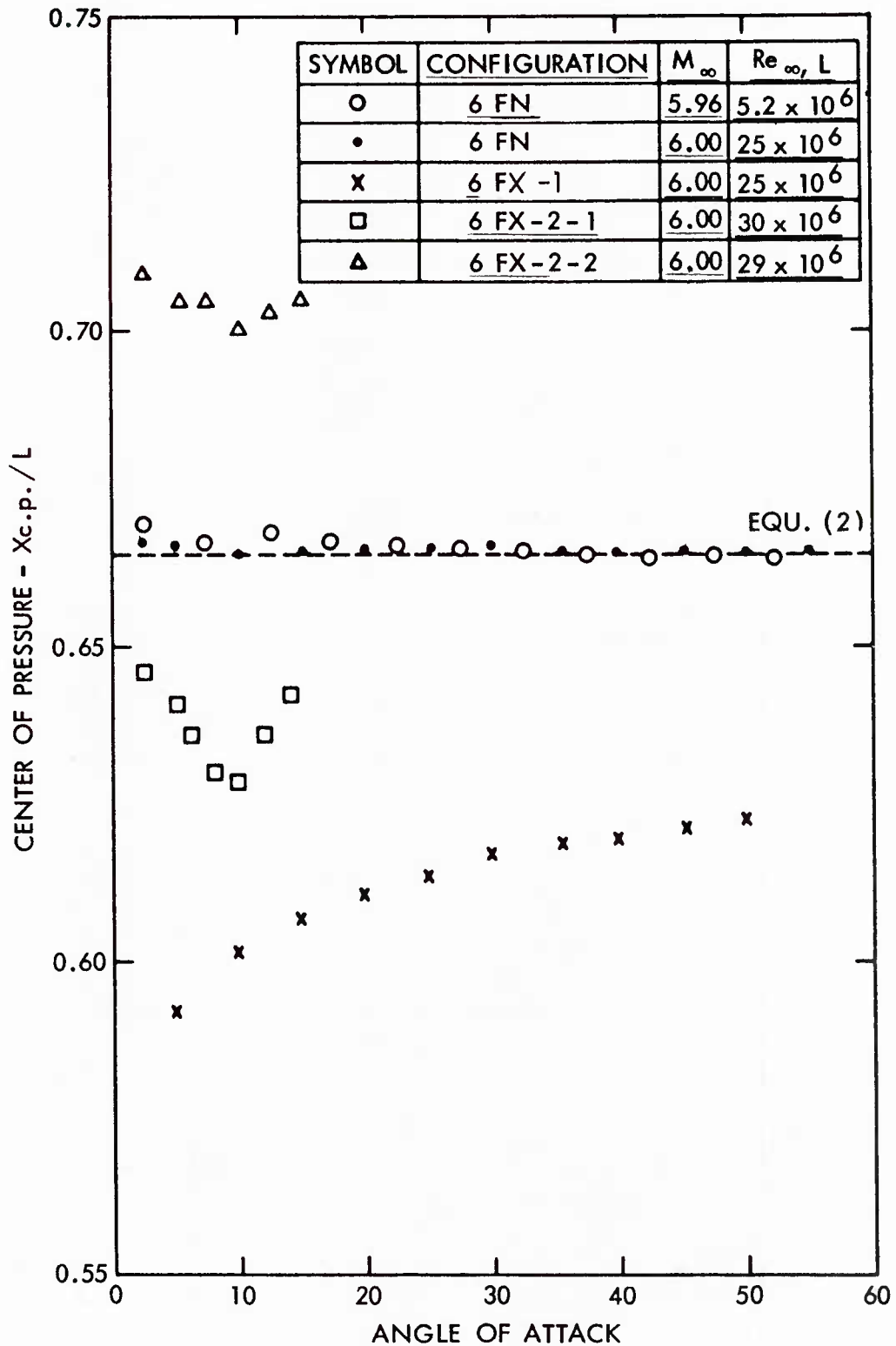


(U) Fig. 20 Lift and Drag Coefficients and Lift to Drag Ratio-Configuration 6FX-2-1

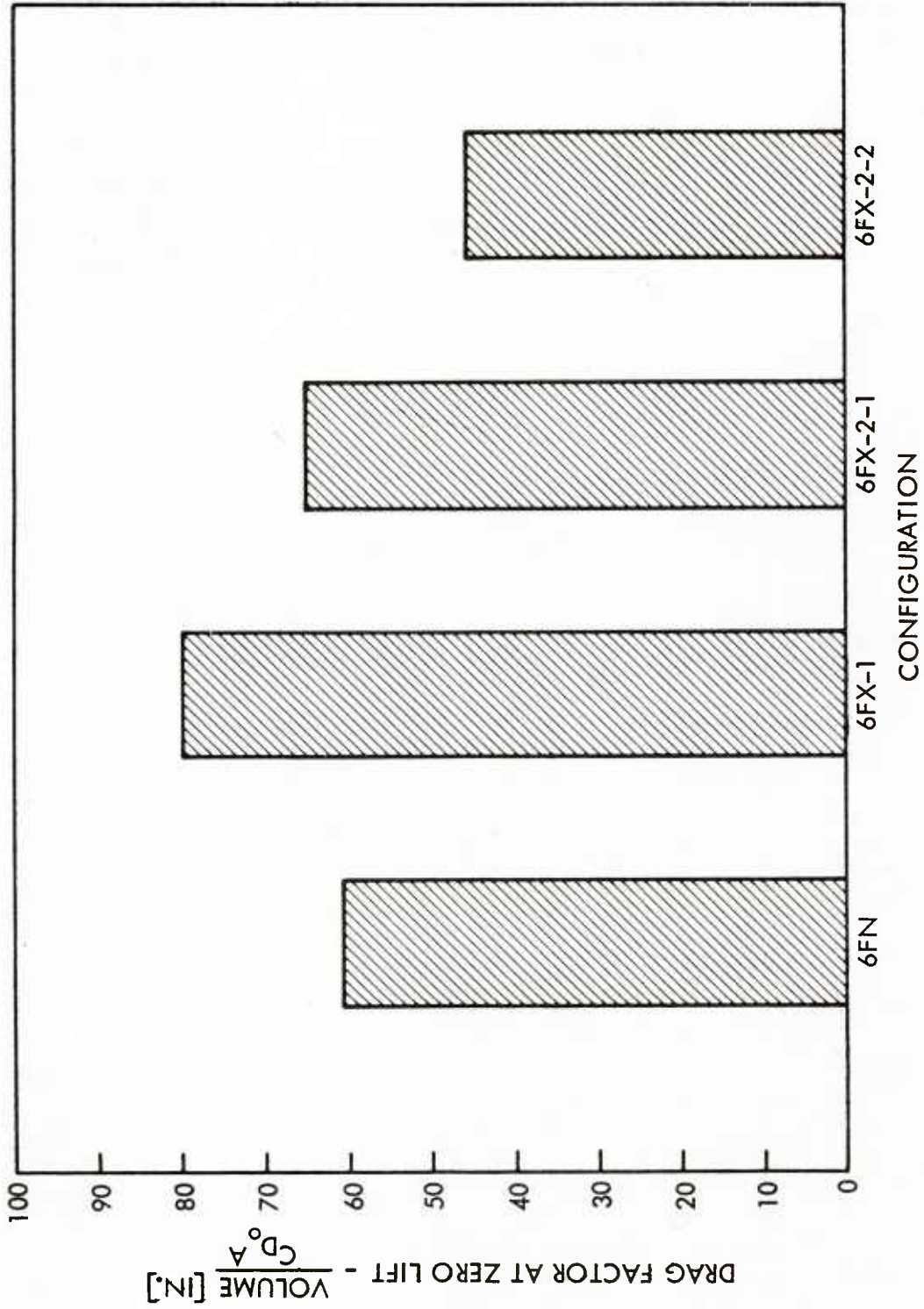
Vol. 1



(U) Fig. 21 Lift and Drag Coefficients and Lift to Drag Ratio-Configuration 6FX-2-2

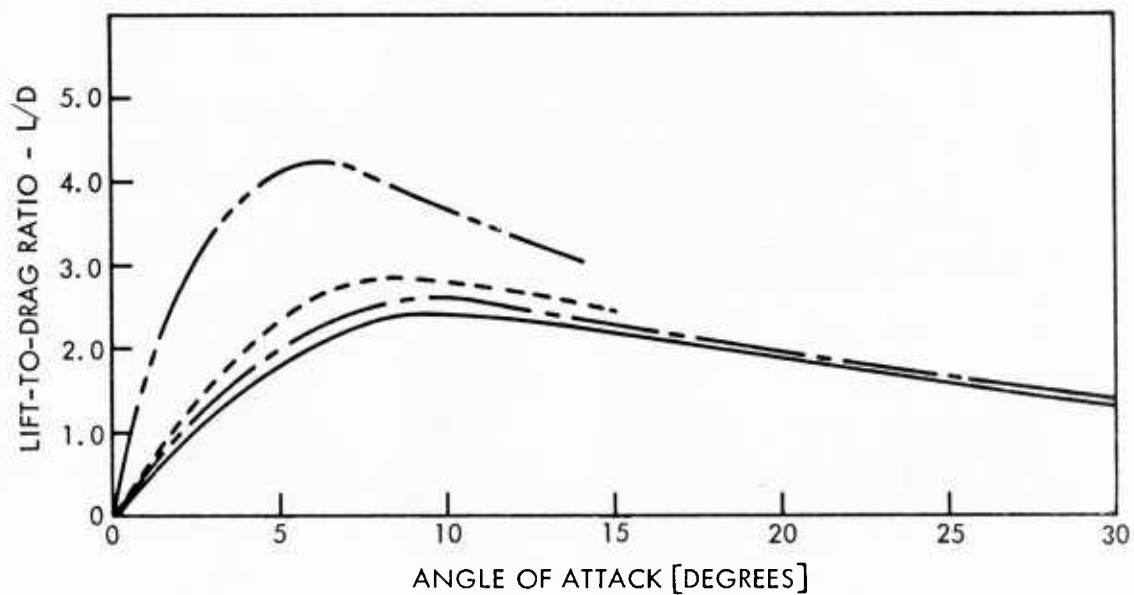
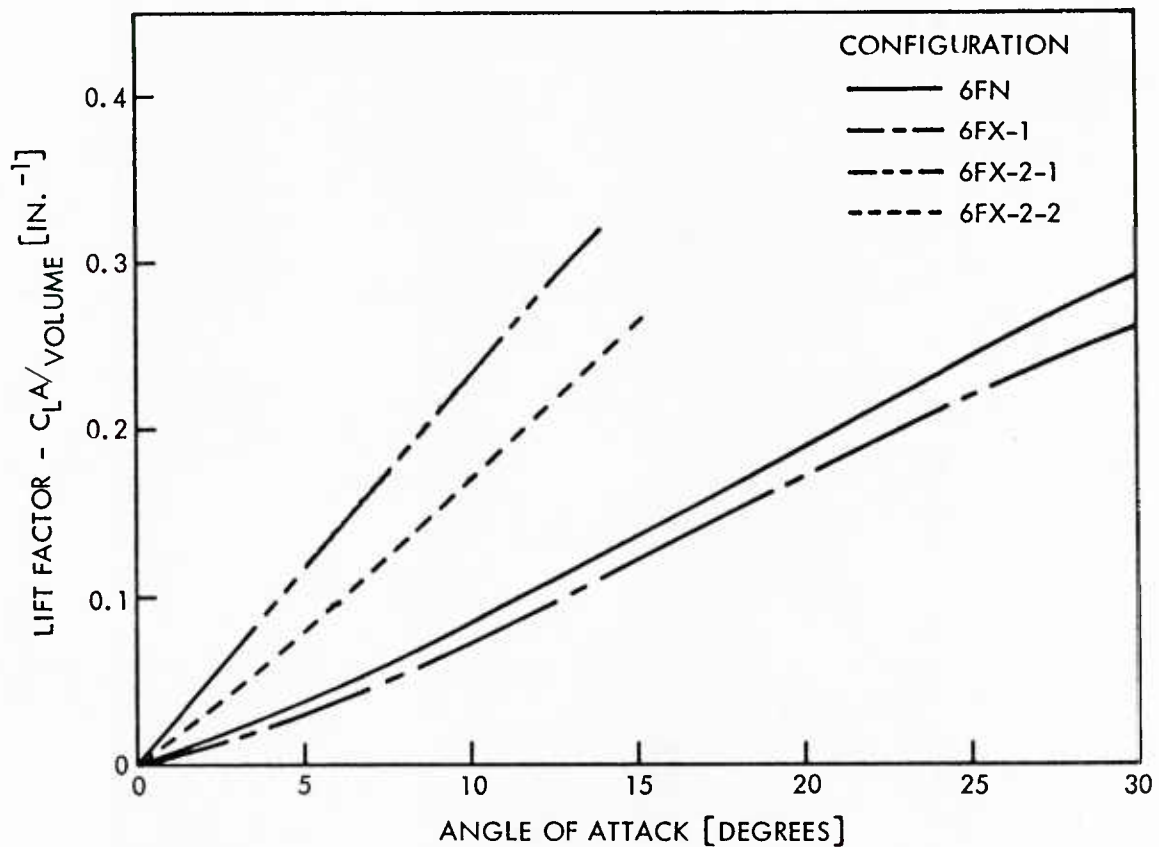


(U) Fig. 22 Variation of Center of Pressure

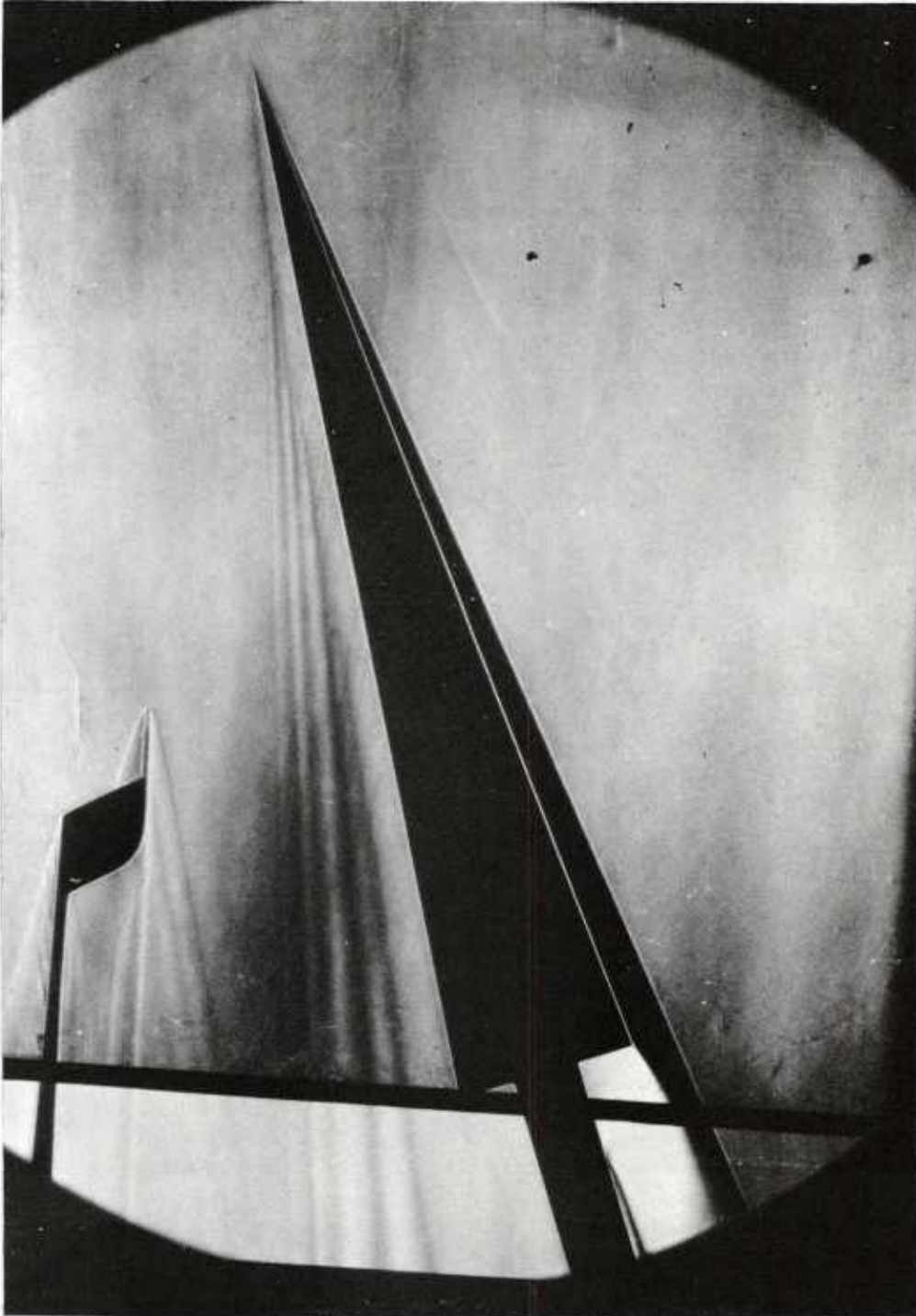


(U) Fig. 23 Drag Factor at Zero Lift

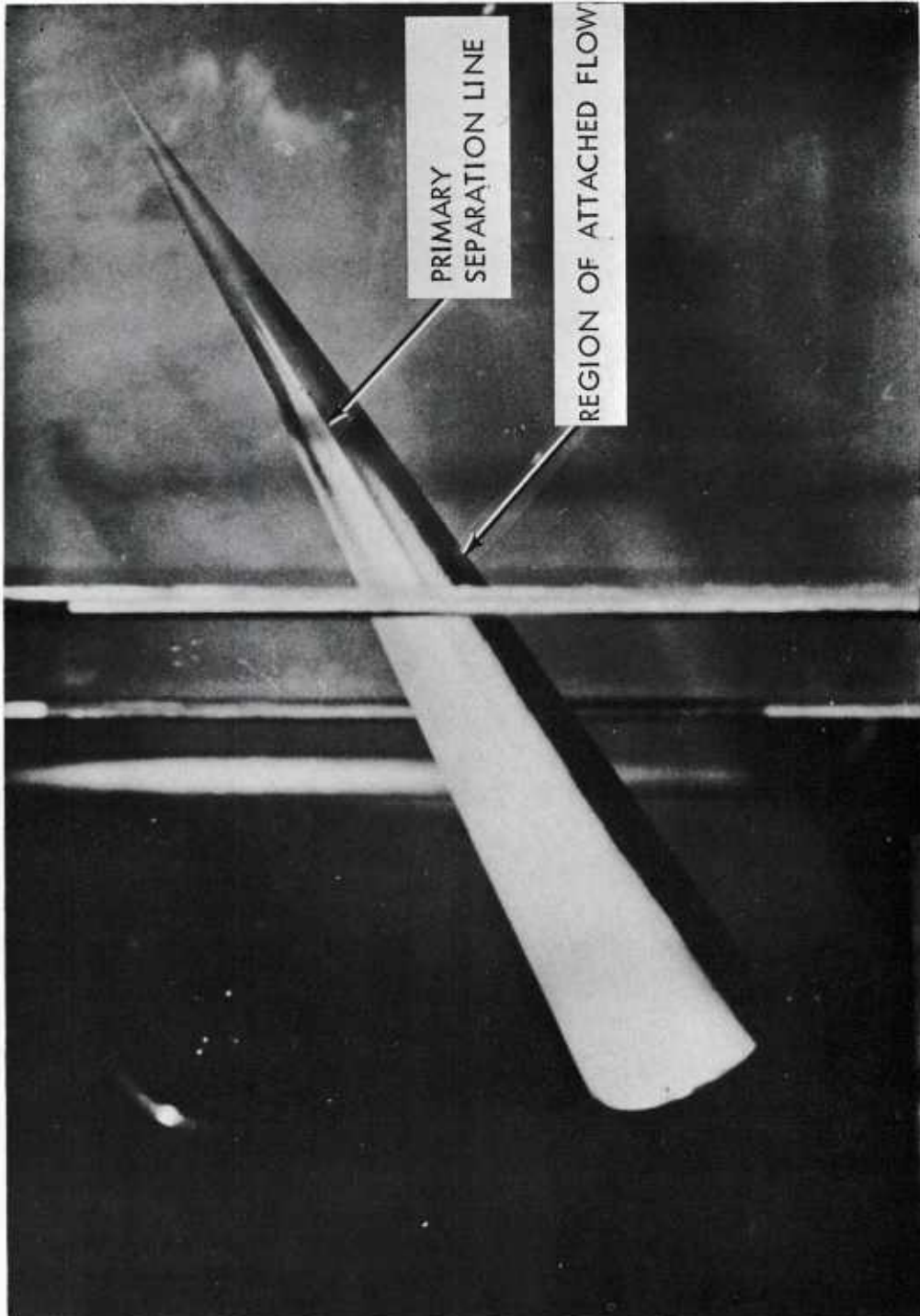




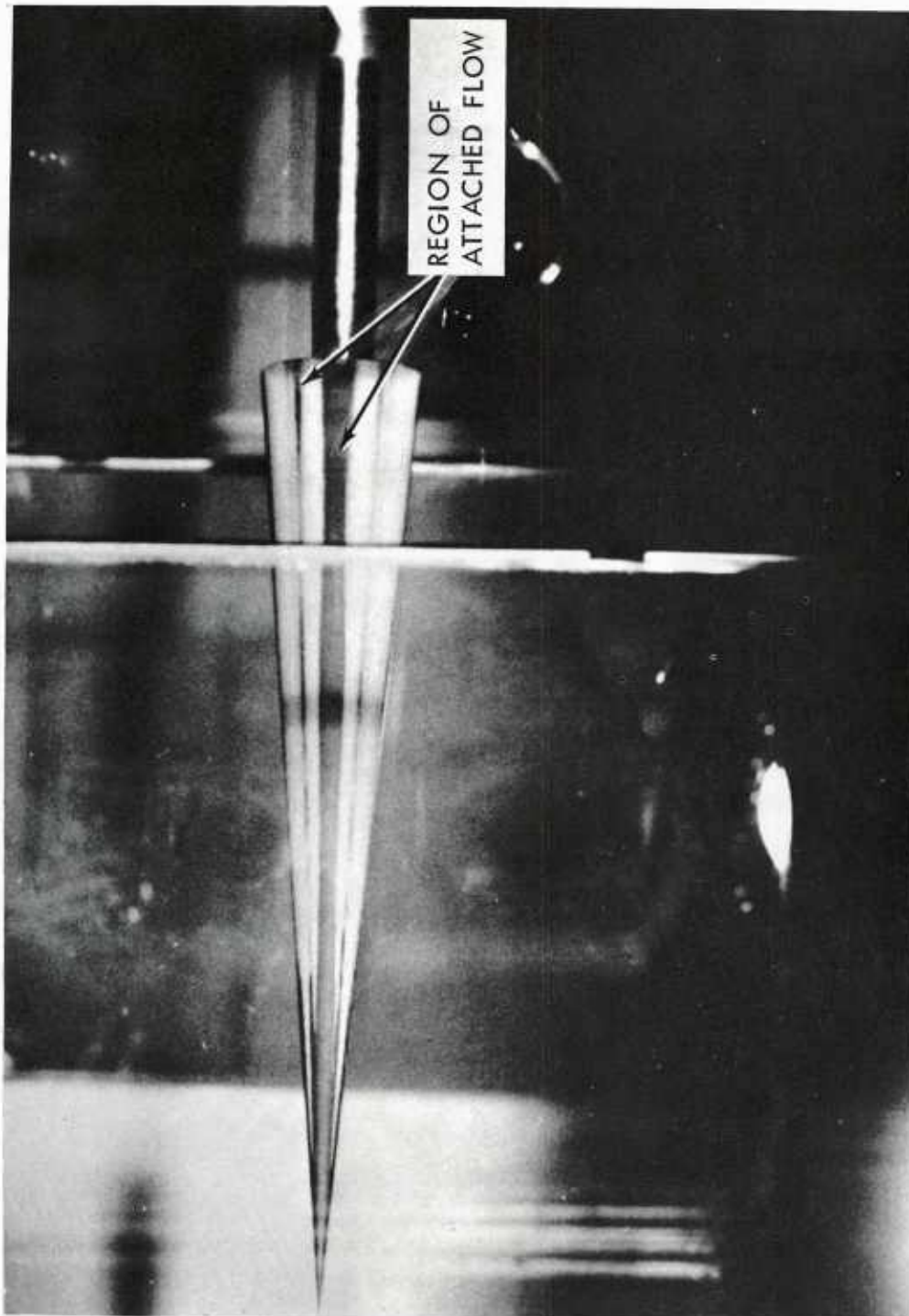
(U) Fig. 24 Maneuverability Characteristics



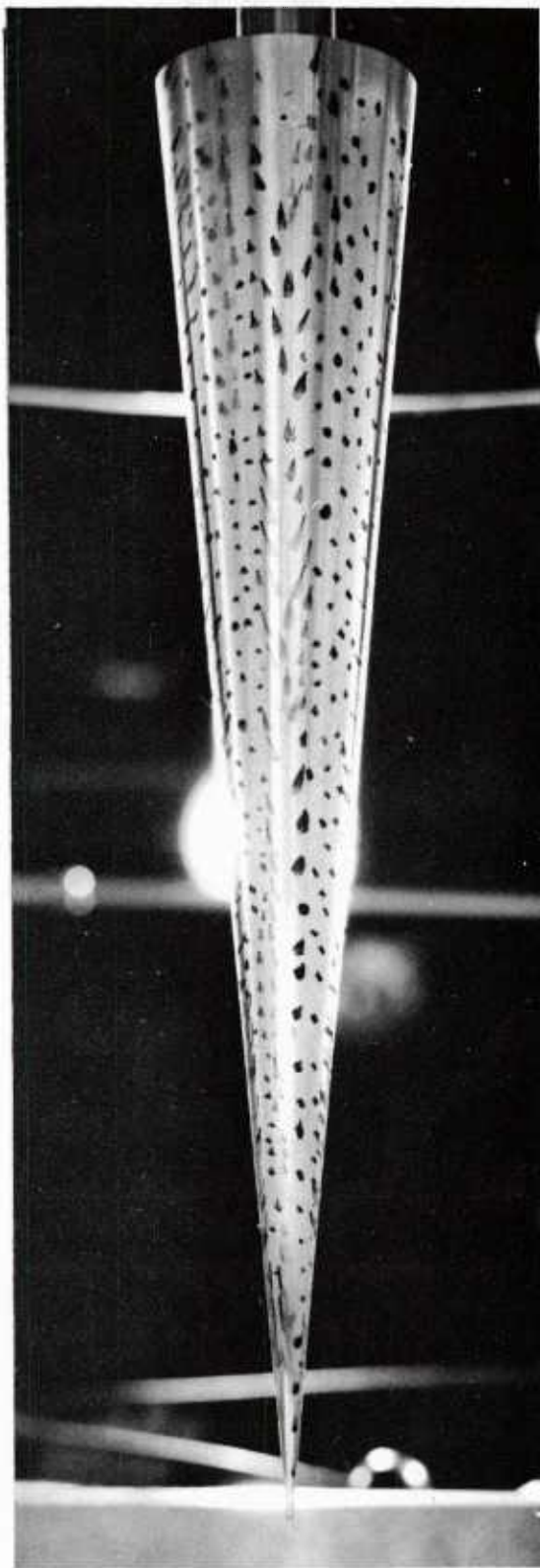
(U) Fig. 25. Schlieren Photograph of an Inclined Slender Cone ( $\alpha = 20^\circ$ )



(U) Fig. 26 Azobenzene Coated Model - Side View - ( $\alpha = 40^\circ$ )

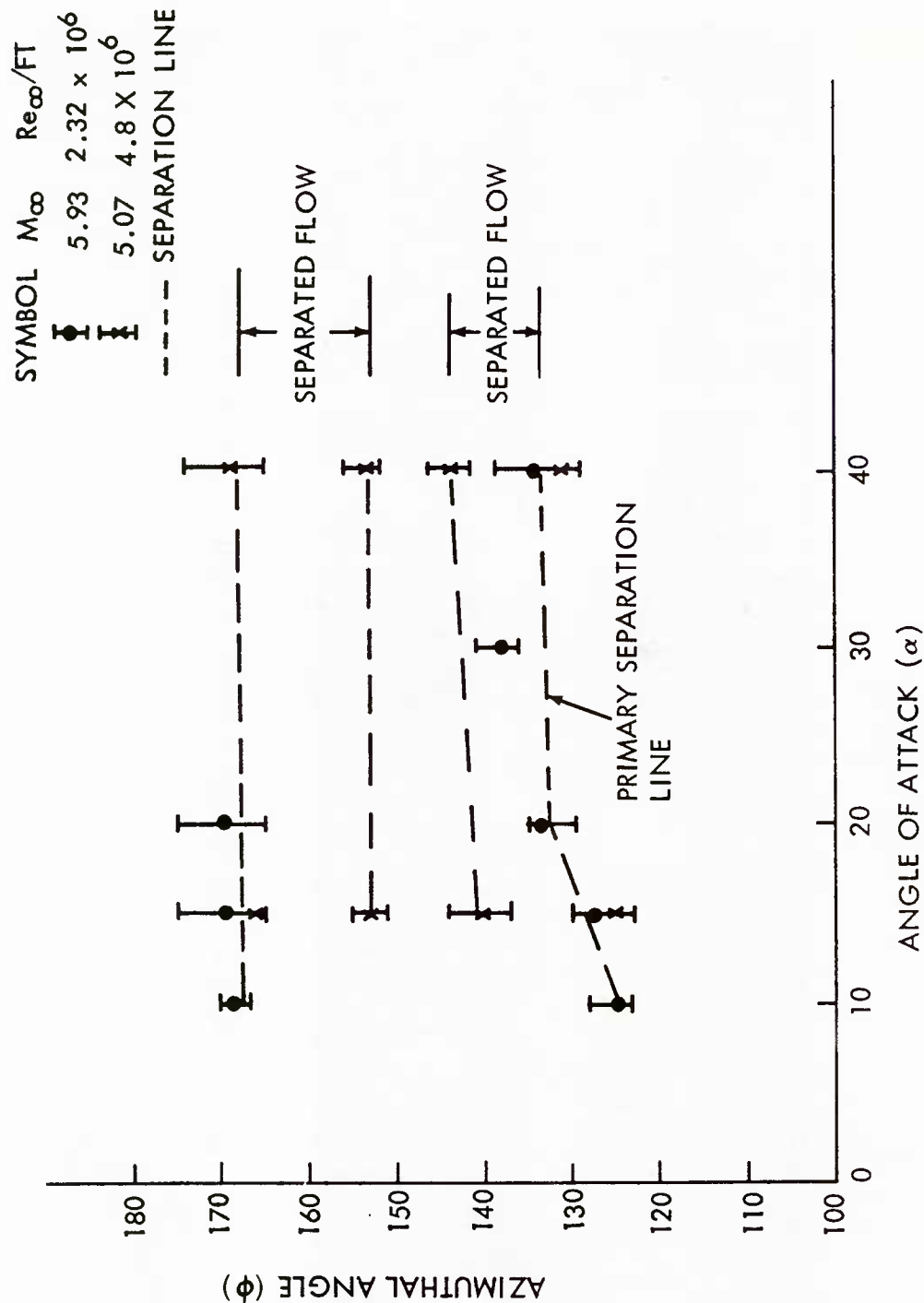


(U) Fig. 27 Azobenzene Coated Model - Leeward Side (  $\alpha = 15^\circ$  )



(U) Fig. 28 Surface Oil Flow Pattern Leeward Surface-  $\alpha = 15^\circ$

Vol. 1



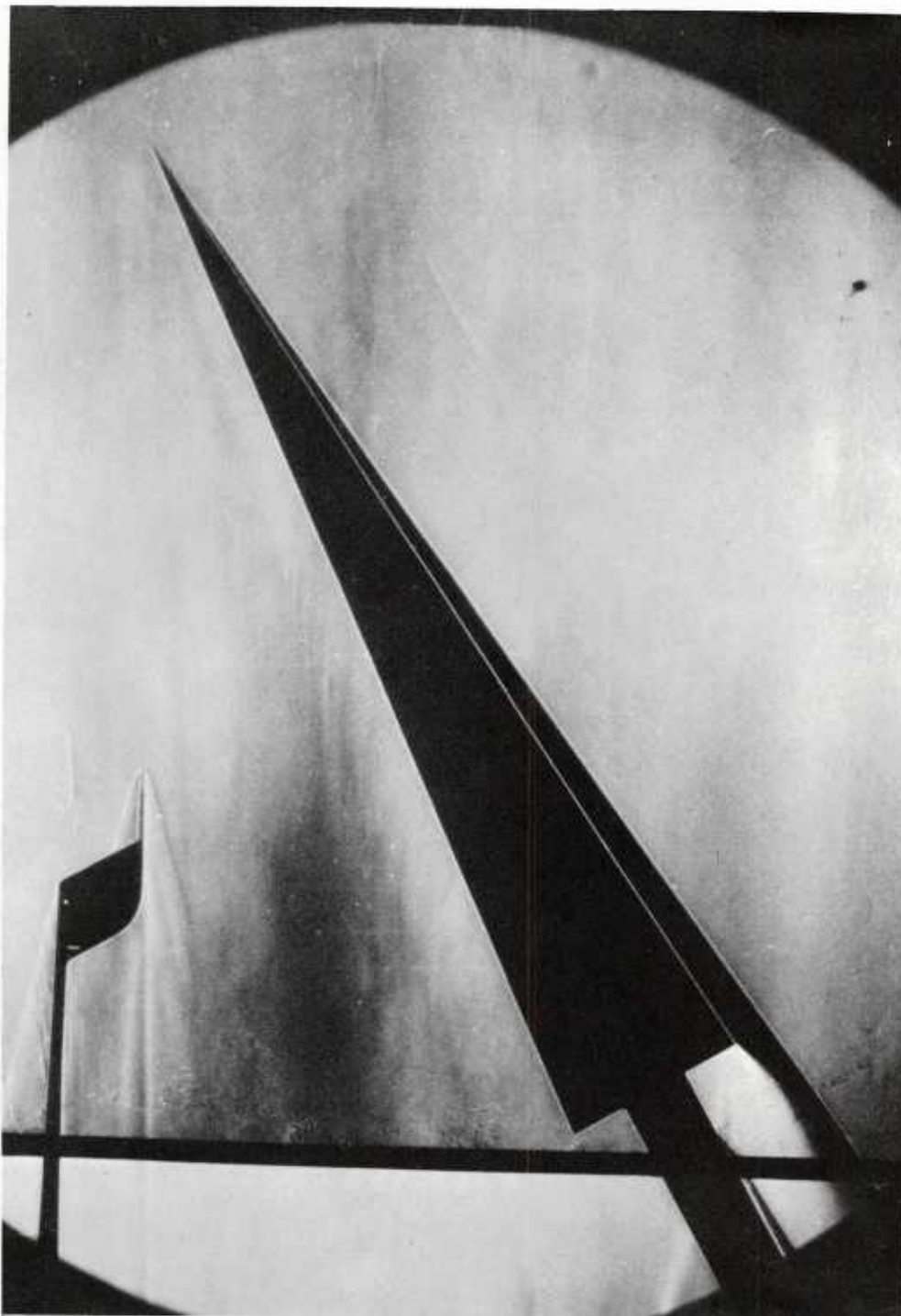
(U) Fig. 29 Separation Measurements



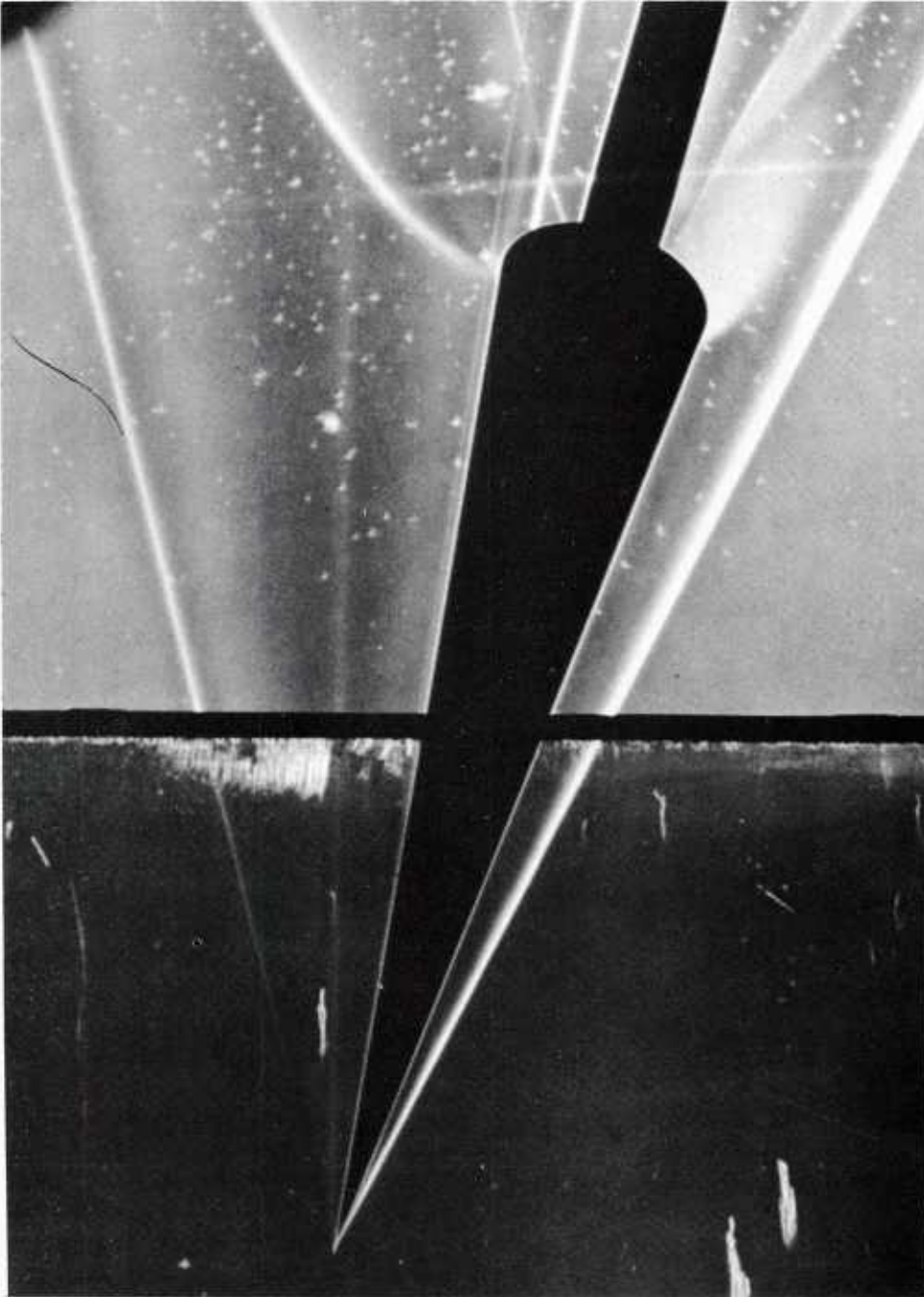


(U) Fig. 30 Schlieren Photograph of an Inclined Slender Cone ( $\alpha = 15^\circ$ )

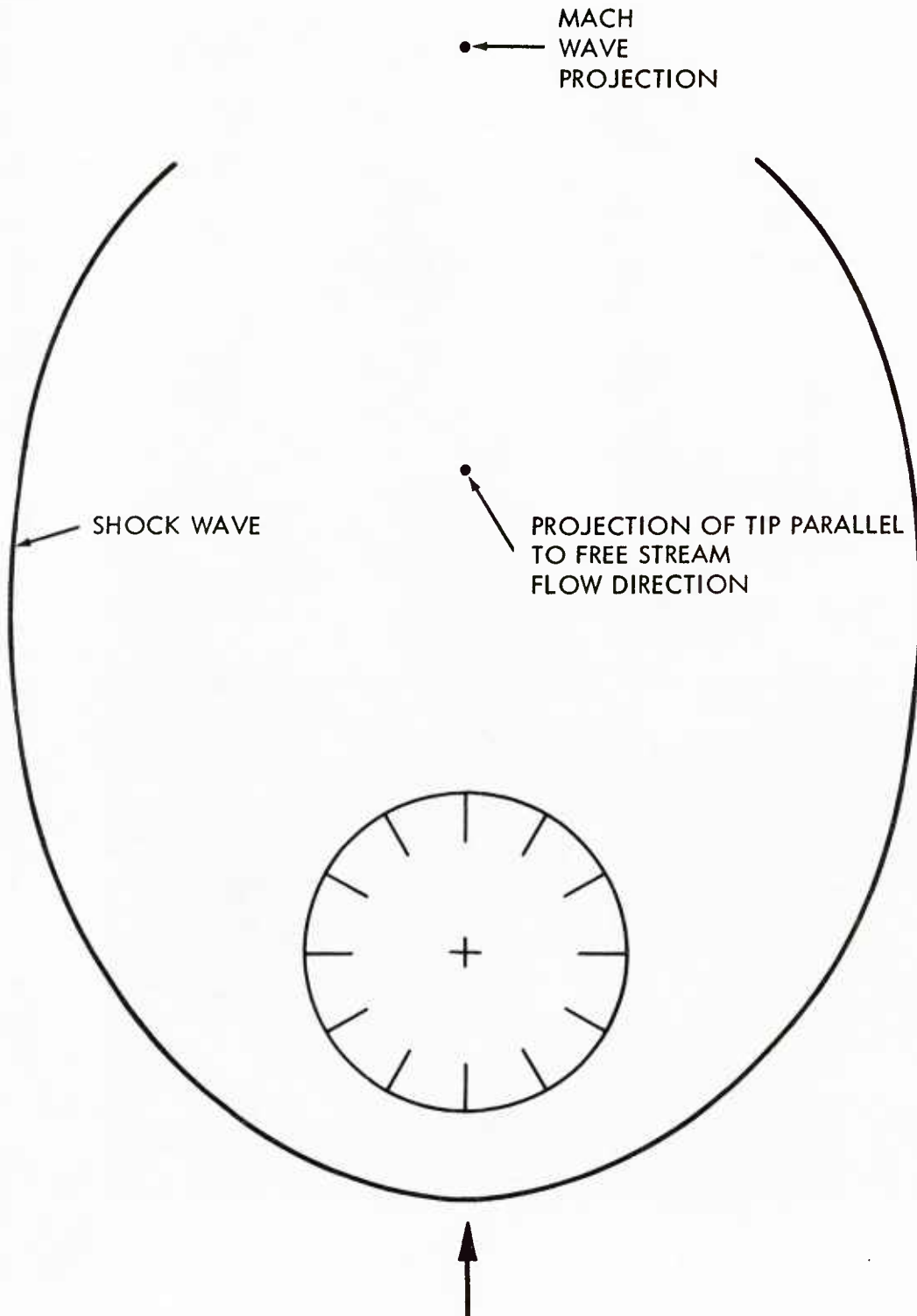




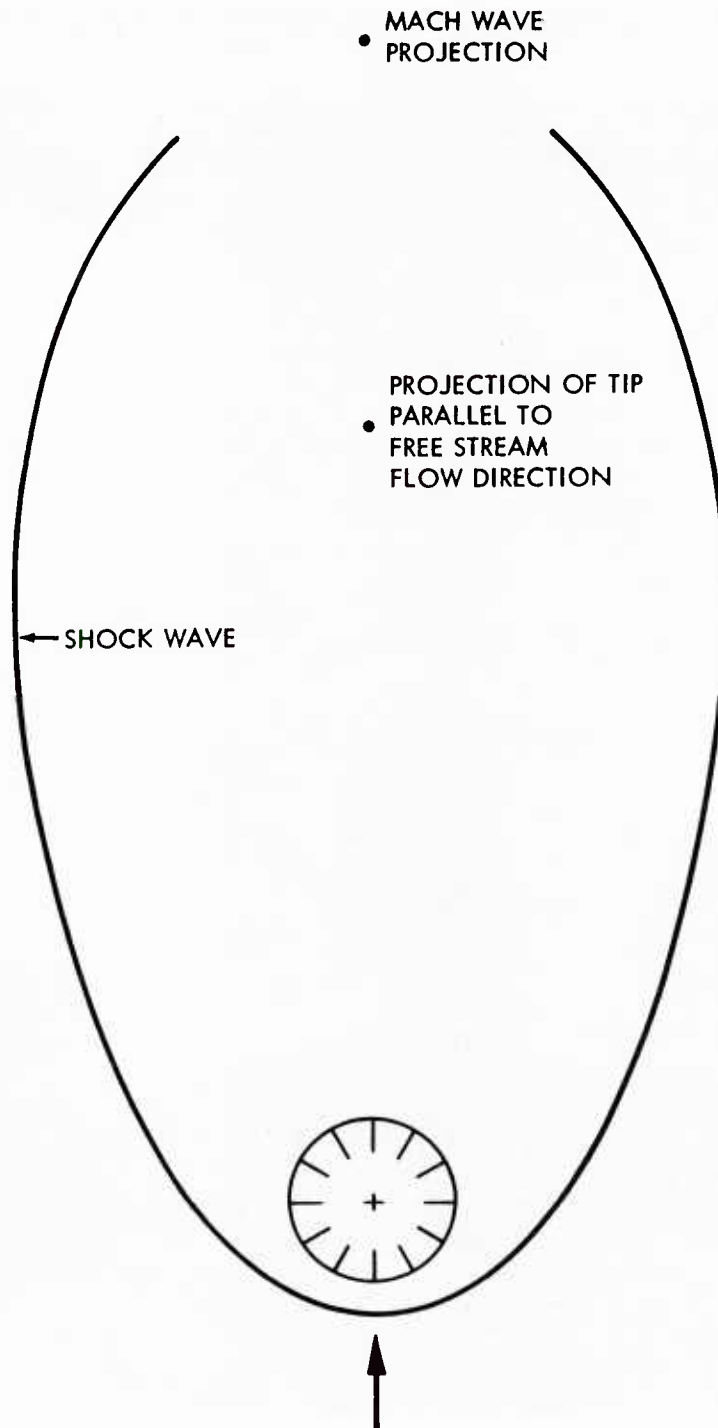
(U) Fig. 31 Schlieren Photograph of an Inclined Slender Cone (  $\alpha = 30^\circ$  )



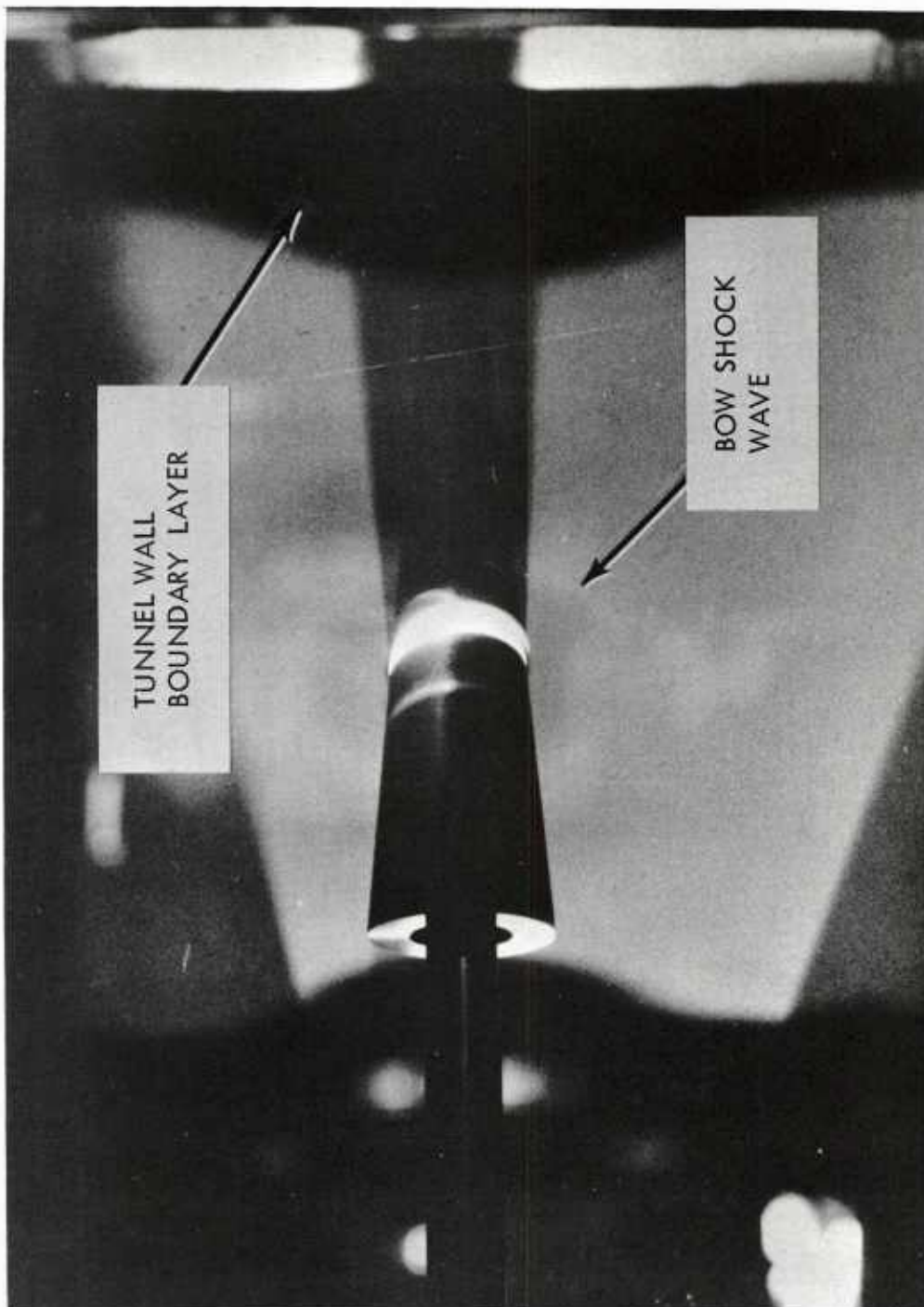
(U) Fig. 32 Color Schlieren Photograph (black and white print)  
of an Inclined Slender Cone ( $\alpha = 40^\circ$ ,  $\omega = 70^\circ$ )



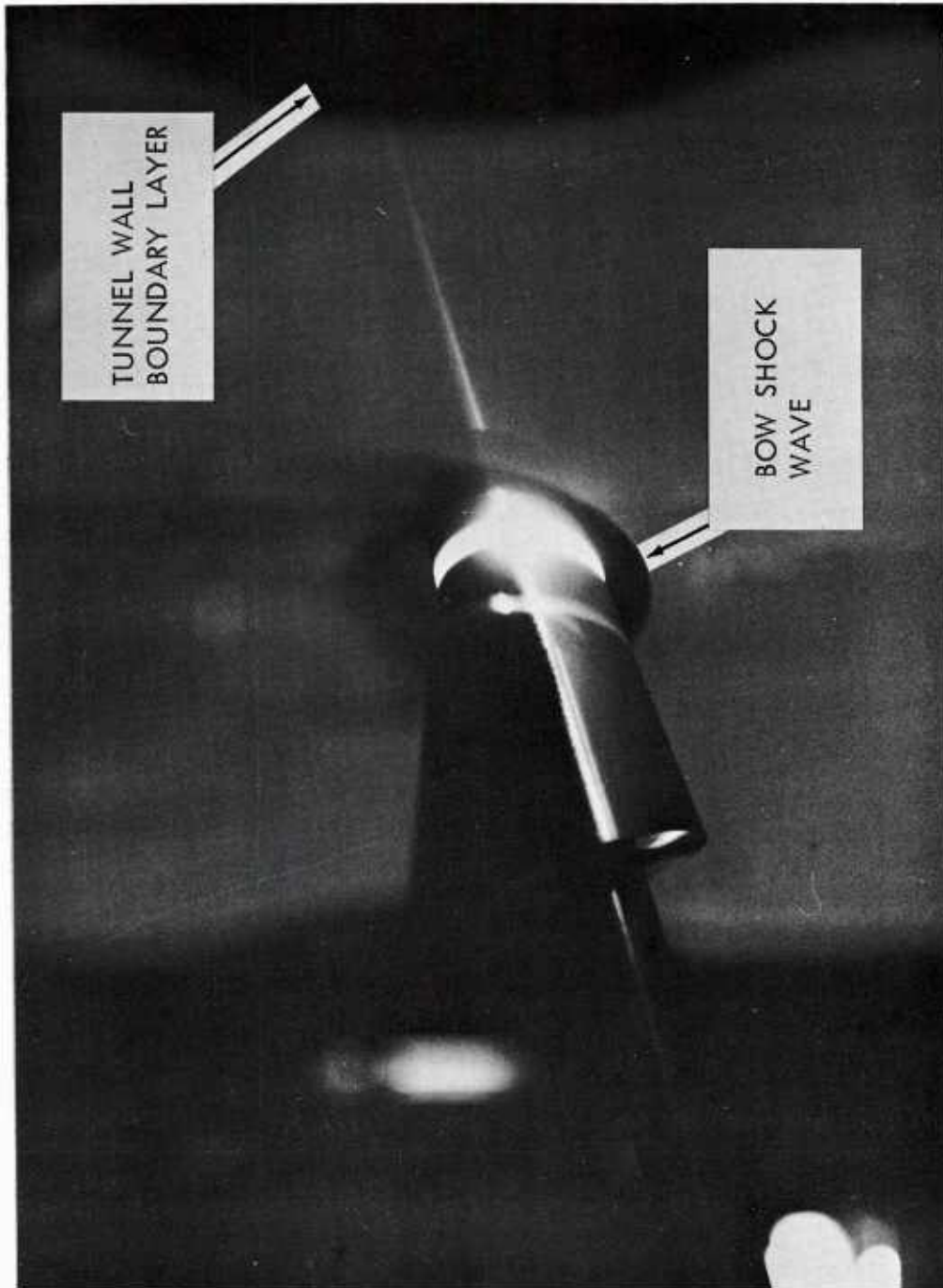
(U) Fig. 33 Shock Wave Shape in a Cross-Flow Plane -  $\alpha = 15^\circ$



(U) Fig. 34 Shock Wave Shape in a Cross-Flow Plane -  $\alpha = 40^\circ$

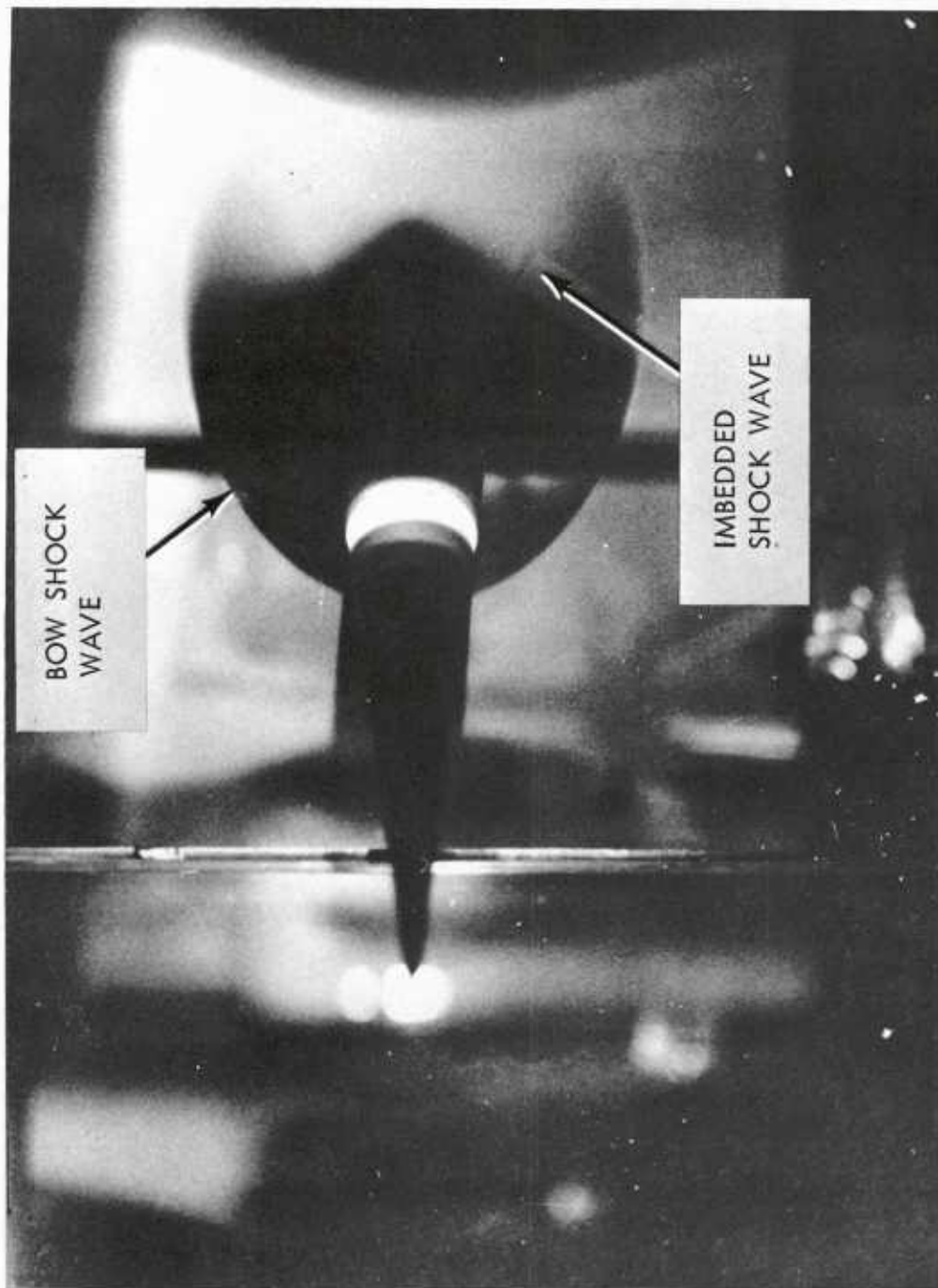


(U) Fig. 35 Vapor Screen Photograph -  $\alpha = 0^\circ$  (Camera II)



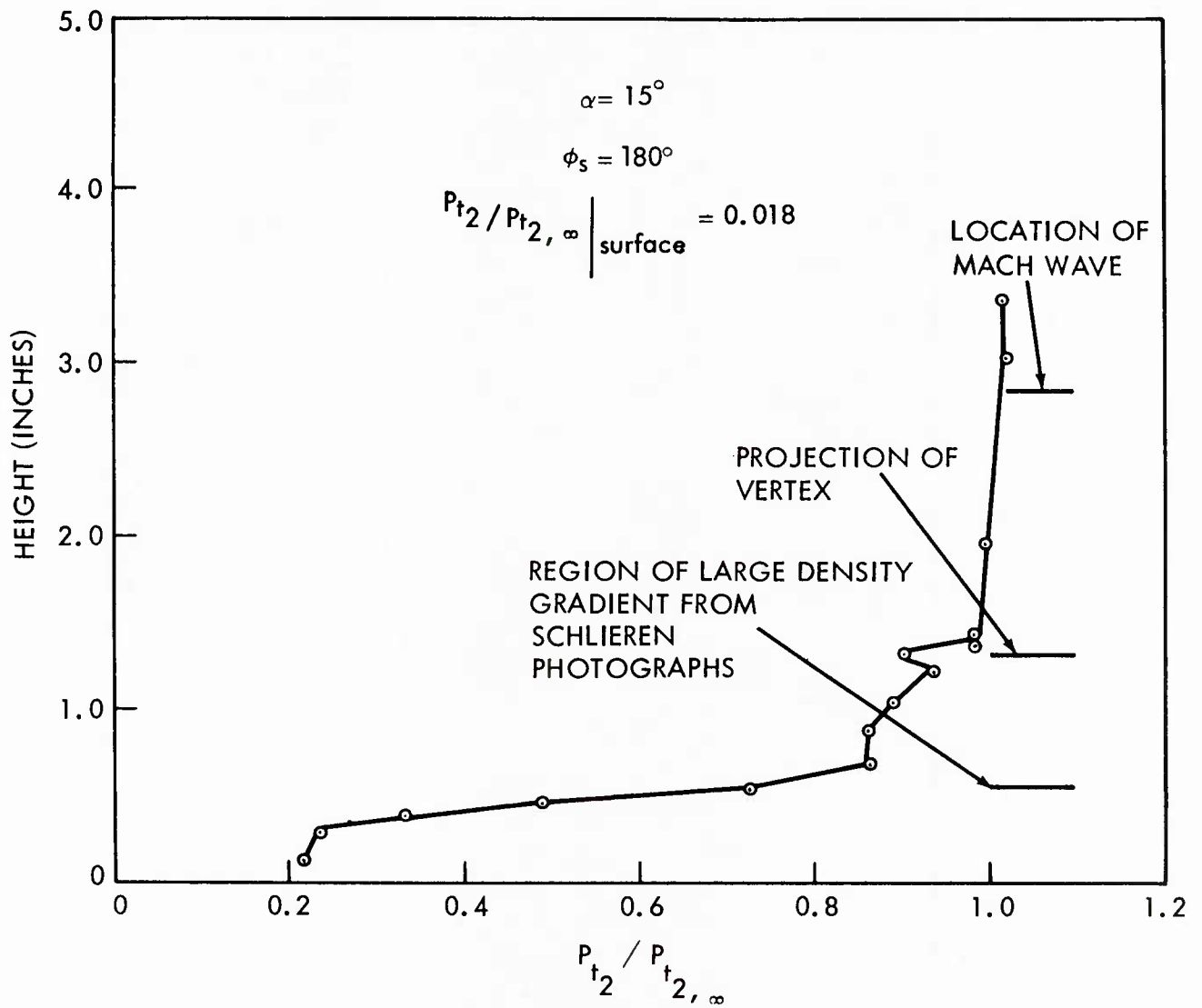
(U) Fig. 36 Vapor Screen Photograph -  $\alpha = 15^\circ$  (Camera II)



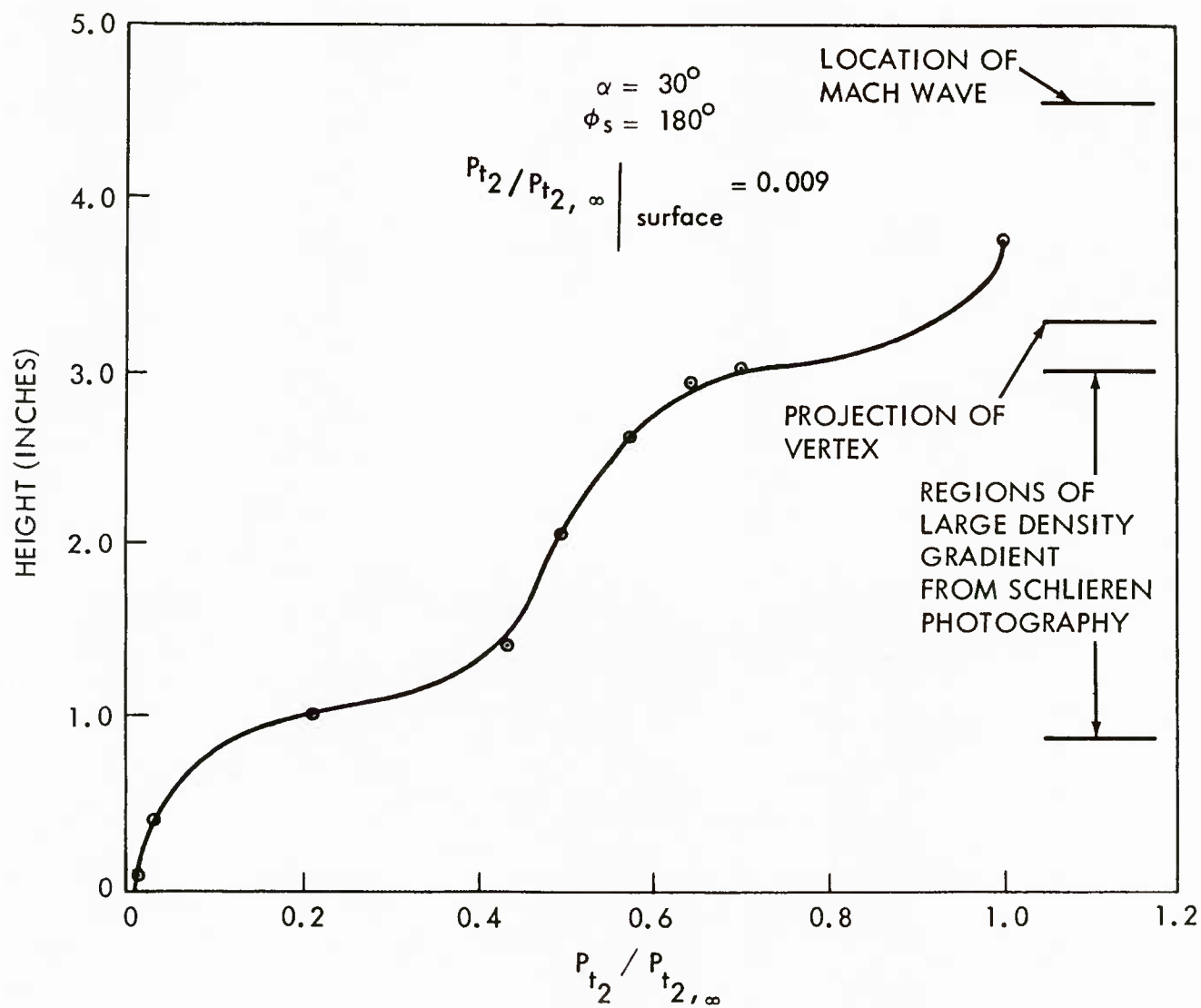


(U) Fig. 37 Vapor Screen Photograph -  $\alpha = 40^\circ$  (Camera I)





(U) Fig. 38 Pitot Tube Survey



(U) Fig. 39 Pitot Tube Survey

## Paper No. 3

ANALYTICAL INVESTIGATION ON LAMINAR FLOW FIELD  
AND HEAT TRANSFER ON LEEWARD SIDE OF A  
SHARP NOSED HYPERSONIC CONE AT  
LARGE ANGLE OF ATTACK

(U)

(Paper UNCLASSIFIED)

by

Paul K. Chang, Mario J. Casarella,  
and Russell A. Smith  
The Catholic University of America  
Washington, D.C. 20017

SUMMARY

(U) At a large angle of attack, the flow over a sharp nosed hypersonic cone separates on the leeward side, and forms downstream a large viscous separated region between the wrapped shock and cone surface. The complex physical aspects of the attached boundary layer region and the downstream separated flow have been reviewed and consequently the problems to be solved have been identified. An insight and understanding of the separated flow phenomena have been gained by the performed analysis, which is based upon a proposed analytical model.

(U) For convenience, the viscous flow field on the leeward side is divided into the following regions; separation point, constant pressure mixing, imbedded shock reattachment, far downstream flow, and recirculating flow, where spiral vortices may be formed. By investigating each of these regions of the laminar separation, a simplified analysis of the overall method has been developed to determine a distorted body shape. This computational procedure is based upon the matching of the pressure distribution in the leeward meridional plane.

(U) For this analysis, the configuration of the distorted body shape is considered as the boundary of inviscid and viscous flow field. The boundary conditions of viscous and inviscid flow are then to be matched along the distorted body shape. A generalized design procedure of the distorted body shape involving the laminar flow separation for given

Vol. 1

flow conditions, such as free stream Mach number, angle of attack, cone half angle and wall temperature has been formulated by using the limited available experimental data. Two sample numerical calculations have been carried out to determine the distorted body shape and the values of the properties of flow and temperature along the outer boundaries of the distorted body shape.

(U) In addition, an attempt has been made to evaluate the laminar convective heat transfer in the neighborhood of rear stagnation based upon the proposed laminar flow model. It appears that the coefficient of laminar convective heat transfer may be computed by the available analysis for laminar flow over a slender ellipse rather than a circular cylinder.

SYMBOLS

(U) a	Exponential parameter for velocity profile
b	" " " " "
h	Convective heat transfer coefficient
k	Conductivity of heat
M	Mach number
p	Pressure
u	Streamwise velocity component
$u_r$	Reverse velocity component
$u^*$	$u^* = u_d/u_3$
X-x	Transformed coordinate
Y-y	Transformed coordinate
$\bar{Y}$	$\bar{Y} = Y - Y_d$
x	Cartesian physical coordinate, also distance along the surface measured from rear stagnation point
y	Cartesian physical coordinate
T	Temperature
$\alpha$	Angle of attack

$\gamma$  Ratio of specific heat

$\delta$  Shear layer thickness

$\delta^*$  Displacement thickness of shear layer

$$\Delta = \delta_1 - \delta_2$$

$\delta_1$  Shear layer thickness above dividing stream line

$\delta_2$  Shear layer thickness below dividing stream line

$$\eta = \frac{\bar{Y} + \delta_2}{\Delta}$$

$\theta$  Momentum thickness of shear layer

$$\text{also } \theta = \frac{T - T_w}{T_e - T_w}$$

$\theta_c$  Cone half angle

$$\lambda = 1 - \frac{u_r}{u_e}$$

$\nu$  Kinetic viscosity

$\psi$  Stream function

$$\xi = \frac{\nu_e x}{u_e \theta_o^2}$$

Vol. 1

SUBSCRIPTS:

(U) d	dividing stream line
e	outer edge of shear layer
o	initial condition at separation
r	reverse flow
s	rear stagnation
stag	stagnation
w	wall
z	zero velocity line
3	flow property at the edge of shear layer immediately downstream of imbedded shock

INTRODUCTION

(U) The considered range of investigation is:

Free stream Mach number: 5-15

Altitude: 10,000 - 100,000 ft.

Angle of Attack:  $0^\circ$  -  $60^\circ$  and possibly higher

(U) The flow field around a slender body of revolution at large angle of attack and at hypersonic free stream velocity is schematically represented in Figure 1. The viscous boundary layer on the body surface separates due to the streamwise adverse pressure gradient and the separated flow region is extended into the shock layer within the outer wrapped shock. Since extension of this viscous separated region becomes larger as the angle of attack increases, the aerodynamic performance of slender hypersonic vehicle as affected by the characteristics of the flow and heat transfer at high angles of attack are strongly dependent on the features of viscous separation.

(U) A limited number of experimental investigations have been carried out for a cone at relatively large angles of attack, in which detailed measurements were attempted in the separated flow region on the leeward meridian. Tracy [1] performed the extensive experiments on the cone separated region in laminar flow at free stream Mach Number 7.95, and Rainbird [2] has investigated the turbulent separated flow of a cone up to numerical Mach Number of 4.25.

(U) The phenomena of separated flow downstream of a circular cone at angle of attack exhibits special unique features compared to other separated flow phenomena which have been investigated extensively in the past. As shown in Figure 2, the separated flows downstream of a circular cylinder and a wedge of infinite span have much in common with that behind a circular cone, but the essential nature of the flow structures are distinctly different, because the separation downstream of a cone is a closed one in the cross sectional plane perpendicular to the central axis, although the separated flow downstream of a circular cylinder is open, similar to wedge as well as cylinder, having a long trail of wake.



Vol. 1

(U) An important special feature of the leeward side of cone flow is the so-called "vortical singularity" introduced by Ferri [3]. This point may be thought of as a point of convergence for the inviscid streamline within the wrapped shock that one considers solely in the cross-sectional plane. Although this topic has been discussed and analyses performed proving its existence, it appears that further investigations involving the matching of inviscid and viscous flow regions are needed for further understanding.

(U) Since the flow structure of leeward separated flow downstream of a circular cone is different from that of circular cylinder and wedge as discussed previously, the analytical solution of Crocco and Lees [4] for the latter cases matching the near and far wake flow at the critical point, is not applicable for the cone separated flow. Thus, a new approach is needed for an analytical solution to the cone separated flow. Hence, a first attempt is made to formulate a laminar separated flow model which represents the most important aspects of the complex flow structure on the leeward side of the cone. Then, a simplified analysis is pursued which would both evaluate the flow model, involving heat transfer, by confirming existing experimental results, and, in addition, give insight as to what improvements can be made in the postulated model.

(U) Based upon this model, characteristics of the attached and separated shear layers of the cone are computed, and, as shown in Figure 3, the distorted body shape is evaluated based upon the displacement thickness of the shear layer. In order to confirm the distorted body shape, a heat transfer analysis is made and compared with the experimental data. If the values of properties flow as well as heat transfer of inviscid and viscous flow are matched along the outer edge of the distorted body, then the analytical solution of the complete shock layers are obtainable.

(U) For convenience, the separated flow field is divided into six regions, which are:

- Region 1. Separation point region.
- Region 2. Constant pressure free shear mixing.
- Region 3. Imbedded shock region.
- Region 4. Reattachment point region.
- Region 5. Swirling vortex region.
- Region 6. Recirculating flow region.

(U) An analysis of each region is made from which a design procedure is to be proposed for the distorted body shape. Some of the analyses for the respective regions made certain assumptions for which improvements may be incorporated whenever new experimental data are available.

(U) The details for the flow model, procedure of calculation, results of computation, are referred to in references [5] and [6].

## 2. SIMPLIFIED ANALYSIS OF LAMINAR SEPARATED FLOW IN THE LEEWARD SIDE OF A HYPERSONIC CONE.

(U) The simplified analysis of laminar separated flow in the leeward side of a hypersonic cone is presented in this section. Then in Section 3, simplified analysis of convective heat transfer is presented.

### 2a. SIMPLIFIED ANALYSIS OF VISCOUS FLOW BEHAVIOR IN THE LEEWARD SIDE OF HYPERSONIC CONE.

(U) The analysis is based on the proposed model constructed on the static pressure distribution along the leeward meridian.

The assumptions made in the proposed computational scheme are:

- (1) Leeward separated region as well as outer wrapped shock.
- (2) The effect of axial flow field to the flow phenomena of cross-flow components of the separated shear layer is negligible.
- (3) The qualitative features of the flow behavior are not significantly affected by the heat transfer.
- (4) The edge of the shear layer and positive outer wrapped shock on the leeward meridian are known.

(U) Assumption (2) implies that the proposed model is essentially two-dimensional with cross-flow simplifying the calculation. The applicability of such computations are to be judged finally in comparison to the pertinent results.

(U) The analyses of six different regions, separation point, constant pressure free shear mixing, imbedded shock, reattachment, swirling vortex and recirculating flow are presented separately, using the sketch of Figure 4.

#### Region 1. Separation point region:

(U) The properties of flow at the separation point are referred to as the initial values for the leeward separated region. They are calculated by the three-dimensional attached flow analysis, up to separation, as presented in Ref. 5 and 6. A simplified two-dimensional

Vol. 1

analysis such as Cohen and Reshotko [7] can also be applied; however, a proper correction will be necessary to compensate for the discrepancies between the two methods.

Region 2. Constant pressure-free mixing region.

(U) The analysis of constant pressure free mixing determines the streamwise velocity distribution, location of dividing streamline as well as zero velocity lines.

(U) The boundary layer equations are reduced to the incompressible form by using Howarth transformation

$$X = x, Y = \int_0^y \left( \frac{\rho}{\rho_e} \right) dy$$

where (x, y) coordinates originate at the separation point and x is the distance measured in the downstream direction and y is the normal to x.

(U) The sketch of velocity profile for constant pressure mixing region is shown in Figure 5. Consider a velocity profile of the form

$$\frac{u_e - u}{u_e - u_r} = f(\eta) = (1 - \eta^a)^b \quad \begin{matrix} a > 1 \\ b > 1 \end{matrix} \quad (1)$$

where

$$\eta = \frac{\bar{Y} + \delta_2}{\Delta_1}, \quad \bar{Y} = Y - Y_d(\xi), \quad \xi = \frac{v_e X}{u_e \theta_0^2}$$

$$\Delta = \delta_1 + \delta_2$$

The boundary conditions are

$$u = u_e \quad \text{at} \quad \bar{Y} = \delta_1 \quad \text{or} \quad \eta = 1$$

$$u = 0 \quad \text{at} \quad \bar{Y} = \delta_z \quad \text{or} \quad \eta = \eta_z$$

$$u = u_r \quad \text{at} \quad \bar{Y} = \delta_2 \quad \text{or} \quad \eta = 0$$

The constants a and b are selected in such a way that the velocity profile has an initial displacement thickness  $\delta_0$  and momentum thickness  $\theta_0$  at the separation point, in agreement with the initial values.

by introducing

$$\frac{u}{u_e} = 1 - \lambda \cdot f(\eta)$$

where

$$\lambda = 1 - \frac{u_r}{u_e}$$

The velocity along the dividing streamline is then given by

$$\frac{u_d}{u_e} = 1 - \lambda f(\eta_d)$$

where

$$\eta_d = \delta_2 / \Delta$$

The location of the zero velocity line is

$$\lambda f(\eta_z) = 1 \quad \text{or} \quad \eta_z = \frac{\bar{Y}_z + \delta_2}{\Delta} + \left[ 1 - \left( \frac{1}{\lambda} \right)^{\frac{1}{b}} \right]^{\frac{1}{a}}$$

In the physical plane

$$\bar{Y}_z = (\eta_z - \eta_d) \Delta$$

The location of dividing stream line can be computed by the expression

$$\frac{Y_d(\xi)}{\delta_o} = -0.3746 \left( \frac{\theta_o}{\delta_o} \right) \sqrt{2\xi}$$

(U) A unique solution is obtained by matching the shear stress at the dividing streamline and maintaining a mass balance of the recirculating flow with the flow between the dividing stream line and zero velocity line.

(U) For the simplest form of the approximation,  $\rho\mu$  is considered constant and Prandtl number as unity. Furthermore, it is assumed that boundary layer approximations are valid in the mixing layer, provided that the dividing stream line is prescribed since it depends on the interaction with the outer flow and is, therefore, related to the higher order terms.

## Vol. 1

(U) By substituting the velocity profile given in equation (1), the integrated form of the transformed boundary layer equations, is obtained for the shear flow above the dividing stream line as

$$\frac{d}{d\xi} \left\{ \Delta \lambda \int_{\eta_d}^1 f(\eta) [1 - \lambda f(\eta)] d\eta \right\} = \frac{\theta_o^2 \lambda}{\Delta} f_1(\eta_d) \quad (2)$$

and for the shear flow below the dividing stream line as

$$\frac{d}{d\xi} \left\{ \Delta \lambda \int_0^{\eta_d} [1 - f(\eta)] [1 - \lambda f(\eta)] d\eta \right\} = \frac{\theta_o^2 \lambda}{\Delta} f_1(\eta_d)$$

(U) By matching the shear stress along the dividing streamline at each positive  $x$ , and expression for the thickness of the mixing region related to the other parameter is obtained as:

$$\frac{\Delta}{\delta_o} = \frac{1}{\lambda} \left( \frac{\theta_o}{\delta_o} \right) \left( \frac{1}{\beta_1 - \beta_2} \right) \quad (3)$$

where

$$\beta_1 = \int_{\eta_d}^1 f(\eta) [1 - \lambda f(\eta)] d\eta$$

$$\beta_2 = \int_0^{\eta_d} [1 - f(\eta)] [1 - \lambda f(\eta)] d\eta$$

In addition, from the required condition of mass flow between the dividing stream line and zero velocity line to be equal to the reverse mass flow of the lower stream, one obtains

$$\frac{\eta_d}{\lambda} = \int_0^{\eta_d} f(\eta) d\eta \quad (4)$$

(U) A unique numerical solution for the shear layer flow characteristics is obtained by numerically integrating equation (2) along with equations (3) and (4) for the unknown  $\Delta$ ,  $\lambda$  and  $\eta_d$ . These results can be represented in dimensionless form by introducing variable

$$\xi = \frac{X^2}{\theta_o^2} \quad \frac{1}{Re_x} = \frac{x v_e}{\theta_o^2 u_e}$$

(U) Figure 6 shows the velocity profile and the value of the dividing streamline velocity of  $u_d/u_e$  vs.  $\xi$  obtained by numerical integration. The streamwise  $u_d$  velocity along the dividing streamline  $u_d$  is in good qualitative agreement with that obtained by Denison and Baum [8].

(U) The displacement thickness above the zero velocity line is obtained by

$$\delta^*(\xi) = \int_{\eta_y}^1 [1 - \lambda f(\eta)] d\eta$$

(U) A calculation shows that the displacement thickness in the constant pressure region appears to remain approximately constant, however, the location of the zero-velocity line is significantly affected by the temperature field.

#### Region 3. Imbedded shock region.

(U) The pressure rise due to imbedded shock contributes to the reattachment of flow along the dividing streamline. For simplicity, the imbedded shock is regarded as a straight oblique shock. Thus, the flow properties downstream of the imbedded shock are calculated by using the well-known oblique shock compression based upon the properties upstream of the imbedded shock, assuming the pressure rise is equal to the pressure difference between the leeward surface pressure and minimum surface pressure. For sufficiently large angles of attack, the imbedded shock is scattered near the shear layer. It can be expected that as the angle of attack becomes quite large the wrapped shock will start to open along the leeward plane and a necking region develops. The imbedded shock may approach the so-called "wake shock" near the necking region similar to that observed in the hypersonic wake for a cylinder. The value of either  $\alpha$  or  $\alpha/\theta_s$  and other parameters at which the wrapped shock starts to open remains an important unknown for which, to the best of our knowledge, no data are available.

#### Region 4. Reattachment point region.

(U) The reattachment process is assumed to be isentropic compression of streamwise flow along the dividing stream line.

(U) At the reattachment point, which may be considered the rear stagnation point, the velocity is zero where the dividing stream line and the zero velocity line meet. The streamwise velocity profile may be considered similar to that of separation involving  $\partial u/\partial y = 0$  at  $y = 0$ . Harper [9] shows that for the incompressible two-dimensional flow, with its direction perpendicular to a flat plate, the flow phenomena is



## Vol. 1

inviscid, in the neighborhood of the flat plate, although upstream and downstream on the wall from this inviscid zone, the viscous flow prevails. This indicates that for incompressible flow near the reattachment, the compression process is isentropic. Thus, for hypersonic cone, the reattachment process is assumed to be isentropic compression of streamwise flow along the dividing streamline and the stagnation pressure at the reattachment is computed by the following equation given by Weiss [10]

$$p_{\text{stag}} = p_3 \left[ 1 + \frac{\gamma-1}{2} M_3^2 \left( \frac{u_d}{u_3} \right)^2 \left( \frac{T_3}{T_d} \right)^{\gamma/(\gamma-1)} \right] \quad (5)$$

where subscript 3 refers to flow properties at the edge of shear layer immediately downstream of the imbedded shock and d refers to the properties along the dividing stream line. The temperature ratio in this equation is computed by

$$\frac{T_d}{T_3} = \frac{T_w}{T_3} + \left( 1 - \frac{T_w}{T_3} \right) u_3^* + \frac{(\gamma-1)}{2} M_3^2 u_3^* (1-u_3^*) \quad (6)$$

where  $u_3^* = u/u_3$ . For the successful evaluation of  $p_{\text{stag}}$  at the reattachment, it is necessary to determine the reliable value of  $u^*$  which depends upon the value of  $\xi$  at the location of the imbedded shock as shown in Figure 6.

Region 5. Swirling vortex region requiring experimental investigation.

(U) The flow phenomena in this region is quite complicated and least understood. From Figure 4, it is seen that due to the closed boundary of the separated flow region, the mass rate of flow above the dividing stream line must flow away perpendicular to the meridional plane. The velocity profile at reattachment which is similar to that of separation has an inflection point indicating the instability of the flow, tending to form a vortex. Thus, it appears that in the region of downstream reattachment, a swirling vortex is formed. The size of the swirling vortex flow region is approximately determined by the conservation of mass flow. A critical question is the location of the vortical singularity or edge of shear layer on the leeward meridian. At this stage of the investigation, semi-empirical data are used to locate the farthest downstream edge of separated region in the leeward meridian.



Region 6. Recirculating flow region.

(U) In this region, the magnitude of recirculating or reverse flow is small. Nevertheless, this reverse flow plays a role as will be demonstrated in Section 3, by computing the convective heat transfer in the rear stagnation region on the body surface. The recirculating flow region is considered a closed region bounded by the dividing stream line, leeward meridian, and body surface.

2b. DESIGN PROCEDURE FOR THE DISTORTED BODY SHAPE.

(U) The solution of the separated flow field in the leeward plane is obtained by matching the flow field upstream and downstream at the reattachment. For the numerical computation, a pressure distribution along the leeward meridian is given as sketched in Figure 7.

(U) This diagram serves for two purposes simultaneously. One purpose is for the constructing of the distorted body shape, and the other is the establishment of boundary conditions for the outer boundary of the distorted body. The latter is used to match the inviscid and viscous flow solutions. In order to obtain the final solution, a part of the procedure of calculating the pressure distribution on this diagram requires an iteration process. This is because the positioning of the imbedded shock is not known apriori. In Figure 7, the positions 4 and 5 on the leeward meridional plane are fixed using semi-empirical data. The point of reattachment is determined as follows:

(U) The slope of the dividing streamline at separation is assumed equal to that of the cross-flow component of the external inviscid velocity. This slope is extended from the separation point by a straight line until it intercepts the meridional plane, thus locating the reattachment point, point 3. The magnitude of the static pressure at 5 is computed from shock wave analysis. The value of static pressure at 4 may be determined because the static pressure gradient between 4 and 5 is approximately constant for layer angles of attack as measured by Tracy [1]. Hence, by drawing a straight line between 5 and 4, representing the constant static pressure gradient, the pressure at point 4 is determined in the pressure diagram.

(U) Now, consider the left hand side of the diagram. Point 1 is already fixed because the static pressure at the rear stagnation point is determined using the surface pressure distribution. Next, assume the location of the imbedded shock, point 2, which lies between the rear stagnation point and its reattachment point. The pressure at point 2 on the pressure diagram is fixed by assuming the pressure is constant between point 1 and 2.

Vol. 1

(U) Then, draw a straight line between point 2 and 4 passing through point 3, again assuming a constant static pressure gradient. With this procedure, the diagram is complete. However, since the position of the imbedded shock has been assumed, the diagram is thus far arbitrary. The correct diagram is obtained by a trial and error method, in which the computed stagnation pressure at point 3 must match with that obtained on the pressure diagram.

2c. NUMERICAL EXAMPLES

(U) Two examples of the distorted body shape computation using Tracy's measurement of  $\alpha = 20^\circ$  and  $24^\circ$  at  $M_\infty = 7.95$  for cone half angle  $10^\circ$  are presented in Figure 8 and 9.

(U) The results of these two cases show that agreeable matching of the upstream and downstream flows may be made by the proposed iterative computational scheme. The displacement thickness is defined by

$$\delta^* = \int_0^\delta \left( 1 - \frac{\rho u}{\rho_e u_e} \right) dy \quad (7)$$

by taking the streamwise coordinate along the zero velocity line based upon the computed values of flow properties up to the reattachment point. By adding this displacement thickness above the zero velocity line, the distorted body shape is constructed.

3. Analysis of laminar convective heat transfer at the rear stagnation region.

(U) An attempt is made to analyze convective heat transfer at rear stagnation region of a cone, based upon the proposed model presented. This analysis may serve for two purposes: one purpose is to determine whether the proposed model which is based on pressure is applicable for heat transfer computation and another purpose is to establish a computational procedure for heat transfer.

(U) At first a comparative study of heat transfer at the rear stagnation region at subsonic and hypersonic speeds is made.

(U) Figures 10 and 11 show the flow field and measured convective heat transfer around the circular cylinder at subsonic air speed. Figure 11 shows the proposed flow model and measured convective heat transfer along the circumferential surface of a hypersonic cone at angles of attack.

(U) Roshko [11], after reviewing concepts in the separated flow at finite Reynolds number, emphasized the existence of the closure of the separated flow region which contains the vortices as sketched in Figure 10. The reverse flow near the center line combines with the forward flow in the free shear layer to form the vortex pattern. Although for subsonic separated flow, unsteadiness involving vortex shedding and turbulence are readily observable, the closure is, in general, not obvious. While for supersonic flow, closure of separated region due to the reattachment is unmistakable.

(U) Roshko [11] used Hama's photographs of subsonic separated flow behind a circular cylinder to observe the decrease of downstream width of separated region indicating the existence of the closure of separated flow further downstream. Hama's picture, taken in a shorter time compared to the vortex shedding period shows the vortex pattern, while another picture taken with a longer time span compared to vortex-shedding period, indicates apparently the closure point in the separated region far downstream. In 1958, Russell [12] found that if the streamlines representing the mean values of velocities measured in the subsonic separated flow are constructed, then the surface, by discontinuity, does not extend to the infinity, but closes.

(U) From Figures 10 and 11, it is seen that although similarities of reverse flow structure in closed recirculating flow region and pressure distribution exist, between subsonic and hypersonic separated flows if the swirling vortex in the hypersonic case is not considered, there exist also differences in size and geometrical configuration of closed recirculating flow region. Next consider the convective heat transfer. Figure 10 shows the Giedt's [13] measurement along the cylinder surface at subsonic speed. Since the flow conditions at Reynolds number larger than 140,000 are turbulent, one lowest curve representing  $Re = 70800$  is laminar flow case, to be compared with the hypersonic laminar flow heat transfer. After studying the heat transfer behavior, causing high rate of heat transfer at rear stagnation region, Giedt [13] conceived that the reverse flow boundary layer is formed on the leeward surface of the cylinder and its build up continues toward the point of separation. However, it was not possible to prove this concept by his experiment, because the attempted measurement of the build up of the boundary layer was not conclusive due to the small response of the probe in the separated flow region.

(U) The convective heat transfer measured by Tracy [1] on the cone of  $10^\circ$  half angle exposed to  $M_\infty = 7.95$  are shown in Figure 11. At the rear stagnation point, a pronounced increase of heat transfer is noticed similar to the case of subsonic speed.

Vol. 1

(U) From this brief comparative study, the following hypothesis is made:

The phenomena of the flow and heat transfer in the vicinity of rear stagnation point are essentially those of the boundary layer formed by reverse flow.

3a. Proposed analysis for the rear stagnation region.

(U) For the analysis, it is proposed to apply the Falkner-Skan solution of two dimensional incompressible laminar boundary layer and energy equations given by

$$f'''' + ff'' + \bar{\beta} (1 - f'^2) = 0$$

$$\theta'' + f \theta' = 0$$

By definition

$$f = \frac{\psi}{u_e} \left( \frac{1}{\sqrt{\bar{\beta}}} \frac{du_e}{dx} \right)^{1/2} \quad (8)$$

$$\theta = \frac{T - T_w}{T_e - T_w} \quad (9)$$

(U) Furthermore,

$$u = \frac{\partial \psi}{\partial y}$$

$$\eta = y \left( \frac{1}{\sqrt{\bar{\beta}}} \frac{du_e}{dx} \right)^{1/2} = \frac{y}{x} \sqrt{\frac{u_e x / \nu}{2 - \bar{\beta}}}$$

$\bar{\beta}$  is a constant and is given by

$$\frac{du_e}{dx} = C u_e^{2(\bar{\beta} - 1)/\bar{\beta}}$$

where the superscript (') refers to differentiation with respect to  $\eta$ .

(U) The subscripts e and w are referred to outer edge of shear layer and wall respectively. The coordinate x is measured along the body surface from the stagnation point and y is perpendicular to x where C is constant.

(U) The convective heat transfer coefficient h around the leeward surface of a cone may be computed then by

$$h = \frac{k dT/dy|_{y=0}}{T_e - T_w} = \left( \frac{1}{v} \frac{du_e}{dx} \right)^{1/2} k \frac{d\theta}{d\zeta} \Big|_0 = \frac{k}{\sqrt{v}} \left( \frac{du_e}{dx} \right)^{1/2} \frac{d\theta}{d\zeta} \Big|_0$$

$$\zeta = y \left( \frac{1}{v} \frac{du_e}{dx} \right)^{1/2} = \bar{\beta} \cdot \eta$$

(U) The applicability of the Falkner-Skan solution to the flow downstream of separation is shown by Stewartson [14]. The numerical solution is obtained rapidly by these equations, in particular using the already tabulated results such as published in the monograph of Evans [15].

(U) The Falkner-Skan solutions are applicable to similarity conditions involving constant values of  $\bar{\beta}$ , but, in the vicinity of stagnation point on the blunt body surface,  $\bar{\beta}$  is not constant, and its value decreases from unity at the stagnation point, requiring the correction. However, in the vicinity of the stagnation point, higher order correction terms formulated by the product of derivative of  $\bar{\beta}$  with respect to integration of  $(u_e/u_\infty)x$  with respect to x, where x is distance measured from stagnation point and integral for  $(u_e/u_\infty)x$  with respect to x are small, thus, solutions involving only the first order term are sufficiently accurate [16]. The presented Falkner-Skan solutions, equations (8), (9), (10), are the first order solutions.

### 3b. Numerical examples of convective heat transfer in the rear stagnation region.

(U) For the numerical evaluation of heat transfer in the vicinity of rear stagnation point on a hypersonic cone, the property values computed from the proposed flow model and the Falkner-Skan solutions are used. This calculation serves also to confirm the applicability of proposed flow model to heat transfer, if the predictions are in agreement with experiment data. Although limited, the following numerical examples show that the predictions of heat transfer based upon the

## Vol. 1

proposed hypothesis of flow phenomena in the vicinity of rear stagnation are consistent with the experimental data.

(U) Tracy [1] measured laminar convective heat transfer around the circumferential surface of a cone of half angle  $10^\circ$  at  $M_\infty = 7.95$  at two different angles of attack  $\alpha = 20^\circ$  and  $24^\circ$ . For convenience, these two test conditions are designated

Case I for  $\alpha = 20^\circ$

Case II for  $\alpha = 24^\circ$

(U) The results of numerical computations of convective heat transfer coefficients  $h_s$  at the rear stagnation point are listed in the following table with the measured data of Tracy [1].

Table I Convective heat transfer coefficient at rear stagnation point.

	Case I	Case II
$T_\infty$ ( $^\circ\text{R}$ )	359.8	415.7
$u_\infty$ (ft/sec)	426	447
$\frac{k}{\sqrt{v}}$ ( $\frac{\text{Btu} \cdot \text{sec}^{1/2}}{\text{hr } ^\circ\text{R}}$ )	.0445	.0417
$h_s$ ( $\frac{\text{Btu}}{\text{hr ft}^2 ^\circ\text{R}}$ )	2.68	2.57
<u>Measured</u>		
$h_s$ ( $\frac{\text{Btu}}{\text{hr} \cdot \text{ft}^2 \cdot ^\circ\text{R}}$ )	2.08	2.32

(U) The discrepancy among the computed values and experimental data may be attributed to effects of three dimensionality of flow, approximate values obtained from the flow model, viscosity and heat transfer effects.



(U) The predicted behavior of  $h_s$  in the vicinity of the rear stagnation point on the hypersonic cone is shown in Figure 12. The variation of  $\bar{\beta}$  in the vicinity of rear stagnation point on cone which corresponds to the measured data of pressure and convective heat transfer indicates that the phenomena of flow as well as heat transfer on hypersonic cone are smaller to those on slender ellipse stagnation region.

(U) Apparently the geometry of the recirculatory flow region near the body surface is an important factor for the stagnation phenomena. Since the zero velocity line is affected by heat transfer, the variation of geometry of recirculatory flow region due to heat transfer is to be investigated.

(U) As concluding remarks on the heat transfer effects on the proposed flow it may be said that the geometrical boundary and boundary conditions of the distorted body may be used for the approximate computation of heat transfer.

#### CONCLUSIONS

(U) After studying the phenomena of the separated laminar flow region, a simplified two-dimensional laminar analysis and design procedure has been presented to compute a distorted body shape. This analysis accounts for the effect of the separated viscous flow at large angles of attack. This distorted body shape is based upon the static pressure distribution along the leeward meridional plane. The limitation of the obtained results is due to a lack of experimental data on properties of the leeward side flow phenomena. A simplified analysis of convective heat transfer in the rear stagnation region based upon the proposed flow model yields a reasonable agreement with experimental data. This has shed more light toward the understanding of the complex separated flow.



REFERENCES

1. Tracy, R. R., "Hypersonic Flow Over Yawed Circular Cones", Hypersonic Project, Memo 69, 1963. California Institute of Technology.
2. Rainbird, W. J., "Turbulent Boundary-Layer Growth and Separation on a Yawed Cone, AIAA Journal, Vol. 6, No. 12, Dec. 1968, pp. 2410-2416.
3. Ferri, A., "Supersonic Flow Around Circular Cones at Angles of Attack", NACA TN 2236, 1950.
4. Crocco, L., and Lees, L., "A Mixing Theory for the Interaction Between Dissipative Flows and Nearly Isentropic Streams", JAS, Vol. 19, No. 10, pp. 649-676, Oct. 1952.
5. Chang, P. K., "The Investigation for the Aerodynamic and Heat Transfer Characteristics of Slender Hypersonic Vehicles Over a Wide Range of Angles of Attack", Department of Mechanical Engineering, The Catholic University of America, Washington, D. C., July 1969, Technical Report, Contract No. N-00017-67-C-0008.
6. Chang, P. K., Smith, R. A., Casarella, M. J., Oh, Y. H., "Analysis of Laminar Flow and Heat Transfer on a Hypersonic Cone at High Angle of Attack", Department of Mechanical Engineering, The Catholic University of America, Washington, D. C., Aug. 1968, Technical Report No. 2, Contract No. N-00017-67-C-0008.
7. Cohen, C. B. and Reshotko, E., "The Compressible Laminar Boundary Layer With Heat Transfer and Arbitrary Pressure Gradient", NACA Rept 1294. 1956. Supersedes NACA TN 3326, 1955.
8. Denison, M. R., Baum, E., "Compressible Free Shear Layer with Finite Initial Thickness", AIAA Journal, Vol. 1, pp. 342-349, 1963
9. Harper, J. F., "On the Boundary Layers in Two-Dimensional Flow With Vorticity", Journal of Fluid Mechanics, Vol. 17, Part I, Sept., 1963, pp. 141-153.
10. Weiss, R. F., "The Near Wake of a Wedge", AVCO-Everett Research Lab., Research Rept. 197, Dec. 1964.

11. Roshko, A., "A Review of Concepts in Separated Flow", General Lectures, Canadian Congress of Applied Mechanics, Laval University, May 22-26, 1967, pp. (3-081) - (3-115).
12. Russell, A. J. T., "Aerodynamics of Wakes Existence of Unsteady Cavities", Engineering, Vol. 186, No. 4838, pp. 701-702, Nov. 28, 1958.
13. Giedt, W. H., "Effect of Turbulence Level of Incident Air Stream on Local Heat Transfer and Skin Friction on a Cylinder", Journal of the Aeronautical Sciences, Vol. 18, No. 11, Nov. 1951, pp. 725-730.
14. Stewartson, K., "Further Solutions of the Falkner-Skan Equation", Proc. Cambridge, Phil. Soc., Vol. 50, Part 3, pp. 454-405, 1954.
15. Evans, H. L., "Laminar Boundary Theory", Addison-Wesley Publishing Co., 1968.
16. Merk, H. J., "Rapid Calculations for Boundary Layer Transfer Using Wedge Solutions and Asymptotic Expansions", Journal of Fluid Mechanics, Vol. 5, pp. 460-480, 1959.

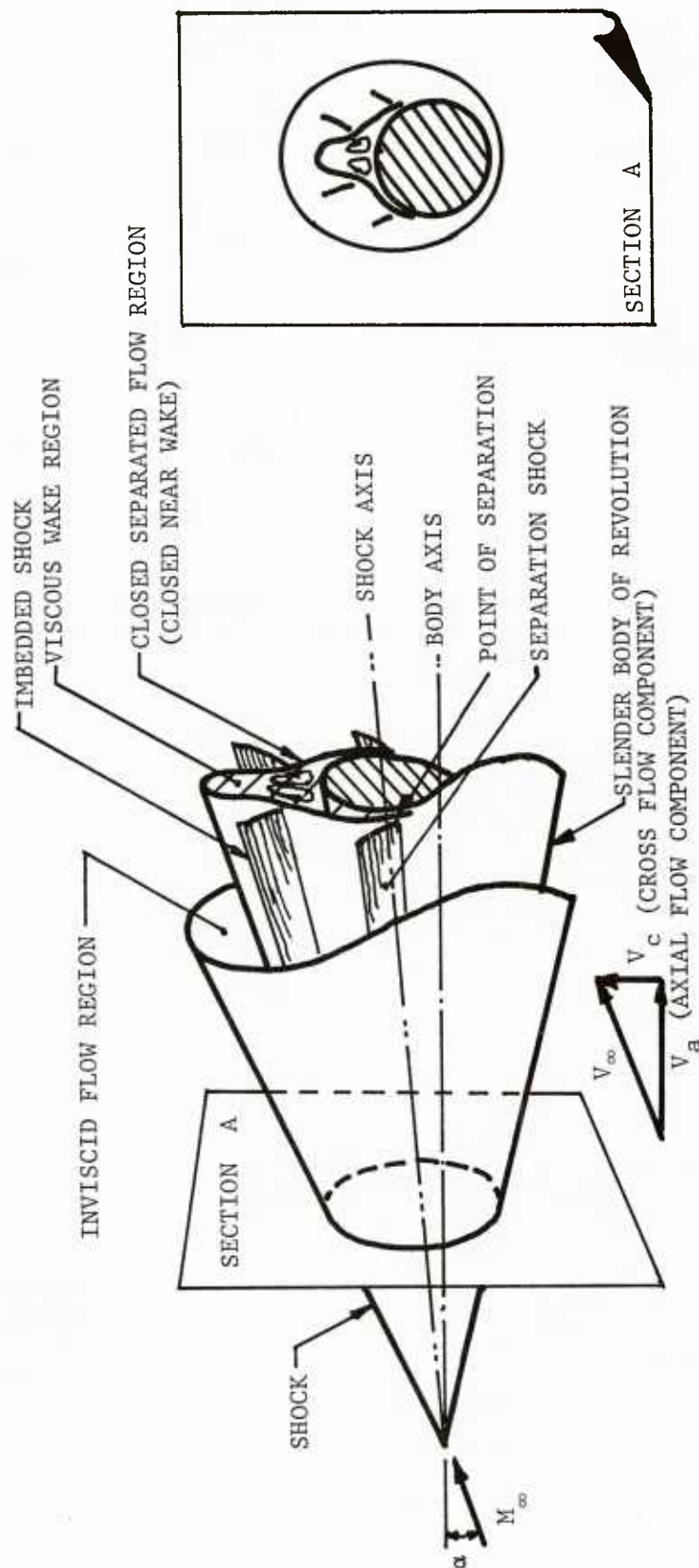
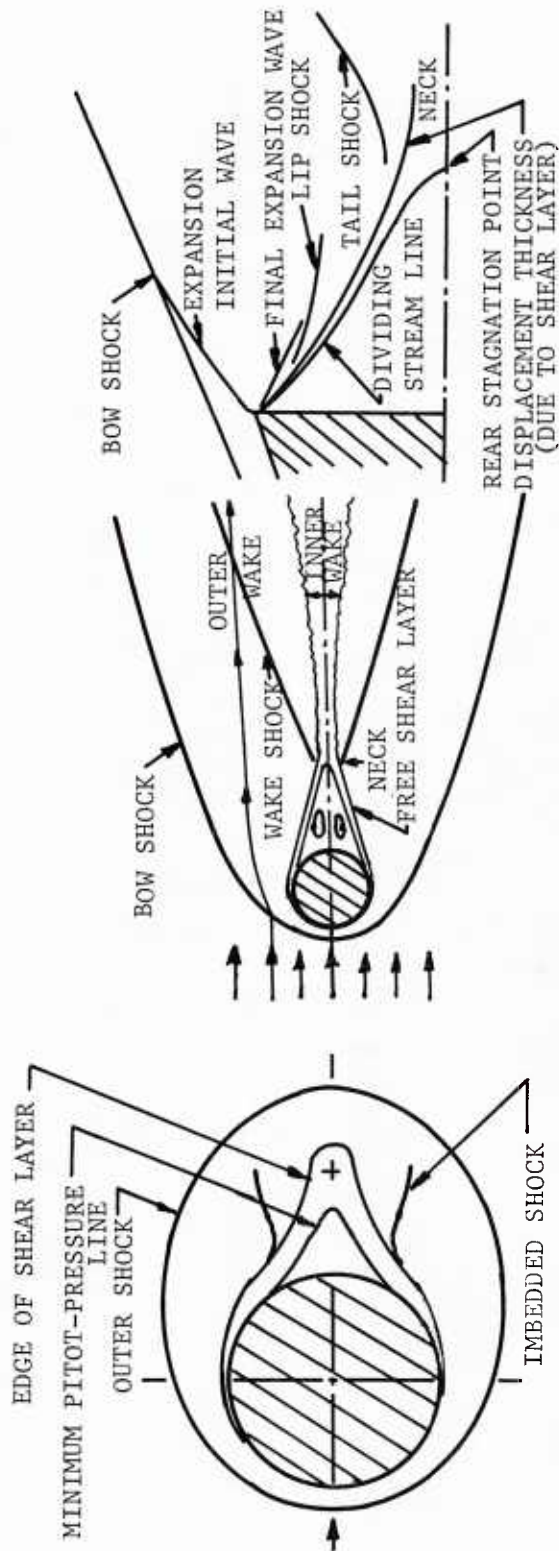


FIGURE 1 SCHEMATIC DIAGRAM OF FLOW FIELD ABOUT SLENDER BODY OF REVOLUTION AT ANGLE OF ATTACK



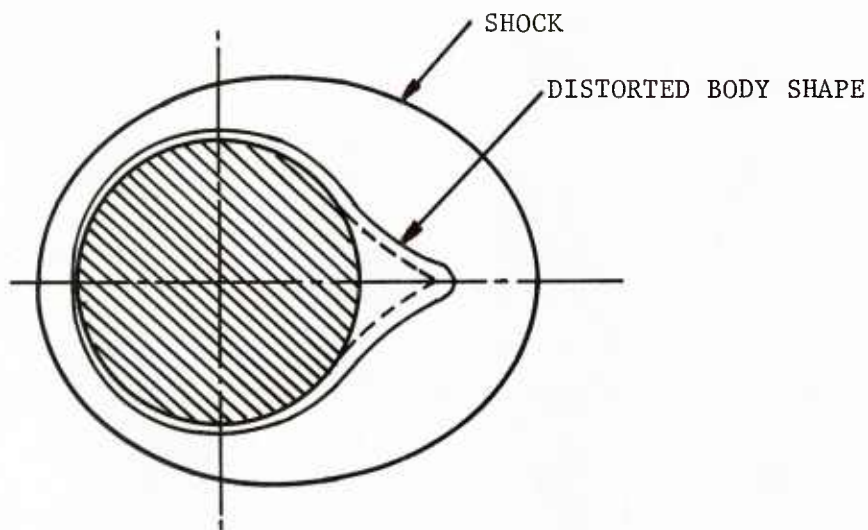
10° HALF ANGLE CONE AT 20° ANGLE OF  
ATTACK.  
TRACY, C.I.T. MEMO NO. 69-63

WAKE BEHIND BLUNT BODY AT  
HYPERSONIC SPEEDS.  
LEES AND HROMAS, IAS PAPER  
NO. 62-71

SCHEMATIC OF NEAR WAKE FLOW  
FIELD.  
WEISS, AIAA PAPER NO. 67-63

FIGURE 2 COMPARISON OF THE SEPARATED FLOW FIELD FOR VARIOUS GEOMETRIC CONFIGURATIONS

$\alpha \approx 10^\circ$



$\alpha \approx 30^\circ$

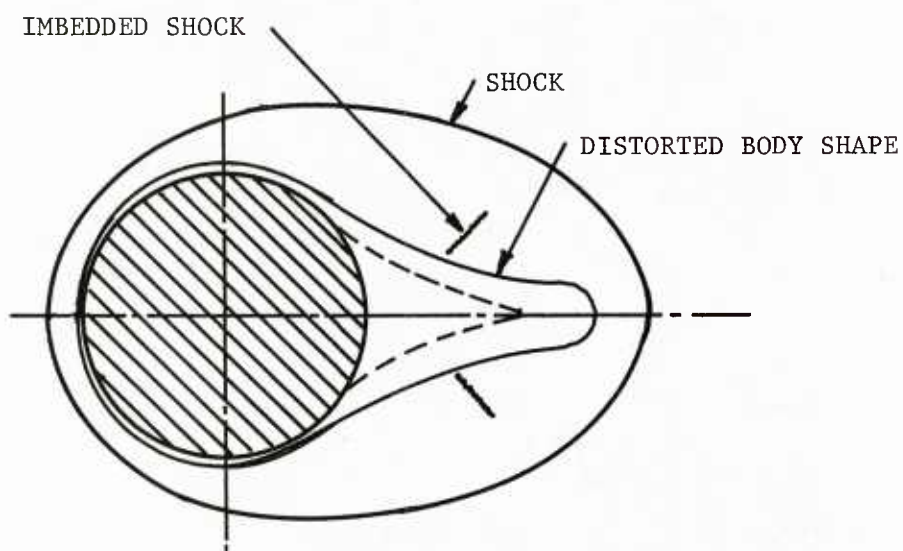


FIGURE 3 SCHEMATIC DIAGRAM OF THE DISTORTED BODY SHAPE

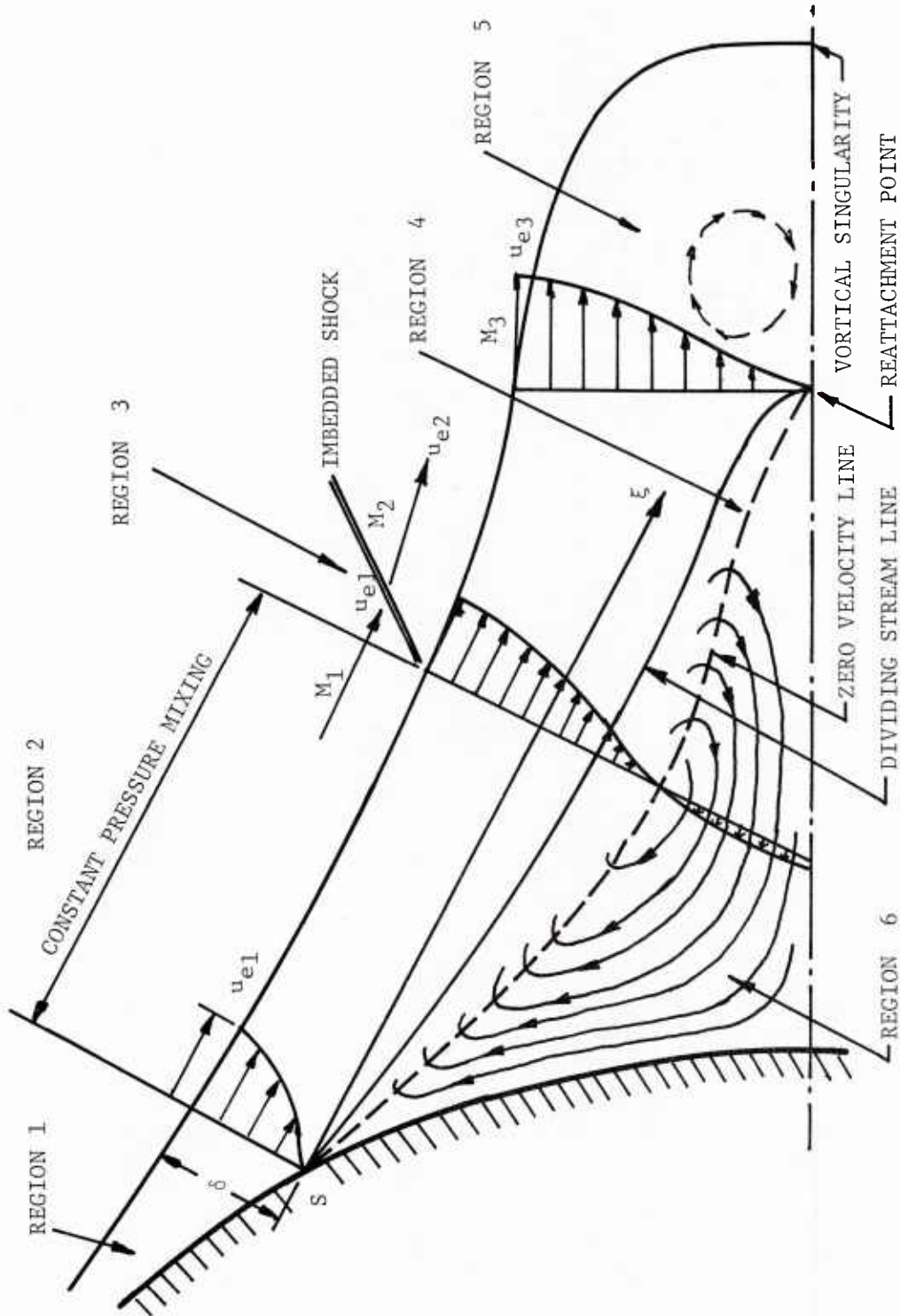


FIGURE 4 ANALYTICAL MODEL OF THE VISCOUS FLOW FIELD ON THE LEEWARD SIDE



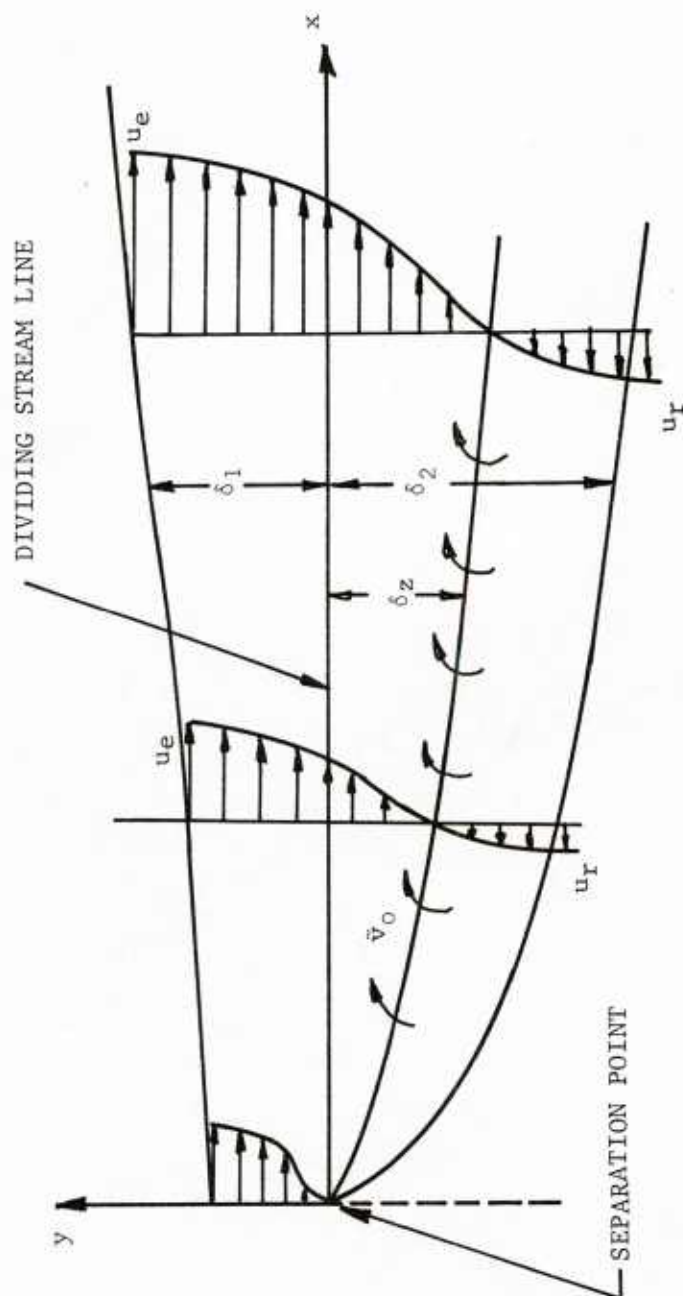


FIGURE 5 VELOCITY PROFILE FOR CONSTANT PRESSURE MIXING REGION



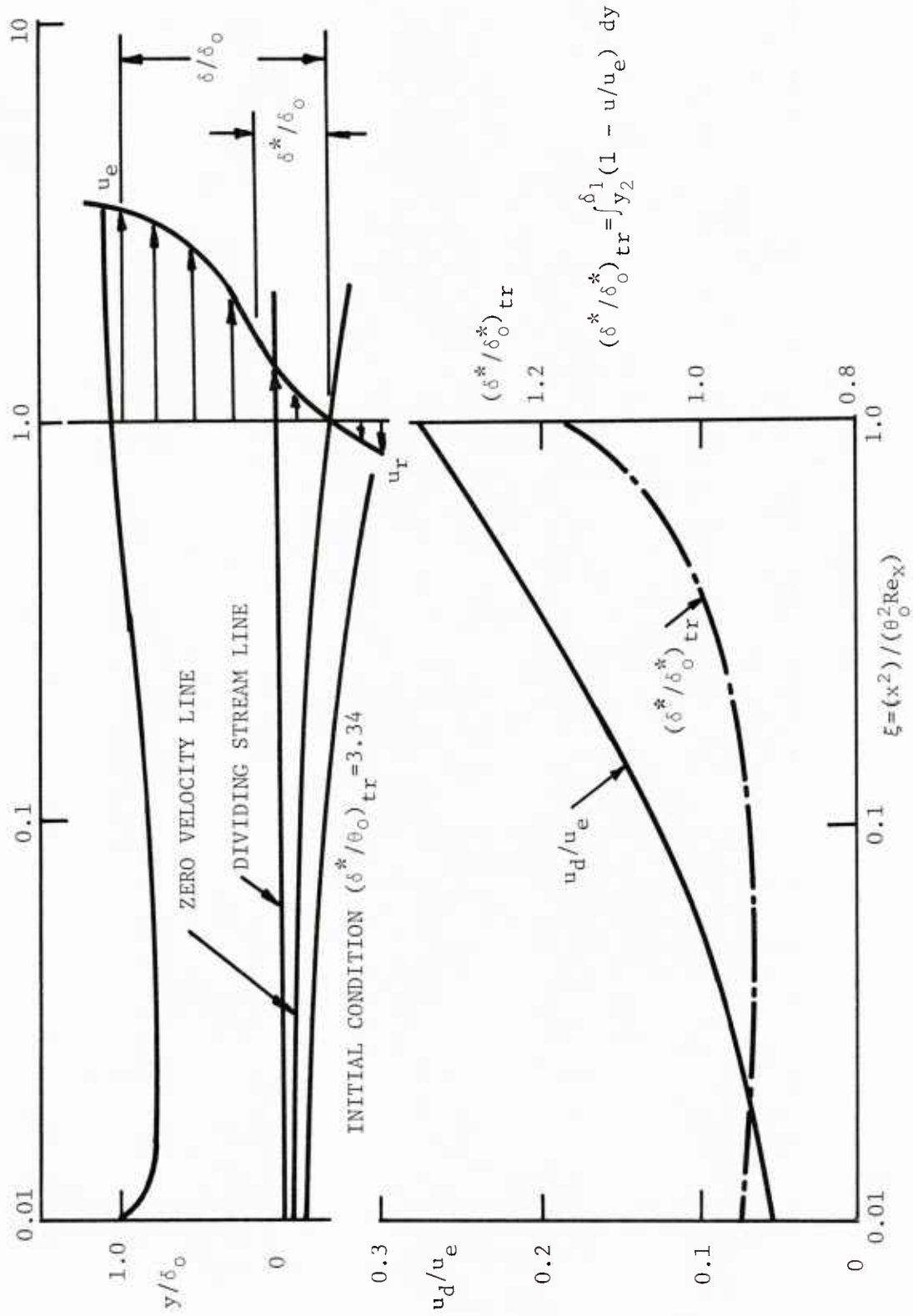


FIGURE 6 NUMERICAL RESULTS FOR CONSTANT PRESSURE SHEAR MIXING

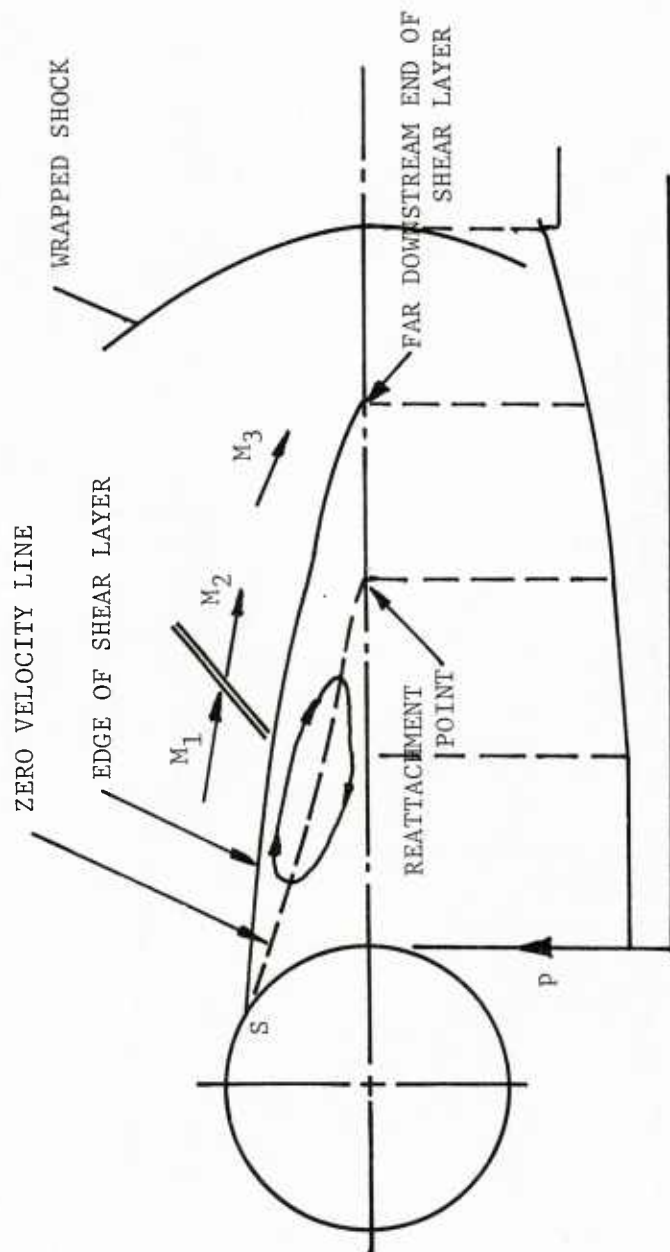


FIGURE 7 SKETCH OF THE CROSS-SECTIONAL PLANE ALONG THE LEEWARD SIDE

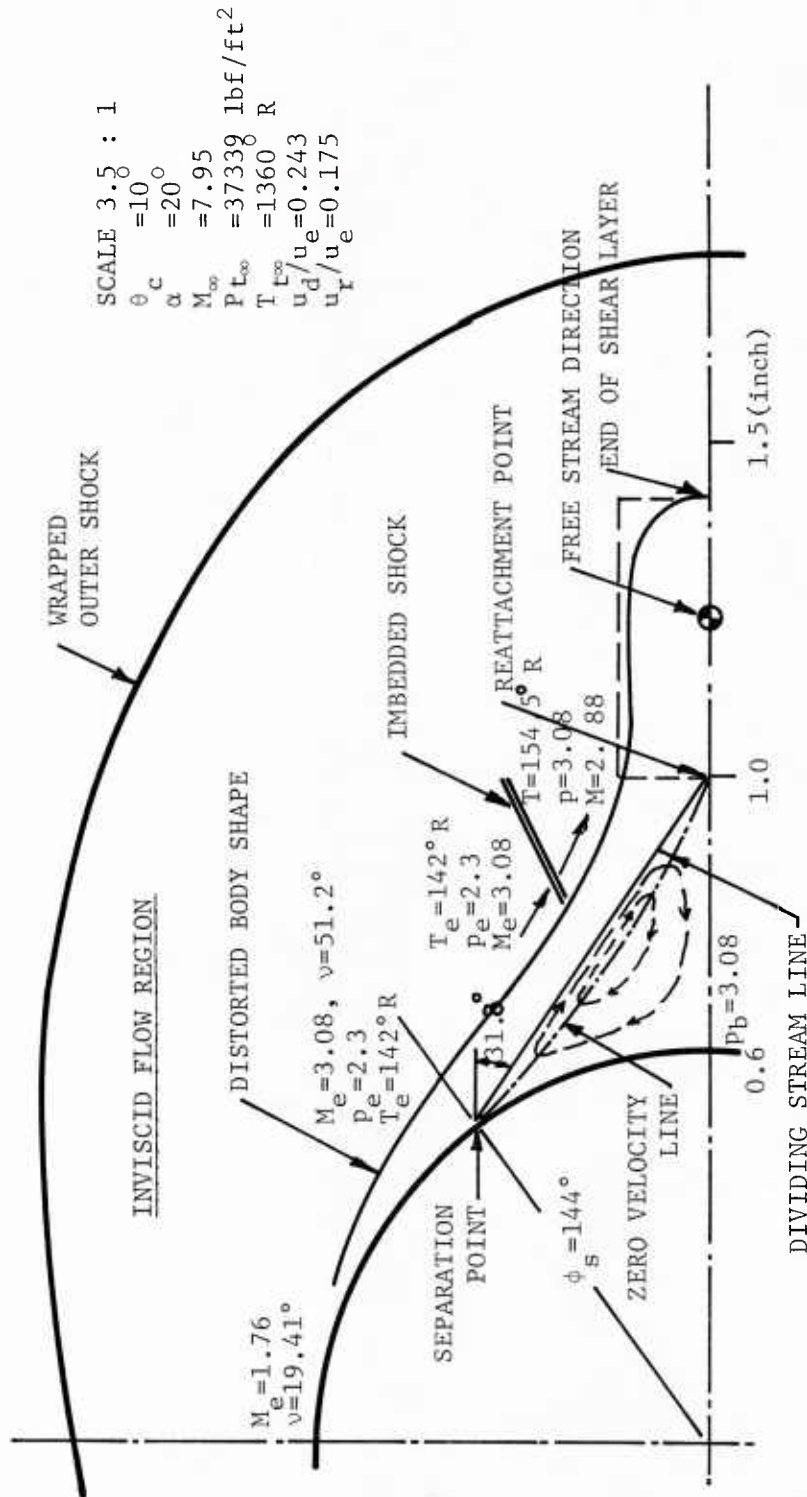
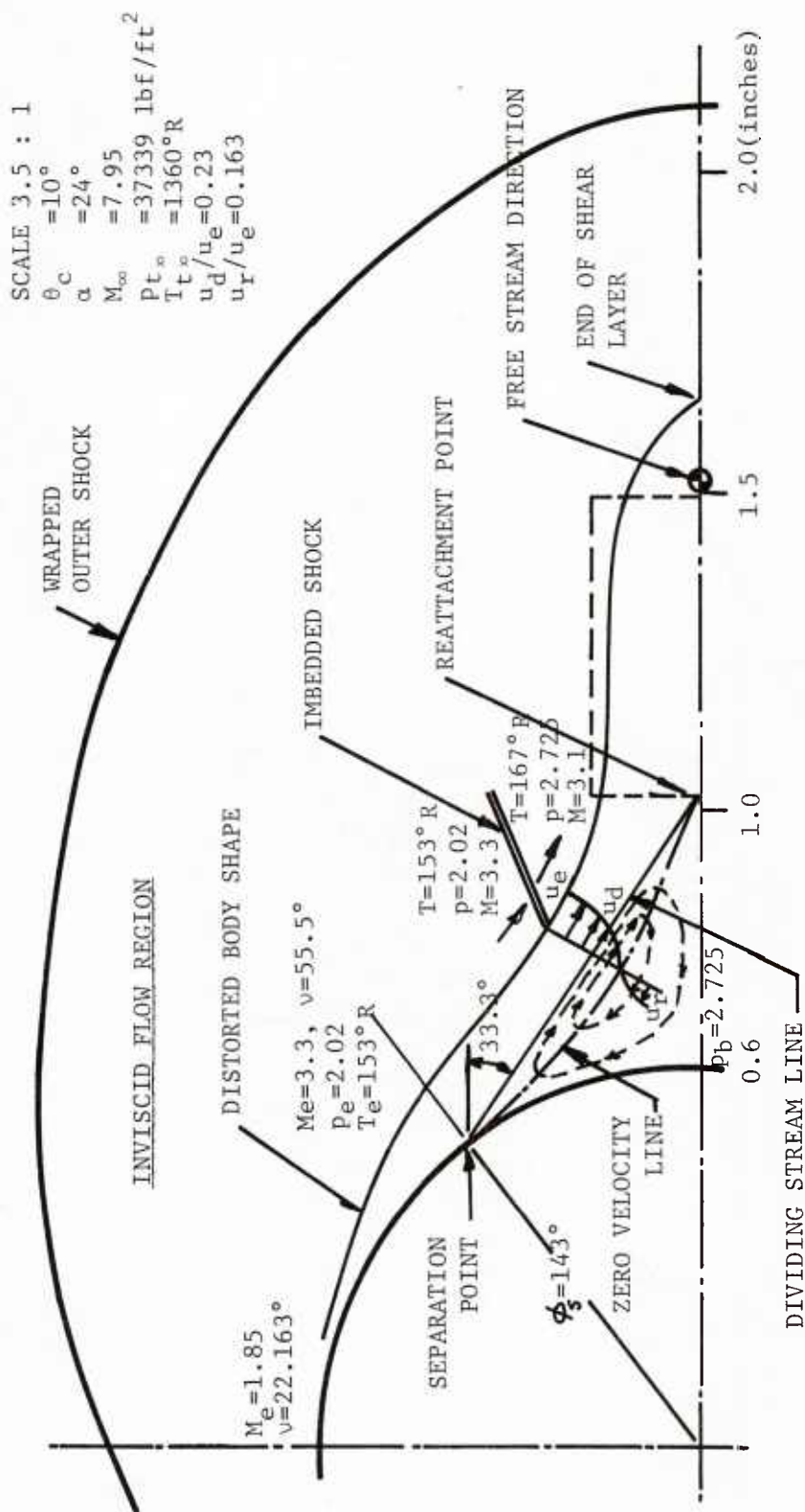


FIGURE 8 SAMPLE COMPUTATION OF DISTORTED BODY SHAPE (BASED ON DATA OF TRACY  $\alpha = 20^\circ$ )

FIGURE 9 SAMPLE COMPUTATION OF DISTORTED BODY SHAPE (BASED ON DATA OF TRACY  $\alpha = 24^\circ$ )

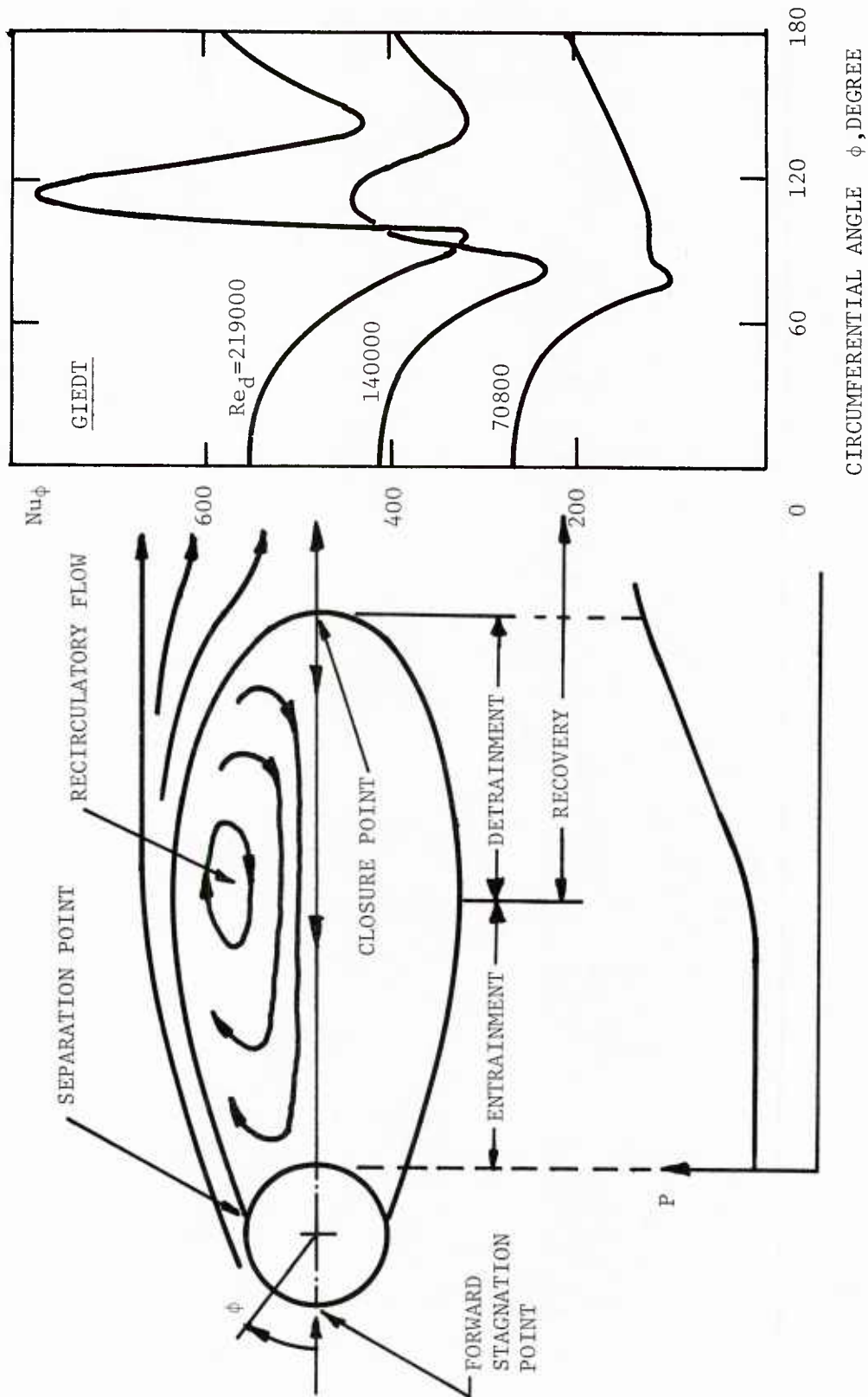


FIGURE 10 FLOW FIELD AND MEASURED CONVECTIVE HEAT TRANSFER OF A SUBSONIC CYLINDER

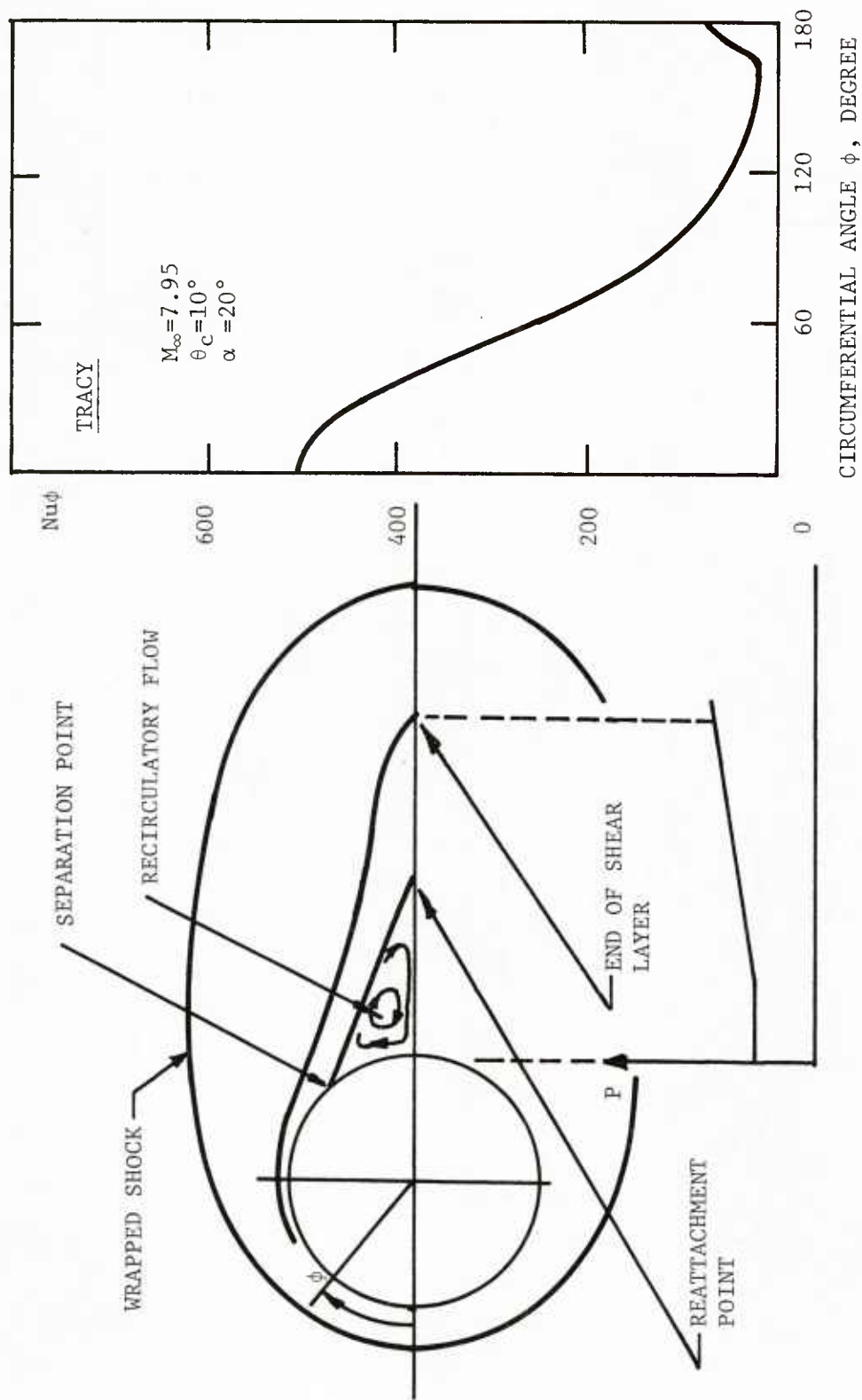
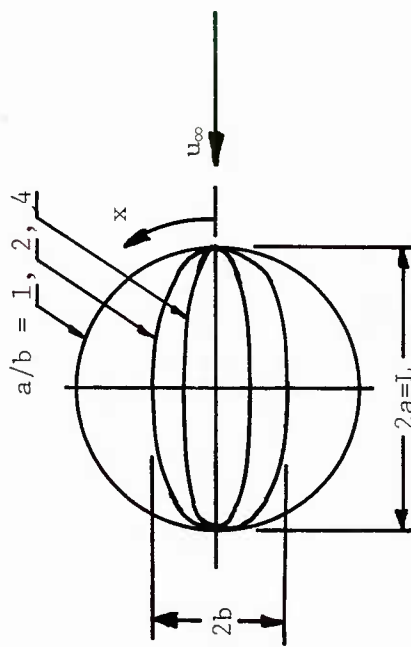
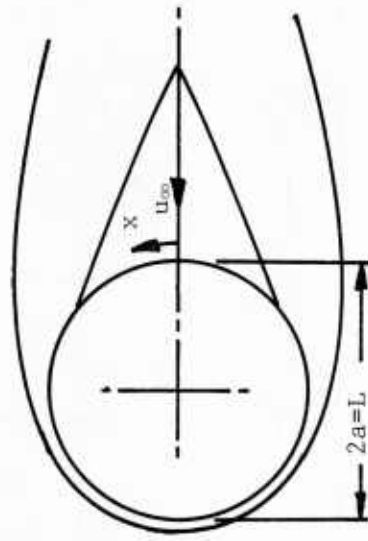


FIGURE 11 FLOW MODEL AND MEASURED CONVECTIVE HEAT TRANSFER OF A HYPersonic CONE AT ANGLES OF ATTACK



(A) WINDWARD SURFACE OF SUBSONIC BLUNT BODY



(B) LEEWARD SURFACE OF HYPERSONIC CONE

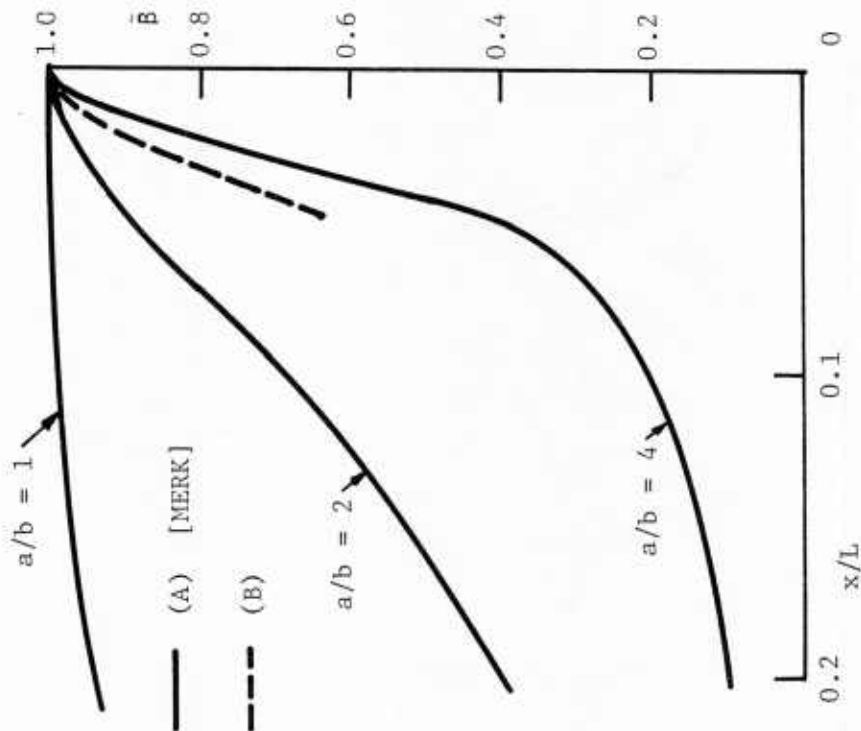


FIGURE 12 DISTRIBUTION OF  $\tilde{\beta}$  IN THE STAGNATION REGION



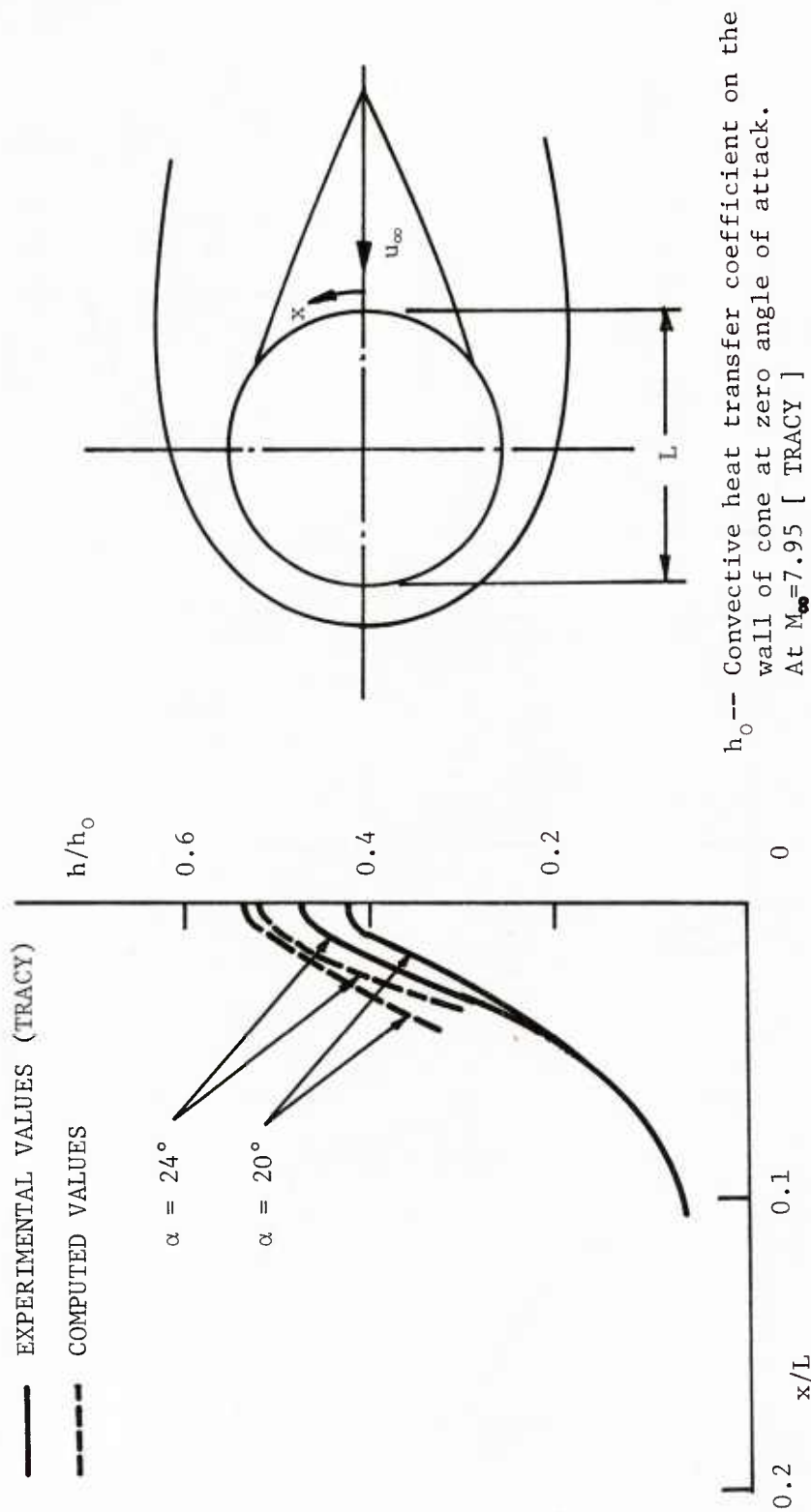


FIGURE 13 CONVECTIVE HEAT TRANSFER ALONG THE CONE SURFACE

Paper No. 4

PRESSURE DISTRIBUTION ON BODIES AT LARGE ANGLE OF ATTACK  
(U)

(Paper UNCLASSIFIED)

by

Howard R. Kelly  
Naval Weapons Center  
China Lake, Calif. 93555

ABSTRACT. A simple engineering method is proposed for finding pressure distributions about certain bodies of revolution at moderately large angles of incidence. It improves upon the accuracy of previous methods, and is more amenable to machine calculation. Its simplicity makes it useful for subroutines to find approximate pressure distributions for heat transfer calculations.

## INTRODUCTION

The prediction of pressure distribution has become increasingly important in modern missile technology. One of the more urgent needs for pressure data is to aid in the calculation of heat transfer. Increasing speed of aircraft and missiles magnifies the heating problem, and increasing complexity of missile components tends to make them more vulnerable to heating damage. In addition, the requirement of high maneuverability, requiring high angles of incidence, adds to the complexity of the problem.

The first step toward solving the problem of pressure prediction is to improve our ability to predict the pressure on bodies of revolution. Then, hopefully, the effects of fins and other appendages can be added to those of the basic body. The flow field about bodies of revolution in axial flow is already fairly well known. An attempt is made here to improve the prediction of pressure distribution for bodies at moderate to large angles of incidence, with flow separation on the leeward side of the body.

## EXISTING THEORETICAL METHODS

A number of theoretical methods of computing pressure exist, each with its own limitations, and some of these will be discussed separately in succeeding paragraphs. The earliest attempts at theoretical methods included first-order approximations, such as that of Tsien<sup>1</sup>, and linearized theory, first considered by Lighthill.<sup>2</sup> The applicability of these is limited to very slender bodies at moderate Mach numbers, and very small angles of incidence. These predictions do not compare well with exact theory for practical cases, so they are of little interest here. A much better result was obtained by Van Dyke<sup>3</sup> in his study of second order theory, and an application of his methods is discussed below, since it is useful at moderate supersonic Mach numbers. Flow at high supersonic Mach numbers, usually called hypersonic flow, requires a different approach, such as Newtonian flow theory.<sup>4</sup> The only really general theory, that applies to all supersonic Mach numbers, is the method of characteristics, as described by Ferri.<sup>5</sup> This has been developed for the case of small angles of incidence, and is considered to be the most accurate method available. This accuracy requires very long and tedious calculations, so the method is primarily used as a standard of comparison for simpler methods, and is little used for practical calculations.

Many other methods have been developed for bodies of special shapes. A very accurate method for axial flow over cones is due to Taylor and Maccoll<sup>6</sup>, and an extension to cones at small angles of incidence was made by Stone<sup>7</sup>. The results of these theories were tabulated by Kopal<sup>8,9,10</sup>. These results are quite useful for cases where tabulated values can be used. The search for a practical method for non-conical bodies led to the shock-expansion method of Eggers and Savin<sup>11, 12</sup>, later modified by Syvertson and Dennis<sup>13</sup> and by Fenter<sup>14</sup>.

It is evident that an exact theoretical description of the flow about a body at incidence is often very difficult if not impossible. Such an exact description is not needed, however, for missile design problems. Therefore, an engineering approximation is sought, using available theory and extending its domain with semi-empirical methods. The primary aim is simplicity, so the results will be useful as an input to computer programs for prediction of heat transfer effects. The present method will be restricted to the simplest case, that of a sharp-nosed body.

#### PREVIOUS ENGINEERING APPROXIMATION

One of the first good engineering methods for supersonic and hypersonic pressure distributions is due to Vendemia<sup>15</sup>. He discusses some of the above-mentioned theories in detail and chooses the most useful for several classes of bodies. Since the tangent ogive is of primary interest here, we shall discuss only his method for such a body shape.

Vendemia calculates the pressure distribution along the meridian lines (or generating lines) of the body of revolution. A starting value at the windward side of the nose tip is found from cone tables, and pressures calculated on various meridian lines at the tip from the Generalized Newtonian Theory, such as used by Lees<sup>16</sup>:

$$C_p = C_{p_{\max}} \sin^2 \delta \quad (1)$$

where  $\delta$  is the angle between the free stream and the tangent to the body surface. Then, for a given meridian, the Generalized Newtonian method is used to compute pressure coefficients along the meridian until an appropriate matching point is reached, where it can be matched to the Shock Expansion Method<sup>12</sup>. In this way, the pressure distribution is computed along each meridian to the nose-body junction.

Vendemia then assumes that the pressure coefficient along the cylindrical body tends to approach zero asymptotically. He computes values of this decaying pressure coefficient from the method of Fenter<sup>14</sup>, where

$$C_p = C_{p(x/\ell = 1)} e^{-\frac{\Delta x/\ell}{K}} \quad (2)$$

In this equation  $\ell$  is the nose length,  $x$  is axial distance along the body, measured from the nose tip,  $\Delta x$  the axial distance measured from the nose-body junction, and  $K$  the hypersonic similarity parameter, which is the ratio of the Mach number to the nose fineness ratio:

$$K = \frac{M_o}{\ell/d} \quad (3)$$

The engineering approximation of Vendemia seems to work very well when compared with experimental data from Perkins and Jorgensen<sup>17</sup>, for an angle of incidence of five degrees ( $\alpha = 5^\circ$ ). Some discrepancies appear, however, for the case of  $\alpha = 10^\circ$ . He attributes this to the presence of separated flow. This is quite true, but his assumption that the pressure coefficient will tend to zero along the body is also unrealistic. Another disadvantage of his method is that extensive interpolation in tables is required, especially at the high angle of incidence. In addition, the Kopal tables used do not always cover the range of values of Mach number and cone angle needed for practical cases. A new improved engineering method is needed to treat the pressure distribution along the body more realistically and, at the same time, be more amenable to simple machine calculation.

#### A NEW ENGINEERING METHOD

##### CROSSFLOW ON A CYLINDER

##### Prediction of Lift

In 1954, the present author developed a method of predicting forces on a body of revolution at large angles of incidence<sup>18</sup>. This was based on the assumption that the axial flow and cross flow are essentially independent, and that the cross flow develops along the body in much the same way that the flow develops on a cylinder moving side-ways through a fluid, when started impulsively from rest. It is well known that a cylinder moving sideways through a perfect (non-viscous) fluid will experience no drag. The actual drag on a cylinder in a viscous fluid is due to flow separation and shedding of vortices. The various theories of lift on bodies of revolution at incidence neglect the effect of viscosity and usually predict a linear dependence of lift on angle of incidence. The actual lift is non-linear with angle at large angles, due to flow separation in the actual viscous flow. The viscous contribution to the normal force on a body of revolution was correlated with the empirical drag data for a cylinder as measured by Schwabe<sup>19</sup>.

The success of the prediction of lift by semi-empirical methods suggests that a similar procedure may be used to predict pressure distributions. While the measurements of Schwabe were made in terms of flow speeds, they were also plotted in terms of pressure distribution, and these pressures were used in an attempt to improve the prediction of pressure on the lee side of bodies at angle of incidence. The results were not satisfactory for several reasons.

First, the Schwabe measurements were made for incompressible flow at low Reynolds number. Other data for fully developed cross flow indicate that the pressure varies with both Mach number and Reynolds number.

Second, the necessary computations are quite involved. Interpolation must be made in functions of both time and azimuthal angle. If one also were to include Mach number and Reynolds number, the corrections will not be simple enough to be practical.

Last, the pressure correction cannot be expected to be as successful as the correction applied to the lift force. This is primarily because the lift is the integral of the pressure, so that errors in pressure distribution will sometimes be cancelled out in the integration process. In addition, the pressure near the ninety-degree position in azimuth, as measured from the windward side, will contribute little or nothing to the lift. For these reasons, it is much more difficult to obtain a completely accurate pressure correction than to obtain a correction for the lift force. This, along with lack of simplicity, ruled out this method of correction.

#### The Asymptotic Pressure

A simpler approach to the problem is suggested by Vendemia<sup>15</sup>, as described above. We can modify his method of exponential decay so that the equilibrium pressure is not the free-stream value, corresponding to zero pressure coefficient, but is a value determined by existing cross flow. Howarth<sup>20</sup> has shown pressure coefficient distributions about cylinders as measured by Ferri. From these can be deduced the asymptotic values of pressure coefficient on a very long cylinder.

The principal pertinent results shown by Howarth are reproduced here in Fig. 1. The pressure coefficient on a cylinder in cross flow is shown as a function of azimuthal angle for four different Mach numbers. The pressure coefficient is found to be insensitive to Mach number and Reynolds number in supersonic crossflow, so if the crossflow Mach number  $M_1 = M_\infty \sin \alpha > 1.0$ , the assumption is made that the curve for  $M_1 = 1.85$  is a good approximation. If the cross flow is subsonic ( $M_1 < 1.0$ ), then the pressure coefficient may be quite sensitive to Mach number, but sensitive to Reynolds number only at very low Mach number. For simplicity, it is assumed that the dependence on Mach number is quadratic:



## Vol. 1

$$C_p = A + BM_1 + CM_1^2 \quad (4)$$

The coefficients A, B, C are different for each azimuthal angle  $\phi$ . After normalizing the curves to  $C_p = 1$  at  $\phi = 0$ , the value of  $(C_p)_{\text{supersonic}}$  and the coefficients A, B, and C are as follows, for thirty-degree intervals:

$\phi$ (degrees)	$(C_p)_{\text{supersonic}}$	A	B	C
0	1.00	1.00	0.0	0.0
30	0.75	0.24	0.458	-0.042
60	0.27	-0.19	-0.617	1.583
90	-0.08	-0.85	0.029	0.229
120	-0.14	-1.00	0.467	-0.083
150	-0.16	-1.07	0.671	-0.229
180	-0.17	-1.07	0.671	-0.229

These values, when multiplied by the Newtonian pressure coefficient from Equation 1, determine the asymptotic pressure coefficients along the body.

## OGIVE-CYLINDER AT LOW SUPERSONIC MACH NUMBER

No single theory will provide a simple method of estimating the pressure distributions on a body for all Mach numbers, all angles of incidence, and all body shapes. We therefore break down the problem into different categories and try to make these categories as general as possible. One simple body shape is the tangent-ogive-cylinder. We shall consider this in some detail at both low and high supersonic Mach numbers.

A good example of the ogive-cylinder at low Mach number is found in the measurements at Mach 2, reported by Perkins and Jorgensen<sup>17</sup>. As was mentioned before, this example was chosen by Vendemia to test his method, which was found to be good at  $\alpha = 5^\circ$  and not as good at  $\alpha = 10^\circ$ .

Vendemia had used Newtonian and Shock Expansion methods for computing pressure along the nose. It was decided to use the Van Dyke method instead, since this method was designed for low supersonic Mach numbers. The computations for the ogival nose were carried out according to the method used by Dunn<sup>21</sup>, an interpretation of the Van Dyke method for practical computation. For the cylindrical body, the pressure coefficient was allowed to approach asymptotically the expected pressure coefficients for a cylinder. This expected value is found from the Newtonian Law for the windward meridian (see Eq. 1), and the values at other meridians related to this by ratios determined from Howarth<sup>20</sup>, using the existing crossflow Mach number.



## OGIVE-CYLINDER AT HIGH SUPERSONIC MACH NUMBER

The above method depends heavily on the Van Dyke second order theory, which is valid only if the hypersonic similarity parameter  $K$  (Eq. 3) is less than unity. If this parameter is greater than unity, the flow may be called truly hypersonic, and one is tempted to simply replace the Van Dyke theory by Newtonian flow theory. This works moderately well in some cases, but fails on the leeward side of the nose ( $\phi = 180$  degrees), since the angle between the body surface and the free stream direction passes through zero and becomes negative.

The method used by Vendemia works well at small angles of incidence, but not too well at larger angles. It also becomes quite involved at the larger angles, not only from the several numerical tables that must be used for interpolation, but also the complication of choosing a matching point between the Newtonian theory and the Prandtl-Meyer expansion method.

The method used here is to find the Newtonian pressure coefficients at the tip of the nose and use Prandtl-Meyer expansion all the way to the nose-body junction. This requires only a minimum number of tabular values, and, surprisingly, gives as good results as Vendemia's method at moderate angles of incidence (up to 10 degrees), without the complications.

The pressure coefficients along the body are found just as before. The value on a given meridian at the nose-body junction is allowed to decay exponentially to the equilibrium value on that meridian, as determined in the table derived from Howarth.

## CONE-CYLINDERS

The cone has one of the simplest geometries of nose shapes for a rocket or guided missile, and as such has been the subject of more thorough aerodynamic study than any other shape. Extensive tables (8, 9, 10) of aerodynamic parameters for cones have been in use since 1949, and refinements to the method of using these tables have been proposed, particularly by Ferri<sup>22</sup>.

There are two main disadvantages to using the tables for engineering approximation to pressure distribution, such as we are discussing here. The principal objection is that the use of numerous tables for search and interpolation in a computer program may lead to storage problems. Also, the tables are limited with respect to Mach number and cone angle, and may not include some of the cases of interest. Extrapolation from these tables is not very accurate.

The best high Mach number pressure data for cones at incidence were used by Ferri<sup>22</sup>, and taken from Cooper and Robinson<sup>23</sup>. The test bodies consisted of a 20-degree cone on a cylindrical body of four-diameter length, and were tested at a Mach number of 6.86. The method of Ferri predicts the pressure on the conical nose quite well, but the Newtonian

### Vol. 1

theory of Grimmer<sup>4</sup> is even better, except on the leeward side at high angles, as will be noted later. Since the hypersonic similarity parameter is greater than 2.4, the Newtonian theory was selected as suitable for the conical nose. It is also much simpler to program for computation than the Ferri method, or the direct use of Kopal's tables. The computation is especially simple for the conical nose, since pressures are constant along each meridian, by conical flow theory.

To compute the pressure on the cylindrical body, one must first find the pressure jump for each meridian by using a Prandtl-Meyer expansion at the cone-cylinder junction. This starting value on the cylindrical body is then allowed to decay exponentially along the body to an equilibrium value for that meridian in exactly the same way as was done for the ogive-cylinder.

At low supersonic Mach number the procedure is similar. The principal difference is that the theory of Van Dyke is used instead of Newtonian theory for the cone.

### COMPARISON WITH EXPERIMENT

A few examples have been chosen to illustrate the results of the present method at moderate angles of incidence. In some cases, other methods are included for comparison.

#### OGIVE-CYLINDER AT LOW SUPERSONIC MACH NUMBER

The results of this calculation for  $M = 2$  for the windward meridian ( $\phi = 0^\circ$ ) are shown in Fig. 2 for angles of incidence of  $5^\circ$ ,  $10^\circ$  and  $15^\circ$ . In addition to the Perkins and Jorgensen data and curves from the present method, curves are shown for the method of Vendemia, and for the Van Dyke method along both head and body, as interpreted by Perkins and Jorgensen. Figure 3 shows corresponding results for a meridian at azimuth of  $\phi = 120$  degrees.

In comparison with the method of Vendemia, the present method gives comparable results for azimuth  $\phi$  less than 90 degrees. For greater than 90 degrees, Vendemia's results are not as good, particularly at  $\alpha = 10$  degrees. It may be expected that his method would show even less favorable results at  $\alpha = 15$  degrees. For the cylindrical body, the fallacy of allowing the pressure coefficient to approach zero is evident, since the experimental values tend toward non-zero asymptotes in many cases.

The interpretation of Van Dyke by Perkins and Jorgensen tends to disagree with the present method at the nose tip, for some unknown reason. It seems evident from the data shown, as well as from others not shown that the present method predicts the pressure distribution on a tangent-ogive cylinder at low supersonic Mach numbers better than any other simple engineering method.

## OGIVE-CYLINDER AT HIGH SUPERSONIC MACH NUMBER

As mentioned before, the results of this method were not expected to be precise, but are better than expected. In order to check this method, a few data points have been excerpted from a test by Lord and Ulmann<sup>24</sup>. One of their models was an ogive-cylinder with nose fineness ratio of about 3 and Mach number of about 4, which gives a hypersonic similarity parameter of 4/3. Comparison with theory is made for azimuth meridians of 0, 45, 90 and 180 degrees.

Figures 4-7 show that the present method gives very good results at 5 and 10 degrees incidence, except for the case  $\alpha = 10$  degrees,  $\phi = 180$  degrees. This method fails at higher angles of incidence, but could be used for approximate results at  $\alpha = 15$  degrees.

## CONE-CYLINDERS

A comparison with experiment is made in Fig. 8-10. The Mach number, as mentioned above, is 6.86 and angles of incidence are 6.7, 14 and 20 degrees. Azimuth meridians are  $\phi = 0, 60$  and 180 degrees. The agreement with experiment is excellent except for  $\phi = 180$  degrees, where Newtonian theory is not expected to be valid for  $\alpha = 14$  and 20 degrees, since the angle of incidence is greater than the cone semi-angle, and these meridians lie in the aerodynamic shadow of the cone. It is obvious from Fig. 10 the  $C_p = 0$  is a good approximation for this case.

It is recommended, on this basis, that pressure coefficients be computed by the above method, and then  $C_p = 0$  substituted on the cone for any position in the aerodynamic shadow. The criterion for this is that  $\sin \delta < 0$ , where

$$\sin \delta = \sin \theta_N \cos \alpha + \cos \theta_N \sin \alpha \cos \phi.$$

Good data for cones at low supersonic Mach number (hypersonic similarity parameter less than one) are scarce. The best are shown by Ferri<sup>22</sup> for a Mach number of 1.6, but for cones only, with no cylindrical afterbody. In keeping with the need for simplicity, we prefer to avoid the method used by Ferri, or the direct use of Kopal's tables. The obvious method is to use Dunn's interpretation of the Van Dyke theory, as was done for ogive-cylinders at low supersonic Mach number.

A comparison is made between the Ferri and Dunn methods in Fig. 11. Since data are available only on the cone, Fig. 11 shows the theoretical results and experimental data for  $\alpha = 6$  degrees at azimuths from 0 degrees (windward) to 180 degrees (leeward). This comparison shows that the Ferri and Dunn methods both represent the data equally well.

In Fig. 11, additional curves show the results of using Kopal's tables directly. Data from Ref. 9, for yawing cones, and Ref. 10, for cones at large yaw, are shown. Both show very poor agreement with the experimental data and with the Ferri and Dunn methods. This disagreement

### Vol. 1

becomes progressively worse at larger angles  $\alpha$ . Since the Dunn method is simpler to use than either Ferri or the Kopal tables, it appears to be the best method for our engineering approximation for the case of hypersonic similarity parameter less than unity.

### CONCLUSION

Computer programs have been written for the prediction of pressure distribution on ogive-cylinders and cone-cylinders at incidence. These may readily be modified for use as subroutines in other programs. These programs are applicable for all supersonic and hypersonic Mach numbers and for angles of incidence up to about 15 degrees. Two sources of error tend to inhibit accuracy above this angle of incidence. First, most theoretical methods give poor results on the nose for larger angles. Second, the presence of shed vortices along the body tends to distort the pressure distribution at larger angles. An attempt to correct for the presence of these vortices has failed.

The approximation used here for the cylindrical body may also prove useful for cylinders with blunt nose shapes provided the pressure coefficient is known at the nose-body junction.

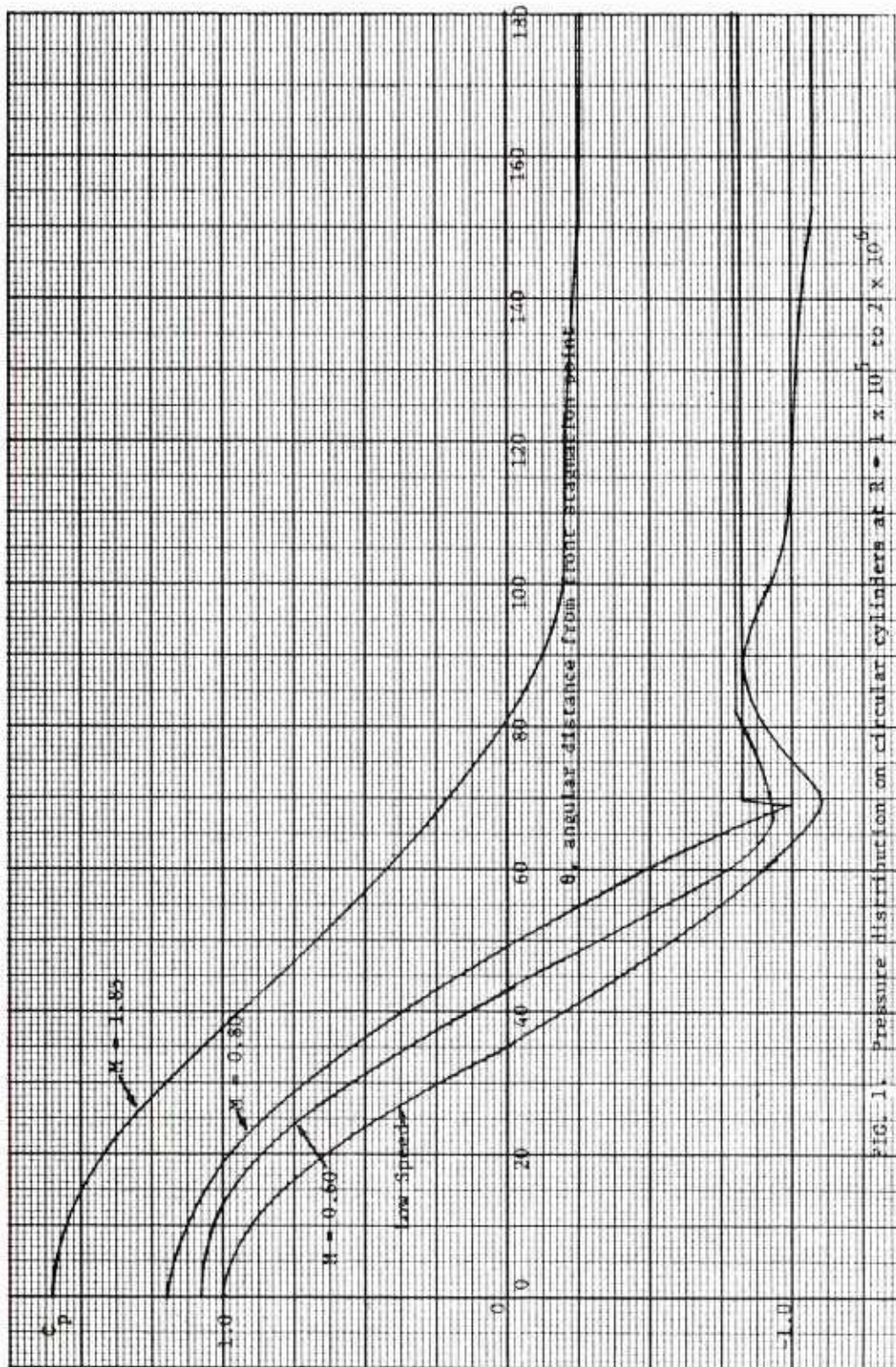
## REFERENCES

1. Supersonic Flow Over an Inclined Body of Revolution, by H.S. Tsien, J. Aeronaut. Sci., Vol 12, Oct. 1938, pp. 480-483.
2. Supersonic Flow Past Slender Pointed Bodies of Revolution at Yaw, by M.J. Lighthill, Quart. J. Mech. and Appl. Math., Vol I, Pt. I, March 1948, pp. 76-89.
3. National Advisory Committee for Aeronautics, A Study of Second Order Supersonic Flow Theory, by M.D. Van Dyke, NACA Report 1081, 1952.
4. Lift on Inclined Bodies of Revolution in Hypersonic Flow, by G. Grimminger, R.P. Williams, and G.B.W. Young, J. Aeronaut. Sci., Vol 17, No. 11, Nov. 1950.
5. National Advisory Committee for Aeronautics, Application of the Method of Characteristics to Supersonic Rotational Flow, by A. Ferri, NACA TN 1135, Sept. 1946.
6. The Air Pressure on a Cone Moving at High Speeds - I and II, by G.I. Taylor and J.W. Maccoll, Proc. Roy. Soc. London, Series A, Vol 139, Feb. 1933, pp. 278-311.
7. On Supersonic Flow Past a Slightly Yawing Cone, by A.H. Stone, Journ. Math and Phys., Vol 27, 1948, pp. 67-81.
8. Massachusetts Institute of Technology, Tables of Supersonic Flow Around Cones, by Zdenek Kopal, Tech. Report No. 1, 1948.
9. \_\_\_\_\_ Tables of Supersonic Flow Around Yawing Cones, by Zdenek Kopal, Tech. Report No. 3, 1947.
10. \_\_\_\_\_ Tables of Supersonic Flow Around Cones of Large Yaw, by Zdenek Kopal, Tech. Report No. 5, 1949.
11. National Advisory Committee for Aeronautics, Approximate Methods for Calculating the Flow about Non-Lifting Bodies of Revolution at High Supersonic Airspeeds, by A.I. Eggers and R.C. Savin, NACA TN 2579, Dec. 1951.
12. \_\_\_\_\_ Application of the Generalized Shock-Expansion Method to Inclined Bodies of Revolution Traveling at High Supersonic Airspeeds, by R.C. Savin, NACA TN 3349, April 1955.
13. \_\_\_\_\_ A Second Order Shock-Expansion Method Applicable to Bodies of Revolution Near Zero Lift, by C.A. Syvertson and D.H. Dennis, NACA Report 1328, 1957.



### Vol. 1

14. University of Texas, An Approximate Method for the Calculation of the Aerodynamic Characteristics of Ogive-Cylinders near Zero Lift, by F.W. Fenter, DRL Report 390, Defense Research Laboratory, Univ. of Texas, Jan. 1957.
15. The Johns Hopkins University, An Engineering Method for Rapid Calculations of Supersonic-Hypersonic Pressure Distributions on Lifting and Non-Lifting Pointed Bodies of Revolution, by R.J. Vendemia, Jr., The Johns Hopkins University Applied Physics Laboratory, Tech. Memo TG 752, Nov. 1965.
16. Hypersonic Flow, by Lester Lees, Proceedings IAS-RAES Fifth International Aeronautical Conference, Los Angeles, Calif., June 1955.
17. National Advisory Committee for Aeronautics, Comparison of Experimental and Theoretical Normal Force Distributions (Including Reynolds Number Effects on Ogive-Cylinder Body at Mach Number 1.98, by E.W. Perkins and L.H. Jorgensen, NACA TN 3716, May 1956.
18. U.S. Naval Ordnance Test Station, The Estimation of Normal Force and Pitching Moment Coefficients for Blunt-Based Bodies of Revolution at Large Angles of Attack, by H.R. Kelly, NOTS TM-998, May 1953.
19. National Advisory Committee for Aeronautics, Pressure Distribution in Non-Uniform Two-Dimensional Flow, by M. Schwabe, NACA TM 1039 (translated from Ingenieur - Archiv., Vol. VI, No. 1, February 1935), Jan. 1943.
20. Modern Developments in Fluid Dynamics, High Speed Flow, by L. Howarth, Vol II, p. 682, Oxford University Press, 1953.
21. U.S. Naval Ordnance Test Station, Some Results of a Systematic Theoretical Pressure Distribution Program on Bodies of Revolution, by E.L. Dunn, NOTS TM 919, April 1953.
22. National Advisory Committee for Aeronautics, Supersonic Flow Around Circular Cones at Angles of Attack, by Antonio Ferri, NACA TN 2236, November 1950.
23. An Investigation of the Aerodynamic Characteristics of a Series of Cone-Cylinder Configurations at a Mach Number of 6.86, by Ralph D. Cooper and Raymond A. Robinson (U), December 1951 (NACA RM L51 J09, publication Confidential).
24. National Advisory Committee for Aeronautics, Pressure Measurements on an Ogive-Cylinder Body at Mach Number 4.04 (U), by Douglas R. Lord and Edward F. Ulmann, NACA Washington, February 1952 (NACA RM L51 L20, publication Confidential).

FIG. 1. Pressure distribution on circular cylinders at  $M = 1 \times 10^5$  to  $2 \times 10^5$



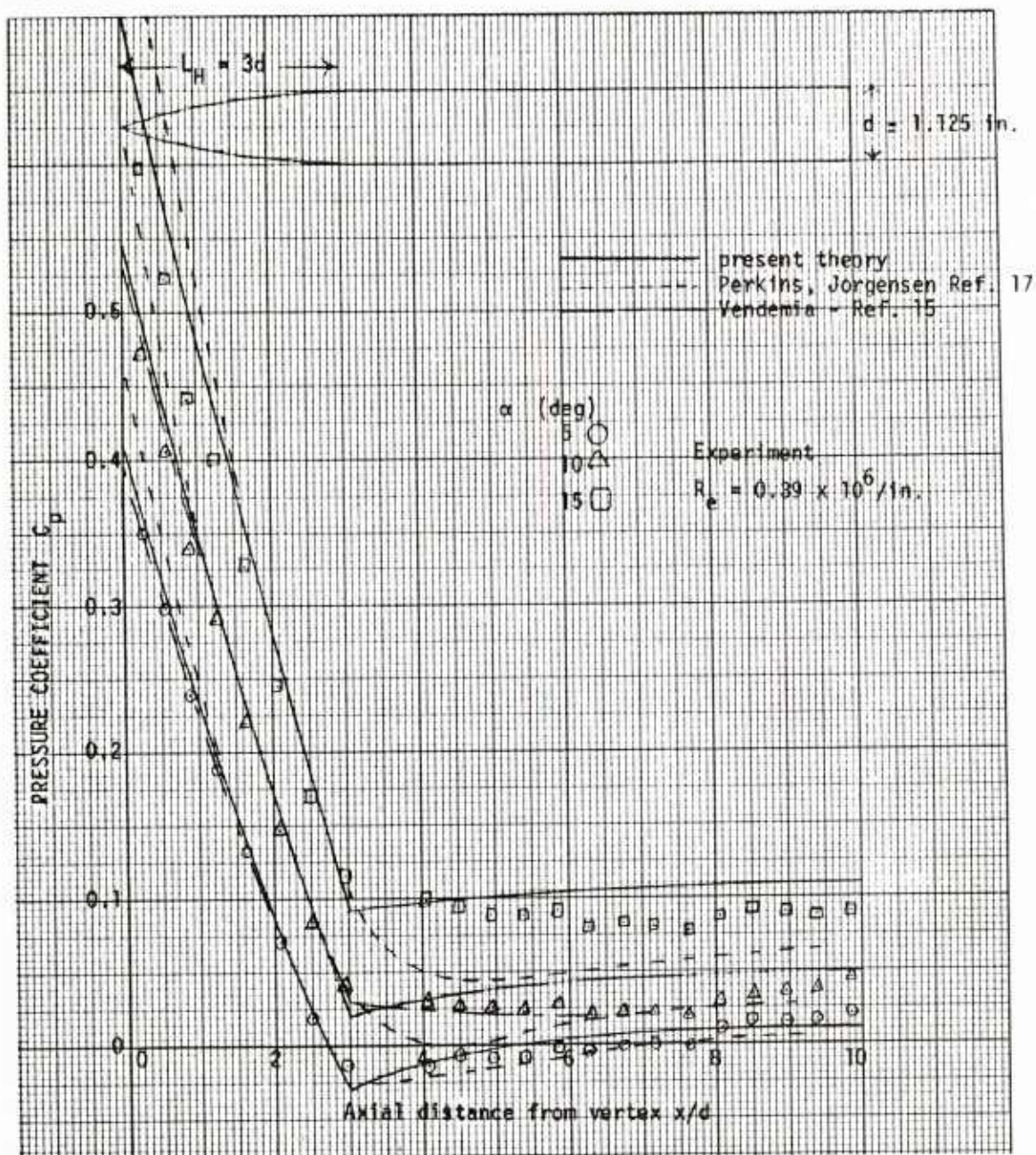


FIG. 2 - Comparison of Theoretical and Experimental Pressure Distribution on a Tangent-Ogive Cylinder at Various Angles of Incidence:  $M = 2$ ,  $\phi = 0$  degree



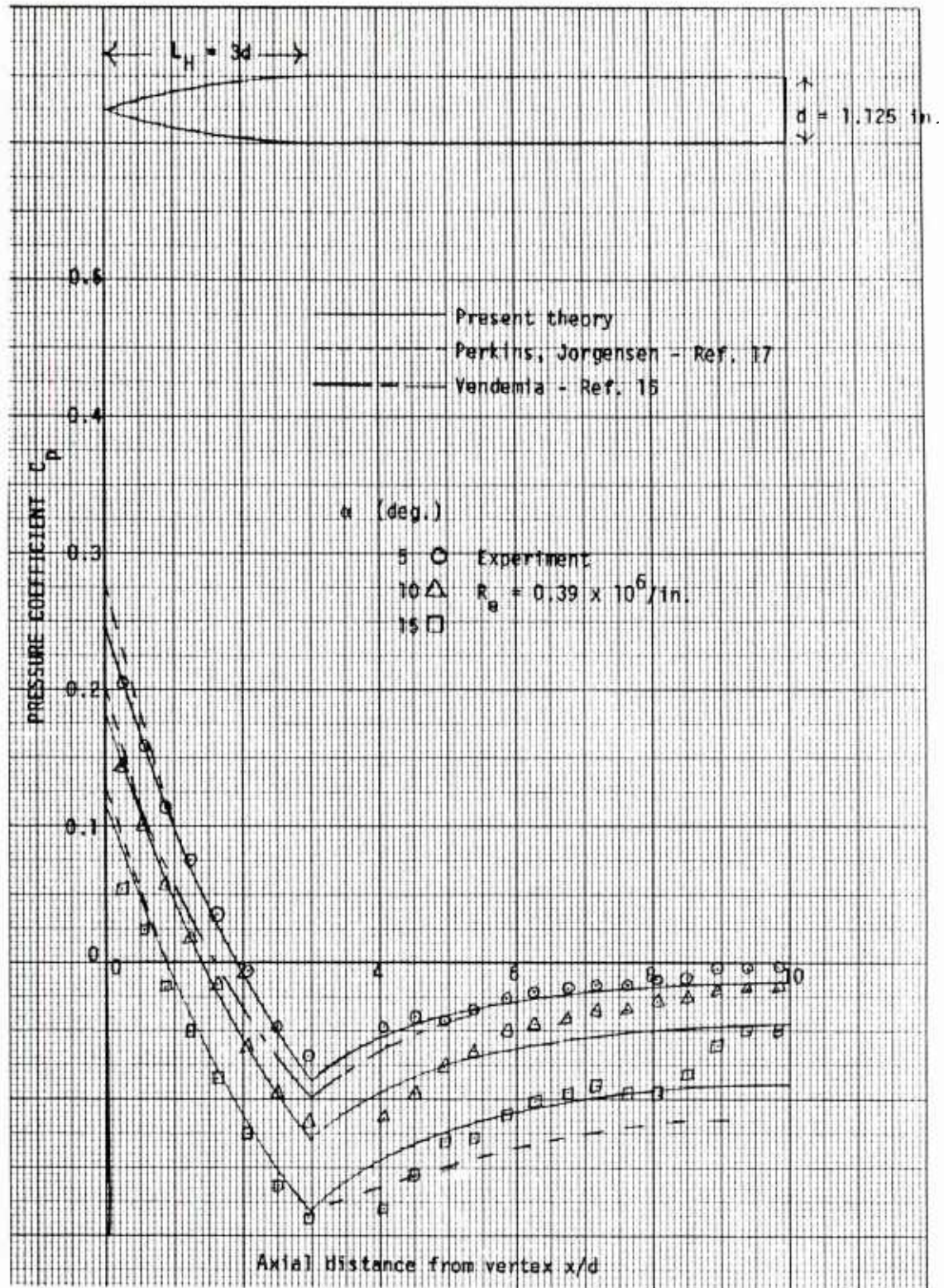


FIG. 3 - Comparison of Theoretical and Experimental Pressure Distribution on a Tangent-Ogive Cylinder at Various Angles of Incidence:  $M = 2$ ,  $\phi = 120$  degrees



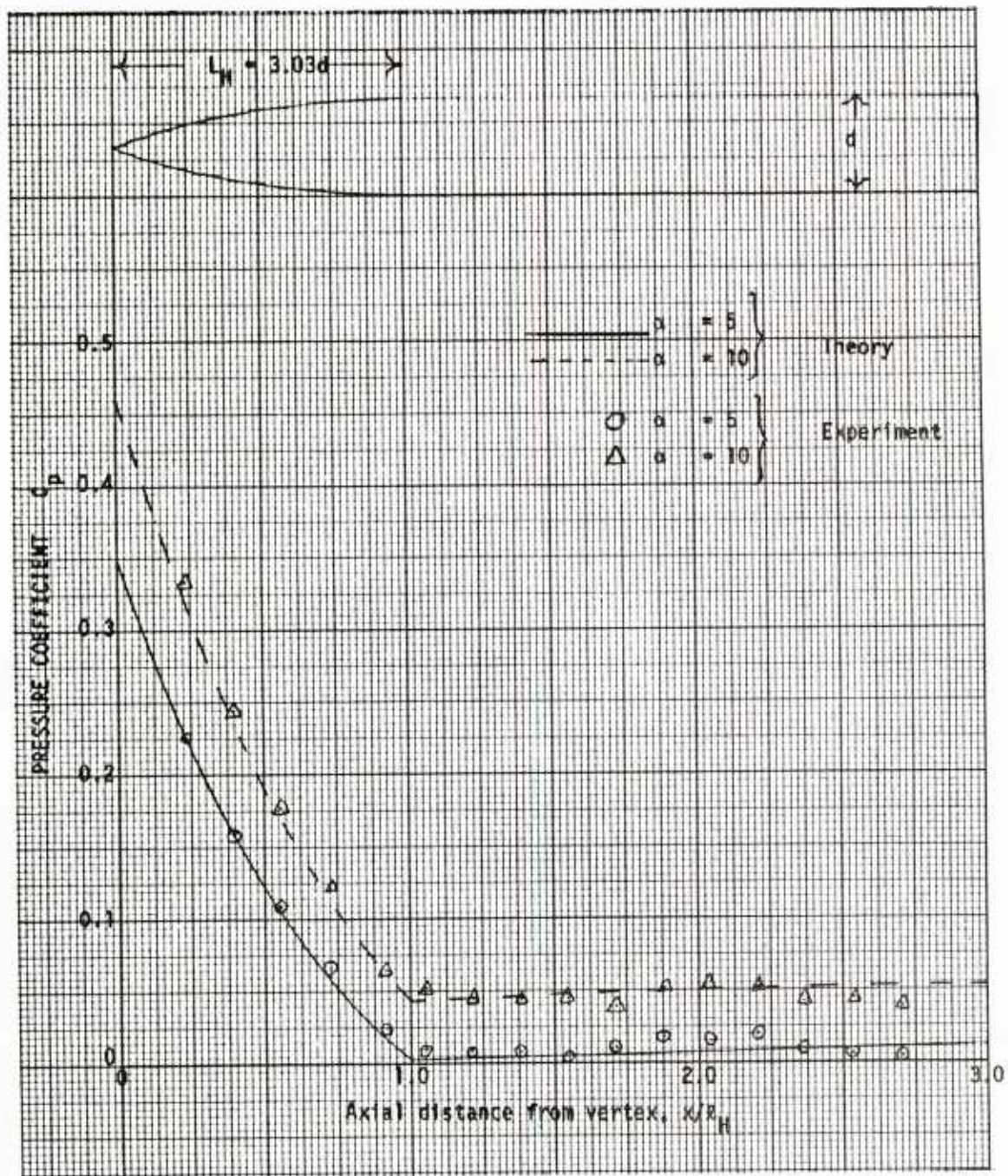


FIG. 4 - Comparison of Theoretical and Experimental Pressure Distribution on a Tangent-Ogive Cylinder at Two Angles of Incidence:  $M = 4.04$ ,  $\phi = 0$  degree

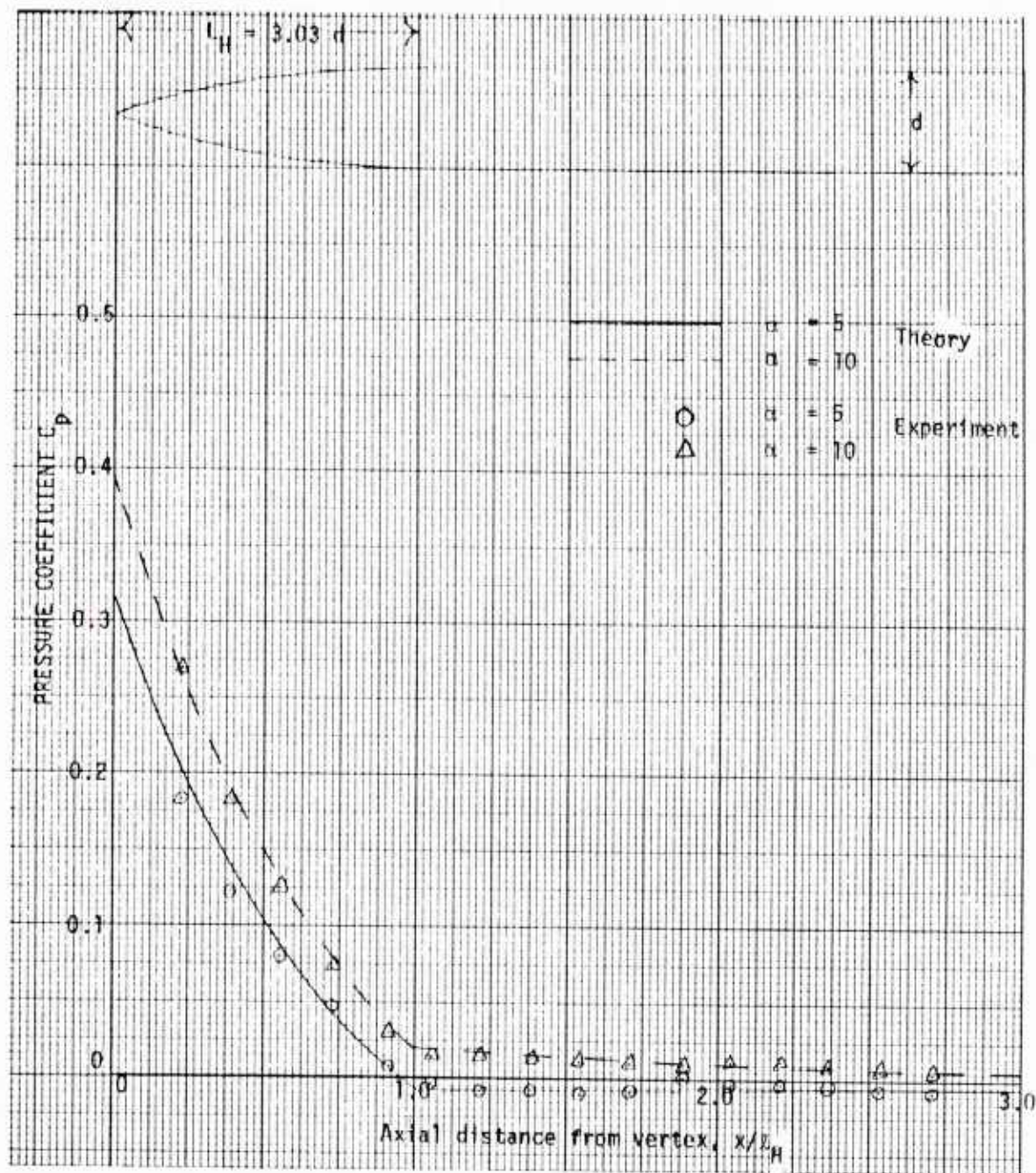


FIG 5 - Comparison of Theoretical and Experimental Pressure Distribution on a Tangent-Ogive Cylinder at Two Angles of Incidence;  $M = 4.04$ ,  $\phi = 45$  degrees



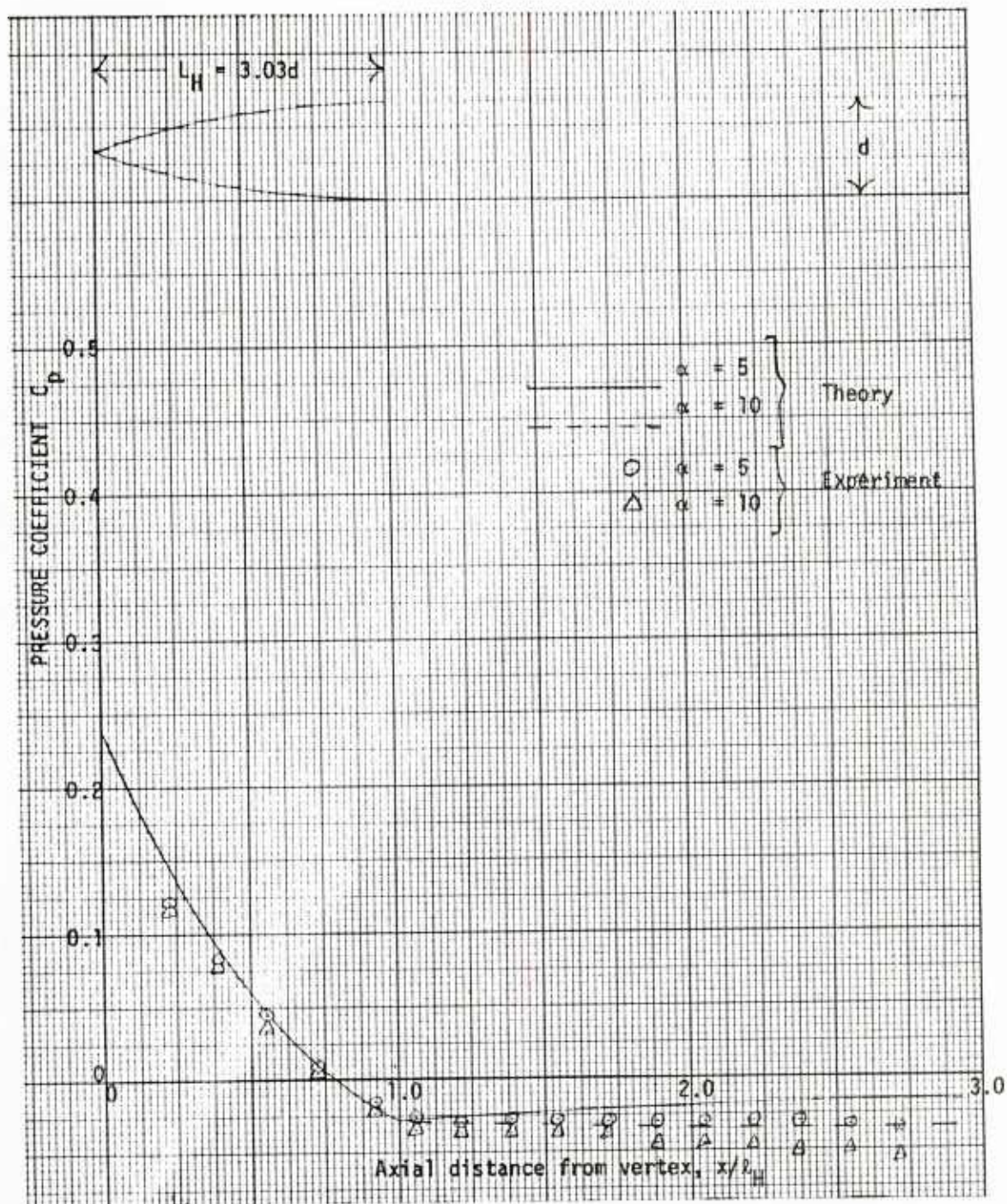


FIG. 6 - Comparison of Theoretical and Experimental Pressure Distribution on a Tangent-Ogive Cylinder at Two Angles of Incidence;  $M = 4.04$ ,  $\phi = 90$  degrees



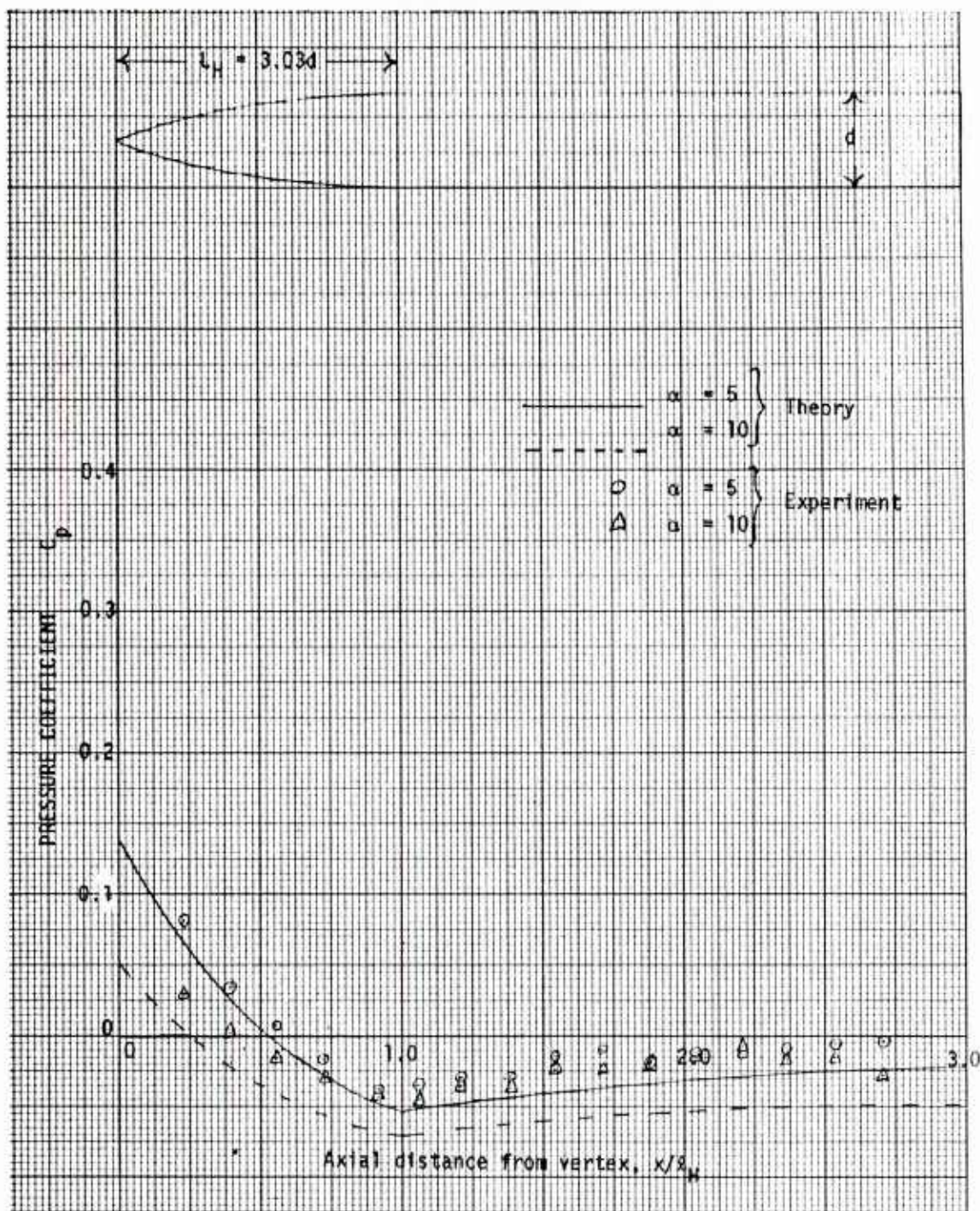


FIG. 7 - Comparison of Theoretical and Experimental Pressure Distribution on a Tangent-Ogive Cylinder at Two Angles of Incidence;  $M = 4.04$ ,  $\phi = 180$  degrees



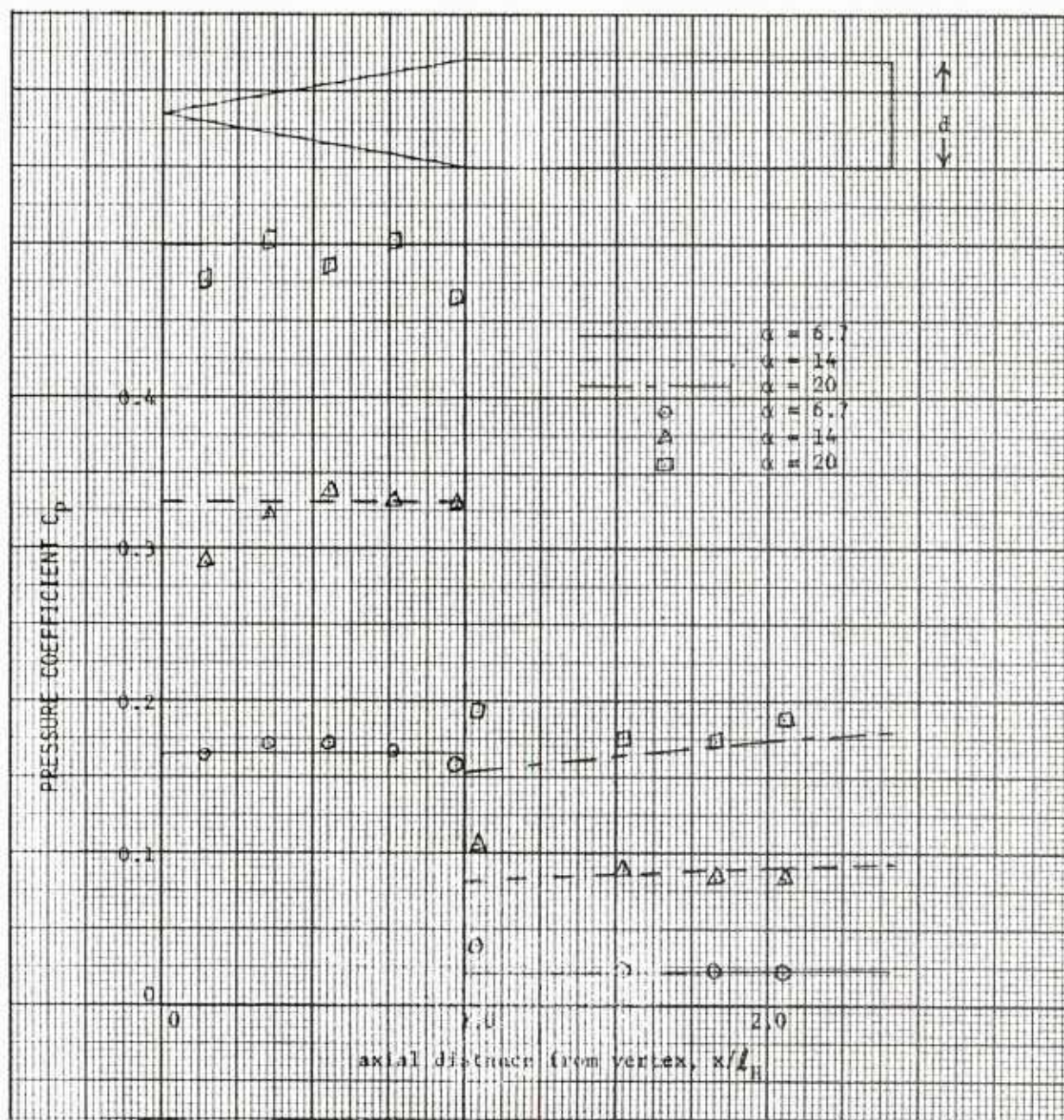


FIG. 8 - Comparison of Theoretical and Experimental Pressure Distribution on a Cone-Cylinder at Various Angles of Incidence,  $M = 6.86$ ,  $\phi = 0$  degrees



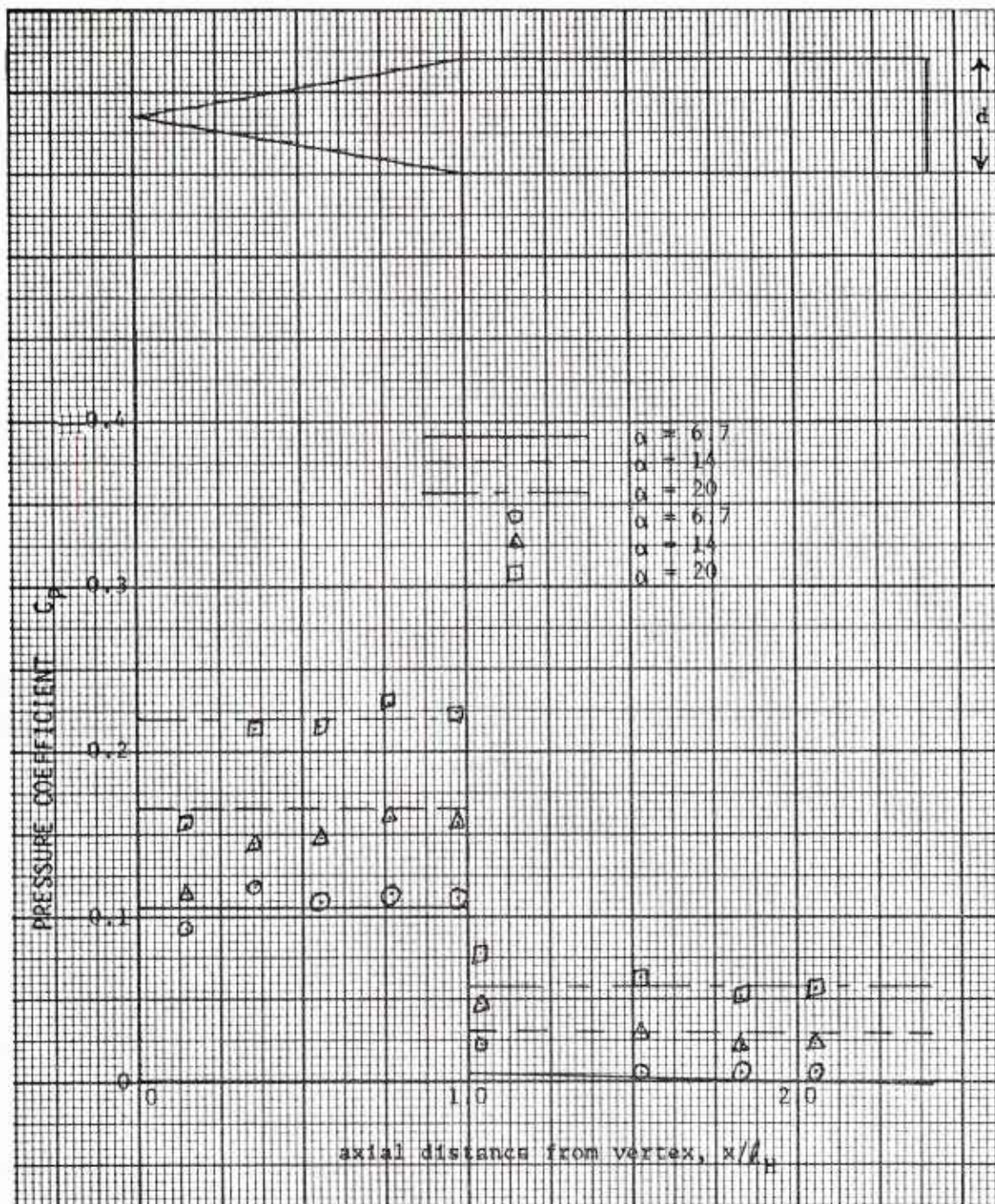


FIG. 9 - Comparison of Theoretical and Experimental Pressure Distribution on a Cone-Cylinder at Various Angles of Incidence;  $M = 6.86$ ,  $\phi = 60$  degrees



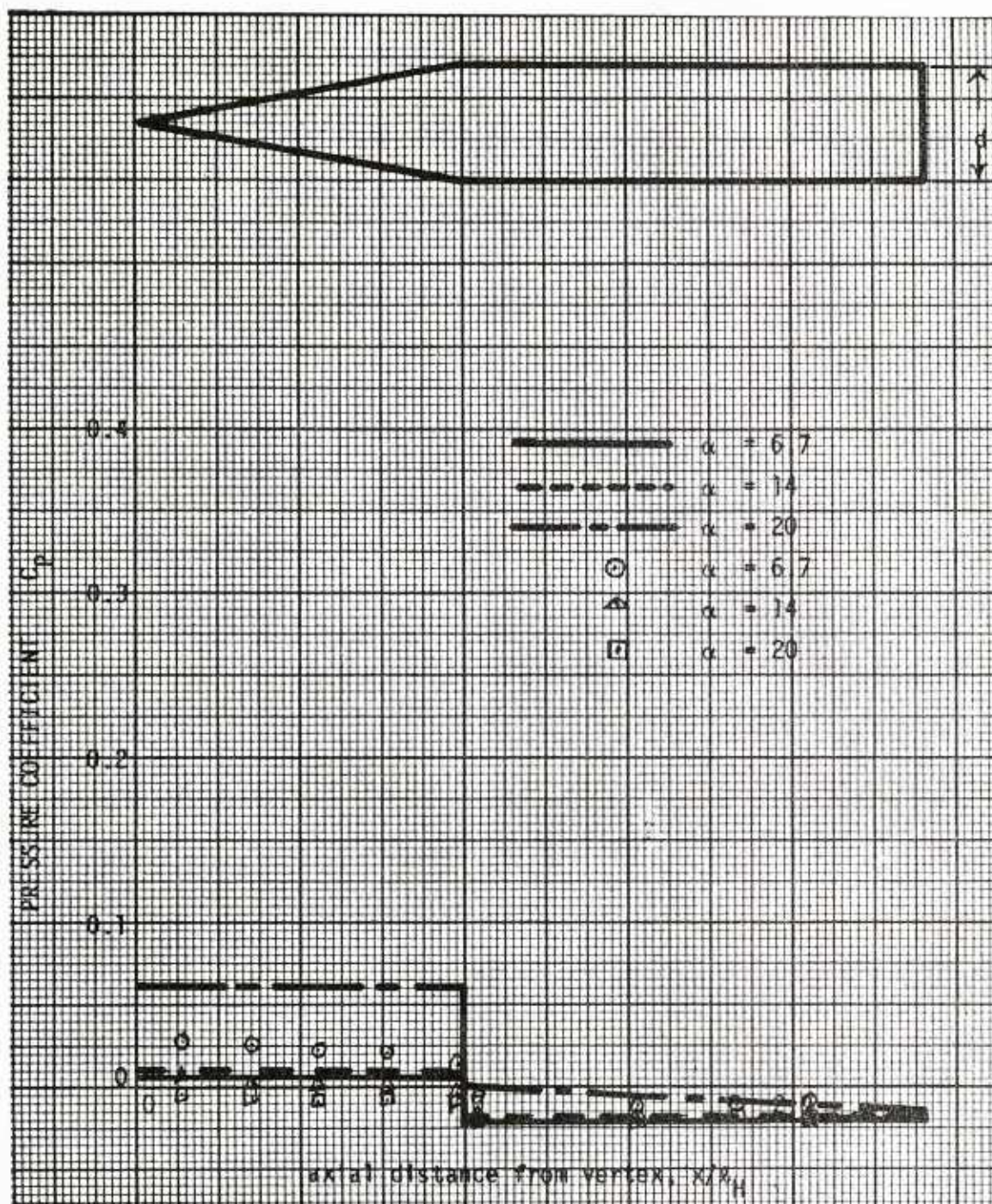


FIG. 10 - Comparison of Theoretical and Experimental Pressure Distribution on a Cone-Cylinder at Various Angles of Incidence;  $M = 6.86$ ,  $\phi = 180$  degrees



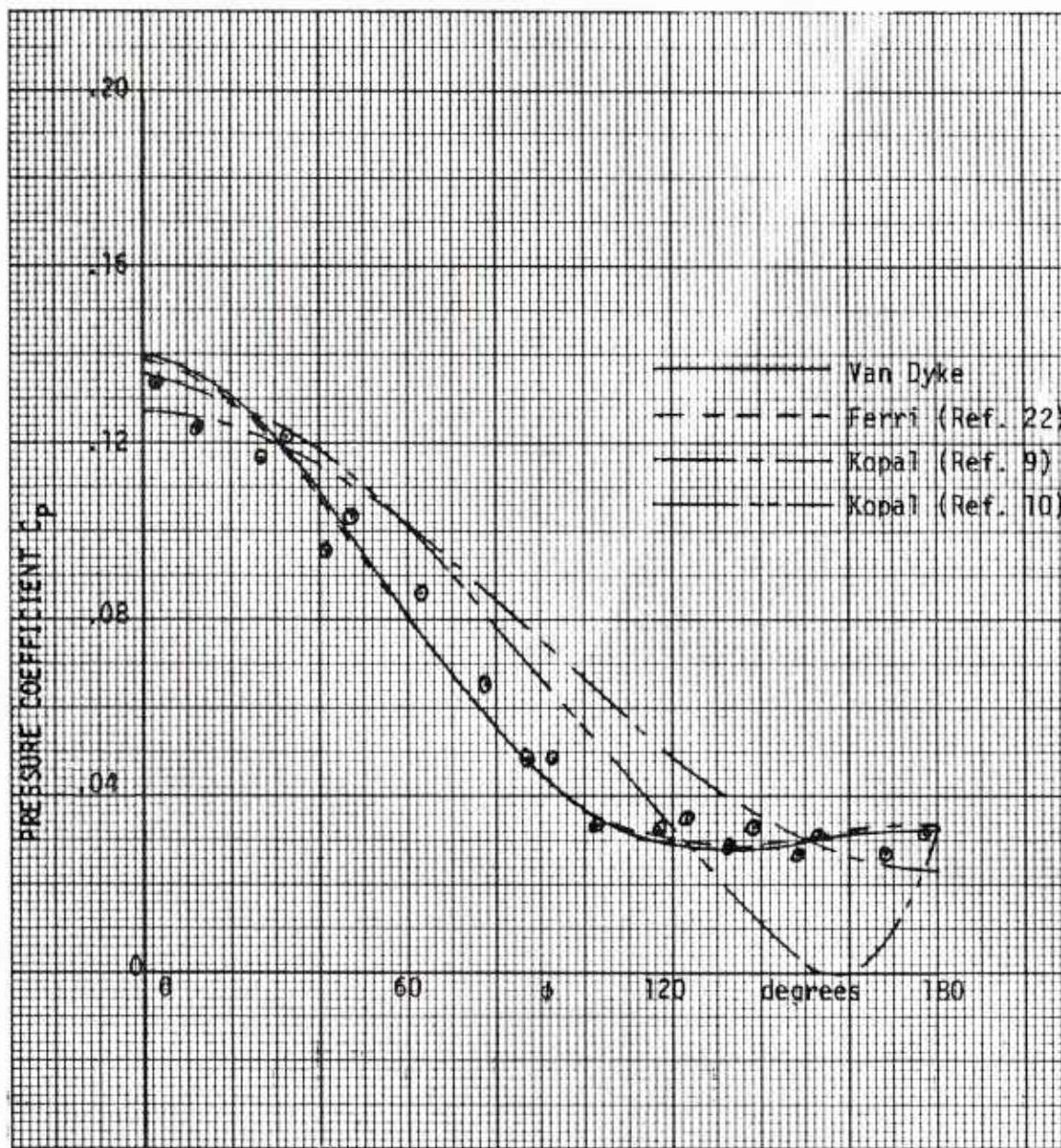


FIG. 11 - Comparison of Experimental Pressure Distribution with Theoretical Curves for Various Azimuth Angles  $\phi$  at Angle of Incidence  $\alpha = 6$  Degrees

## Paper No. 5

COMPACT GAS-TRANSPIRATION COOLING SYSTEM ANALYSIS  
(U)

(Paper UNCLASSIFIED)

by

R. W. Allen and R. W. Newman  
Applied Physics Laboratory  
The Johns Hopkins University  
Silver Spring, Md. 20910

ABSTRACT (U) Gas-transpiration cooling is capable of providing a controllable and re-usable means of protecting critically heated surfaces of high-speed flight vehicles. In future system installations made under tight space restrictions, lateral coolant motion will be superimposed on the coolant motion toward the permeable wall of the plenum chamber. We call this space-restricted system "compact" in order to distinguish it from systems equipped with large plenum chambers. A meaningful thermal analysis must couple the variables of the compact gas-transpiration system to external radiation and aerodynamic heating of the prescribed flight. This is accomplished through a flexible, multi-noded computer program which allows external heating influences to act on lateral coolant pressure and temperature in the compact plenum chambers of candidate compact transpiration systems. Internal coolant pressure and temperature distributions in turn govern the blowing effects on aerodynamic heating and permeable wall heat conduction. The necessary terms are included in the governing equations processed by the computer program. Special compact-plenum experiments were made to determine plenum-coolant pressure drop and momentum-change parameters associated with lateral flow. By Reynolds analogy, the corresponding compact coolant channel heat transfer from the wall to the gas was inferred.

## INTRODUCTION

Although gas-transpiration cooling has been researched in considerable detail (Reference 1), its use in thermal protection service is limited. It can be said however, that gas-transpiration cooling systems, like ducted cooling systems, have promise where cooling rate control, system re-usability, or geometry preservation are significant considerations. When compared to ducted cooling systems, gas-transpiration cooling systems are inherently capable of making more effective use of on-board coolant reserve because of the external blocking effect.

Up to the present time it appears that existing and proposed gas-transpiration systems have employed amply-sized plenum chambers coupled to a sufficient number of feeder lines so that spatial variations in coolant pressure and temperature in the plenum were virtually precluded. However in future installations (e.g. leading edges) where critically heated structural elements will provide less and less space for plenum passages, the necessity of designing for and operating with reduced plenum size must be considered. At the same time, tighter space restrictions will undoubtedly limit the number of coolant feeder lines. When plenum chambers are sized and operated under these space restrictions, characteristic pressure and temperature distributions will develop in the plenum coolant and the thermal task will revolve around the determination of these distributions and their interaction with the external heating load.

The foregoing considerations have led to a design concept called the compact gas-transpiration cooling system (Reference 2) wherein passages simultaneously serve as plenum chambers and as ducts or channels to convey coolant to more distance downstream points. For analytical purposes, a computer program has been devised which handles compact plenum heat and mass flows in conjunction with external thermal radiation, aerodynamic heating and structural heat conduction. The program is multi-noded and provides for a variety of thermal interconnections between the flight environment, the flight vehicle, and coolant conditions within the compact plenum. The following account describes the finite-difference engineering heat and mass transfer relations used in formulating the computer program. Also described are special compact-plenum experiments which were performed to determine the effect of negative blowing on channel flow in a bench-test model. These experiments were necessitated by the lack of

published information on the channel-flow case. Future plans are indicated at the conclusion of this paper.

## NOMENCLATURE

A	area
B	blowing parameter
Bi	Biot number $h\delta/k$
$c_p$	specific heat
C	thermal capacitance
D	hydraulic diameter
f	skin-friction coefficient
F	configuration factor
Fo	Fourier number $\alpha\theta/\delta^2$
g	transpiration parameter $\dot{m}c_p\delta/kA$
h	heat transfer coefficient
H	enthalpy
k	thermal conductivity
$K_p$	permeance
L	length
m	ratio of coolant mass flux to free stream mass flux
$\dot{m}$	transpiration mass flow
$\dot{M}$	channel mass flow
M	molecular weight
N	a constant
P	pressure
Q,q	heat flow
r	recovery factor
Re	Reynolds number
St	Stanton number
T	temperature
t	time
u	stream velocity



### Vol. 1

$v$	velocity normal to walls
$w$	width of transpiring section
$x$	external distance downstream
$\Delta x$	axial length of control volume

### GREEK LETTERS

$\alpha$	a constant or thermal diffusivity
$\beta$	flow-geometry factor
$\delta$	slab thickness
$\epsilon$	emittance
$\theta$	elapsed time
$\eta$	film cooling effectiveness
$\mu$	absolute viscosity
$\Phi, \psi$	functions
$\rho$	density
$\sigma$	Stefan-Boltzmann constant
$\tau$	shearing stress

### SUBSCRIPTS

$a$	air
$aw$	adiabatic wall
$b$	bulk
$c$	average coolant gas at external porous surface
$f$	friction
$g$	coolant gas
$H$	enthalpy
$in$	inside surface or entrance
$i, j$	entrance and exit of compact-plenum gas control volume
$m$	matrix
$o$	no blowing or no film cooling
$out$	external surface of porous wall
$r$	radiation
$s$	subsurface
$St$	Stanton number

st        static  
w        wall  
w,a      wall, apparent

## SUPERSCRIPTS

o        no blowing

## THE COMPACT GAS-TRANSPIRATION SYSTEM

In order to establish the physical nature of a typical problem, we consider a hypothetical leading edge in flight. The cross section view of Figure 1 shows an oncoming external flow passing through a shock wave and forming an aerodynamic boundary layer on a flight body. The severely heated part of the leading edge in Figure 1 is fabricated from a permeable porous metal, with the permeable segment backed up by a compact plenum. The latter is shown as a simple cylindrical flow passage running in the spanwise direction along the leading edge. Portions of the stream of gaseous coolant flowing axially in the compact plenum are forced into and through the permeable wall by the pressure being maintained in the plenum. The passing of coolant mass from the main stream into the wall is usually called suction but the term negative blowing generally leads to a clearer understanding of the process with respect to channel flow in the plenum. After coolant penetrates the permeable wall, it transpires through it and emerges on the external side. Here it produces the well-known blowing effect which tends to block the incoming aerodynamic heat load. This action will be called positive blowing. Blown coolant merges with, and develops along the external permeable surface up to its juncture with the solid external wall. There, a film-cooling region begins and thereafter the cooling effect dies out as the boundary layer is followed further aft.

Overall, a compact gas transpiration system is made up of components shown in Figure 2. Coolant flow can be traced from the reservoir into supply piping, through the coolant flow-control device, and into the compact plenum where it flows spanwise inside the leading edge. Of foremost concern is the fact that spanwise variations in the positive blowing rate and spanwise variations in temperature will occur as the blown coolant emerges from the leading edge. They will be functions of internal coolant pressure and temperature distribution along the compact-plenum flow axis as well as the external spanwise pressure and heat load variation. The primary goal of the present analysis is to develop a method for determining the internal pressure and temperature distributions and their effect on external thermal protection performance.

### PROBLEM DEFINITION AND FINITE DIFFERENCE SCHEME

A proposed compact gas-transpiration system layout together with the local structural configuration of the flight body constitutes the region of analytical interest. About this region of interest, specified unsteady flow and thermal conditions are given in terms of flight time. The initial thermal condition of the flight body is prescribed. A specification is made of exactly how the coolant mass-flow control device is to operate and the gas flow resistance characteristics of the porous wall are assumed to be known. Structural material and coolant thermal properties, specified as a function of temperature, complete the definition of the problem.

In analogic terms we can say that the mathematical model consists of an array of network nodal plug-in points and electric conductance elements which can be plugged in between any pair of nodes. Some, but not all, nodes are permanently connected to grounded capacitors. These capacitors are set to the thermal capacitance values of corresponding regions of flight-body material while conductances are chosen to agree with the thermal conductance value for the internodal path in question. Provisions are made for temperature dependency of both thermal capacitance and thermal conductance. Many other nodes are not connected to grounded capacitors. These are used for surface, external air, radiation, and internal coolant gas temperatures. No capacitance is required for air duct coolant because gases are invariably found to have negligible thermal capacitance when compared to the flight-body material. External aerodynamic heat transfer is introduced in an engineering form by calculating the local thermal conductance corresponding to the local external convective heat transfer coefficient of the boundary layer. At those points where external heat transfer takes place between the boundary layer and a permeable surface, the heat transfer coefficient is reduced in proportion to the blocking effect of positive blowing. Nodes for coolant gas temperatures in flow passages receive a net coolant enthalpy influx. They are also connected to thermal conductances corresponding to local pipe-flow heat transfer coefficients. At points on the permeable surface of the compact plenum, the convective heat transfer coefficient is increased in proportion to the effect of negative blowing.

In addition to heat transfer calculations, coolant mass-flow distribution over the positively blown external surface is determined by satisfying the continuity equation and momentum equation of fluid mechanics throughout the coolant piping system and permeable medium.

A grid of pressure nodes is established in the coolant piping system. Coolant pressure values, consistent with the governing equations, are computed in an iterative process.

### EXTERNAL FLOW AND SURFACE HEAT TRANSFER

External flow conditions are specified in terms of the Mach number, pressure, and temperature of the oncoming flow (Figure 1) as a function of flight time. Local flow conditions between the shock wave and boundary layer are calculated at points opposite each surface node. This provides the adiabatic wall enthalpy needed to make the energy balance on a non-capacitive surface area. Figure 3 depicts the energy-balance procedure schematically with respect to surface (1) located on the permeable blowing surface. Letting subscript 1 denote a condition evaluated at the surface, we have the following energy equations with respect to surface (1), Figure 3

$$Q_{\text{rad, in}} = \sigma A_1 \epsilon F_{r1} (T_r^4 - T_1^4) \quad (1)$$

$$Q_{\text{convection in}} = h_{H1} A_1 (H_{\text{aw},1} - H_1) \quad (2)$$

$$Q_{\text{conduction out}} = k_{1s} \frac{A_1}{L_{1s}} (T_1 - T_s) \quad (3)$$

External boundary-layer heat transfer coefficient  $h_H$  is the net value after the positive blowing effect has been included in accordance with Eckert's (Reference 3) recommendation

$$h_H = h_H^\circ \left\{ 1 - \Phi \left[ \frac{\dot{m}_g}{A} \times \frac{\sqrt{1-\beta/2}}{h_H^\circ} \times \left( \frac{M_a}{M_g} \right)^N \right] \right\} \quad (4)$$

Likewise, the adiabatic wall enthalpy  $H_{\text{aw}}$  is computed from a recovery factor which is the net value after the positive blowing effect has been included (Reference 3).

$$r = r^\circ \left\{ 1 - \Psi \left[ \frac{\dot{m}_g}{A} \times \frac{\sqrt{1-\beta/2}}{h_H^\circ} \times \left( \frac{M_a}{M_g} \right)^N \right] \right\} \quad (5)$$

Both functions  $\Phi$  and  $\Psi$  usually have a linear dependency on the positive blowing rate  $\dot{m}_g$ . Later on we shall see how the positive coolant blowing

Vol. 1

rate  $\dot{m}_g$  is computed when continuity and momentum-law principles are applied to coolant flow in the compact plenum and in the porous matrix.

Following the external boundary layer along the porous surface to the solid surface, we encounter a region of film cooling where

$$H_{aw} = H_{aw}^{\circ} - \eta_H (H_{aw}^{\circ} - H_c) \quad (6)$$

gives the necessary change from the non-film-cooled adiabatic wall enthalpy  $H_{aw}^{\circ}$  to the film cooled value  $H_{aw}$ . According to Goldstein, Shavit, and Chen (Reference 4) the film-cooling effectiveness downstream from a porous section is most accurately predicted by the Kutateladze and Leont'ev (Reference 5) relation

$$\eta_H = \left[ 1 + 0.24 \frac{x}{mw} \left( \frac{\dot{m}_g w}{\mu_g A} \right)^{-0.25} \right]^{-0.8} \quad (7)$$

In the film cooling method, no adjustment is made in the local heat transfer coefficient computed from local flow conditions.

#### INTERNAL HEAT CONDUCTION AND TRANSPIRATION

An imaginary element buried in the transpired porous leading edge receives net heat flow by net heat conduction and net coolant enthalpy flow into the control region defining the element. Figure 3 depicts a porous element (2) and the schematic energy flows with respect to its control surfaces. Thermal energy is stored in the element by virtue of the thermal capacitance of the metal matrix. Turning to Figure 3 we can show the energy balance on permeable element (node) (2) in more detail. One-dimensional heat flow sufficiently portrays the basic terms as follows

$$\begin{aligned} & k_m \frac{A_{12}}{L_{12}} (T_1 - T_2) + k_m \frac{A_{23}}{L_{23}} (T_3 - T_2) + \dot{m}_g c_{pg} (T_{ag} - T_{bg}) \\ & = C_2 \frac{T'_2 - T_2}{\Delta t} \end{aligned} \quad (8)$$

where subscripts 1, 2, and 3 correspond to three adjacent permeable elements numbered in ascending order in the direction of gas flow and where gas enters element 2 at  $T_{ag}$  and leaves at  $T_{bg}$ . We use an explicit form with nodal temperature  $T_2$  occurring at the beginning of time interval  $\Delta t$  and  $T'_2$  occurring after  $\Delta t$  has elapsed. It will be noted that we have assumed that the coolant gas (subscript g) does not contribute to heat conduction or thermal capacitance but does give

rise to the net enthalpy inflow  $\dot{m}_g c_{pg} (T_{ag} - T_{bg})$ . Only in exceptional cases will porous passages be large enough to require that we differentiate between the local temperature of the transpiring gas on the one hand and the local temperature of the passage walls (i.e. matrix temperature) on the other. That is, in the majority of cases

$$T_{ag} = T_a \text{ and } T_{bg} = T_b \quad (9)$$

where, for equally sized elements, entering and leaving coolant temperatures are the average internodal temperatures of the matrix

$$T_a = \frac{T_1 + T_2}{2} \text{ and } T_b = \frac{T_2 + T_3}{2} \quad (10)$$

For unequally sized elements we introduce geometric weighting coefficients. The energy balance on impermeable wall elements has the same form as equation (8) with the coolant term removed.

#### COOLANT PRESSURE AND TEMPERATURE IN PLENUM AND PIPING

The continuity condition on gaseous coolant flow in the compact plenum is illustrated with respect to a finite control volume in Figure 4. The negative-blowing mass flux (3) leaving the side wall of cylindrical control volume (4) depletes the main stream flowing in the compact plenum. Letting subscripts i and j denote channel flow conditions at entrance and exit circular faces of control volume (4), respectively, we have the finite-difference equation

$$\dot{M}_i - \dot{M}_j = \dot{m}_g \quad (11)$$

Where  $\dot{m}_g$  is negative blowing with respect to control volume (4). As in boundary layer flow, mass storage in the control volume is negligible for typical density change rates. The negative blowing mass flux enters porous wall segment (2), Figure 4, in the pores of which transpiration flow is also essentially steady. In most systems, transpiration through the porous wall is nearly one-dimensional, hence it suffices to divide the segment into prescribed channels leading from the compact plenum to the external surface. Thus, by continuity the negative blowing mass flux  $\dot{m}_g$  is equal to the sum of flows to those channels fed by the side wall of control volume (4).

The momentum equation of channel flow in a compact plenum with negative blowing must include the effect on wall friction and momentum, produced by motion of gas toward the porous wall. Figure 4 depicts the principal terms. The corresponding finite-difference equation is



$$(P_i - P_j)A + (\dot{M}_i u_i - \dot{M}_j u_j) - \left( \frac{2 \bar{f} \dot{M} u \Delta x}{D} \right)_{\text{axial mean}} = 0 \quad (12)$$

The bar over the wall friction factor indicates the averaging of friction effects over both solid-wall and porous-wall zones about the cylindrical periphery of the control volume. The skin friction effect in porous wall zones is physically increased by the action of negative blowing which causes the stream-wise velocity profile of turbulent flow to fill out near the wall. That is, the coefficient  $\bar{f}$  in equation (12) is numerically greater than the coefficient  $f^\circ$  without blowing and at the same channel-flow Reynolds number. Experiments to be discussed later show that a modified form of an equation due to Mickley, et al (Reference 6), namely

$$\left( \frac{\bar{f}}{f^\circ} \right)_{\text{At a given channel Re}} = \frac{B_f}{B_f - 1} \quad (13)$$

is applicable. We call  $B_f$  the blowing parameter for friction and define it as a measure of the ratio of the blowing velocity  $v_w$  (which has a negative value for negative blowing) to the main stream bulk velocity  $u_b$  by the relation

$$B_f = \frac{2v_w}{u_b f^\circ} \quad (14)$$

As the blowing parameter becomes small, a linear approximation to equation (13)

$$\frac{\bar{f}}{f^\circ} = 1 - \frac{1}{2} \frac{2v_w}{u_b f^\circ} \quad (15)$$

can be found. We would then say that the dimensionless friction blowing factor was 1/2 in turbulent channel-flow.

Negatively blown coolant gas passes into the porous matrix (2), Figure 4, where the pressure-drop associated with coolant flow through interconnected pores depends primarily on the permeability coefficient of the matrix. If flow through interconnected pores is laminar, incompressible, and isothermal, the coefficient of permeability is a constant and the pressure field of transpiration flow obeys Darcy's law. In practice however, flow through interconnected pores is turbulent and compressible. Flow is also non-isothermal due to spatial and time variations in temperature associated with the transient heat transfer processes. Under these complex conditions it is appropriate to make use of the fact that transpiration flow is predominantly one dimensional and to employ a modified form of Darcy's law

$$\dot{m}_g = K_p (P_{in} - P_{out})^\alpha \quad (16)$$

relating local transpiration mass flow  $\dot{m}_g$  to the overall pressure drop in a prescribed local flow direction. The wall permeance  $K_p$  and the exponent  $\alpha$  are determined from available information on the matrix in question including laboratory permeance measurements.

The energy equation of channel flow in the compact plenum accounts for the net total-enthalpy flow into a finite control volume (4), Figure 3, and heat transfer across the cylindrical portion of the control surface. The latter is taken to be in contact with the plenum wall and bar is placed over the Stanton number to indicate averaging over the cylindrical portion of the control surfaces. Thus the energy equation for control volume (4) is

$$\begin{aligned} \dot{m}_i \left( H_i + \frac{u_i^2}{2} \right) - \dot{m}_j \left( H_j + \frac{u_j^2}{2} \right) - \dot{m}_g \left( H_w + \frac{v_w^2}{2} \right) \\ + \left( \frac{4\bar{St} \dot{M}_c \Delta x}{D} \right) (\bar{T}_w - \bar{T}_g) = 0 \end{aligned} \quad (17)$$

axial mean

where  $H_w$  denotes the average enthalpy of negatively blown coolant leaving the control volume and entering the porous wall. As in the case of the skin friction coefficient  $f$ , the Stanton number  $St$  is evaluated in the presence of negative blowing. Although channel-flow data are not available on the Stanton number with negative blowing, Reynolds' analogy suggests that a slightly modified form of Mickley's (Reference 6) equation

$$\left( \frac{St}{St^\circ} \right)_{\text{Fixed Channel Re}} = \frac{B_{St}}{B_{St} - 1} \quad (18)$$

is applicable. We call the parameter  $B_{St}$  the blowing parameter for heat transfer and define it by the relation

$$B_{St} = \frac{v_w}{u_b St^\circ} \quad (19)$$

where  $St^\circ$  is the Stanton number of unblown flow. In gas flows for which Reynolds analogy

$$St^\circ \approx \frac{f^\circ}{2} \quad (20)$$

## Vol. 1

holds we conclude that  $B_f$  and  $B_{st}$  are numerically the same. As noted in the discussion of friction, a linear approximation

$$\frac{St}{St^\circ} = 1 - \frac{1}{2} \frac{v_w}{u_b St^\circ} \quad (21)$$

is applicable at low blowing rates. We would then say that the dimensionless heat transfer blowing factor was 1/2 in turbulent channel-flow. Because of Reynolds' analogy, the value is the same as for friction. The value of 1/2 for turbulent channel flow can be compared to Eckert's (Reference 3) recommended value of 0.37 for turbulent boundary-layer flow.

## COMPACT-PLENUM FLOW EXPERIMENTS

Although Mickley et al (Reference 6) experimented with negative blowing effects on boundary-layer flow and Tennekes (Reference 7) has recently obtained improved results, there is no literature dealing with negative blowing effects on the skin friction and heat transfer of channel flows. For this reason a somewhat idealized but basic compact-plenum bench test apparatus was devised. As shown in Figure 5 in part (a) the basic apparatus was a porous tube test section. The tube was 0.4 inch o.d., 0.160 i.d. porous sintered stainless steel, of 1 to 1 1/2 micron pore size and 15% porosity. The tube shown in part (a) of Figure 5 was about 8 inches long. It was supplied from the left with metered, clean, dry, room-temperature nitrogen gas. A sliding pressure probe on the axis was used to determine the streamwise static pressure distribution. A sliding collection chamber, part (b) of Figure 5, was used to measure the streamwise variation in the negative blowing rate.

Tests were first conducted with the tube wrapped to prevent negative blowing. Basic no-blowing skin friction coefficients  $f^\circ$  were determined by computing the net pressure force and momentum change. The resulting plot of  $f^\circ$  versus Reynolds number indicated friction was about 10% above the smooth annulus  $f^\circ$  value. This difference was attributed to surface roughness.

Tests were next conducted with the wrapping removed. The measured streamwise variations of negative blowing rate and static pressure were used in calculations of the coefficient of skin friction  $f$  at ten local points along the flow axis. The local skin friction ratio  $f/f^\circ$  was then formed and plotted against each of three different negative blowing (suction) parameters. The three parameters were taken from the boundary layer literature and modified by replacing free-stream velocity with bulk velocity. The three parameters are

$\frac{v_w}{u_b}$	(Olsen and Eckert (Reference 8) positive blowing pipe-flow experiments)
$\frac{v_w}{u_b} \sqrt{\frac{2}{f^\circ}}$	(Tewfik (Reference 9), boundary layer experiments, and Rannie (Reference 10), sublayer theory)
$\frac{v_w}{u_b} \frac{2}{f^\circ}$	(Mickley et al (Reference 6), boundary layer experiments)

Figures 6, 7, and 8 show a progressive improvement in correlation of the results as  $f^\circ$  plays a stronger role in the blowing parameter. Figure 8 shows how well the modified film theory equation of Mickley fits the results of these tests. For engineering purposes, we conclude that negative blowing effects on axisymmetric channel flow are covered by the modified Mickley equation

$$\frac{f}{f^\circ} = \frac{B_f}{e^{B_f} - 1} \quad (22)$$

It has already been pointed out that equation (22) reduces to the linear form

$$\left. \frac{f}{f^\circ} \right|_{\text{small } B_f} = 1 - \frac{1}{2} B_f \quad (23)$$

at low negative blowing rates. This relation is obtained by differentiating equation (22) to find the slope at  $B_f = 0$ . Large negative blowing rates cause the exponential term to drop out of the denominator of equation (22) thus  $f/f^\circ$  is asymptotic to  $-B_f$ , i.e.

$$\left. \frac{f}{f^\circ} \right|_{\text{Large negative } B_f} = -B_f \quad (24)$$

This also follows if we accept the premise, based on turbulent boundary layer experimental evidence, that large negative blowing rates cause the  $u$ -velocity profile of two-dimensional channel flow to approach the slug profile shape. For such an asymptotic channel-flow velocity profile shape, the sidewise momentum transport to the channel wall is  $-\rho v_w u_b$  per unit wall area. The apparent shearing stress  $\tau_{w,a}$  is defined by the relation

## Vol. 1

$$\tau_{w,a} = \frac{f \rho u_b^2}{2} \quad (25)$$

Assuming that apparent shear overshadows viscous shear we find the skin friction coefficient with negative blowing,

$$f = - \frac{2v_w}{u_b} \quad (26)$$

Thus

$$\left. \frac{f}{f^\circ} \right|_{\substack{\text{Asymptotic} \\ \text{slug profile}}} = - \frac{2v_w}{u_b f^\circ} \quad (27)$$

where the right hand side is  $-B_f$ , by definition.

The heat transfer relation follows from the above discussion by establishing the asymptote based on sidewise energy transport  $-\rho v_w c_p (T_b - T_w)$  per unit wall area and the definition

$$-q_w = St (\rho u_b c_p) (T_w - T_b) \quad (28)$$

By equating the energy transport to  $-q_w$  and dividing this by  $St^\circ$  we find

$$\left. \frac{St}{St^\circ} \right|_{\substack{\text{Asymptotic} \\ \text{slug profile}}} = - \frac{v_w}{u_b St^\circ} \quad (29)$$

By similar arguments, the overall trend of channel flow experiments can be expected to follow the prediction of Mickley et al (Reference 6) as modified for channel flow, i.e.

$$\frac{St}{St^\circ} = \frac{B_{St}}{B_{St} - 1} \quad (30)$$

The experimental friction apparatus can be instrumented as shown in parts c and d of Figure 5 to test this theory on an electrically heated apparatus. Such work is planned for the future.

## COMPUTER PROGRAM VALIDATION

At present there are no test data available by means of which the entire computer program might be checked out. It is essential that this be done and future work is aimed at that goal. Meanwhile, as each portion of the program has been completed, its successful operation has been proven out by check runs confined to the portion of the program in question.

The first example of program check out is the computation of transient temperatures in a transpiration cooled porous matrix. An initially isothermal transpiring plane porous slab, Figure 9, is supplied at one face with coolant at a fixed temperature. The sudden application of convective heating at the other face causes the outer face temperature to rise and reach an equilibrium value, Figure 10. Temperature rise of the outer face is plotted against the Fourier number of the slab for one value of the Biot number and two values of the transpiration parameter  $g$ . Plotted points portray computer results which, because of the actual temperatures used, reflect the reference temperature effect on the otherwise constant convective coefficient. When Schneider's (Reference 11) theoretical results are adjusted downward to reflect the changing Biot number the agreement is seen to be very good. On this basis the finite-difference energy portions of the program involving transpiration effects were judged to be working satisfactorily.

The interaction of the coolant continuity equation, the momentum equation, and the modified version Darcy's law were checked out in a computer run utilizing actual test data from the compact plenum apparatus previously described. In this run, the known local permeance characteristics of the wall of the porous tube were fed into the program along with the modified Mickley equation governing the negative blowing effect. The program run then computed the negative blowing (radial mass flow  $\dot{m}$ ) from Darcy's law and the static pressure distribution in the compact plenum chamber. In Figure 11, the close agreement between computed radial mass flows (negative blowing rates) and measured values is due to the fact that input permeance values were based on the test measurements. The close prediction of static pressure distributions in the compact plenum is an indication of the reliability of the modified Mickley equation and of the reliability of the finite differencing and iterative schemes involved in the channel-flow portions of the program.



### Vol. 1

The bulk temperature of the coolant main stream in a compact plenum cannot be measured locally without upsetting conditions further downstream. However some unreported external porous surface temperatures have been measured in the laboratory and calculated by means of the computer program. The results indicate that the computer program is performing consistently and as designed. Discrepancies between computed and measured values are undoubtedly due to the difficulty of developing meaningful surface temperature measurement techniques for porous wall models. More intensive work in this area is planned for the future.

Film cooling computer-program procedures have been checked out against the downstream measurements of Goldstein, Shavit and Chen (Reference 4) using the effectiveness equation of Kutateladze and Leont'ev (Reference 5) and the finite-difference model. Results for the model shown in Figure 12 are presented in Figure 13 and indicate satisfactory performance of the computer program.

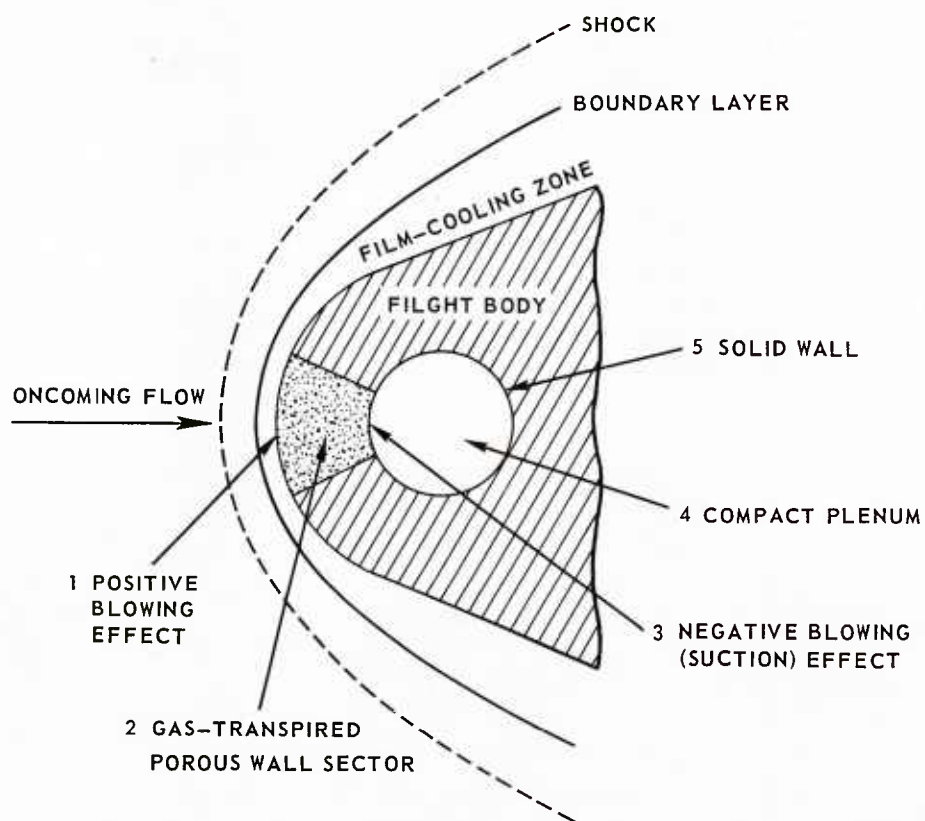
### FUTURE PLANS

In order to prove out the computer program, an instrumented wind-tunnel test model of a compact system will be designed and tested under controlled conditions. The controlled conditions will correspond to those described under "Problem Definition". They will provide the necessary inputs to the computer program along with model specifications. Instrumentation will give readings of key body temperatures and coolant pressures against which computed values will be compared.

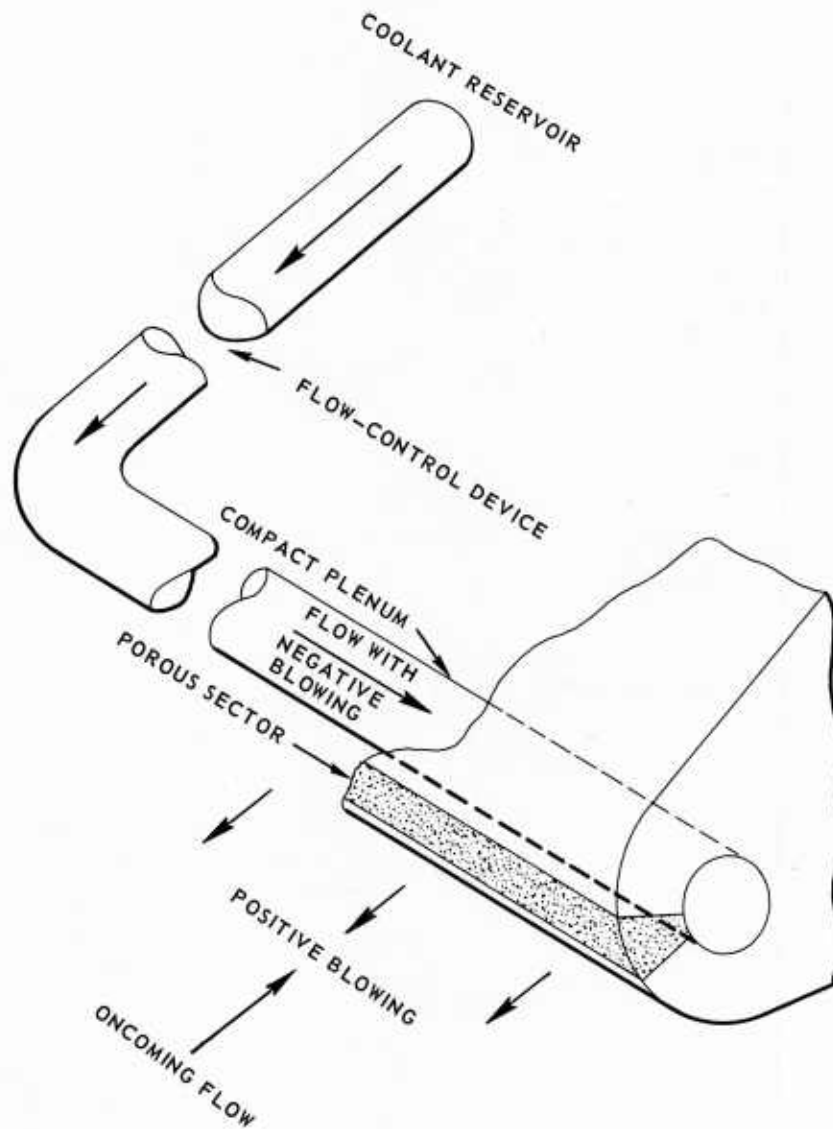
### REFERENCES

1. Jet Propulsion Center. Transpiration Cooling - Its Theory and Application, by J. B. Kelly and M. R. L'Ecuyer. Purdue University, June 1966. (Report No. TM 66-5, publication Unclassified).
2. Applied Physics Laboratory, Johns Hopkins University. Transient Heat Transfer Calculation Procedures for Gas Transpiration Cooling with Compact Systems (U), by R. W. Allen. Silver Spring, Md., August 1965. (TG-723, publication Confidential).
3. Wright Air Development Center. Survey of Boundary Layer Heat Transfer and High Velocities and High Temperatures, by E. R. G. Eckert. University of Minnesota, April 1960. (WADC Technical Report 59-624, publication Unclassified).

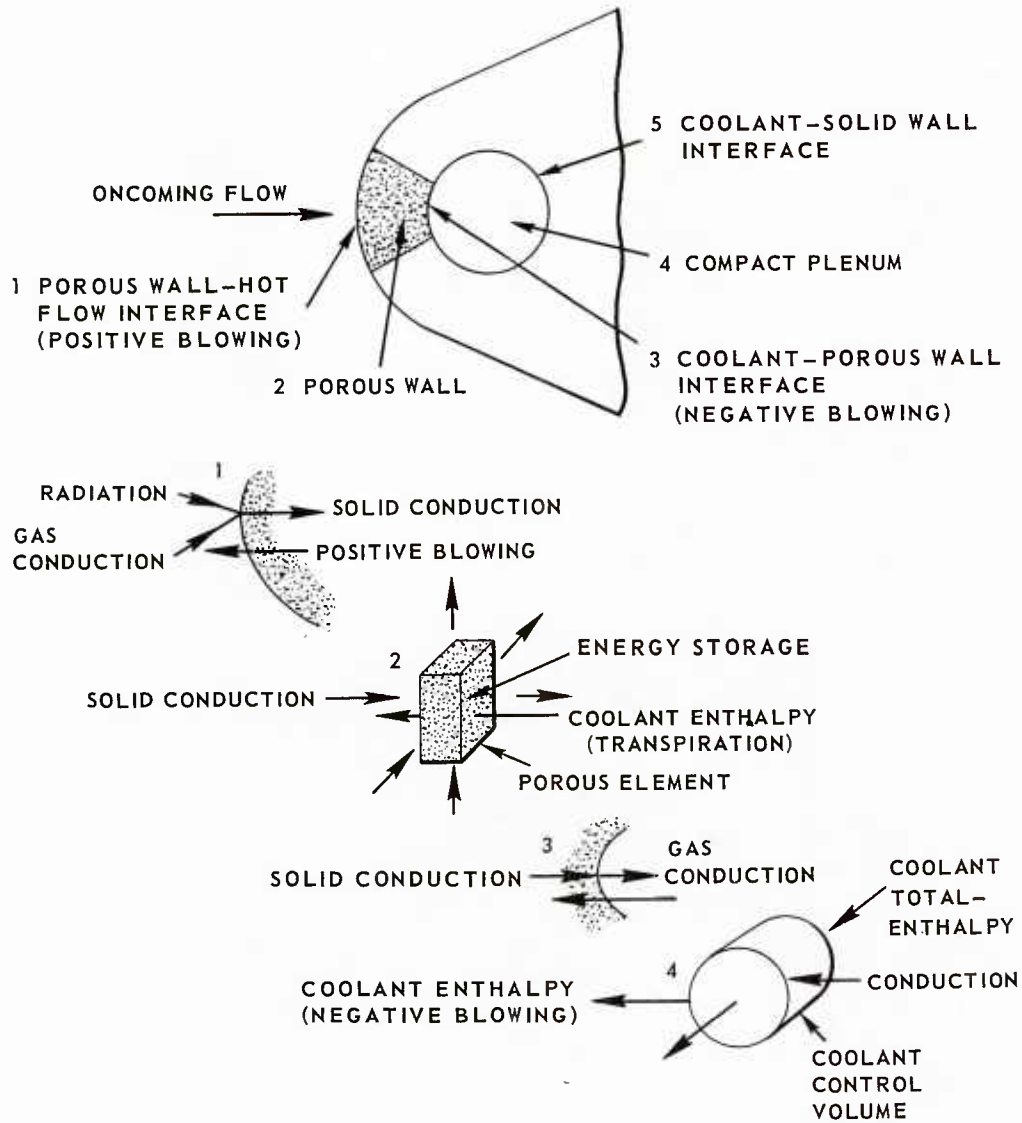
4. Journal of Heat Transfer. Film Cooling Effectiveness with Injection Through a Porous Section, by R. J. Goldstein, G. Shavit, and T. S. Chen. University of Minnesota, August 1965. 353-361 pp. (Vol. 87, Series 6, publication Unclassified).
5. Translated from Telpofiziko Vysokikh Temperature. The Heat Curtain in the Turbulent Boundary Layer of a Gas, by S. S. Kutateladze and A. I. Leont'ev. September-October 1963 (Vol. 1, No. 2, publication Unclassified).
6. National Advisory Committee of Aeronautics. Heat, Mass, and Momentum Transfer for Flow Over a Flat Plate with Blowing or Suction, by H. S. Mickley, R. C. Ross, A. L. Squyers, and W. E. Stewart. Massachusetts Institute of Technology, July 1954. (TN-3208, publication Unclassified).
7. Journal of Fluid Mechanics. Similarity Laws for Turbulent Boundary Layers with Suction or Injection, by H. Tennekes. Technological University, Delft, The Netherlands, July 1964. 689-703 pp. (Vol. 2, Part 4, 1965, publication Unclassified).
8. Journal of Applied Mechanics. Experimental Studies of Turbulent Flow in a Porous Circular Tube with Uniform Fluid Injection Through the Wall, by R. M. Olsen and E. R. G. Eckert. University of Minnesota, 1966. 7-19 pp. (Transactions of ASME, Vol. 88, Series E, publication Unclassified).
9. American Institute of Aeronautics and Astronautics. Some Characteristics of the Turbulent Boundary Layer with Air Injection, by O. E. Tewfik. June 1963. 1306 pp. (Vol. 1, No. 6, publication Unclassified).
10. Jet Propulsion Laboratory. A Simplified Theory of Porous Wall Cooling, by W. D. Rannie. November 1947. (Progress Report No. 4-50, publication Unclassified).
11. John Wiley & Sons, Inc. Temperature Response Charts, by P. J. Schneider. New York, New York, 1963. (publication Unclassified).



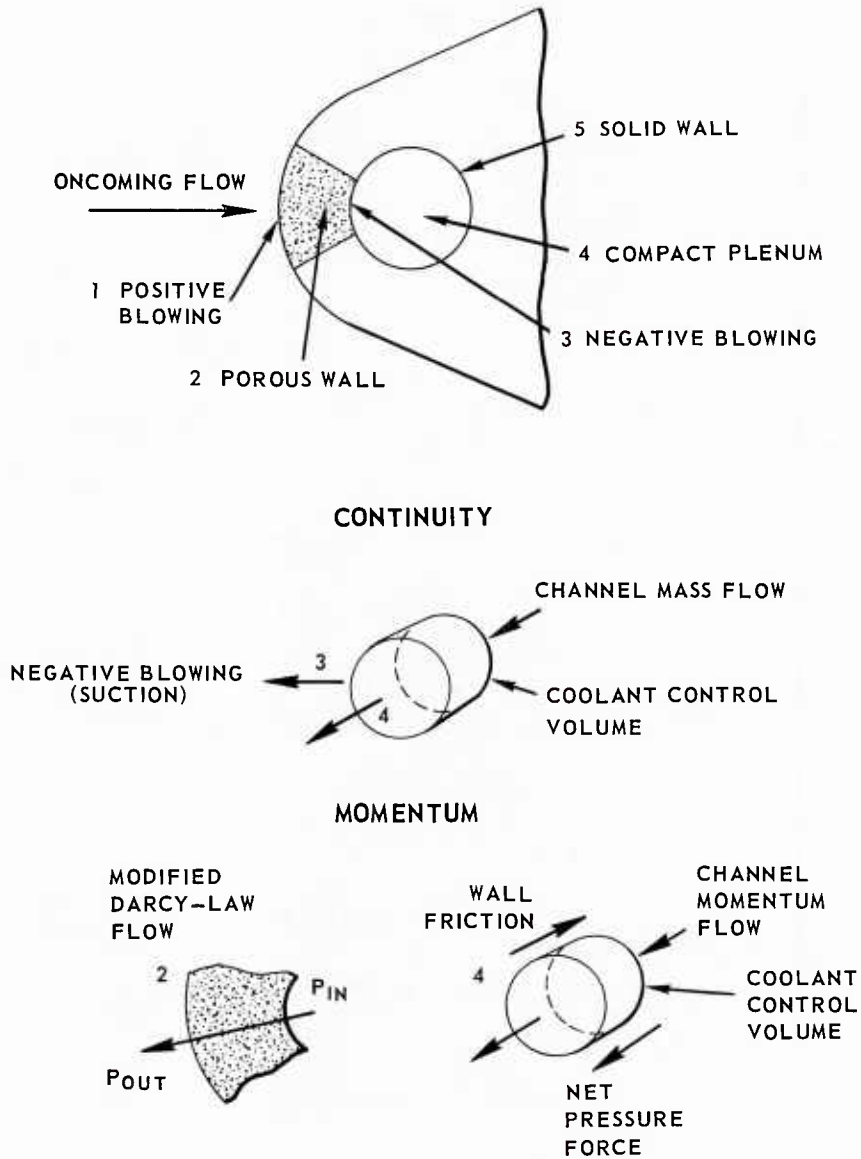
(U) Fig. 1 A LEADING-EDGE COMPACT-PLENUM INSTALLATION IN FLIGHT



(U) Fig. 2 BASIC ELEMENTS OF A COMPACT GAS-TRANSPIRATION SYSTEM

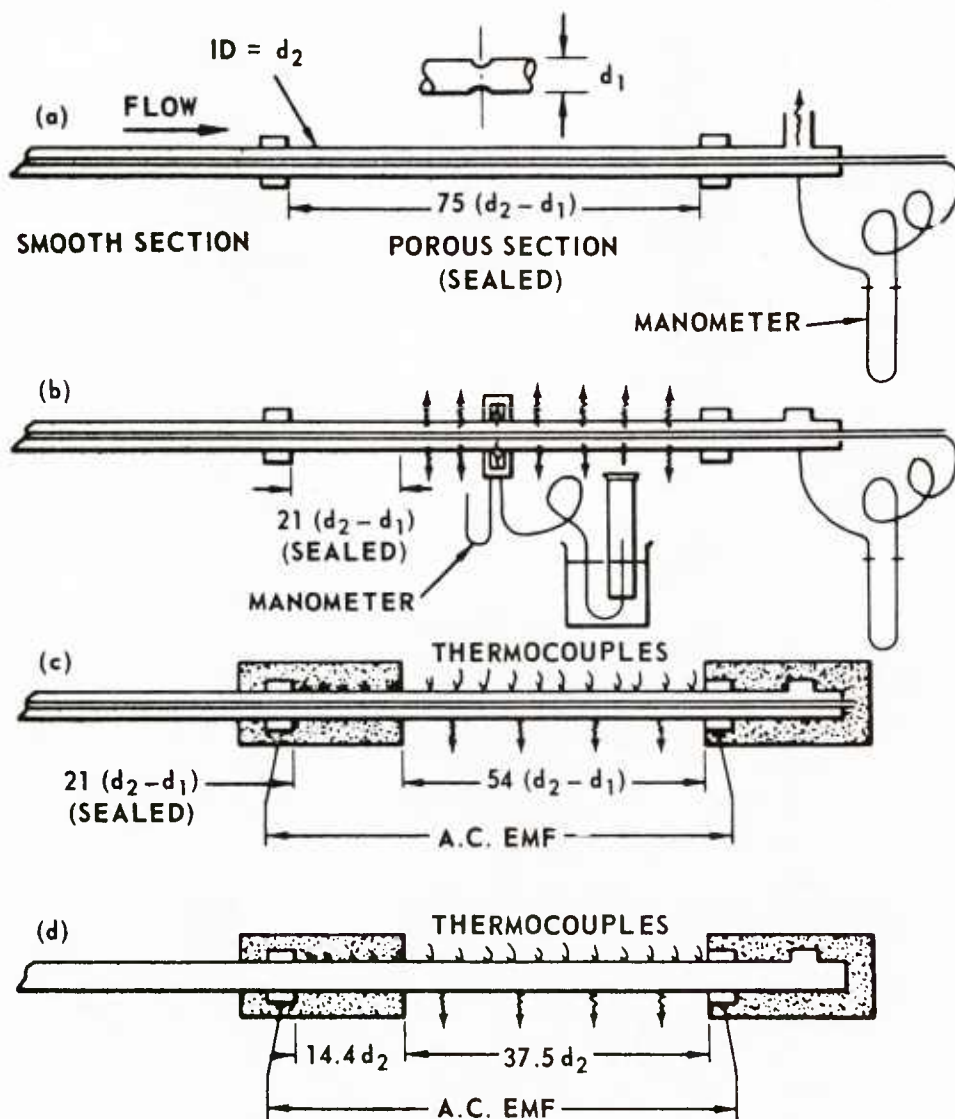


(U) Fig. 3 BASIC APPROACH TO ENERGY RELATIONS

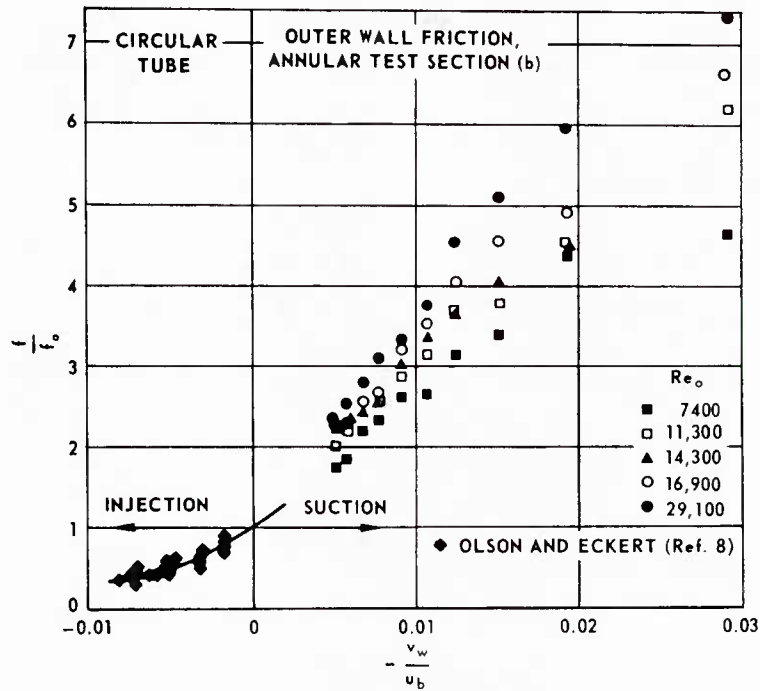


(U) Fig. 4 BASIC APPROACH TO COOLANT CONTINUITY AND MOMENTUM RELATIONS

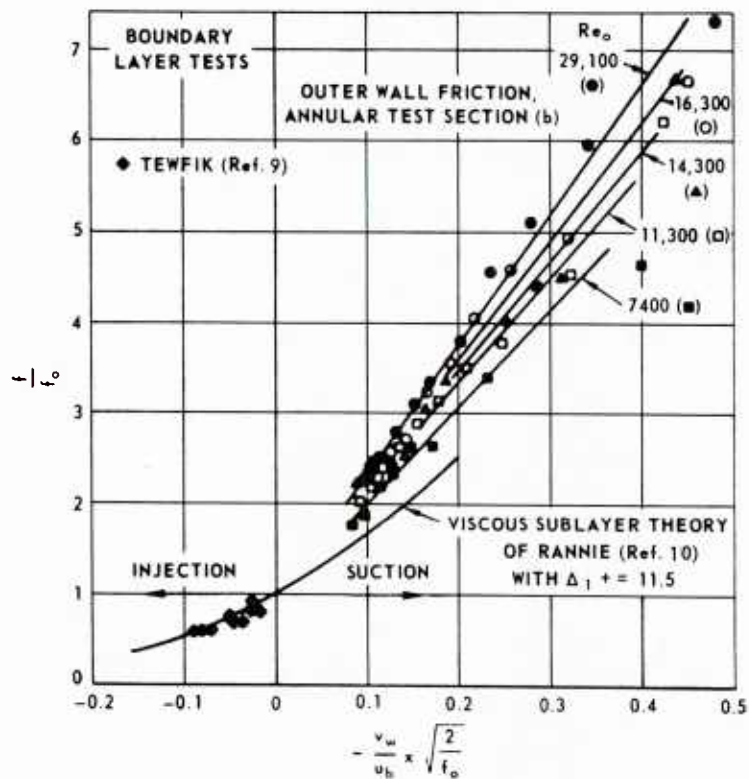




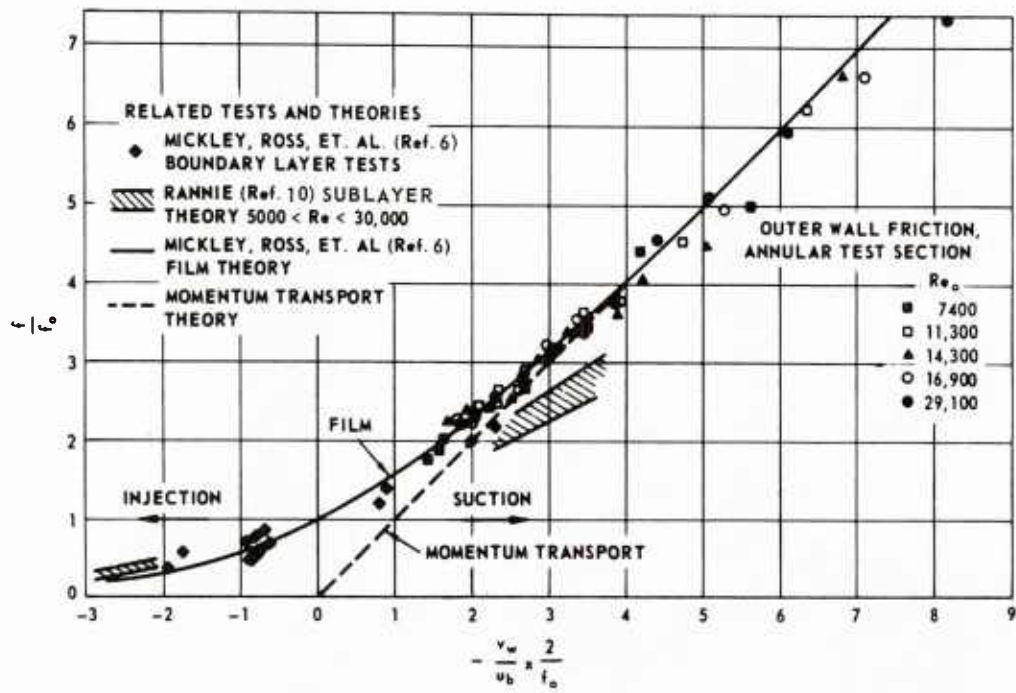
(U) Fig. 5 TEST ARRANGEMENTS FOR TRANSPIRATION EXPERIMENTS



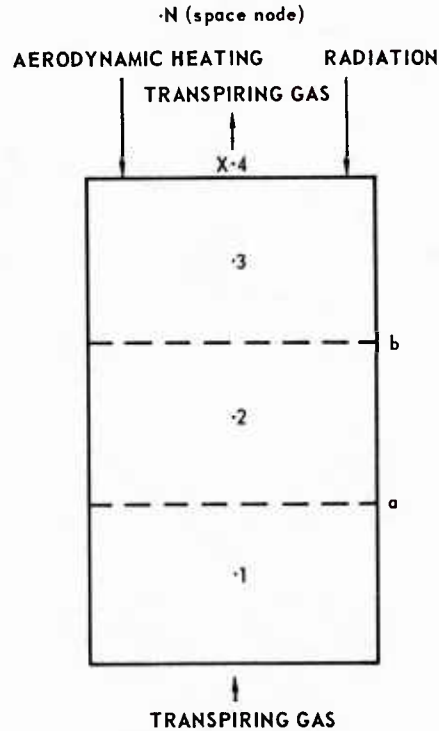
(U) Fig. 6 LOCAL SUCTION RATE PARAMETER NO. 1



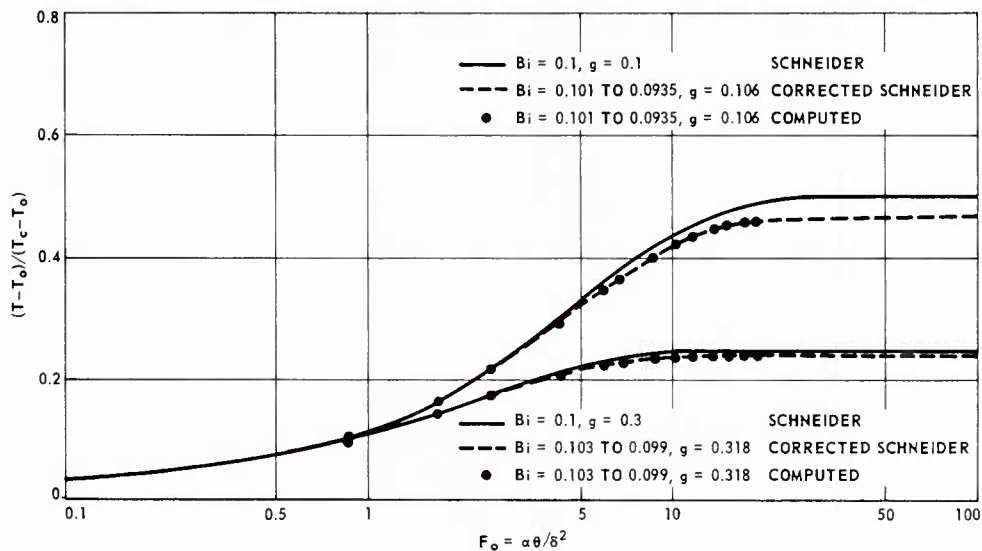
(U) Fig. 7 LOCAL SUCTION RATE PARAMETER NO. 2



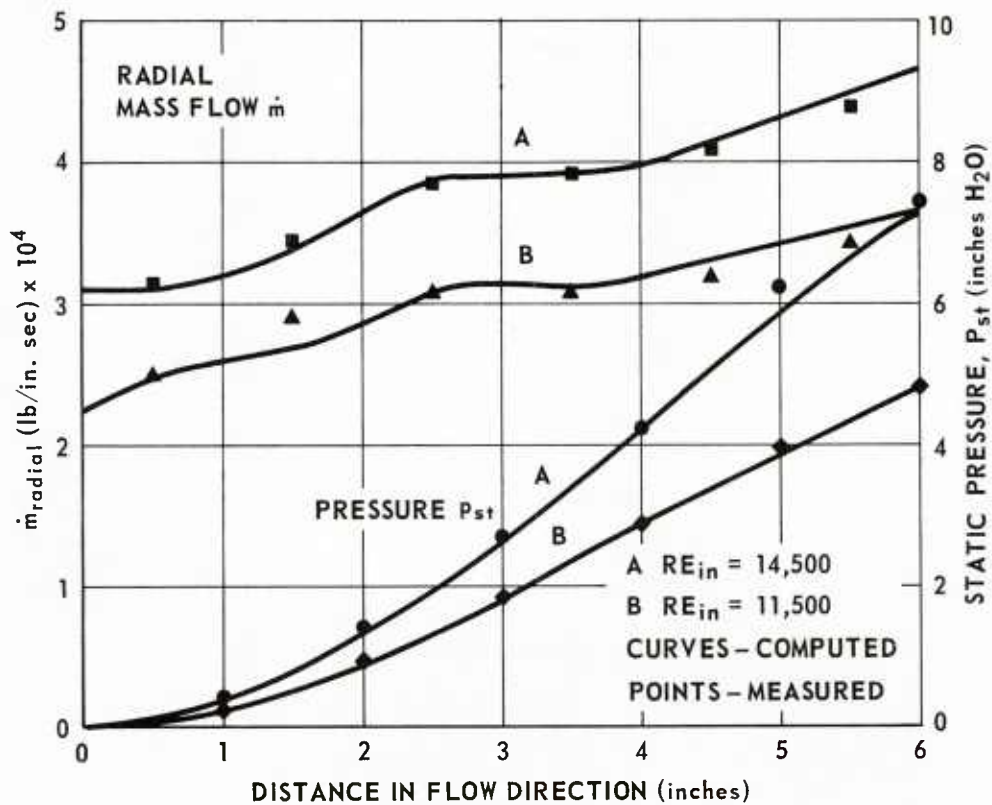
(U) Fig. 8 LOCAL SUCTION RATE PARAMETER NO. 3



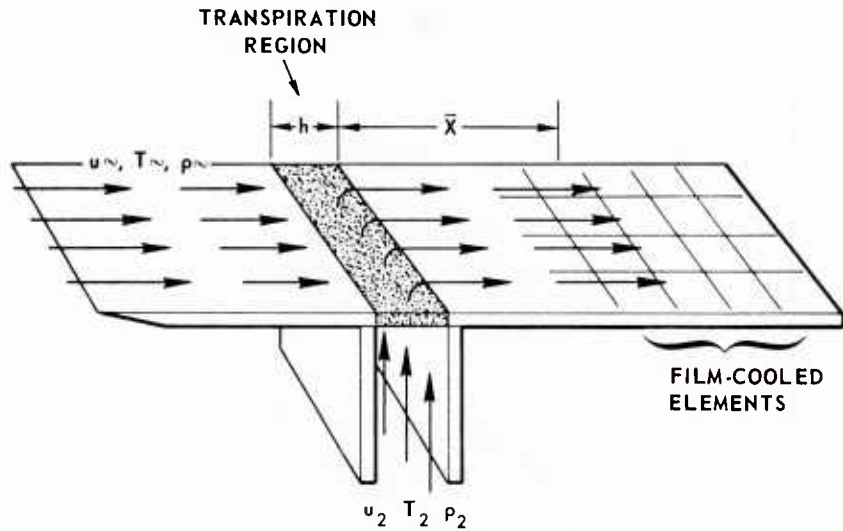
(U) Fig. 9 THERMAL MODEL



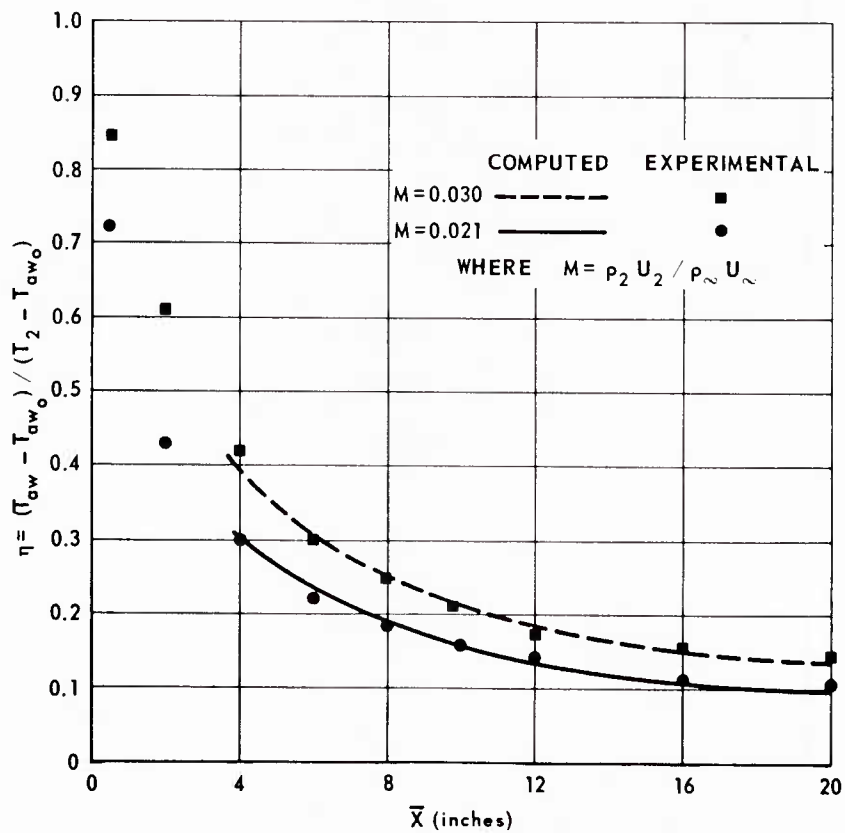
(U) Fig. 10 TEMPERATURE RESPONSE AT  $x = 0$  OF A POROUS PLATE,  $0 < x < \delta$ , AFTER EXPOSURE TO A UNIFORM TEMPERATURE CONVECTIVE ENVIRONMENT  $T_c$  AT  $x = 0$  AND COOLED BY A STEADY FLOW OF TRANSPIRATION FLUID THROUGH THE PLATE ENTERING AT  $x = \delta$  WITH  $T = T_0$  AT  $x \gg \delta$ , FOR VARYING BIOT NUMBERS ( $Bi$ ) AND COOLANT FLOW PARAMETERS ( $g$ )



(U) Fig. 11 COMPARISON OF THEORETICAL PREDICTIONS AND EXPERIMENTAL RESULTS OF PRESSURE AND RADIAL MASS FLOW IN A POROUS TUBE



(U) Fig. 12 EXPERIMENTAL MODEL USED TO CHECK FILM COOLING COMPUTER PROGRAM



(U) Fig. 13 FILM COOLING EFFECTIVENESS VERSUS DISTANCE FROM TRANSPIRING SECTION





Paper No. 6

EXPERIMENTAL INVESTIGATION OF TRANSPIRATION  
COOLING NEAR THE STAGNATION POINT OF A CYLINDER

(U)

(Paper UNCLASSIFIED)

by

Richard L. Humphrey  
U.S. Naval Ordnance Laboratory  
White Oak, Silver Spring, Md. 20910

ABSTRACT. (U) A series of tests were made with a cylindrical model equipped with transpiration cooling over a region  $\pm 15$  degrees from the stagnation line. The model was instrumented with thermocouples to measure wall and reservoir temperatures. Air was used as a cooling medium. The tests were made at a nominal Mach number of 6.5 and stagnation point gas temperatures of 2500 to 3500°K and a Pitot pressure of 0.14 atm. The dimensionless temperatures agree within 5 to 7 percent with predictions while heat-transfer rates agree within 15 percent.

(U) The effect of the external pressure distribution on the local coolant flow rate and wall temperature is discussed. Varying wall thickness and permeability may not be the whole answer.

NOMENCLATURE

$C$	= velocity gradient
$c_p$	= specific heat at constant pressure
$H$	= enthalpy
$\dot{m}$	= mass flow of coolant
$N_u$	= Nusselt number
$Pr$	= Prandtl number
$q$	= heat transfer rate
$Re$	= Reynolds number
$t$	= time
$T$	= temperature
$W$	= weight of matrix along coolant path
$\theta$	= angle from stagnation line
$\mu$	= viscosity
$\rho$	= density

Subscripts

$c$	= cavity (reservoir)
$e$	= edge of boundary layer
$k$	= side wall conduction
$m$	= matrix
$o$	= stagnation point
$a$	= ambient

oc = stagnation point cooled  
ouc = stagnation point uncooled  
sh = shielding from transpiration  
 $t_1$  &  $t_2$  = time 1 and time 2  
w = outside wall of porous section  
2 = inside wall of porous section

## INTRODUCTION

(U) Transpiration cooling is an attractive means of providing protection for surfaces subjected to moderate to high heat-transfer rates for long periods of time. This would be the case for a ramjet vehicle or a hypersonic transport operating at normal flight altitudes. Highest heat loads are encountered on stagnation lines such as engine air inlets, aerodynamic surface leading edges and body noses. Most of these surfaces are two dimensional and close to cylindrical.

(U) When the present studies were initiated, a considerable amount of information was available on flat-plate and three-dimensional (conical and spherical) transpirational cooling. However, two-dimensional data particularly near the stagnation line were missing. Most leading edges proposed for aircraft wings and air inlets are very small in radius, in the case of ramjet air inlets as small as 0.050 inch. This led us to attempt as small a model as was practicable to manufacture and instrument. It was recognized that the strong pressure gradients over the cylindrical surface would result in a variation of mass injection rate and wall temperatures near the stagnation line and the design was modified to minimize these effects.

## DESCRIPTION OF MODELS

(U) Considerations of available materials, ease of instrumentation, tunnel blockage requirements, and wind tunnel conditions led us to choose a cylinder 0.500 inch in diameter as the basis of the model. The model design is detailed in Fig. 1. The model consists of a holder for mounting in the tunnel-injector mechanism, a gas reservoir, a porous tube holder, the porous tube and an external steel sheath.

### Vol. 1

(U) The porous tube is nominally one-half inch in diameter with 0.125-inch walls and is sintered from 10 or 20 microns type 316 stainless-steel spheres. This size wall thickness, material, and particle size are standard filter elements manufactured by the Mott Metallurgical Company. The porous tube is held in a cradle and the two parts are mounted in a holder that covers the ends of the tube and is as thick as the tube diameter.

(U) The exterior of the model is covered by a sheet of 0.003-inch type 304 stainless steel. The sheet has a cutout two-inches long by 0.125-inch wide along the stagnation line of the model. The sheet is electron beam welded airtight along all exposed edges and the cutout. Around the cutout the sheet is welded directly to the porous tube. Thus the transpiring fluid is ejected from the model only along the stagnation line and  $\pm 15^\circ$  from it.

(U) The coolant fluid is brought into the model through a single tube opening into a rear reservoir. It passes through a series of connecting passages to the cavity inside the porous tube. From here it filters through the porous tube and out the cutout along the stagnation line. The mass flow of coolant air ( $\dot{m}$ ) was measured with a variable area glass-tube flowrater. The air was obtained from the house air system (100 psi;  $-50^\circ\text{F}$  to  $-140^\circ\text{F}$  dew-point), filtered and reduced to the desired pressure with a regulator. The flow rate of coolant was independent of the external pressure on the model over the range of 400  $\mu$  Hg to 200 mmHg.

(U) Three thermocouples are mounted in the model. The chromel-alumel thermocouples are of number 36 (0.005 inch) wire and are located on the outside wall ( $T_w$ ), inside wall ( $T_2$ ) and in the cavity ( $T_c$ ). The outside wall thermocouple passes through the wall in two insulator tubes 0.125 inch apart and the bead is formed between them. The thermocouple bead is in a region where the flow of the coolant is undisturbed and thus is more likely to indicate the actual cooled wall temperature.

### TEST PROCEDURES

(U) The tests were conducted in the Naval Ordnance Laboratory (NOL) 3 Megawatt Arc Tunnel. The nominal Mach 6.4 nozzle was used. When tunnel pressures had stabilized, a quick injection mechanism with a transit time of 150 ms was

used to insert the model into the gas stream. The model remained in the stream for five or seven seconds. Coolant flow in the model was established before starting the tunnel.

(U) Conditions for the runs with the first model are given in Table 1. Arc heater and Pitot pressures remain very stable during tunnel operation but the heater temperature reaches a steady state slowly. Thus there is a variation of stagnation point temperature and Mach number during the time the model is in the hot gas. This is reflected in the steadily increasing wall temperatures recorded on the models, for example Fig. 2. However, the model does achieve a steady state with respect to the stagnation point temperature.

(U) After a run, the surface of the model was found to be coated with a fine oxide deposit. This deposit did not appear to cause any nonuniformity in the coolant distribution. This is probably because the pressure drop across the wall is large compared to the external pressure. Wiping the surface with solvent restored the appearance.

(U) At the lowest mass flow of coolant the stainless steel sheath failed at the stagnation line near the ends. Since the porous window does not extend to the ends of the model, this region is uncooled except by internal conduction. The damaged area appears to have ruptured outward from the pressure inside the wall. Examination of the model revealed that the sheath had remained welded to the porous tube all around the window. All three thermocouples and the Pitot tube were still working and the porous surface was unharmed.

## RESULTS AND ANALYSIS

### Temperatures

(U) Figure 2 shows typical temperature history results for the transpiration cooled models. The temperatures show a steady increase during the test. After the first three seconds they follow the trend of the stagnation point temperatures. An indication of steady-state temperatures is the difference between  $T_w$  and  $T_2$ , the gradient across the porous wall. After 1.5 seconds  $T_w - T_2$  does not change significantly. The thermal conductivity of the porous wall material is only a weak function of temperature and the constant temperature drop may be taken as an indication of steady-state cooling.



## Vol. 1

(U) The dimensionless temperature function  $(T_e - T_w) / (T_e - T_c)$  given in Fig. 3 shows the rapid approach to steady-state temperatures. Here the values of wall temperatures predicted from the tunnel flow conditions are shown for the three runs with the first model. While the predicted and experimental values do not agree exactly, after about three seconds the trend of the data is in good agreement.

(U) The analysis of Roberts<sup>1</sup> is followed for the calculation of the predicted values of the runs. A somewhat simplified treatment of Roberts' material is given by Truitt<sup>2</sup>. Roberts looks at mass transfer cooling near the stagnation point and considers both two- and three-dimensional flow situations. It is assumed that the velocity parallel to the wall is a linear function of the distance along the wall from the stagnation point. The temperature, velocity, and concentration boundary layers are assumed to be of constant, although different, thicknesses. Gradients in these layers are taken to be a function of the distance from the wall only and the coolant is assumed to be injected at equal velocity along the wall. It is considered that the boundary layer will increase in thickness because of the injection; but the analysis implies that the extra thickness will be small enough to avoid disturbance of the flow field around the body.

(U) The dimensionless temperature function for a two-dimensional body is found by Roberts to be

$$\frac{T_e - T_w}{T_e - T_c} = \frac{P_{rw}^{0.6} \left( \frac{\dot{m}}{(\rho_w \mu_w C)^{1/2}} \right)}{\left( \frac{Nu_w}{Re_w^{1/2}} \right) + \frac{1}{3} \left( \frac{\dot{m}}{(\rho_w \mu_w C)^{1/2}} \right)}$$

where

$$\left( \frac{Nu_w}{Re_w^{1/2}} \right) = 0.570 \left( \frac{\rho_e \mu_e}{\rho_w \mu_w} \right)^{0.4} P_{rw}^{0.4}$$

The various quantities are evaluated at the cooled wall temperature and at the temperature behind the normal shock in front of the body. In so far as

possible real gas thermodynamic and transport properties were used in the evaluation. The coolant flow rate was assumed to be uniform over the porous surface.

(U) The dimensionless temperature function as calculated for the three runs with the first model is shown on Fig. 3. With the exception of the first run, the predicted values of wall temperature are lower than the experimental data. The calculated temperature function for runs 2 and 3 agree with the experimental values within 5 to 7 percent. The different behavior of the first run is believed due to an error in the coolant mass flow or to some error in tunnel flow conditions but has not been found at this time.

(U) The dimensionless temperature function as a function of the mass flow parameter  $\dot{m}/(\rho_w \mu_w c)^{1/2}$  is given in Fig. 4. Both experimental and calculated values are shown. Again with the exception of the first run, agreement is within 5 to 7 percent. The range of mass flows covered is not large but represents relatively large absolute values.

(U) The heat-transfer parameter  $Nu_w/Re_w^{1/2}$  as a function of the relative mass rate is given in Fig. 5. The values calculated from the experimental results are compared with curves for  $P_r = 0.7$  and  $1.0$  taken from Roberts' report. The  $P_r$  of the experiments is about  $0.75$ . From this it seems that the heat-transfer function at these large mass rates is either constant or is increasing with increasing mass injection. These large mass rates may disturb the flow field around the body and may result in the flow near the stagnation point becoming turbulent (ref. 3 for instance).

(U) The analysis of Roberts does not tell us what is happening inside the wall but predicts only the outer wall temperature. The temperature profiles within the wall are vital to the proper choice of material, wall thickness, etc., to allow the wall to sustain the aerodynamic and mechanical loads while meeting the cooling requirements. For these experiments it is important to know if the coolant and matrix or wall temperatures are equal at any location in the wall. If this is true the wall thermocouples will be measuring both the coolant and matrix temperatures correctly.

(U) Koh and del Casal<sup>4</sup> discuss the processes occurring within the wall and develop expressions for determining coolant and matrix temperature and pressure profiles. These are based on the coolant mass flow and the coolant matrix properties. For the model, coolant and flow rates

## Vol. 1

used in these tests and using their relations the coolant and matrix temperatures are found to be equal at every point through the wall.

Heat Transfer

(U) The steady-state heat transfer to the model consists basically of two components,  $q_{sh}$  - the heat transfer blocked by transpiration, and  $q_w$  - the heat transferred to the wall and raising the coolant temperature. Since the tunnel conditions are changing during the tests there is a term  $q_m$  - the rate of heat storage in the matrix as the wall temperatures increase. So the total stagnation point heat transfer to the model is

$$q_{oc} = q_{sh} + q_w + q_m$$

and

$$q_{sh} = (1 - \frac{1}{3} P_{rw}^{-0.6}) (H_e - H_w) \dot{m}$$

$$q_w = (H_w - H_c) \dot{m}$$

$$q_m = W_m c_{pm} \frac{(T_{t2} - T_{t1})}{\Delta t}$$

(U) A breakdown of the average experimental heat-transfer rates for the runs is given in Table 2. The largest item is  $q_{sh}$  which amounts to 70 to 80 percent of the total. Eighteen to 28 percent of the total reaches the wall raising the coolant temperature. The small remainder is the heat storage in the matrix. In a steady state this storage term, of course, would vanish.

(U) The stagnation point heat transfer to an uncooled wall was calculated using standard methods. With the exception of the maverick first run the experimental and calculated stagnation point heat transfer rates agree within 15 percent. This is consistent with previous calorimeter tests made in the tunnel.

(U) The last point in the heat-transfer discussion is the term  $q_k$  listed in the table. This term is given by

$$q_k = \dot{m} (H_c - H_a)$$

and gives the heating of the coolant fluid as it passes through the model to the matrix. This term while small is not negligible. The body of the model is not cooled and  $q_k$  gives an indication of the heat transferred to the cavity through the uncooled sidewalls.

(U) The agreement between the uncomplicated theory of Roberts and the experiments is good. The dimensionless wall temperatures could be calculated within 5 to 7 percent of the experimental results. Agreement of the experimental and calculated stagnation point heat-transfer rates is within normal limits.

(U) The conditions of the tests and the design of the model were such as to minimize problems that must be faced for flight vehicles. The most important of these is "coolant starvation".

#### Coolant Starvation

(U) The external pressure distribution around a body near the nose of an axisymmetric shape or the leading edge on a two-dimensional body may have a profound effect on the local coolant flow rate near the nose. If the porous wall is of uniform thickness and permeability and the plenum or reservoir pressure is constant the coolant flow rate will vary with changes in the external pressure. At the stagnation point the flow for these conditions would be a minimum and would increase away from the stagnation point as the external pressure drops.

(U) This change in coolant flow is dramatically shown in Fig. 6. Two flight conditions and the model test environment are compared. In each case the wall thickness and permeability were uniform and the internal pressure was chosen to provide the desired coolant flow at the stagnation point. Away from the stagnation point a one-dimensional flow analysis with a form of the Darcy pressure drop equation<sup>4</sup> gave the local coolant flow. In the model tests the ratio of cavity pressure to stagnation-point pressure is high while in the sea level flight case it approaches unity. The model will have only a 25 percent increase in coolant flow 15 degrees from the stagnation line while the sea level flight coolant flow will increase to six times the stagnation-point value only 5 degrees from the stagnation line.

### Vol. 1

(U) Recently Schneider<sup>5,6</sup> and others have described this flow variation in some detail and discuss the under-cooling, over-cooling, and coolant starvation that will result if average coolant flow rates are used. Usually the stagnation region would be under-cooled or have "coolant starvation" while regions away from the stagnation point will be over-cooled or have more coolant than needed. As the internal pressure approaches the stagnation point pressure the external flow may be ingested into the stagnation region.

(U) Schneider discusses the effects of varying permeability and wall thickness to control the distribution of coolant over the body. However, if the body is small, as the leading edge of a wing, it may not be practicable to vary thickness or permeability sufficiently to obtain uniform cooling. In this case the system would need to be designed to confine the injection to an area close to the stagnation line. The coolant flow rate would have to be adequate at the stagnation line and still allow for the extra flow away from that point.

(U) In the model tests described here the variation in coolant flow is not large but does cause the wall temperatures to change. Figure 7 gives an estimate of the variation in temperature over the cooled portion of the model. At the edge of the cooled portion the wall temperature is 70 percent of the stagnation point value.

### SUMMARY AND CONCLUSIONS

(U) Agreement between the experiments and the analysis of Roberts is good even with the very high coolant mass rates and the low wall temperature to stagnation-point temperature ratio. Compensation for the variation in coolant flow across the porous section would improve the agreement.

(U) In a flight vehicle with a small diameter leading edge it may not be feasible to adjust the wall thickness and permeability to allow the desired coolant distribution. In such a case it would be essential that the irregular distribution be considered in order that the stagnation point not be starved. An alternative would be to go to a slot injection scheme.



(U) The uncomplicated approach of Roberts can be expected to give satisfactory results if proper consideration is given to the effect of external pressure distribution on coolant flow rates.

## REFERENCES

1. National Aeronautics and Space Administration, "Mass Transfer Cooling Near the Stagnation Point," by Roberts, L., Langley Field, Va., 1959, p 16 (NASA TR R-8, Publication Unclassified)
2. Ronald Press, Fundamentals of Aerodynamic Heating, by Truitt, R. W., New York, N. Y., 1960, p 257 (Publication Unclassified)
3. Royal Aircraft Establishment, "An Experimental Investigation of Contoured Nose Orifices with Ejection at Free-Stream Mach Numbers of 1.86 and 4.3," by Tucker, L. M. and Hall, M. G., Ministry of Aviation, London, W.C. 2, November 1963, p 35 (RAE TN No. AERO 2923, Publication Unclassified)
4. Stanford University Press, "Heat and Mass Flow Through Porous Matrices for Transpiration Cooling," Proceedings of the 1965 Heat Transfer and Fluid Mechanics Institute, by Koh, J. C. Y. and del Casal, E., Stanford, Calif., 1965, pp 263-281 (Publication Unclassified)
5. American Institute of Aeronautics and Astronautics, "Coolant Starvation in a Transpiration-Cooled Hemispherical Shell," by Schneider, P. J. and Mauer, R. E., Journal of Spacecraft and Rockets, Vol. 5, June 1968, New York, N. Y. (Publication Unclassified)
6. American Institute of Aeronautics and Astronautics, "Two Dimensional Transpiration Cooling," by Schneider, P. J. and Mauer, R. E., AIAA Paper 69-96 Presented at the AIAA 7th Aerospace Sciences Meeting, New York, N. Y., January 20-22, 1969 (Publication Unclassified)



(U) TABLE. 1

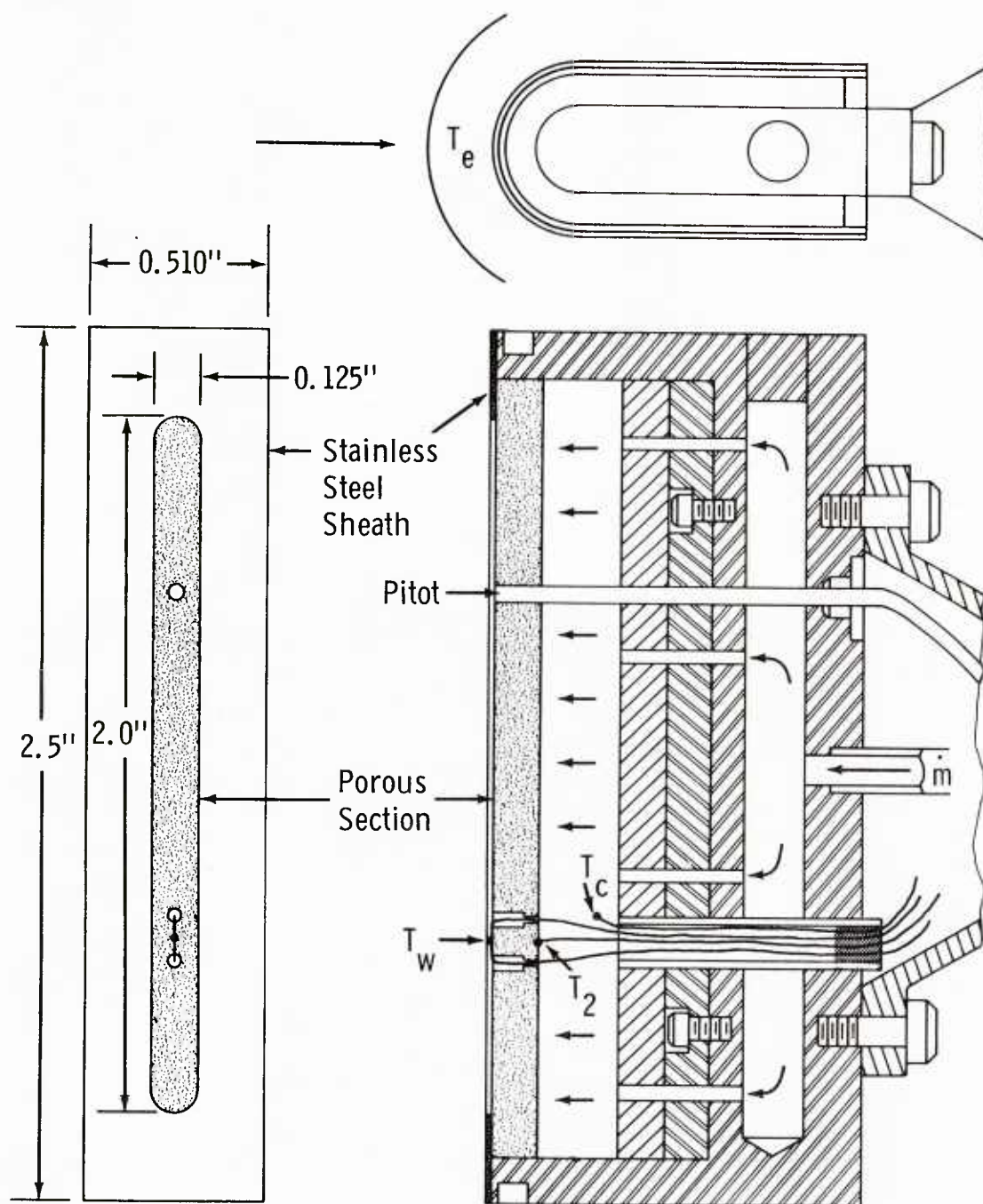
Test Conditions for Runs of Model No. 1

Item	Run No. 1	Run No. 2	Run No. 3
Heater Temp (°K)	3340-3880	2500-3700	2600-3550
(°R)	6012-6984	4500-6660	4680-6390
Heater Press (atm)	21.41	20.71	20.84
Model Stagnation Point Temp (°K)	2950-3250	2400-3180	2470-3090
(°R)	5310-5850	4320-5724	4446-5562
Model Stag Point Press (atm)	0.142	0.140	0.139
Mach Number	7.1-6.65	7.69-6.74	7.65-6.91
Model Immersion Time (sec)	5.03	7.05	7.01
Coolant Mass Flow (lb/sec)	$2.42 \times 10^{-4}$	$3.07 \times 10^{-4}$	$2.12 \times 10^{-4}$

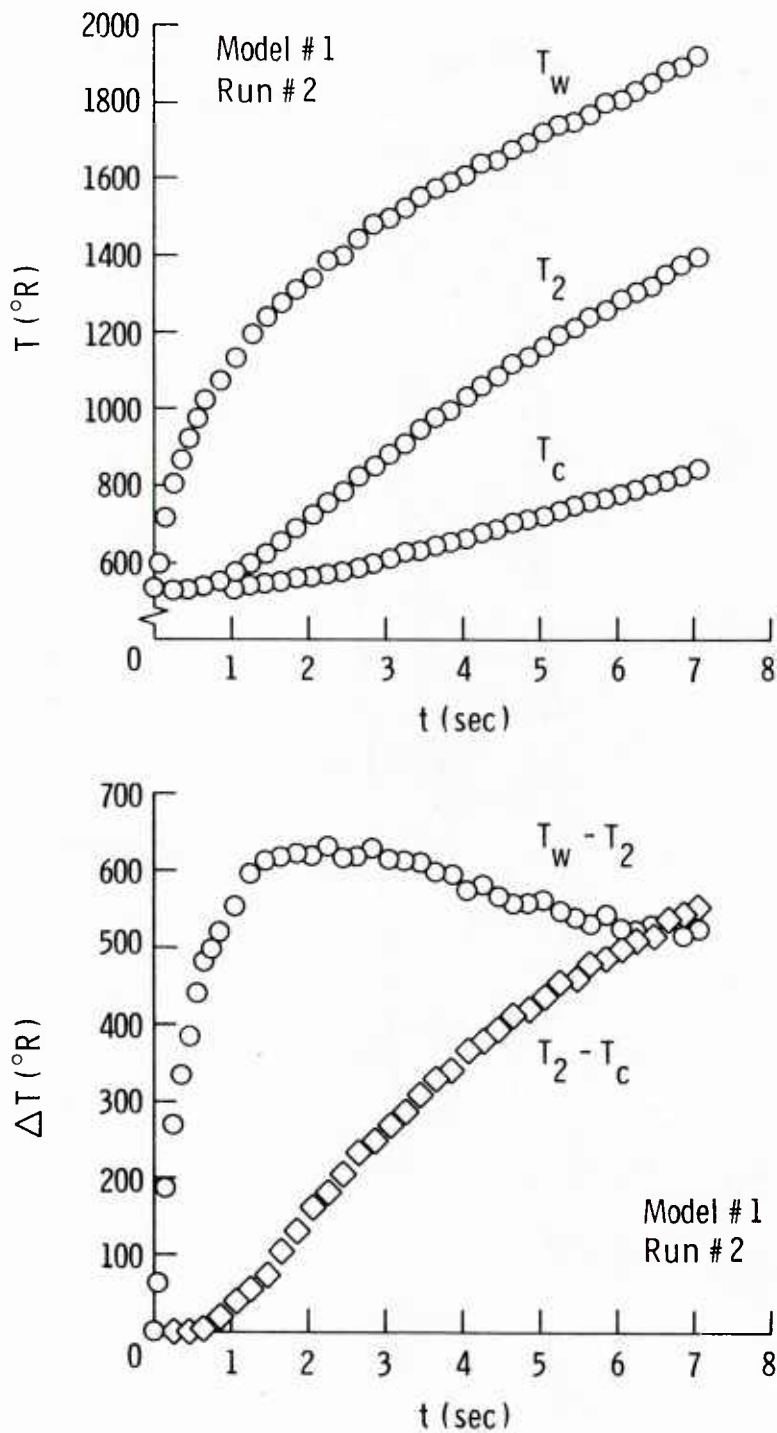
(U) TABLE. 2  
Average Heat Rate Balances for  
20  $\mu$  Particle Model

Item	Run No. 1		Run No. 2		Run No. 3	
	BTU/ft <sup>2</sup> sec	Percent	BTU/ft <sup>2</sup> sec	Percent	BTU/ft <sup>2</sup> sec	Percent
$q_{sh}$	155.6	78.9	184.6	78.3	104.8	68.8
$q_w$	36.8	18.7	47.5	20.1	42.6	28.0
$q_m$	4.7	2.4	3.7	1.6	5.0	3.2
$q_{oc}$	197.1	100.0	235.8	100.0	152.4	100.0
$q_k$	4.9		10.3		9.8	
$q_{ouc}$	307.8		276.8		176.9	
$q_{oc}/q_{ouc}$		64.0		85.2		86.2

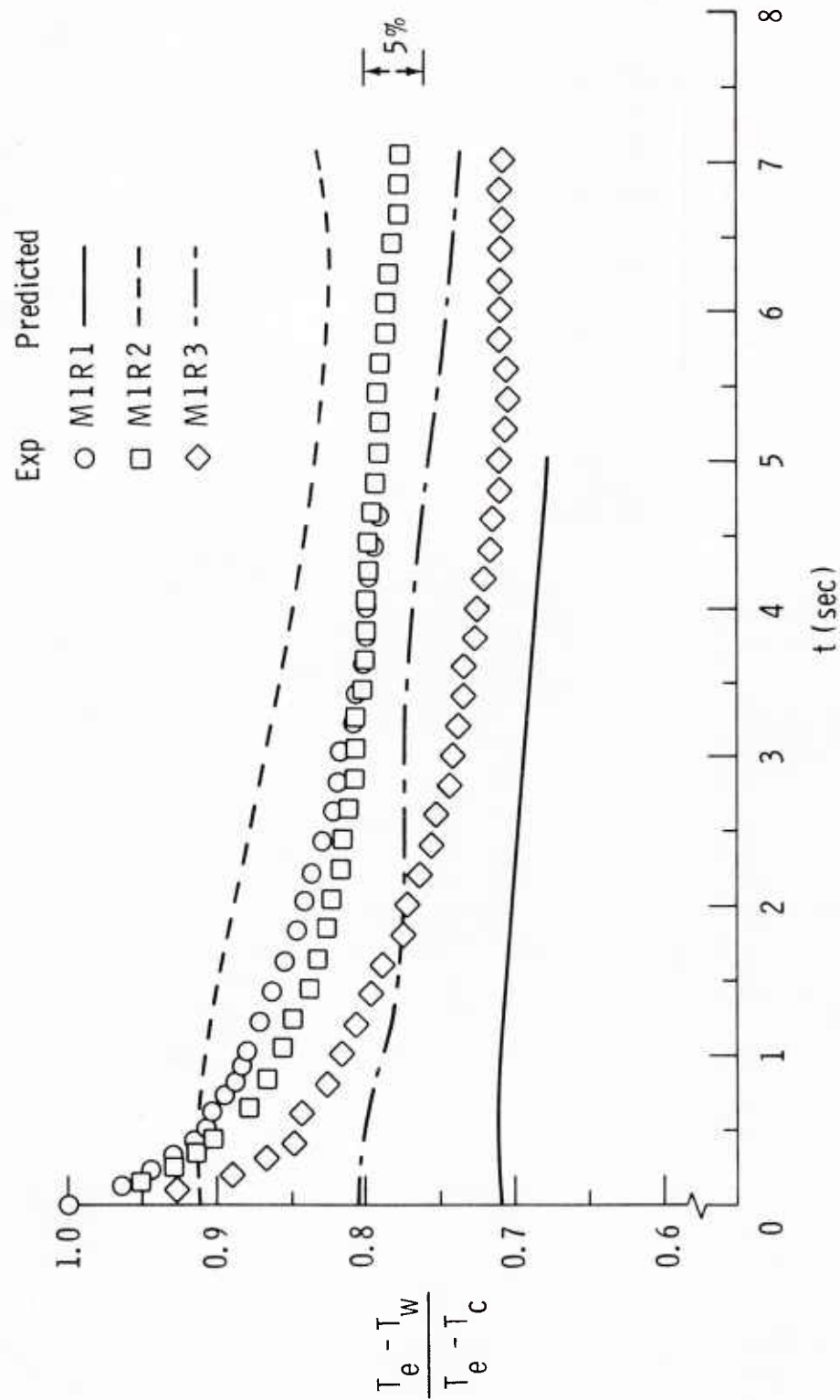
$q_{sh}$  = heat transfer blocked by transpiration  
 $q_w$  = heat transferred to wall and raising coolant temperature  
 $q_m$  = heat storage by matrix  
 $q_k$  = heat transferred to cavity by conduction through side walls  
 $q_{oc}$  =  $q_{sh} + q_w + q_m$  total heat transfer to model  
 $q_{ouc}$  = heat transfer to uncooled model at cooled wall temperature



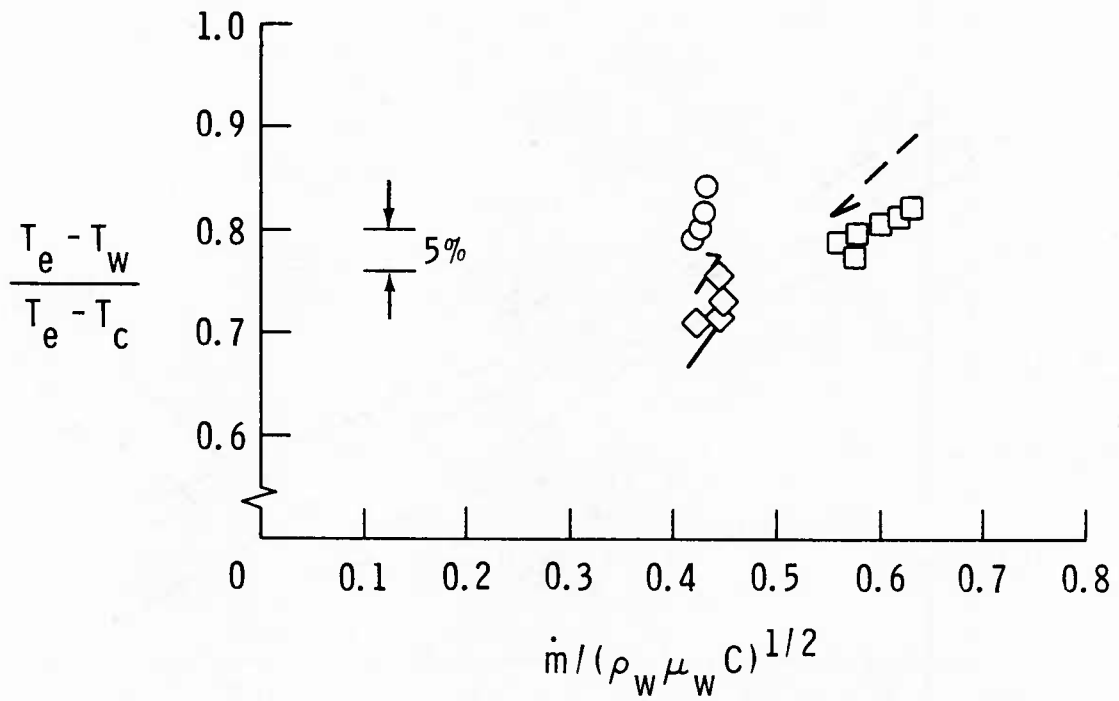
(U) FIG. 1 Details of Two-Dimensional Stagnation Line Transpiration Cooled Model



(U) FIG. 2 Typical Model Temperatures and Temperature Differences during Test Run

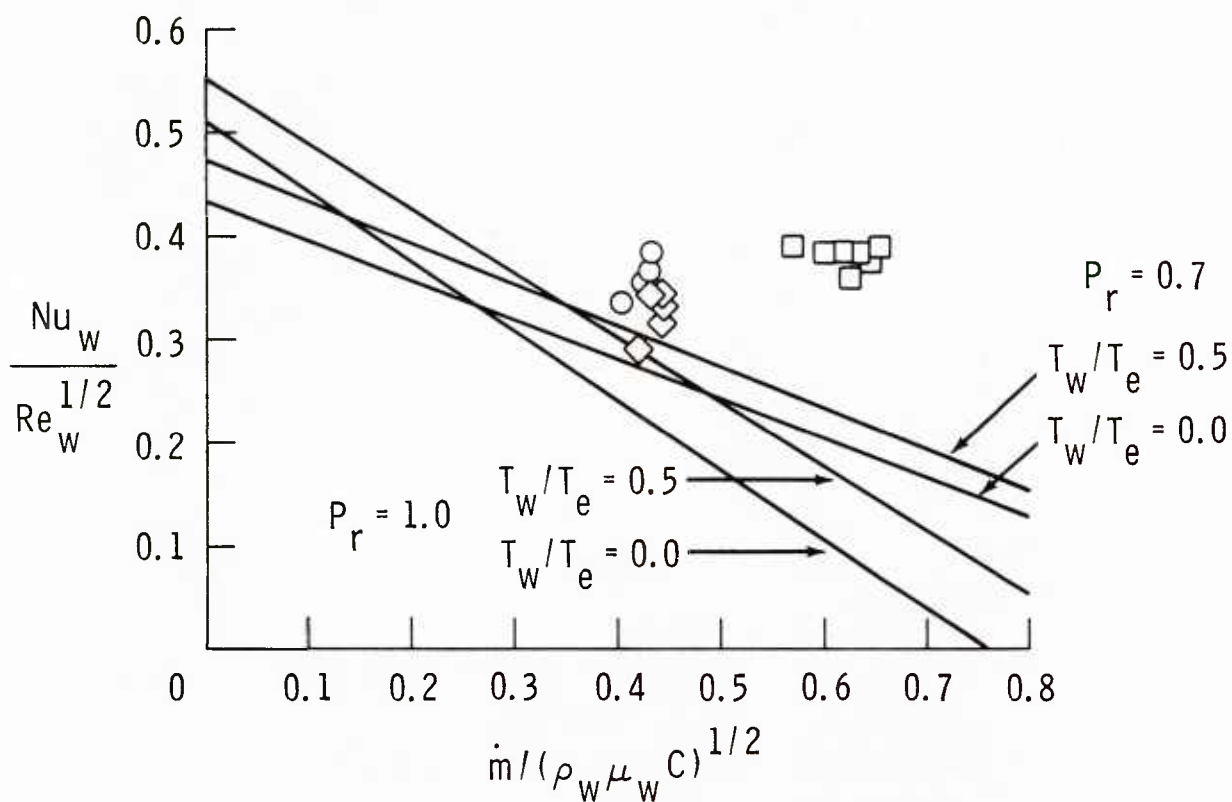


(U) FIG. 3 Dimensionless Wall Temperatures Compared with Predicted Values

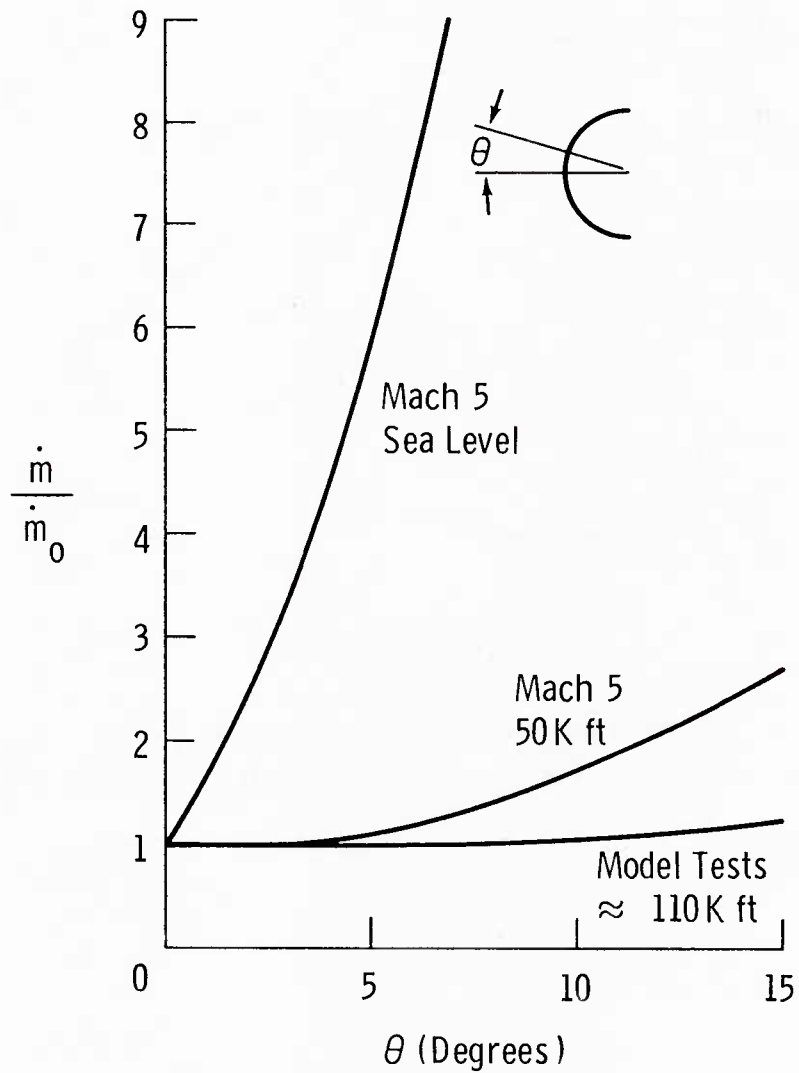


(U) FIG. 4 Dimensionless Wall Temperatures for the Mass Flow Function, Experimental and Predicted



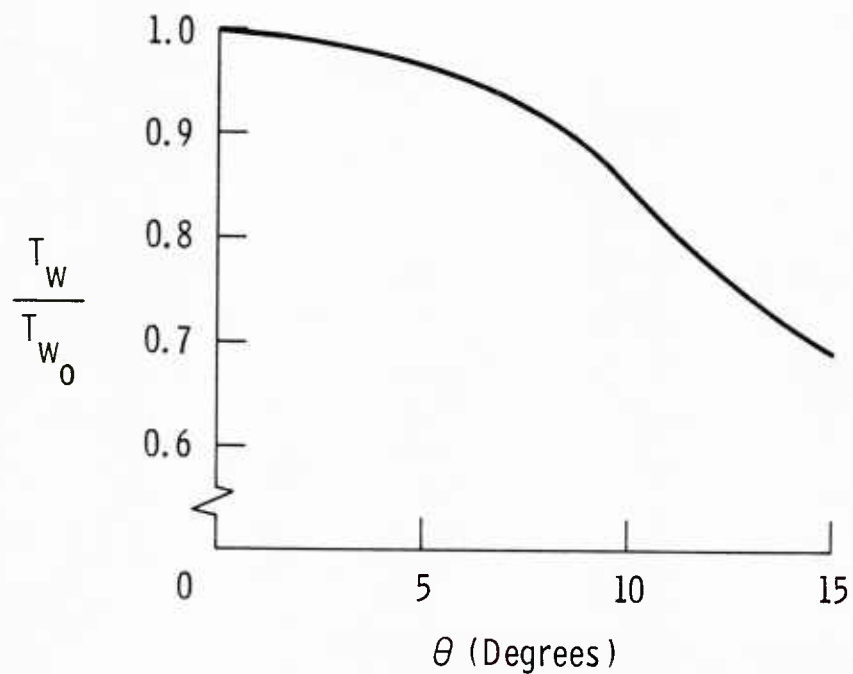


(U) FIG. 5 Comparison of Nusselt-Reynolds Number Function from Test Results with Results of Roberts



(U) FIG. 6 Estimated Effect of External Pressure Distribution on Local Mass Injection Rate for Three Cases

Vol. 1



(U) FIG. 7 Estimated Effect of External Pressure Distribution on Wall Temperatures for Model Tests

## Paper No. 7

**BALLISTICS RANGE EXPERIMENTS ON THE EFFECT OF  
UNIT REYNOLDS NUMBER ON BOUNDARY-LAYER TRANSITION  
(U)**

(Paper UNCLASSIFIED)

by

Norman W. Sheetz, Jr.  
U.S. Naval Ordnance Laboratory  
White Oak, Silver Spring, Md. 20910

**ABSTRACT.** (U) It has been observed in numerous experimental investigations that the unit Reynolds number appears to have a significant effect on the boundary-layer transition Reynolds number. Many wind-tunnel investigations have indicated that, for an increase in the unit Reynolds number of a factor of 10, the transition Reynolds number can increase by a factor of 1.5 to 4, depending upon the particular experiment. Pate and Schueler have published a correlation that attempts to explain this effect in terms of the turbulent boundary layer that existed on the wind-tunnel walls and the aerodynamic noise that is radiated into the test section from these boundary layers. However, tests have been performed by Potter in a ballistics range which also produced a unit Reynolds number effect that cannot be explained by an analysis such as that of Pate and Schueler which would predict no effect in a ballistics range.

(U) In order to help define the effect of varying the unit Reynolds number on transition, a test is currently in progress in the NOL ballistics range. To date, these results indicate the existence of a unit Reynolds number effect, but suggest that it may not be as strong as observed in many previous investigations.

## INTRODUCTION

(U) The importance of boundary-layer transitions in many aerodynamic phenomena is well known. These include as some of the more obvious the viscous drag, aerodynamic heating rates, location of boundary-layer separation, and the base flow characteristics. It is also generally accepted that a large number of parameters affect boundary-layer transition. Some of these parameters include Mach number, surface roughness, heat-transfer rate, mass injection of ablation rate, pressure gradient, nose bluntness, cone angle, and unit Reynolds number. In order to predict conditions under which transition will occur, it is first necessary to understand the role that each of the above-mentioned parameters play in controlling transition.

(U) Judging by the volume of work that has gone into examining boundary-layer transition, Morkovin lists 265 references in a recent comprehensive survey article (Ref. 1), one might suspect that the problem has been solved. Quite the contrary! The contradicting conclusions that can be obtained from many of the investigations have often tended to complicate the picture, rather than to enlighten. In many cases, this has been caused by experiments in which a number of parameters were varied in such a manner that it was not possible to separate and define the effect of the individual parameters. It is the purpose of the present paper to help gain insight on the effect of one parameter, unit Reynolds number, that has been observed by many to influence transition.

(U) Potter and Whitfield (Refs. 2, 3), in a series of wind-tunnel investigations, found that the transition Reynolds numbers that they measured on 6-degree and 10-degree cones changed by more than a factor of two, with a change of approximately an order of magnitude in the unit Reynolds number. Further, it was noted that this variation was dependent on nose bluntness. Unit Reynolds number effects were also reported by Pate and Brillhart (Ref. 4). Their results were obtained on sweptwing plan forms. Van Driest and Blumer (Refs. 5, 6) and Jack, et al (Ref. 7), show increases in the transition Reynolds number for a 10-degree cone with increases in the unit Reynolds number

while, in an earlier investigation, Van Driest and Boison (Ref. 8) found little or no effect under certain test conditions.

(U) While the majority of the above wind-tunnel work, along with a number of others, strongly indicated the existence of a unit Reynolds number effect, many remained skeptical. They pointed to the strong dependence of the turbulence level in the wind tunnel on the unit Reynolds number and suggested that this was the real mechanism by which transition was affected. Pate and Schueler (Ref. 9), pursuing this line, have published a correlation that collapses data obtained from a variety of wind tunnels over a wide range in Mach number and unit Reynolds number into a single curve. The data are correlated in terms of the tunnel diameter and the mean turbulent  $C_F$  and  $\delta^*$  of the tunnel wall boundary layer at the test section. However, tests have been performed by Potter (Ref. 10) in a ballistics range that cannot be explained by an analysis such as that of Pate and Schueler, since the ballistics range does not have a wall boundary layer that can radiate noise into the test section. Potter's tests were made on 10-degree sharp cones at a local Mach number of approximately 4.3. He observed an increase in the transition Reynolds number by a factor of approximately four, for an order of magnitude increase in the unit Reynolds number. The data obtained in the present paper were obtained on 5-degree sharp cones at a higher local Mach number, approximately 6.9, and suggest a somewhat smaller effect at these conditions.

#### DESCRIPTION OF TESTS

(U) The tests were conducted in the NOL Pressurized Ballistics Range (a 3-foot-diameter tube, 270 feet long) and in the NOL 1000-foot Hyperballistics Range (Ref. 11) (a 10-foot-diameter tube, 1000 feet long). The ranges are equipped with 27 and 37 pairs of shadowgraph stations, respectively. In addition, they have X-ray stations at various positions along the range to monitor changes in model contour that may occur during the flight due to aerodynamic melting or damage during launch. The test models were 5-degree half-angle cones with a tip radius of approximately 0.001 inch. The base diameter varied from 0.5 to 1.75 inches. The model tips were machined from a tantalum alloy (Ta10W) and screwed onto a titanium afterbody. The outer surface was finished by grinding, with a



## Vol. 1

resultant surface finish of less than 10 microinches rms. In order to make the models more stable and reduce the effects of angle of attack on transition, the aft portion of the models was hollowed out and an internal ballast was placed in the forward section. In addition, a finned cylindrical afterbody was placed on the smaller-diameter models to help increase their stability. A photograph of the models is shown in Fig. 1.

(U) The location of transition was determined optically from the range shadowgraphs. A shadowgraph of a model in free flight is shown in Fig. 2. It can be seen that the range photographs have sufficient clarity and detail at these test conditions to allow accurate estimates of the location of boundary-layer transition to be made. The transition Reynolds number was obtained by measuring the length of laminar flow and determining the flow properties, such as velocity, temperature, and pressure, from test conditions and trajectory measurements in the range.

(U) The unit Reynolds number was adjusted by controlling the ambient pressure in the range. The higher unit Reynolds numbers were obtained in the Pressurized Ballistics Range. This facility can be pressurized to approximately five atmospheres. Tests were conducted in this facility at range pressures as high as two atmospheres. At these pressures, transition was occurring approximately one inch from the model tip. It was decided not to investigate higher unit Reynolds numbers due to the difficulty in determining shorter lengths of laminar flow from the range shadowgraphs. The smaller-diameter, thus shorter-length, models were used for the higher unit Reynolds number tests. The lower Reynolds number tests were conducted in the 1000-foot Hyperballistics Range. The launchers that are currently available for use with this facility made it possible to launch considerably larger models, thus providing an opportunity to measure longer lengths of laminar runs. To date, at lower Mach numbers, cones with mechanically sharp tips have been tested in the ballistics ranges at NOL with no evidence of melting due to aerodynamic heating (Ref. 12). However, at the present test Mach number of nearly 8, the tips were purposely blunted to a radius of approximately 0.001. This was sufficiently blunt to eliminate the heating problem, but still allowed the local flow properties to recover rapidly to sharp cone properties. Fig. 3 shows the calculated Mach number and Reynolds number distribution over one of the test models. It can be seen that the bluntness effects due to the finite tip radius are quickly "swallowed," reaching 99 percent of cone values within the first 0.4 inch along the surface. The local flow properties were calculated

by a momentum-integral method described by Wilson (Ref. 13). This method takes into account the curved bow shock wave that exists for slightly blunted slender bodies, and allows a variation in total pressure along the outer edge of the boundary layer in the conical portion of the body. It assumes, however, that the static pressure along the surface is constant and equal to the inviscid, sharp-nosed cone value.

## DISCUSSION OF RESULTS

(U) Since the purpose of the present test is to study the effect of unit Reynolds number on boundary-layer transition, considerable attention was given to the other parameters that are known to also affect transition to minimize or eliminate their contribution. The tests were planned for a Mach number of 8. However, the average test Mach number for five of the tests was 7.6 with a variation from 7.3 to 7.8. One additional data point was included at a Mach number of 8.3. Since the ambient temperature in the range was 540°R for all of the tests, and the models were not preheated, the heat-transfer rate varied with the Mach number. To eliminate model geometry effects, all models were made with the same cone angle and tip radius. The variation in length was not significant, since transition was never measured near the base. The surface of the models was ground to finishes of better than 10 micro-inches rms. The maximum size of a discrete roughness protuberance found on the cones was approximately 120 micro-inches. An analysis (Ref. 12) has shown that this is not sufficient to affect transition at the present test conditions.

(U) One of the most undesirable elements in a ballistics range transition program is control of the angle of attack of the models. As mentioned earlier, the models were mass stabilized by hollowing out the base and using internal ballast in the nose section, and in some cones by adding finned cylindrical afterbodies. While in general this was sufficient to keep the models at small angles of attack, occasionally the angles did get sufficiently large to affect drastically the location of boundary-layer transition. To limit the effect of angle of attack on the present tests, only data obtained at angles of less than 1.5 degrees are presented. In general, the angle is less than 1.0 degree.

(U) At combinations of high Mach number and high range pressures, the aerodynamic heating rates in a ballistics

Vol. 1

range become quite high. If the heating rate becomes sufficiently high, it can cause portions of the model to melt, burn, or ablate, depending upon the model material. The problem becomes more acute for configurations with sharp tips, such as those used for the present tests. The resulting effect of a melting tip on boundary-layer transition would be difficult, if not presently impossible, to predict. Fortunately, both the Pressurized Ballistics Range and the 1000-foot Hyperballistics Range have in excess of 25 pairs of shadowgraph and schlieren stations located along the length of the ranges. By observing the results of all of the data stations, any change in the transition location as the temperature of the tip region increases can be detected. If a considerable change in transition location occurred during the flight, only data obtained prior to the change are used.

(U) Transition Reynolds numbers were obtained for each flight by using data from as much of the flight as possible. Approximately 27 orthogonal pairs of shadowgraphs are obtained for each flight in the Pressurized Ballistics Range, and 37 pairs from flights in the 1000-foot Hyperballistics Range. Since the range pressure and temperature are uniform along the entire length of the ranges, and the change in velocity of the model is relatively small due to the high ballistics coefficient, the variation in Mach number and unit Reynolds number during a flight is small. Therefore, to obtain a transition Reynolds number for a flight, all low angle-of-attack readings of transition location are averaged until any evidence of tip melting is observed. Subsequent data are not used.

(U) To date, data have been obtained from six launchings at a nominal Mach number of 7.5 over a range in local unit Reynolds number of approximately  $1 \times 10^6$  to  $1.5 \times 10^7$  per inch. A summary of the test conditions and transition results are shown in Table 1. The data are also shown in Fig. 4. It can be seen that the data strongly suggest that there is a stabilizing effect of increasing the unit Reynolds number. In particular, it appears that, as the unit Reynolds number is increased by a factor of ten, the transition Reynolds number increases by a factor of approximately 1.7. The present data are also compared with data collected by a number of other investigators in Fig. 5. While there is a considerable amount of variation in the trends shown in Fig. 5, in general, the present data show less of an effect than the majority of the other data shown. It again should be pointed out that the present data were obtained in a ballistics range and are, therefore, immune from unit Reynolds number sensitive "tunnel flow noise" that



is found in the wind-tunnel investigations. However, the other range data, that of Potter (Ref. 10) shown in Fig. 5, also show a much stronger effect of unit Reynolds number than the present data.

(U) Caution should be taken in comparing transition data from various experiments at different conditions. An earlier, comprehensive parametric study in the NOL ballistics ranges of the effects of Mach number, temperature ratio, and body geometry on boundary-layer transition shows that they can have a very strong influence. Also, the effect of these parameters can vary, depending upon the magnitude of the various parameters.

(U) Additional tests have been planned for the NOL 1000-foot Hyperballistics Range to extend the present tests to considerably lower unit Reynolds numbers. The tests will be made with models 4 inches in diameter, 20 inches long. If the trend observed in the present tests continues at the lower unit Reynolds numbers, it will be possible to measure transition at unit Reynolds number as low as  $0.25 \times 10^6$  per inch. This is well within the range of test conditions that can be obtained in wind tunnels and would provide an opportunity for a direct comparison of values measured in wind tunnels and ballistics ranges.

#### REFERENCES

1. Critical Evaluation of Transition from Laminar to Turbulent Shear Layers with Emphasis on Hypersonically Traveling Bodies (U), by M. V. Morkovin. AFFDL TR to be published.
2. Effect of Unit Reynolds Number, Nose Bluntness, and Roughness on Boundary-Layer Transition (U), by J. L. Potter and J. D. Whitfield. AEDC-TR-60-5, Mar 1960.
3. Boundary-Layer Transition under Hypersonic Conditions (U), by J. L. Potter and J. D. Whitfield. AEDC-TR-65-99, May 1965.
4. Investigation of Boundary-Layer Transition on Swept Wings at Mach Numbers 2.5 to 5.0 (U), by S. R. Pate and R. E. Brillhart. AEDC-TDR-63-109, Jul 1963.
5. Effect of Roughness on Transition in Supersonic Flow (U), by E. R. Van Driest and C. B. Blumer. NAA Rept MD 60-329, Mar 1960.

Vol. 1

6. Boundary-Layer Transition at Supersonic Speeds - Three-Dimensional Roughness Effects (Spheres) (U), by E. R. Van Driest and C. B. Blumer. NAA Rept SID 61-275, Aug 1961.
7. Effects of Extreme Surface Cooling on Boundary-Layer Transition (U), by J. R. Jack, R. J. Wisniewski, and N. S. Diaconis. NACA TN 4094, Oct 1957.
8. Experiments on Boundary-Layer Transition at Supersonic Speeds (U), by E. R. Van Driest and J. L. Boison. IAS Journal, Dec 1957.
9. Effects of Radiated Aerodynamic Noise on Model Boundary-Layer Transition in Supersonic and Hypersonic Wind Tunnels (U), by S. R. Pate and C. J. Schueler. AEDC-TR-67-236, Mar 1968.
10. The Influence of Ambient Pressure on Boundary-Layer Transition in an Aeroballistic Range (U), by J. L. Potter. Paper presented at the Aerospace Boundary-Layer Transition Specialists Study Group Meeting at San Bernardino, Calif., 11-12 Jul 1967.
11. Free-Flight Boundary-Layer Transition Investigations at Hypersonic Speeds (U), by N. W. Sheetz, Jr. AIAA Preprint No. 65-127, 1965.
12. Ballistics Range Boundary-Layer Transition Measurements on Cones at Hypersonic Speeds (U), by N. W. Sheetz, Jr. Proceedings of Symposium on Viscous Drag Reduction, LTV, May 1968.
13. Laminar Boundary-Layer Growth on Slightly Blunted Cones at Hypersonic Speeds (U), by R. E. Wilson. Journal of Spacecraft Rockets, Vol 2, No. 4, Jul-Aug 1965.

is found in the wind-tunnel investigations. However, the other range data, that of Potter (Ref. 10) shown in Fig. 5, also show a much stronger effect of unit Reynolds number than the present data.

(U) Caution should be taken in comparing transition data from various experiments at different conditions. An earlier, comprehensive parametric study in the NOL ballistics ranges of the effects of Mach number, temperature ratio, and body geometry on boundary-layer transition shows that they can have a very strong influence. Also, the effect of these parameters can vary, depending upon the magnitude of the various parameters.

(U) Additional tests have been planned for the NOL 1000-foot Hyperballistics Range to extend the present tests to considerably lower unit Reynolds numbers. The tests will be made with models 4 inches in diameter, 20 inches long. If the trend observed in the present tests continues at the lower unit Reynolds numbers, it will be possible to measure transition at unit Reynolds number as low as  $0.25 \times 10^6$  per inch. This is well within the range of test conditions that can be obtained in wind tunnels and would provide an opportunity for a direct comparison of values measured in wind tunnels and ballistics ranges.

#### REFERENCES

1. Critical Evaluation of Transition from Laminar to Turbulent Shear Layers with Emphasis on Hypersonically Traveling Bodies (U), by M. V. Morkovin. AFFDL TR to be published.
2. Effect of Unit Reynolds Number, Nose Bluntness, and Roughness on Boundary-Layer Transition (U), by J. L. Potter and J. D. Whitfield. AEDC-TR-60-5, Mar 1960.
3. Boundary-Layer Transition under Hypersonic Conditions (U), by J. L. Potter and J. D. Whitfield. AEDC-TR-65-99, May 1965.
4. Investigation of Boundary-Layer Transition on Swept Wings at Mach Numbers 2.5 to 5.0 (U), by S. R. Pate and R. E. Brillhart. AEDC-TDR-63-109, Jul 1963.
5. Effect of Roughness on Transition in Supersonic Flow (U), by E. R. Van Driest and C. B. Blumer. NAA Rept MD 60-329, Mar 1960.



Vol. 1

6. Boundary-Layer Transition at Supersonic Speeds - Three-Dimensional Roughness Effects (Spheres) (U), by E. R. Van Driest and C. B. Blumer. NAA Rept SID 61-275, Aug 1961.
7. Effects of Extreme Surface Cooling on Boundary-Layer Transition (U), by J. R. Jack, R. J. Wisniewski, and N. S. Diaconis. NACA TN 4094, Oct 1957.
8. Experiments on Boundary-Layer Transition at Supersonic Speeds (U), by E. R. Van Driest and J. L. Boison. IAS Journal, Dec 1957.
9. Effects of Radiated Aerodynamic Noise on Model Boundary-Layer Transition in Supersonic and Hypersonic Wind Tunnels (U), by S. R. Pate and C. J. Schueler. AEDC-TR-67-236, Mar 1968.
10. The Influence of Ambient Pressure on Boundary-Layer Transition in an Aeroballistic Range (U), by J. L. Potter. Paper presented at the Aerospace Boundary-Layer Transition Specialists Study Group Meeting at San Bernardino, Calif., 11-12 Jul 1967.
11. Free-Flight Boundary-Layer Transition Investigations at Hypersonic Speeds (U), by N. W. Sheetz, Jr. AIAA Preprint No. 65-127, 1965.
12. Ballistics Range Boundary-Layer Transition Measurements on Cones at Hypersonic Speeds (U), by N. W. Sheetz, Jr. Proceedings of Symposium on Viscous Drag Reduction, LTV, May 1968.
13. Laminar Boundary-Layer Growth on Slightly Blunted Cones at Hypersonic Speeds (U), by R. E. Wilson. Journal of Spacecraft Rockets, Vol 2, No. 4, Jul-Aug 1965.

TABLE 1

Shot No.	$M_\infty$	$P_\infty$ torr	$X_{tr}$ in.	$Re_{s,tr}$ $\times 10^{-6}$	$Me$	$Re/in.$ $\times 10^{-6}$
5462	7.7	503	2.5	9.3	6.8	3.7
5474	8.3	538	2.5	11.6	7.4	3.6
6435	7.6	1520	1.05	11.4	6.7	10.8
6436	7.8	1520	1.23	14.3	7.0	11.6
1346	7.5	150	7.0	7.7	7.0	1.1
1350	7.3	175	6.5	8.0	6.6	1.2

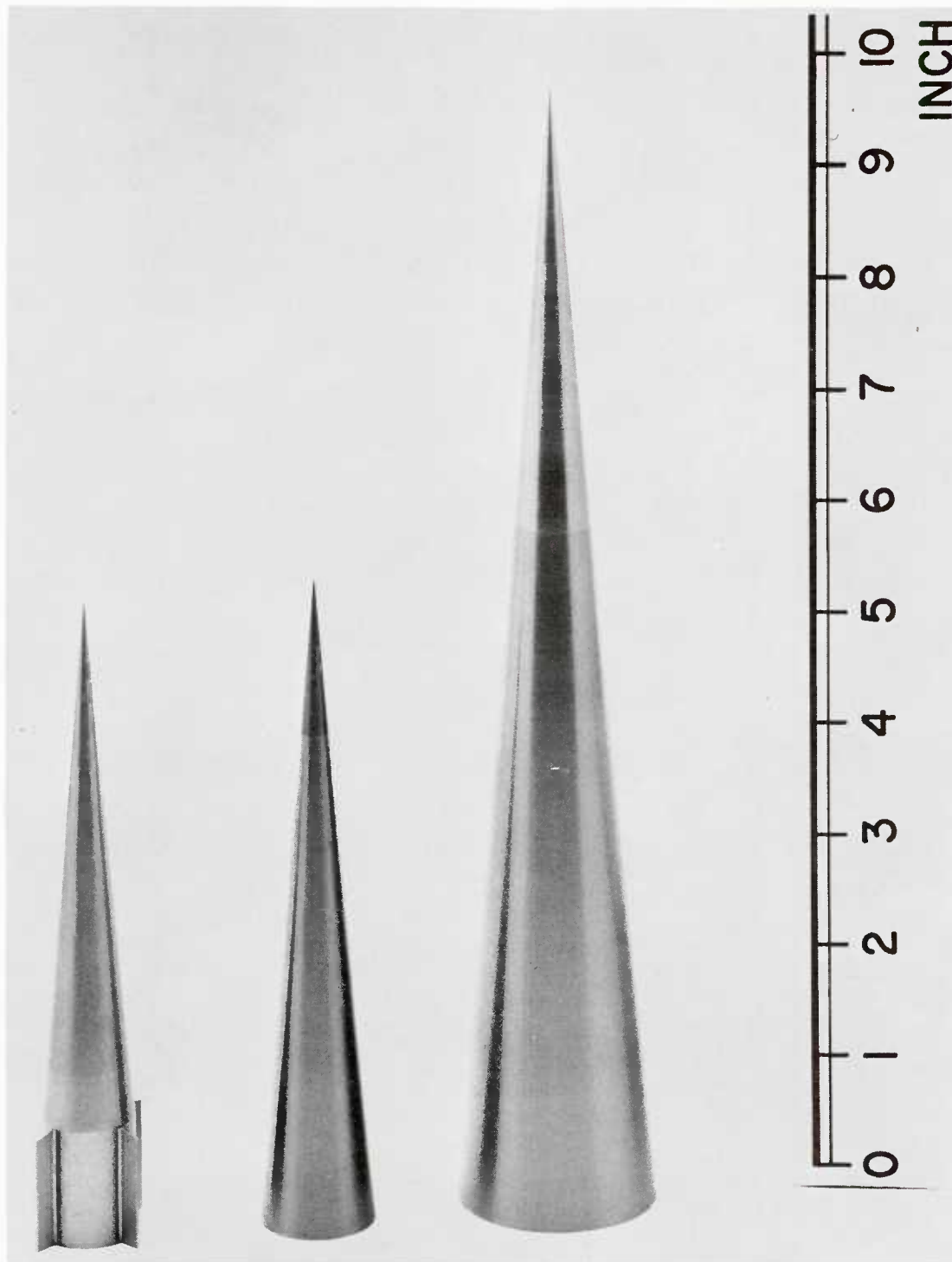


FIG. 1. Range Models

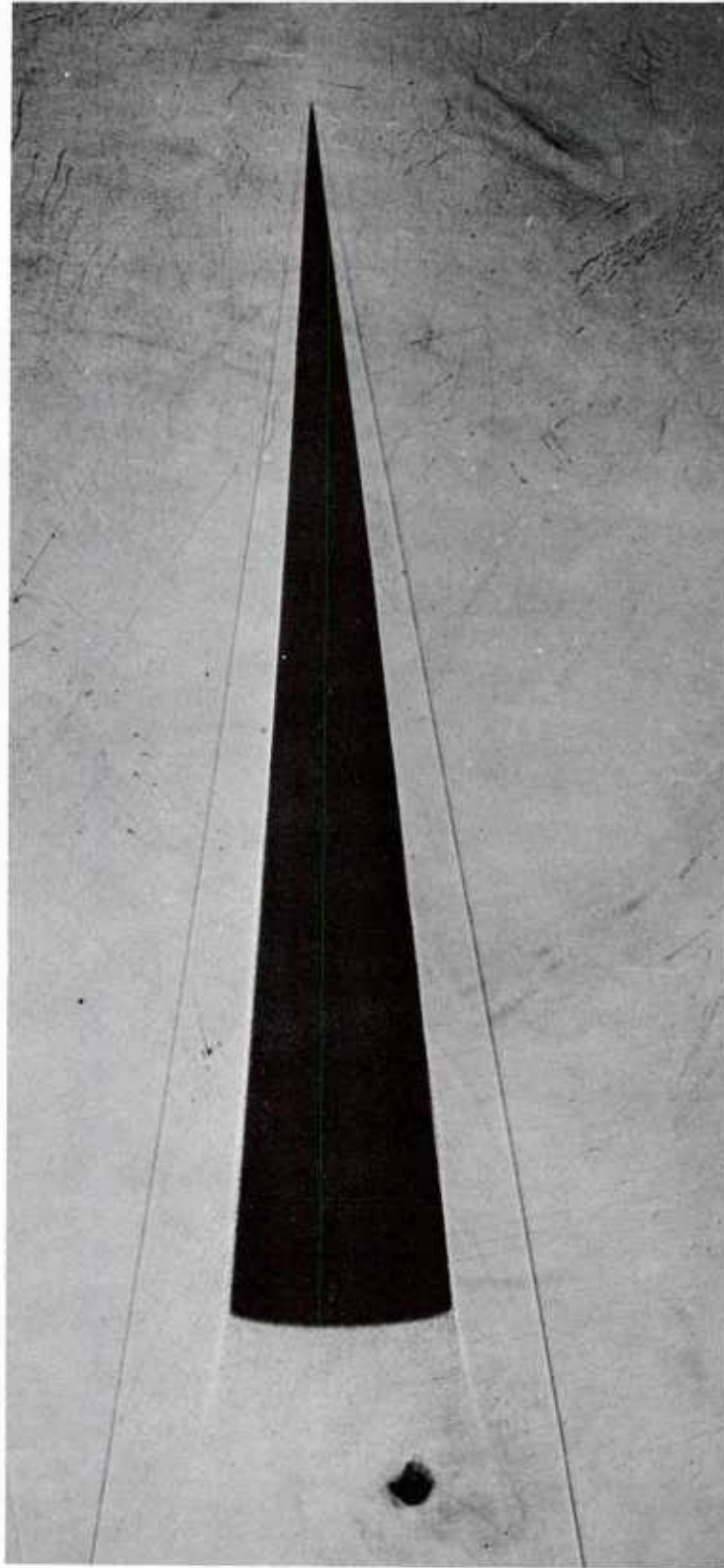


FIG. 2. Shadowgraph of Model in Flight

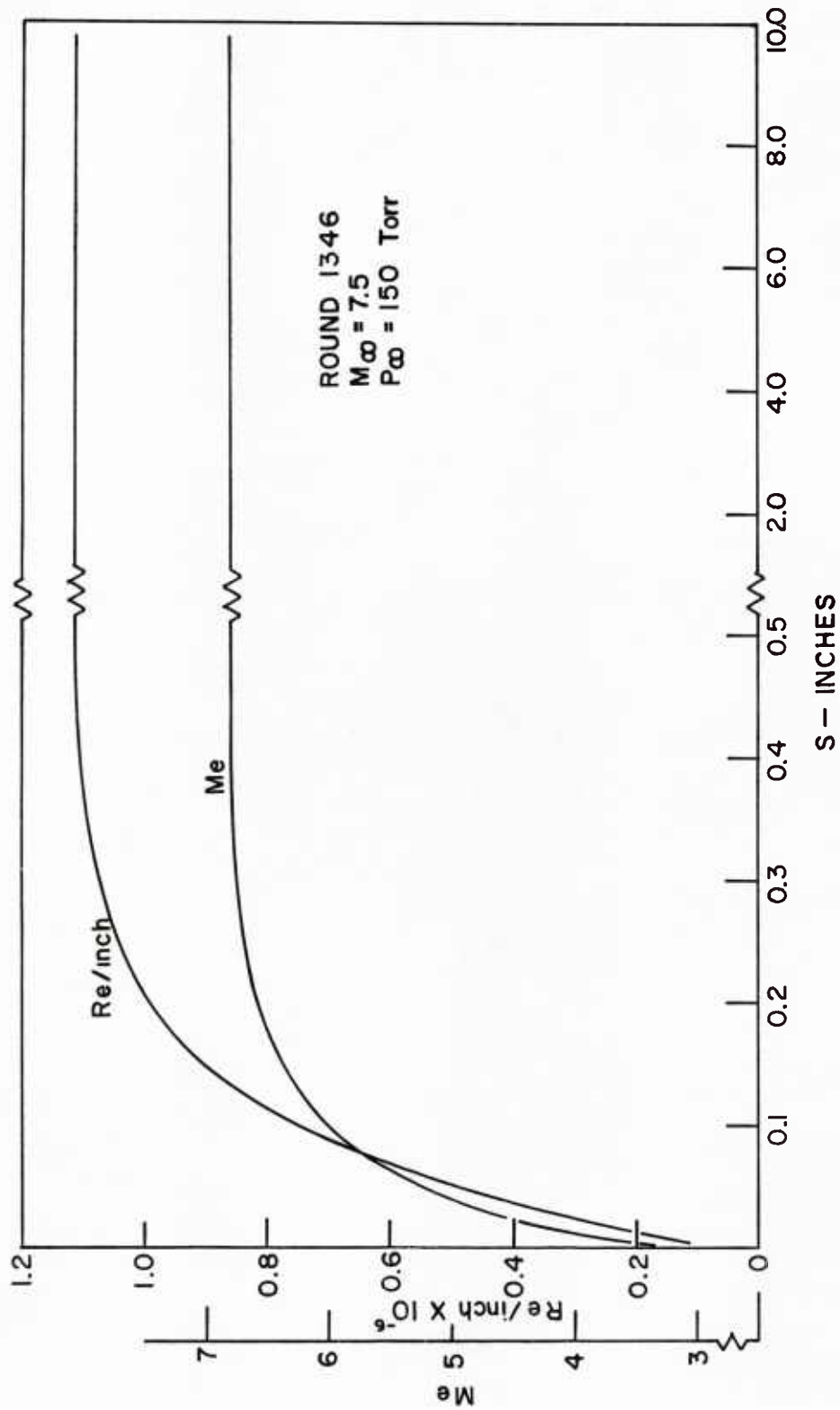


FIG. 3 DISTRIBUTION OF LOCAL PROPERTIES ALONG MODEL SURFACE.

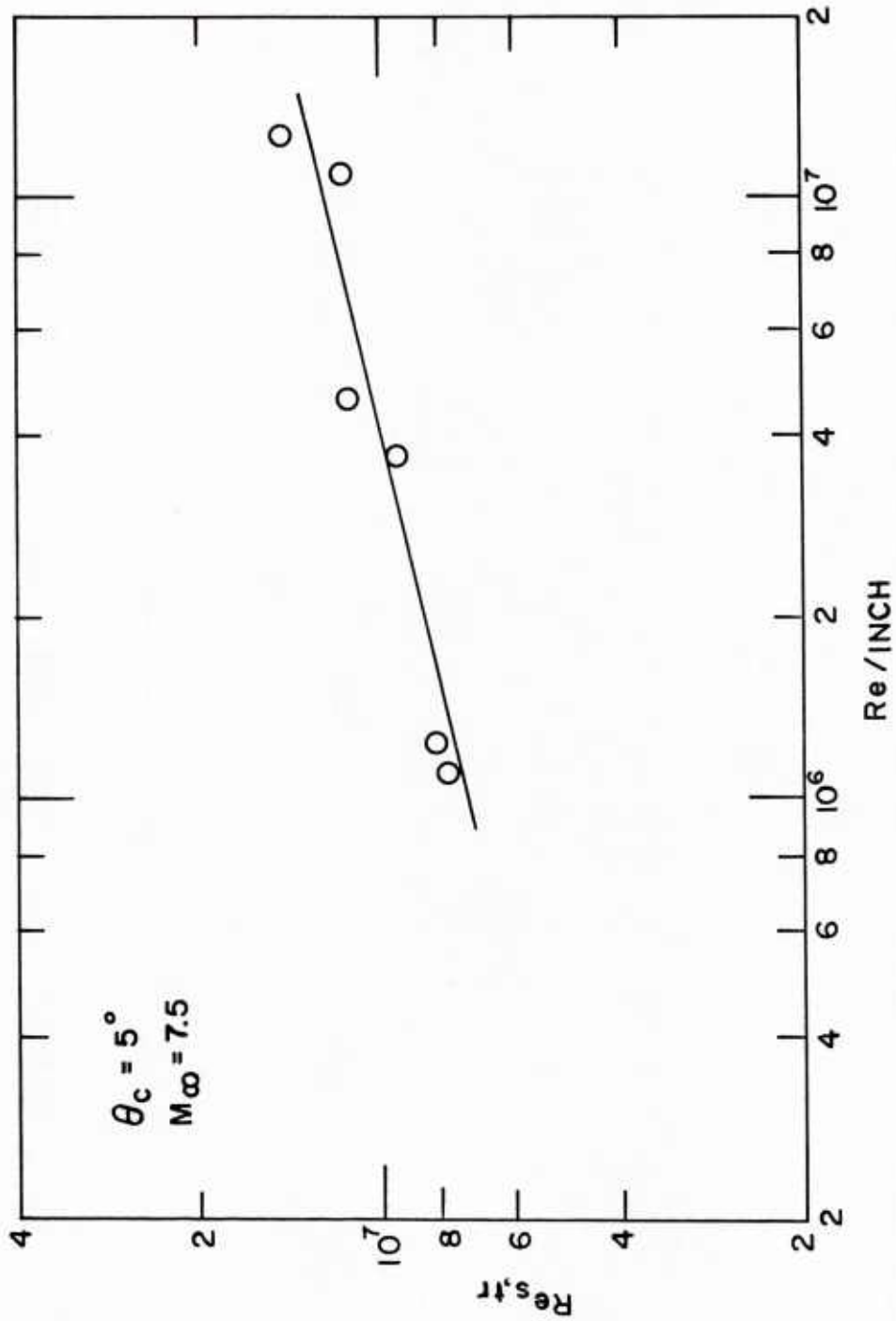


FIG. 4 EFFECT OF UNIT REYNOLDS NUMBER ON  
CURRENT TESTS.



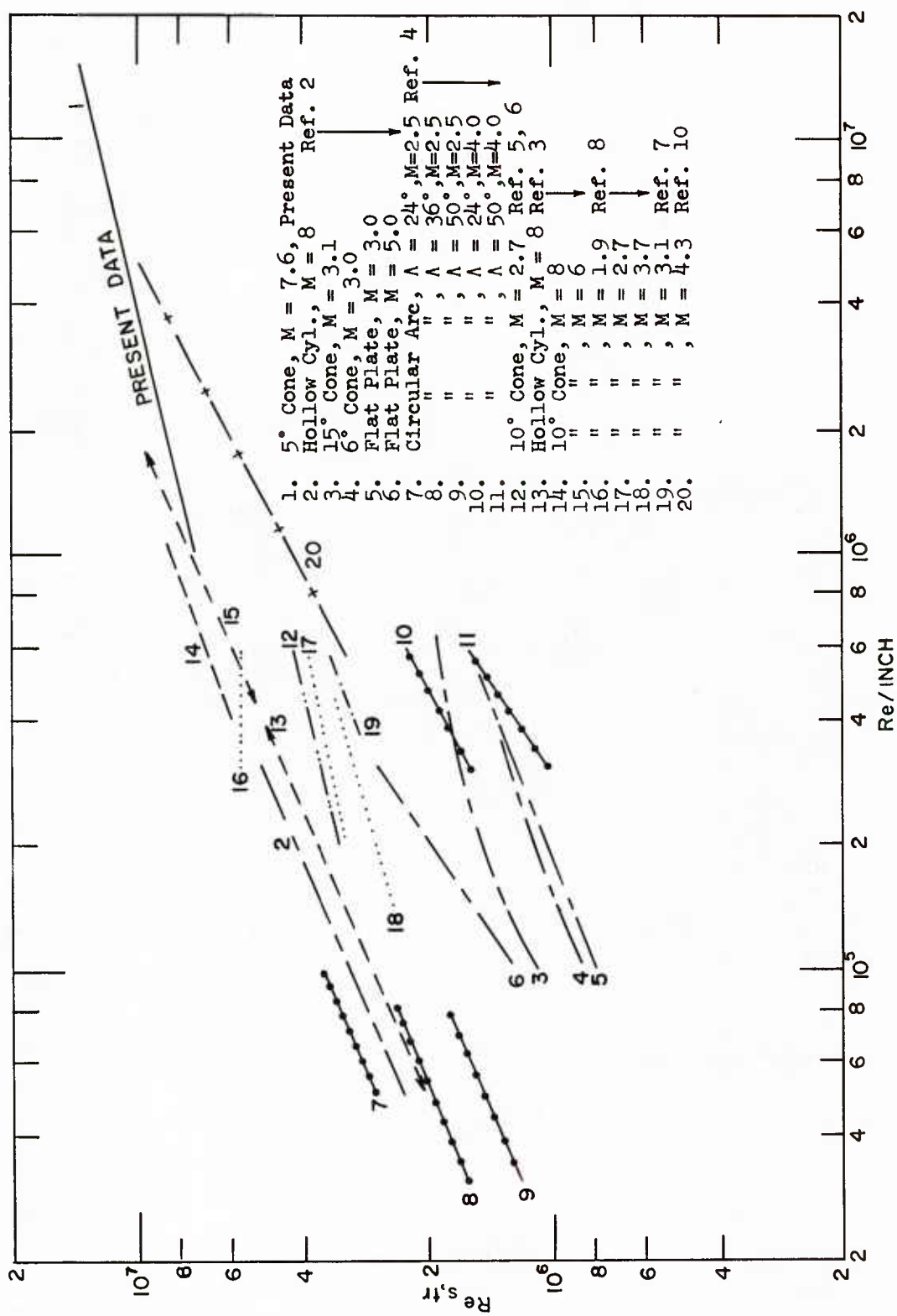


FIG. 5 SUMMARY OF UNIT REYNOLDS NUMBER EFFECTS.

Paper No. 8

CALCULATION OF BLUNT BODY FLOWS USING PADÉ FRACTIONS  
AND THE METHOD OF CHARACTERISTICS  
(U)

(Paper UNCLASSIFIED)

by

Andrew H. Van Tuyl  
Naval Ordnance Laboratory  
White Oak, Silver Spring, Md. 20910

ABSTRACT. (U) A procedure is given for calculating the axially symmetric flow of a perfect gas past a blunt body of revolution, using a method involving Padé fractions in the subsonic region, and the method of characteristics in the supersonic region. The method of calculation in the subsonic region uses the Taylor expansion of the stream function in the neighborhood of the nose of the shock. It is an extension of one published earlier, generalized to include calculation of an arbitrary number of terms of the Taylor expansion. Calculations are made in several special cases, using a method of characteristics program written for the IBM 7090 by R. H. Thompson at the Naval Ship Research and Development Center. The examples computed include sphere-cones, sphere-cylinders, spheroid-cones, and spheroid-cylinders. The extent to which the accuracy in the supersonic region is affected by the number of terms of the Taylor expansion used is investigated.

## INTRODUCTION

(U) A number of methods for calculating the axially symmetric supersonic flow past a blunt body of revolution have appeared in the literature (Refs. 1 and 2, for example). These include inverse methods, in which the bow shock is given and the body which would produce it is calculated, and direct methods, in which the body is given. When the nose of the body is given by a single analytic equation throughout the subsonic region and beyond, it is often possible to solve the direct problem in a region containing the sonic line by iteration of the solution of the inverse problem. If the entire flow over a given body is desired, these methods must usually be supplemented by another method, such as the method of characteristics. Computer programs for calculating axially symmetric flow by the method of characteristics are readily available, as described, for example, in Refs. 3 and 4.

(U) Procedures for finding the Taylor expansion of the stream function in the neighborhood of the nose of the shock in the case of a perfect gas have been given by Lin and Shen (Ref. 5) and Cabannes (Refs. 6 and 7). Calculations by Van Dyke (Refs. 2 and 8) indicate that this Taylor expansion diverges at the body for all free stream Mach numbers, and therefore cannot be used directly to calculate the flow. As shown in Ref. 9, the use of Padé fractions obtained from the Taylor expansion is a means of obtaining convergence. Other methods for removing the divergence of the Taylor expansion at the body have been given by Lewis (Ref. 10), Leavitt (Ref. 11), and Sanematsu and Chapkis (Ref. 12). Moran (Ref. 13) also uses Padé fractions, but his method differs considerably from the present one.

(U) In Ref. 14, a method for calculating the axially symmetric flow of a perfect gas past a blunt body is given in which terms of the Taylor expansion up to and including degree 8 are used. In the present paper, the method of Ref. 14 is generalized to include calculation of an arbitrary number of terms of the Taylor expansion of the stream function, and a procedure is given for calculation of initial values for use with the method of characteristics. Calculations are carried out in several special cases, using a method of characteristics program written for the IBM 7090 by R. H. Thompson at the Naval Ship Research and Development Center (Ref. 4). The examples chosen include sphere-cones, sphere-cylinders, spheroid-cones, and spheroid-cylinders. The number of terms of the Taylor expansion used in these calculations is varied in order to investigate how the downstream accuracy is affected. It is of interest to determine how many terms of the Taylor expansion are required for reasonable accuracy, since the computing time increases rapidly as the number of terms increases.

## OUTLINE OF THE METHOD

(U) As in Ref. 14, let  $x$  and  $r$  be cylindrical coordinates with origin at the nose of the body. We will consider a perfect gas with ratio of specific heats  $\gamma$ . The flow ahead of the shock is assumed uniform and parallel to the  $x$ -axis, with Mach number  $M_\infty$ , density  $\rho_\infty$ , velocity magnitude  $q_\infty$ , and pressure  $p_\infty = \rho_\infty q_\infty^2 / M_\infty^2 \gamma$ . Let  $x_0$  be the shock detachment distance, and let  $R_s$  and  $R_b$  be the radii of curvature of the shock and body noses, respectively. Then for small  $r$ , we will assume that the equations of the shock and body have expansions of the forms

$$\left(\frac{r}{R_s}\right)^2 = 2\left(\frac{x + x_0}{R_s}\right) - B_s \left(\frac{x + x_0}{R_s}\right)^2 + \dots \quad (1)$$

and

$$\left(\frac{r}{R_b}\right)^2 = 2\left(\frac{x}{R_b}\right) - B_b \left(\frac{x}{R_b}\right)^2 + \dots \quad (2)$$

respectively. In agreement with existing notation, the coefficients  $B_s$  and  $B_b$  are called the bluntnesses of the shock and body, respectively. We will assume that  $R_s$  and  $R_b$  are finite and non-zero.

(U) The method of calculation to be described is a direct generalization of that of Ref. 14 to an arbitrary number of terms of the Taylor expansion of the stream function. The Taylor expansions of the stream function and density are first obtained in cylindrical coordinates, starting from Bernoulli's equation and the vorticity equation, as in Ref. 5. The Taylor expansion of the stream function is then transformed to a new system of orthogonal coordinates  $\tau$  and  $\xi$ , as shown in Fig. 1, in which the shock is the coordinate surface  $\tau = 0$ . Rational expressions are obtained for the flow on the body and in the shock layer, as in Ref. 14. Calculations are carried out using subroutines for manipulation of power series. The subroutines used for raising a single or double power series to an arbitrary power are based on algorithms due to Leavitt (Ref. 15).

(U) In the direct problem, a shock is found by iteration from a two-parameter family of rational shock equations. The flow along the body is obtained as a function of the arc length in the inverse problem, and the same variation with respect to arc length is assumed to hold along the given body. Thus, the calculated body in the solution of the inverse problem is never used directly in the calculation of the flow, but only as a means of deciding when a satisfactory shock has been found.

(U) Finally, initial values for use with the method of characteristics are calculated along a suitable curve of the form  $\xi = \text{constant}$ . The curve  $\xi = \text{constant}$ , and the flow quantities along it, are approximated by means of cubics in  $x$  interpolated through four values.

SOLUTION OF THE INVERSE PROBLEM

THE TAYLOR EXPANSIONS IN CYLINDRICAL COORDINATES

(U) If we take  $\rho_\infty = q_\infty = 1$  and make the substitution  $r = z^{1/2}$ , then Bernoulli's equation and the vorticity equation become

$$\frac{\Psi^2}{z} + 4\Psi \frac{\Psi}{z} + \frac{2\gamma}{\gamma-1} F(\Psi) \rho^{\gamma+1} - 2C\rho^2 = 0 \quad (3)$$

and

$$\rho \left( \frac{\Psi}{z} + 4\Psi \frac{\Psi}{z} \right) - \frac{\rho}{z} \frac{\Psi}{z} + \rho^{\gamma+2} \frac{F'(\Psi)}{\gamma-1} = 0 \quad (4)$$

respectively, where

$$C = \frac{1}{2} + \frac{1}{(\gamma-1) M_\infty^2} \quad (5)$$

and  $F(\Psi)$  depends on the shock shape. As in Ref. 5, we have

$$F(\Psi) = \frac{1}{M_\infty^2} \left( \frac{2\gamma}{\gamma+1} M_\infty^2 \sin^2 \sigma - \frac{\gamma-1}{\gamma+1} \right) \left( \frac{\gamma-1}{\gamma+1} + \frac{2}{(\gamma+1) M_\infty^2 \sin^2 \sigma} \right)^\gamma \quad (6)$$

along the shock, where  $\sigma$  is the angle between the shock and the free stream. Denoting the equation of the shock by  $z = z(x)$ , we have

$$\sin^2 \sigma = \frac{z'^2(x)}{4z(x) + z'^2(x)} \quad (7)$$

The values of  $\Psi$  and  $\rho$  on the shock are given by

$$\Psi = \frac{1}{2} z \quad (8)$$

and

$$\rho = \left( \frac{\gamma-1}{\gamma+1} + \frac{2}{(\gamma+1) M_\infty^2 \sin^2 \sigma} \right)^{-1} \quad (9)$$

In order to find the Taylor expansions of  $\Psi$  and  $\rho$  when the expansion of equation (1) is given, it is convenient to set  $R_s = 1$ . We can then find the Taylor expansions in the forms

$$\Psi = \sum_{i=0}^{\infty} \sum_{j=0}^{\infty} \Psi_{ij} z^{i+1} (x + x_0)^j \quad (10)$$

and

$$\rho = \sum_{i=0}^{\infty} \sum_{j=0}^{\infty} \rho_{ij} z^i (x + x_0)^j, \quad (11)$$

respectively. The first step in the calculation of the coefficients is to expand the right-hand sides of equations (6) and (9) in powers of  $\Psi$  and  $x + x_0$ , respectively. The former expansion is obtained from (6), (7), and (8), and the latter, from (7) and (9). On substituting (10) and (11) in (3) and (4) and collecting coefficients of  $z^i(x + x_0)^j$ , we obtain algebraic relations  $A_{ij} = 0$  and  $B_{ij} = 0$ , respectively, between the coefficients of (10) and (11). The  $A_{ij}$  and  $B_{ij}$  are functions of  $\Psi_{mn}$  and  $\rho_{mn}$  for values of  $m \leq i$  and  $n \leq j$ . Similarly, substituting (1) and (10) in (8), and (1) and (11) in (9) and collecting coefficients of  $(x + x_0)^i$ , we obtain algebraic relations  $C_i = 0$  and  $D_i = 0$ . As before,  $C_i$  and  $D_i$  are functions of  $\Psi_{mn}$  and  $\rho_{mn}$  for values of  $m \leq i$  and  $n \leq j$ . These four sets of relations are sufficient to determine all the  $\Psi_{ij}$  and  $\rho_{ij}$ .

(U) The coefficients  $\Psi_{1,0}$ ,  $\Psi_{0,1}$ ,  $\rho_{1,0}$ , and  $\rho_{0,1}$  are found by solving the four simultaneous equations  $A_{1,0} = 0$ ,  $A_{0,1} = 0$ ,  $C_1 = 0$ , and  $D_1 = 0$ . The determination of these coefficients is special, since it involves the choice of the root of a quadratic equation. For  $k > 1$ , the equations  $A_{k,0} = 0$ ,  $A_{k-1,1} = 0$ ,  $C_k = 0$ , and  $D_k = 0$  are four simultaneous linear equations for the coefficients  $\Psi_{k,0}$ ,  $\Psi_{k-1,1}$ ,  $\rho_{k,0}$ , and  $\rho_{k-1,1}$ . All other coefficients  $\Psi_{ij}$  and  $\rho_{ij}$  such that  $2i + j = 2k - 1$  or  $2k$  are then found by recursion.

(U) All the substitutions just described are carried out using subroutines for power series manipulations. When  $K-1$  terms of the series for the shock equation are given, we can calculate the  $\Psi$  and  $\rho$  for  $0 \leq i \leq K-1$  and  $0 \leq j \leq 2K-2i-2$ . In the following, the number of terms used will be specified by the preceding integer  $K$ . Thus, for a given value of  $K$ ,  $K-1$  terms of the series in equation (1) are used.

(U) Finally, we can rewrite (10) and (11) in terms of arbitrary values of the reference quantities in the forms

$$\frac{\Psi}{\rho_{\infty} q_{\infty} R_s^2} = \sum_{i=0}^{\infty} \sum_{j=0}^{\infty} \Psi_{ij} \left( \frac{z}{R_s^2} \right)^{i+1} \left( \frac{x + x_0}{R_s} \right)^j \quad (12)$$

and

$$\frac{\rho}{\rho_{\infty}} = \sum_{i=0}^{\infty} \sum_{j=0}^{\infty} \rho_{ij} \left( \frac{z}{R_s^2} \right)^i \left( \frac{x + x_0}{R_s} \right)^j, \quad (13)$$

respectively.

#### A COORDINATE TRANSFORMATION

(U) As in Ref. 14, let the equation of the shock curve be given by



## Vol. 1

$$\frac{x + x_0}{R_s} = f\left(\frac{r^2}{R_s^2}\right). \quad (14)$$

Then a transformation to coordinates  $\tau$  and  $\xi$  will be defined by the relation

$$\frac{x + x_0}{R_s} + i \frac{r}{R_s} = U(\zeta), \quad (15)$$

where

$$U(\zeta) = \zeta + f(-\zeta^2) \quad (16)$$

and  $\zeta = \tau + i\xi$ . This transformation is orthogonal and isometric, and is such that the shock coincides with the coordinate surface  $\tau = 0$ .

(U) It follows from equation (15) that

$$\frac{x + x_0}{R_s} = \sum_{i=0}^{\infty} \frac{(-1)^i U^{(2i)}(\tau)}{(2i)!} \xi^{2i} \quad (17)$$

and

$$\frac{r}{R_s} = \sum_{i=0}^{\infty} \frac{(-1)^i U^{(2i+1)}(\tau)}{(2i+1)!} \xi^{2i+1}, \quad (18)$$

where the superscripts denote differentiation.

(U) In order to express the Taylor expansion of  $\Psi$  in terms of  $\tau$  and  $\xi$ , we substitute (17) and (18) in (12) by means of subroutines for power series manipulations. We will write the resulting series as a single power series of the form

$$\frac{\Psi}{\rho_{\infty} q_{\infty} R_s^2} = \bar{\Psi} = \sum_{i=1}^{\infty} \bar{\Psi}_i(\tau) \xi^{2i}, \quad (19)$$

where

$$\bar{\Psi}_{i+1}(\tau) = \sum_{j=0}^{\infty} \Psi_{ij} \tau^j. \quad (20)$$

When  $K-1$  terms of the series for the shock equation are used, the series for  $\bar{\Psi}_i(\tau)$  is known through the term of degree  $2K-2i$ .

(U) We note that it is also possible to write equation (20) as a single power series in  $\tau$  with coefficients which are functions of  $\xi^2$ . This is one of two possibilities which are considered by Moran in Ref. 13. The preceding form was chosen in the present paper, however,

because of the fact that coefficients of the expansions of the body equation and flow quantities in power of  $\xi$  are given exactly by finite combinations of the  $\bar{\Psi}_i(\tau)$  and their derivatives. In the calculation of the flow behind a given shock, approximations for the  $\bar{\Psi}_i(\tau)$  and their derivatives need to be calculated only once.

#### PADÉ FRACTIONS

(U) Given a power series

$$f(z) = \sum_{i=0}^{\infty} c_i z^i \quad (21)$$

with  $c_0 \neq 0$ , the Padé fraction  $f_{k,n}(z)$ ,  $k \geq 0$ ,  $n \geq 0$ , is defined as follows: it is a rational fraction with numerator and denominator of degrees less than or equal to  $n$  and  $k$ , respectively, such that the Taylor expansion of  $f_{k,n}(z)$  at the origin agrees with equation (21) to more terms than that of any other rational fraction with numerator of degree  $\leq n$  and denominator of degree  $\leq k$  (Ref. 16). It is determined by the first  $n + k + 1$  coefficients of equation (21), and is unique. When  $k$  is not too large,  $f_{k,n}(z)$  can be calculated conveniently as the quotient of two determinants of order  $k + 1$  or less (Ref. 17, equation (75)). For larger values of  $k$ , the OD algorithm of Rutishauser (Ref. 18) is a convenient method of calculation.

(U) Padé fractions with  $k$  and  $n$  equal or nearly equal often give good results for relatively small values of  $n$ , even when the given power series does not converge. A proof of convergence is not available in the present problem, but numerical results indicate that the sequences of Padé fractions obtained converge at the body, while the original power series diverge.

(U) Finally, the following property of Padé fractions is of importance in the calculation of the flow in the shock layer: Let  $f(z)$  be a rational function reduced to lowest terms with numerator of degree  $q$  and denominator of degree  $p$ . Then  $f_{k,n}(z)$  is identical with  $f(z)$  when  $k \geq p$  and  $n \geq q$ . This result is discussed in Ref. 17, page 22.

#### RATIONAL APPROXIMATIONS FOR THE $\bar{\Psi}_i(\tau)$ AND THEIR DERIVATIVES

(U) We will obtain rational approximations for the  $\bar{\Psi}_i(\tau)$  and their derivatives by forming Padé fractions from the corresponding partial sums. The  $\bar{\Psi}_i(\tau)$  and their even derivatives are replaced by rational functions with numerator and denominator of equal degrees, and all odd derivatives are replaced by fractions in which the degree of the denominator exceeds that of the numerator by one.

(U) The accuracy of these rational approximations is greatest at the shock, and decreases as the body is approached. When  $K - 1$  terms of the series for the shock are given, the rational approximations for

## Vol. 1

the  $\bar{\Psi}_i(\tau)$  are sufficiently accurate at the body only for  $i$  less than about  $K/2$ . Similarly, the order of the derivatives of  $\bar{\Psi}_1(\tau)$  must be less than about  $K/2 - i$  at the body.

## CALCULATION OF THE BODY

(U) In coordinates  $\tau$  and  $\xi$ , the equation of the body is given by a series of the form

$$\tau - \tau_0 = a_1 \xi^2 + a_2 \xi^4 + \dots, \quad (22)$$

where  $\tau_0$  is the smallest positive root of the equation  $\bar{\Psi}_1(\tau) = 0$ . When  $K - 1$  terms of the series for the shock equation are given, the numerator and denominator of  $\bar{\Psi}_1(\tau)$  are of degree  $K - 1$ . We obtain the coefficients in equation (22) successively by substituting (22) in (19), collecting like powers of  $\xi^2$ , and equating the coefficients to zero. Substituting (22) in (17) and (18) and collecting like powers of  $\xi$ , we obtain  $x/R_s$  and  $r/R_s$  along the body as power series in  $\xi$ , together with values of  $x_0/R_b$  and  $R_b/R_s$ . Finally, eliminating  $\xi$  between these equations, we obtain the equation of the body in the form shown in equation (2).

(U) The coefficients of equation (2) calculated in this way involve the  $\bar{\Psi}_1(\tau)$  and their derivatives evaluated for  $\tau = \tau_0$ . When  $K - 1$  terms of equation (1) are given, we can calculate only about  $K/2$  terms of equation (2) with sufficient accuracy.

(U) We obtain increased accuracy in the calculation of the body by replacing the right hand side of equation (2) by a Padé fraction. When  $K = 9, 10$ , and  $11$ , the rational approximation found in this way is of the form

$$\left(\frac{r}{R_b}\right)^2 = 2 \left(\frac{x}{R_b}\right) \frac{1 + b_1(x/R_b) + b_2(x/R_b)^2}{1 + b_3(x/R_b) + b_4(x/R_b)^2} \quad (23)$$

(U) We also need an expansion for  $\xi$  in powers of the arc length  $s$  along the body. From equation (18) and the expansion of the arc length in powers of  $r$ , and using the calculated value of  $R_b/R_s$ , we obtain

$$\xi = h_1 \left(\frac{s}{R_b}\right) + h_2 \left(\frac{s}{R_b}\right)^3 + \dots \quad (24)$$

When  $K = 11$ , we find a rational approximation of the form

$$\xi^2 \approx h_1^2 \left(\frac{s}{R_s}\right)^2 \frac{1 + H_1(s/R_b)^2 + H_2(s/R_b)^4}{1 + H_3(s/R_b)^2 + H_4(s/R_b)^4} \quad (25)$$

## CALCULATION OF THE FLOW ON THE BODY

(U) We obtain the density on the body from the equation

$$\frac{\bar{\psi}_\tau^2 + \bar{\psi}_\xi^2}{(r/R_s)^2 |U'(\xi)|^2} = 2C \left( \frac{\rho_{st}}{\rho_\infty} \right)^2 \left[ \left( \frac{\rho}{\rho_{st}} \right)^2 - \left( \frac{\rho}{\rho_{st}} \right)^{\gamma+1} \right] \quad (26)$$

where  $\rho_{st}$  is the density at the stagnation point. We have

$$\frac{\rho_{st}}{\rho_\infty} = \left[ \frac{(\gamma - 1)C}{\gamma F(0)} \right]^{\frac{1}{\gamma-1}} \quad (27)$$

Substituting the expansion

$$\frac{\rho}{\rho_{st}} = 1 + d_1 \xi^2 + d_2 \xi^4 + \dots \quad (28)$$

in equation (26) and collecting like powers of  $\xi^2$ , we can determine the coefficients of equation (26) successively. Finally, from (24) and (28), we have

$$\frac{\rho}{\rho_{st}} = 1 + r_1 \left( \frac{s}{R_b} \right)^2 + r_2 \left( \frac{s}{R_b} \right)^4 + \dots \quad (29)$$

We obtain expansion for the pressure and velocity magnitude on the body by substituting (28) in the equations

$$\frac{p}{p_{st}} = \left( \frac{\rho}{\rho_{st}} \right)^\gamma \quad (30)$$

and

$$\frac{q}{q_\infty} = \left\{ 2C \left[ 1 - \left( \frac{\rho}{\rho_{st}} \right)^{\gamma-1} \right] \right\}^{1/2} \quad (31)$$

respectively, where

$$p_{st} = \rho_\infty q_\infty^2 F(0) \left( \frac{\rho_{st}}{\rho_\infty} \right)^\gamma \quad (32)$$

is the pressure at the stagnation point.

(U) As in the calculation of the body, it is found that convergence is improved when the preceding partial sums are replaced by Padé fractions. When  $K = 11$ , we have

$$\frac{q}{q_\infty} \approx \frac{\alpha_1 (s/R_b) + \alpha_2 (s/R_b)^3}{1 + \alpha_3 (s/R_b)^2 + \alpha_4 (s/R_b)^4} \quad (33)$$

and

$$\frac{p}{p_{st}} \approx \frac{1 + P_1(s/R_b)^2 + P_2(s/R_b)^4}{1 + P_3(s/R_b)^2 + P_4(s/R_b)^4} \quad (34)$$

with an approximation of the same form as (34) for  $\rho/\rho_{st}$ .

#### CALCULATION OF THE FLOW IN THE SHOCK LAYER

(U) Immediately behind the shock, the quantities  $u$ ,  $p$ ,  $\rho$ ,  $c^2$ , and  $q^2$ , where  $u$  is the x-component of velocity and  $c$  is the speed of sound, are rational functions of  $\cos^2\sigma$  such that the degrees of the numerators and denominators are less than or equal to 2 and 1, respectively (Ref. 19). As in Fig. 1, let  $\alpha$  at a given point be the angle between the tangent to the curve  $\tau = \text{constant}$  at that point and the positive x-axis. Since  $\alpha$  is equal to  $\sigma$  at the shock, it follows from the special property of Padé fractions stated earlier that if we expand the preceding flow quantities in powers of  $\cos^2\alpha$  in the shock layer, then all Padé fractions formed from these series with  $k \geq 1$  and  $n \geq 2$  are exact at the shock.

(U) In order to find these expansions, we first obtain expansions in powers of  $\xi^2$ . In coordinates  $\tau$  and  $\xi$ , Bernoulli's equation becomes

$$\frac{\bar{\Psi}_\tau^2 + \bar{\Psi}_\xi^2}{(r/R_s)^2 |U'(\xi)|^2} + \frac{2\gamma F(\Psi)}{\gamma-1} \left( \frac{\rho}{\rho_\infty} \right)^{\gamma+1} = 2C \left( \frac{\rho}{\rho_\infty} \right)^2 \quad (35)$$

Substituting the expansion

$$\frac{\rho}{\rho_\infty} = R_1(\tau) + R_2(\tau)\xi^2 + R_3(\tau)\xi^4 + \dots \quad (36)$$

in equation (35), collecting like powers of  $\xi^2$ , and equating the coefficients to zero, we first obtain

$$\frac{2\gamma F(0)}{\gamma-1} R_1^{\gamma+1} - 2C R_1^2 + \frac{4\bar{\Psi}_1^2}{U'^4} = 0 \quad (37)$$

For a given value of  $\tau$ , equation (37) is easily solved for  $R_1$  by Newton's method. After finding  $R_1$ , we calculate the remaining coefficients in (36) by recursion.

(U) We obtain expansions of the same form as equation (36) for  $p/\rho_\infty q_\infty^2$ ,  $(c/q_\infty)^2$ , and  $(q/q_\infty)^2$  by using the relations

$$\frac{p}{\rho_\infty q_\infty^2} = F(\Psi) \left( \frac{\rho}{\rho_\infty} \right)^\gamma, \quad (38)$$

$$\left(\frac{c}{q_\infty}\right)^2 = \gamma \frac{p/\rho_\infty q_\infty^2}{\rho/\rho_\infty}, \quad (39)$$

and

$$\left(\frac{q}{q_\infty}\right)^2 + \frac{2}{\gamma-1} \left(\frac{c}{q_\infty}\right)^2 = 2C \quad (40)$$

in the order given. Finally, we obtain an expansion for  $u/q_\infty$  by expanding

$$\frac{\rho u}{\rho_\infty u_\infty} = \frac{-(x/R_s)_\xi \bar{\Psi}_\tau + (x/R_s)_\tau \bar{\Psi}_\xi}{(r/R_s) |U'(\zeta)|^2} \quad (41)$$

in powers of  $\xi^2$  and dividing by (36).

(U) We have

$$\cos^2 \alpha = \frac{[(x/R_s)_\xi]^2}{|u'(\zeta)|^2}, \quad (42)$$

from which we find

$$\xi^2 = E_1(\tau) \cos^2 \alpha + E_2(\tau) \cos^4 \alpha + \dots \quad (43)$$

On substituting (43) in the preceding expansions, we obtain the desired expansions in powers of  $\cos^2 \alpha$ .

(U) When  $K = 11$ , we obtain

$$\frac{p}{\rho_\infty q_\infty^2} \sim \frac{p_0(\tau) + p_1(\tau) \cos^2 \alpha + \dots + p_5(\tau) \cos^{10} \alpha}{1 + p_6(\tau) \cos^2 \alpha + \dots + p_{10}(\tau) \cos^{10} \alpha}, \quad (44)$$

with rational approximations of the same form for  $\rho/\rho_\infty$ ,  $u/q_\infty$ ,  $(q/q_\infty)^2$ , and  $(c/q_\infty)^2$ . These approximations are exact at the shock, and remain accurate throughout most of the shock layer. Near the body, however, higher order coefficients in the expansions become inaccurate, and better accuracy may be obtained by forming Padé fractions from fewer terms of the series. When  $\tau = 0$  in these approximations, the fractions obtained are not necessarily in lowest terms.

(U) We obtain expansions for  $(x + x_0)/R_s$  and  $r/R_s$  in powers of  $\cos^2 \alpha$  by substituting (43) in (17) and (18), respectively. When  $K = 11$ , we obtain the rational approximations

$$\frac{x + x_0}{R_s} \sim \frac{z_0(\tau) + z_1(\tau) \cos^2 \alpha + \dots + z_5(\tau) \cos^{10} \alpha}{1 + z_6(\tau) \cos^2 \alpha + \dots + z_{10}(\tau) \cos^{10} \alpha} \quad (45)$$



and

$$\frac{r}{R_s} \approx \frac{y_0(\tau) \cos \alpha + y_1(\tau) \cos^3 \alpha + \dots + y_4(\tau) \cos^9 \alpha}{1 + y_5(\tau) \cos^2 \alpha + \dots + y_9(\tau) \cos^{10} \alpha} \quad (46)$$

The coordinate transformation depends only on the shock equation, and it is not necessary to use the same number of terms of equation (1) in the calculation of  $x$  and  $r$  as in the calculation of the flow.

(U) Finally, we will need a rational approximation for  $\xi$  in terms of  $\cos \alpha$ . Taking the square root of (43) and forming a Padé fraction, we obtain

$$\xi \approx \frac{e_0(\tau) \cos \alpha + e_1(\tau) \cos^3 \alpha + \dots + e_4(\tau) \cos^9 \alpha}{1 + e_5(\tau) \cos^2 \alpha + \dots + e_9(\tau) \cos^{10} \alpha} \quad (47)$$

Since  $\xi$  becomes equal to  $r/R_s$  when  $\tau = 0$ , it follows that (46) and (47) are identical at the shock.

#### SOLUTION OF THE DIRECT PROBLEM

(U) In the direct problem, we use the two-parameter family of shock equations given by

$$\frac{x + x_0}{R_s} = \frac{1}{2} \left( \frac{r}{R_s} \right)^2 \frac{6\lambda_2 - (4\lambda_3 - 3\lambda_2^2) (r/R_s)^2}{6\lambda_2 - 4\lambda_3 (r/R_s)^2} \quad (48)$$

The Taylor expansion of the right-hand side of (48) at  $r = 0$  begins with the terms

$$\frac{x + x_0}{R_s} = \frac{1}{2} \left( \frac{r}{R_s} \right)^2 + \frac{\lambda_2}{4} \left( \frac{r}{R_s} \right)^4 + \frac{\lambda_3}{6} \left( \frac{r}{R_s} \right)^6 + \dots \quad (49)$$

Comparing with equation (1), we see that  $\lambda_2 = B_s/2$ .

(U) A value of  $\lambda_3$  is first chosen, and  $\lambda_2$  is found by the method of false position so that the bluntness of the calculated body matches that of the given one to a prescribed number of figures. New values of  $\lambda_3$  are then chosen until the calculated body intersects the given one near some prescribed point. Usually two or three choices of  $\lambda_3$  are sufficient to match the given body closely in the subsonic region.

## CALCULATION OF THE SONIC LINE

(U) Sonic speed behind the shock is given by

$$\left(\frac{c}{q_\infty}\right)^2 = \frac{\gamma - 1}{\gamma + 1} + \frac{2}{(\gamma + 1)M_\infty^2} \quad (50)$$

Replacing the left-hand side of (50) by its rational approximation in terms of  $\cos^2\alpha$ , we solve for  $\cos^2\alpha$  by Newton's method for a given value of  $\tau$ . We then find the corresponding values of the cylindrical coordinates from equations (45) and (46). Flow quantities at that point can be found from their rational approximations in terms of  $\cos\alpha$ .

(U) As in Ref. 14, we find the sonic point on the body from the relation

$$\frac{p}{p_{st}} = \left(\frac{2}{\gamma + 1}\right)^{\gamma/(\gamma - 1)} \quad (51)$$

Replacing the left-hand side by equation (34), we solve for  $(s/R_b)^2$  at the sonic point by Newton's method. Finally, we interpolate cubics in  $x$  through the values of  $r/R_b$  and any desired flow quantities evaluated at four values of  $x$ . These values usually include the points on the shock and body.

## CALCULATION OF INITIAL VALUES FOR THE METHOD OF CHARACTERISTICS

(U) A convenient initial curve to use for starting the method of characteristics is a coordinate curve  $\xi = \text{constant}$ . For a given value of  $\tau$ , we can find the value of  $\cos\alpha$  on a curve  $\xi = \text{constant}$  by solving equation (47) by Newton's method. The corresponding values of the cylindrical coordinates and flow quantities are then obtained from their rational approximations in terms of  $\cos\alpha$ . We calculate the flow at the intersection of the initial curve with the body by solving equation (25) for  $(s/R_b)^2$  and substituting the latter in the rational approximations for the flow on the body.

(U) As in the case of the sonic line, the curve  $\xi = \text{constant}$  and flow quantities along it can be approximated accurately by cubics in  $x$ . These cubics are interpolated through values of  $r/R_b$  and the flow quantities at four values of  $x$  exactly as before.

(U) In the program described in Ref. 4, the variables required along the initial curve are  $\tan\theta$ ,  $\sqrt{M^2 - 1}$ , and  $S/c_v$ , where  $\theta$  is the angle between the streamline and the positive  $x$ -axis,  $M$  is the local Mach number,  $S$  is the entropy, and  $c_v$  is the specific heat at constant volume. A typical initial curve and characteristic net is shown schematically in Fig. 2. In the program of Ref. 4, the calculations proceed along the right-running characteristics from top to bottom.

## NUMERICAL RESULTS AND DISCUSSION

(U) Calculations have been carried out on the IBM 7090 for a sphere-cone, sphere-cylinder, spheroid-cone, and spheroid-cylinder, where the half angle of the cone is  $20^\circ$  and the bluntness of the spheroid is 4. All calculations were made with  $\gamma = 1.4$ .

(U) In Fig. 3, the shock, sonic line, and a typical initial curve are shown for the case of a sphere at  $M_\infty = 4$ , with  $K = 7$  and 11. Corresponding results are shown for a sphere at  $M_\infty = 10$  in Fig. 4 and for a spheroid of bluntness 4 at  $M_\infty = 5.98$  in Fig. 5, with  $K = 11$ . The calculated bodies after the iterations have been completed are also shown in Figs. 3, 4, and 5 for  $K = 11$ .

(U) Figs. 6 and 7 show the pressures on the sphere-cone and sphere-cylinder for  $K = 11$  calculated with the initial curves in Figs. 3 and 4, respectively, and Fig. 8 shows the pressures on the spheroid-cone and spheroid-cylinder calculated with the initial curve of Fig. 5 and  $K = 11$ . The pressures in Figs. 6 and 7 are compared with calculations by Chushkin and Shulishnina (Ref. 20). In addition, the pressure on the sphere in Fig. 6 is compared with measurements by Xerikos and Anderson (Ref. 21) at  $M_\infty = 3.975$ . The pressure on the spheroid in Fig. 8 is compared with measurements by Pasiuk (Ref. 22).

(U) As seen in Fig. 3, the calculated flows for  $K = 7$  and  $K = 11$  differ from each other mainly near the sonic line in the vicinity of the body. Even though the pressure found on the sphere for  $K = 7$  is about 5% less than that for  $K = 11$  near the initial curve, the calculated pressures a short distance downstream of the initial curve are nearly identical with each other. The calculations of Figs. 3 and 6 have also been made for  $K = 9$ , and the results are indistinguishable from those for  $K = 11$  on the scale of the figures.

(U) These results indicate that reasonable accuracy is obtained in the calculations for the sphere-cone and sphere-cylinder when  $K = 7$ , and that the results for  $K = 9$  are nearly as accurate as those for  $K = 11$ . The time of computation for one case of the inverse problem is about 15 seconds for  $K = 7$ , 22 seconds for  $K = 9$ , and 50 seconds for  $K = 11$ .

## ACKNOWLEDGEMENT

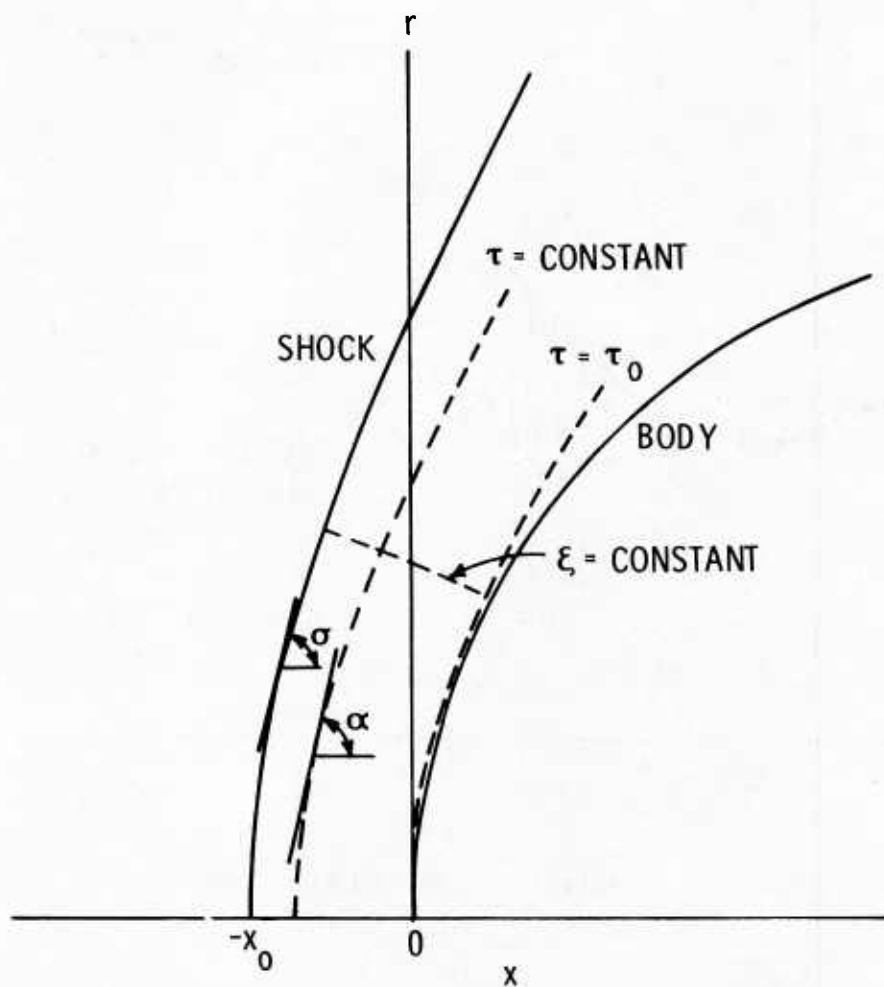
(U) The author wishes to thank Mr. Robert Thompson of the Naval Ship Research and Development Center for furnishing a copy of his method of characteristics program.

## REFERENCES

1. Hayes, W. D. and Probstein, R. F., Hypersonic Flow Theory, Vol. 1, Academic Press, New York (1966), Chapter 6.
2. Van Dyke, M. D., "The Supersonic Blunt Body Problem - Review and Extension", Jour. Aero|Space Sci., vol. 25, 485-496 (1958).
3. Inouye, M., Rakich, J. V., and Lomax, H., "A Description of Numerical Methods and Computer Programs for Two-Dimensional and Axisymmetric Supersonic Flow Over Blunt-Nosed and Flared Bodies" (U), NASA Ames Research Center, TN D-2970 (1965).
4. Thompson, R. H. and Furey, R. J., "Computer Program for Determining the Flow Field About Axisymmetric and Two-Dimensional Bodies in Supersonic Flow" (U), NSRDC Report No. 3032 (to appear).
5. Lin, C. C. and Shen, S. F. "An Analytical Determination of the Flow Behind a Symmetrical Curved Shock in a Uniform Stream" (U), Massachusetts Institute of Technology, NACA TN 2506 (1951).
6. Cabannes, Henri, "Détermination théorique de l'écoulement d'un fluide derrière une onde de choc détachée", O.N.E.R.A. note technique no. 5 (1951).
7. Cabannes, H., "Tables pour la détermination des ondes de choc détachées", La Recherche Aéronautique, no. 49, 11-15 (1956).
8. Van Dyke, M. D. and Gordon, H. M., "Supersonic Flow Past a Family of Blunt Axisymmetric Bodies" (U), NASA Ames Research Center, Report 1 (1960).
9. Van Tuyl, A., "The Use of Rational Approximations in the Calculation of Flows with Detached Shocks" (U), NAVORD Report 6679 (1959); also summarized in Jour. of Aerospace Sci., vol. 27, 559-560 (1960).
10. Lewis, G. E., "Analytic Continuation Using Numerical Methods", Methods in Computational Physics, Academic Press, New York (1965), vol. 4, 45-81.
11. Leavitt, Jay A., "Computational Aspects of the Detached Shock Problem", AIAA Jour., vol. 6, 1084-1088 (1968).
12. Sanematsu, Henry S. and Chapkis, Robert L., "A Conformal Mapping Approach to the Blunt Body Problem", AIAA Jour., vol. 5, 2047-2048 (1967).
13. Moran, J. P., "Two Problems in Gas Dynamics. Part I: The Piston Problem, Part II: The Inverse Blunt Body Problem", Ph.D. Thesis, Cornell University (1965).

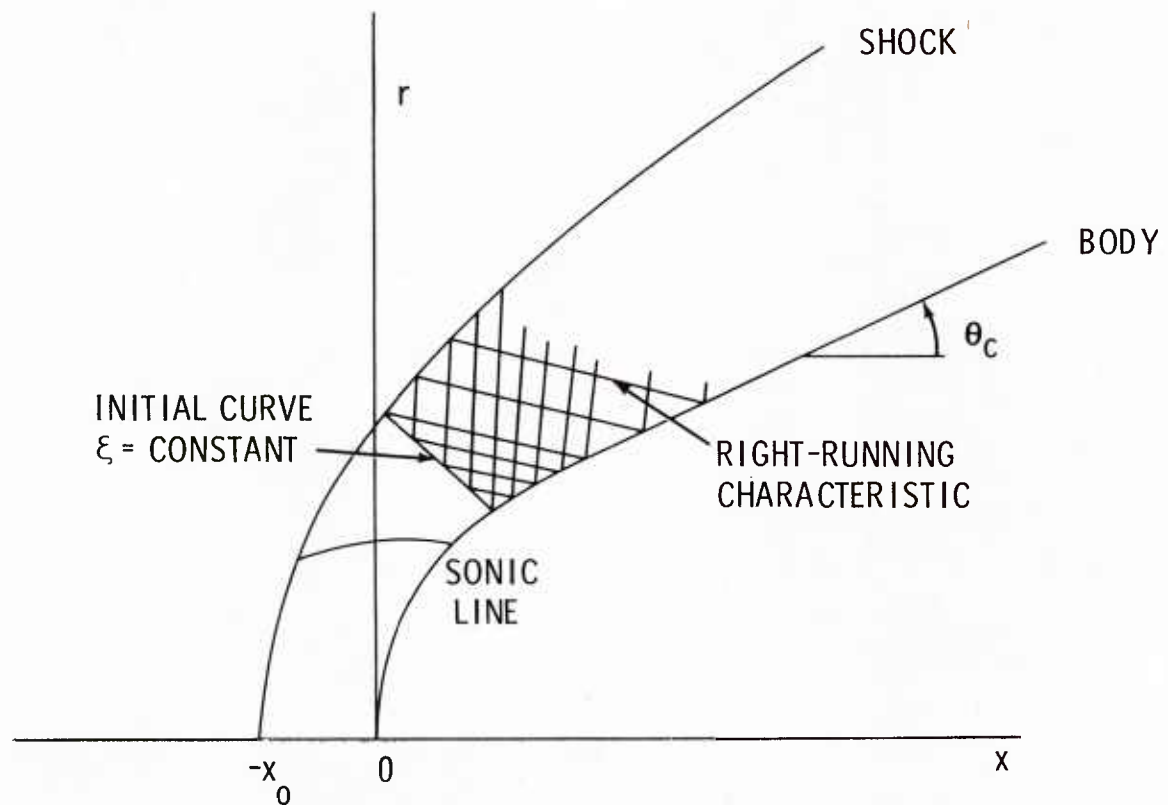
Vol. 1

14. Van Tuyl, Andrew H., "Use of Rational Approximations in the Calculation of Flows Past Blunt Bodies", AIAA Jour., vol. 5, 218-225 (1967).
15. Leavitt, Jay A., "Methods and Applications of Power Series", Math. of Comp., vol. 20, 46-52 (1966).
16. Wall, H. S., Analytic Theory of Continued Fractions, D. Van Nostrand, New York (1948), page 377.
17. Shanks, D., "Non-Linear Transformations of Divergent and Slowly Convergent Sequences", Jour. of Math. and Phys., vol. 34, 1-42 (1955).
18. Henrici, Peter, "The Quotient-Difference Algorithm", Further Contributions to the Solution of Simultaneous Linear Equations and the Determination of Eigenvalues, Nat. Bur. of Standards App. Math. Series no. 49, 23-46 (1958).
19. "Equations, Tables, and Charts for Compressible Flow" (U), Ames Research Staff, NACA Ames Aeronautical Laboratory, Report 1135 (1953).
20. Ellett, D. M., "Pressure Distributions on Sphere Cones" (U), Research Report SC-RR-64-1796, Sandia Laboratory (1965).
21. Xerikos, J. and Anderson, W. A., "An Experimental Investigation of the Shock Layer Surrounding a Sphere in Supersonic Flow", AIAA Jour., vol. 3, 451-457 (1965).
22. Pasiuk, Lionel, "Measurements of the Static Pressure Distributions and Shock Shape on an Oblate Spheroid at Mach Numbers of 3 and 6" (U), NOLTR 66-138 (1966).

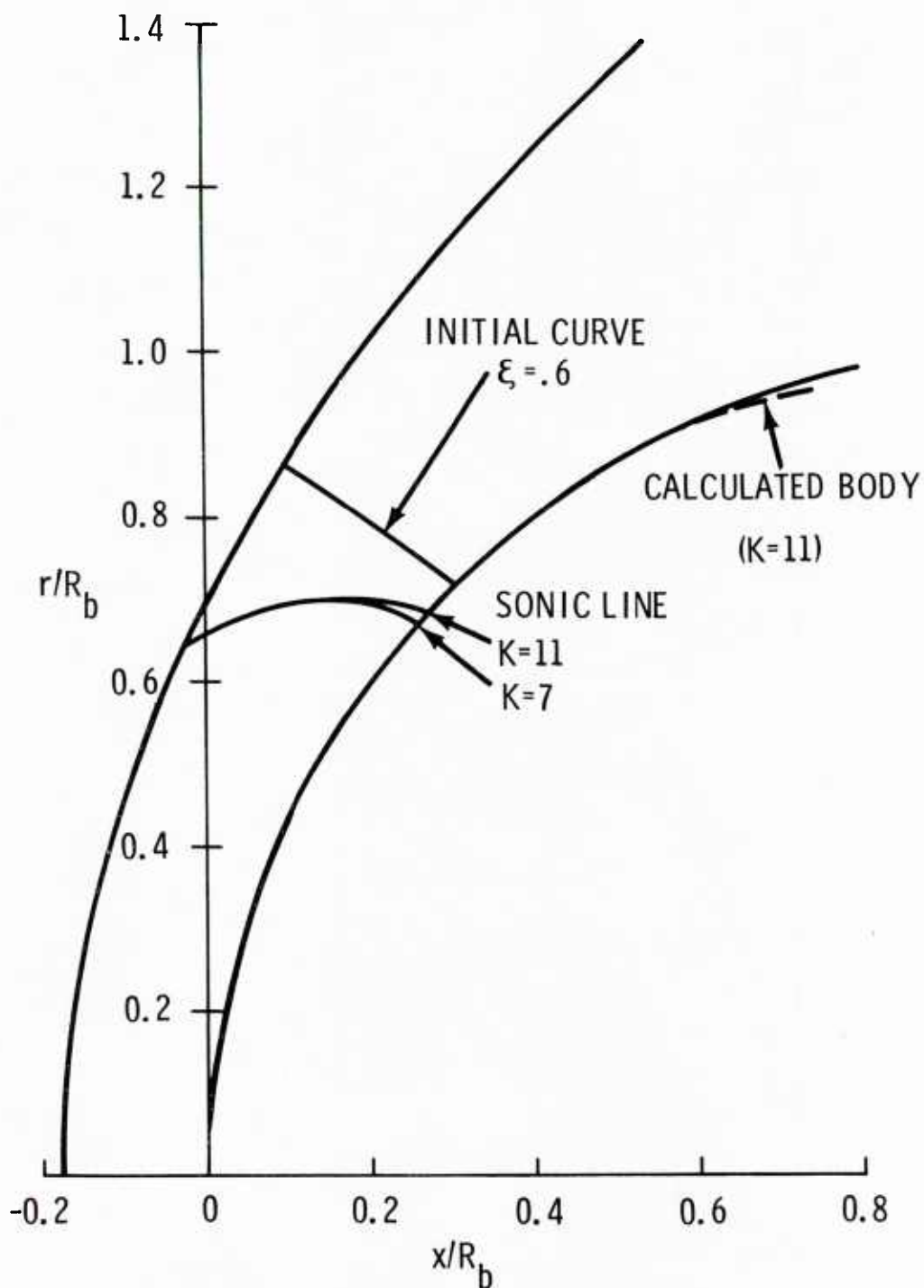


(U) FIG. 1 Coordinate Systems

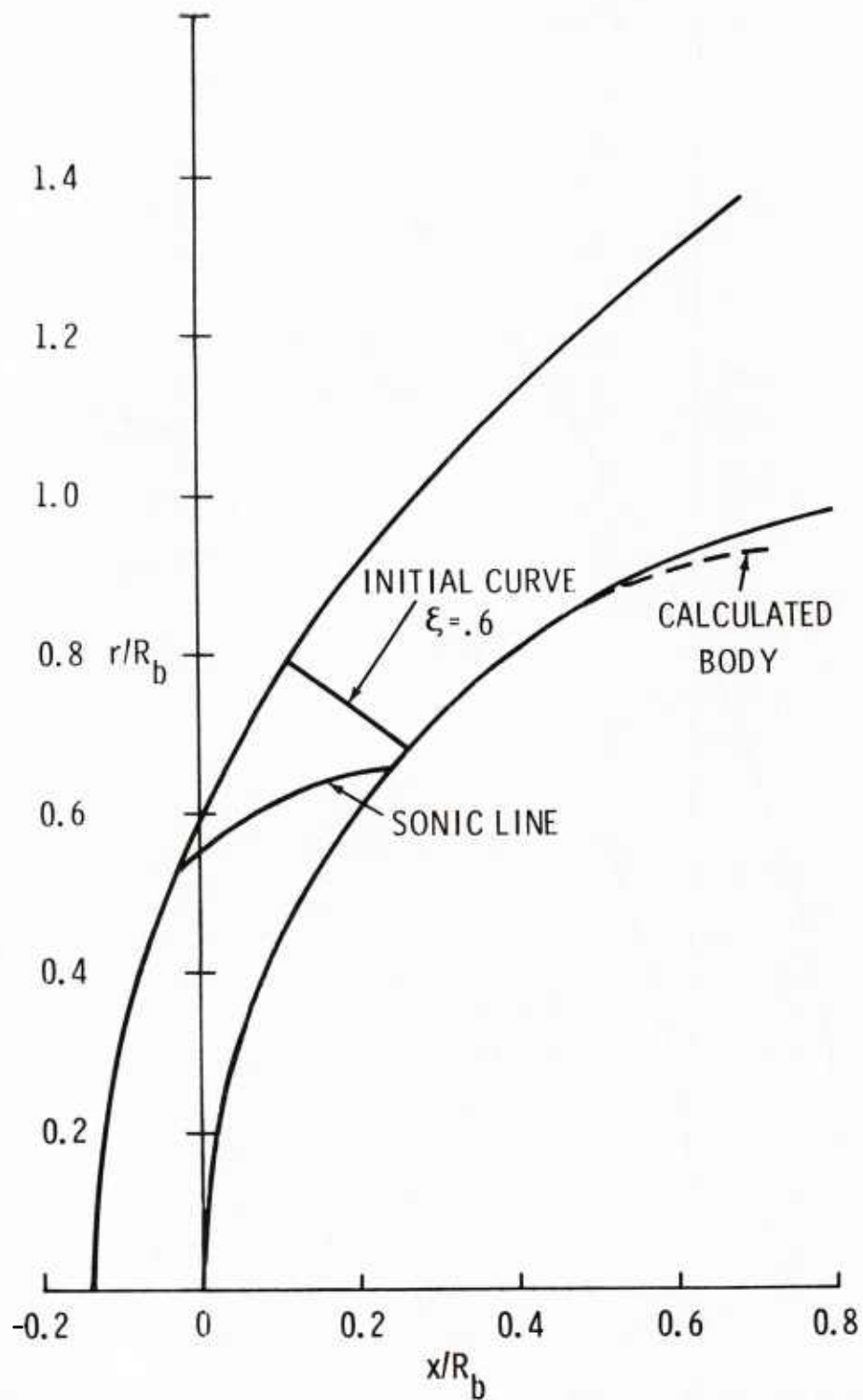




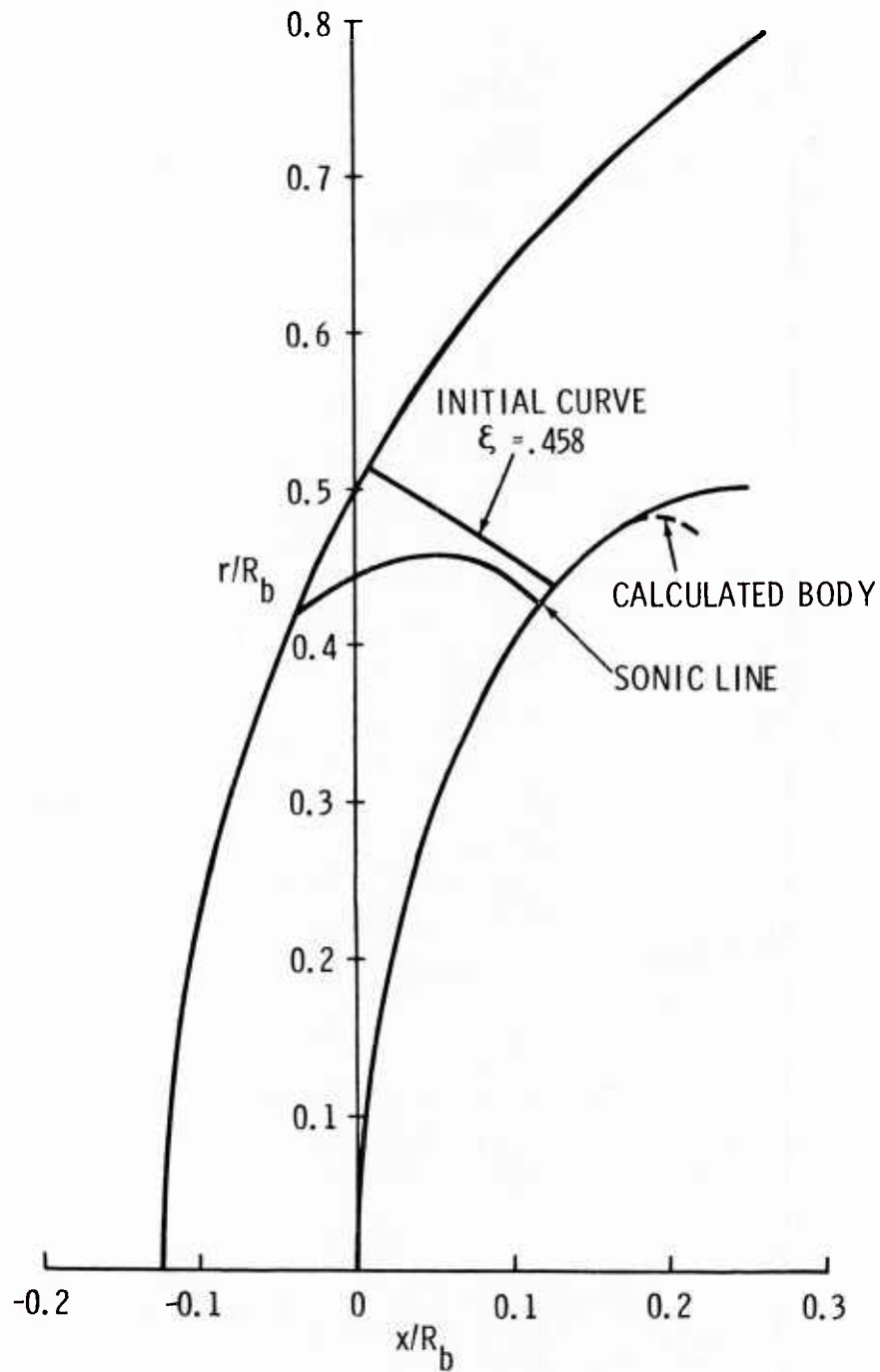
(U) FIG. 2 Characteristic Net



(U) FIG. 3 Sonic Line and Initial Curve in Flow Past a Sphere  
at  $M_\infty = 4$

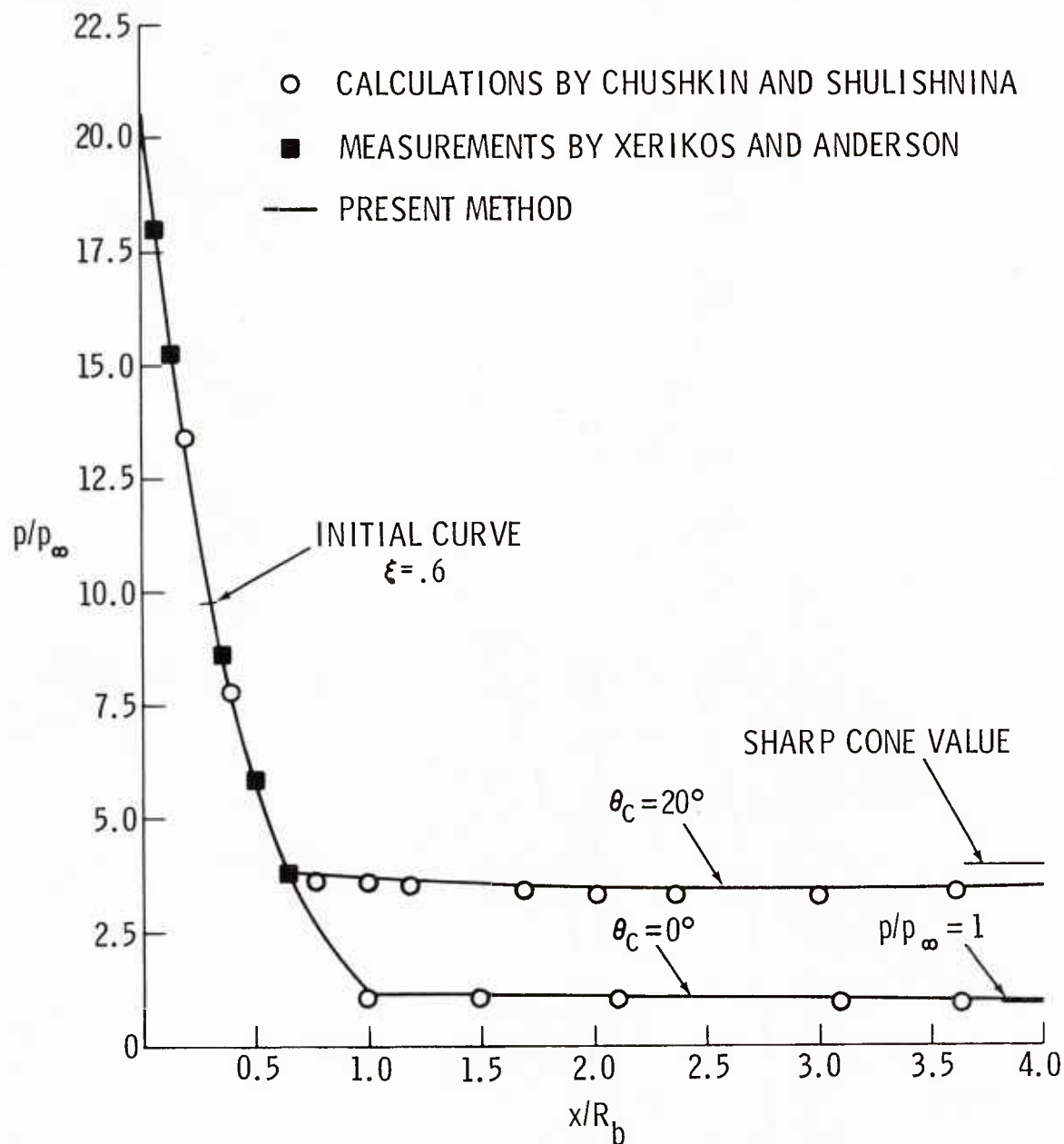


(U) FIG. 4 Sonic Line and Initial Curve in Flow Past a Sphere at  $M_\infty = 10$

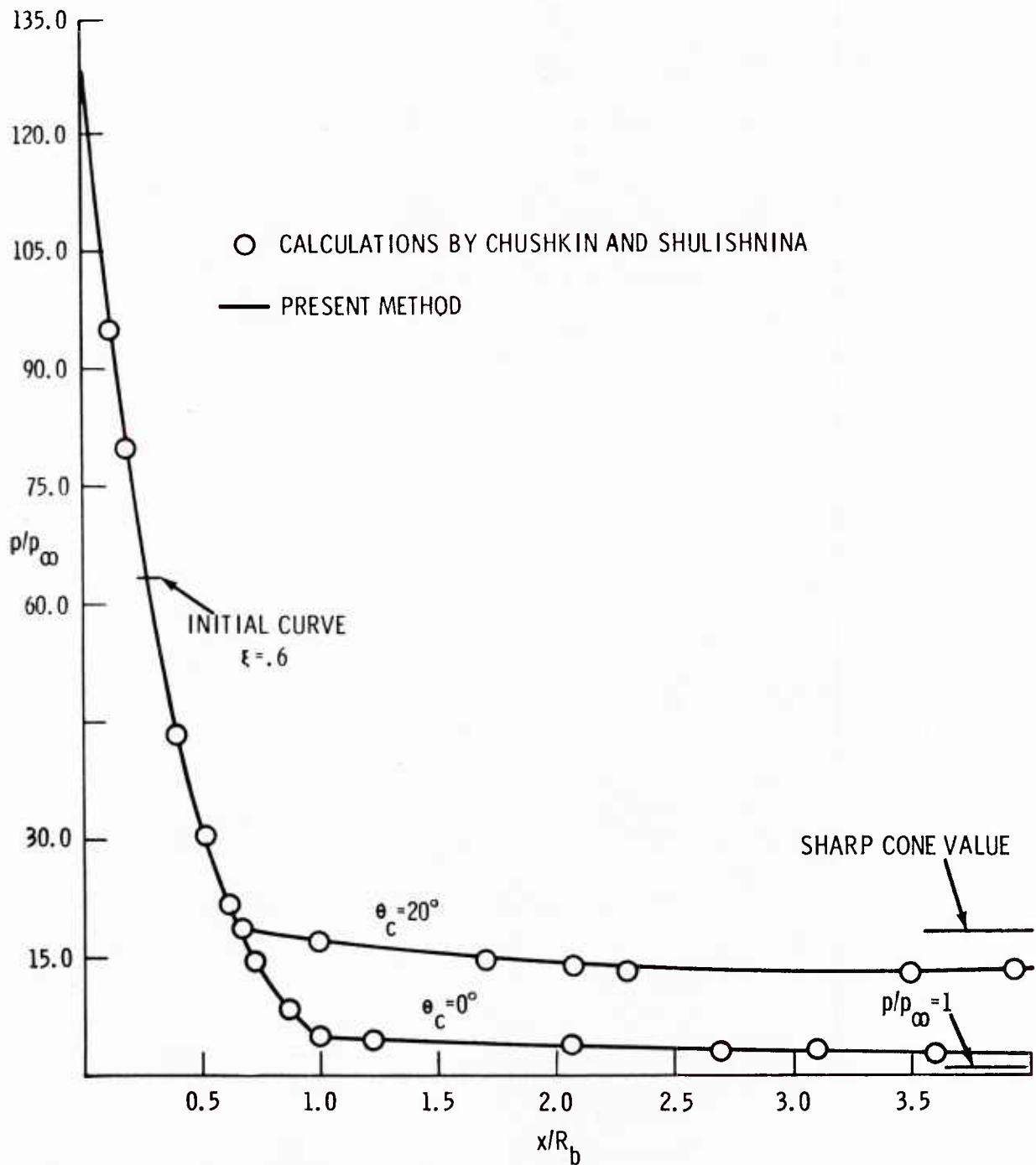


(U) FIG. 5 Sonic Line and Initial Curve in Flow Past a Spheroid of Bluntness 4 at  $M_\infty = 5.98$

Vol. 1

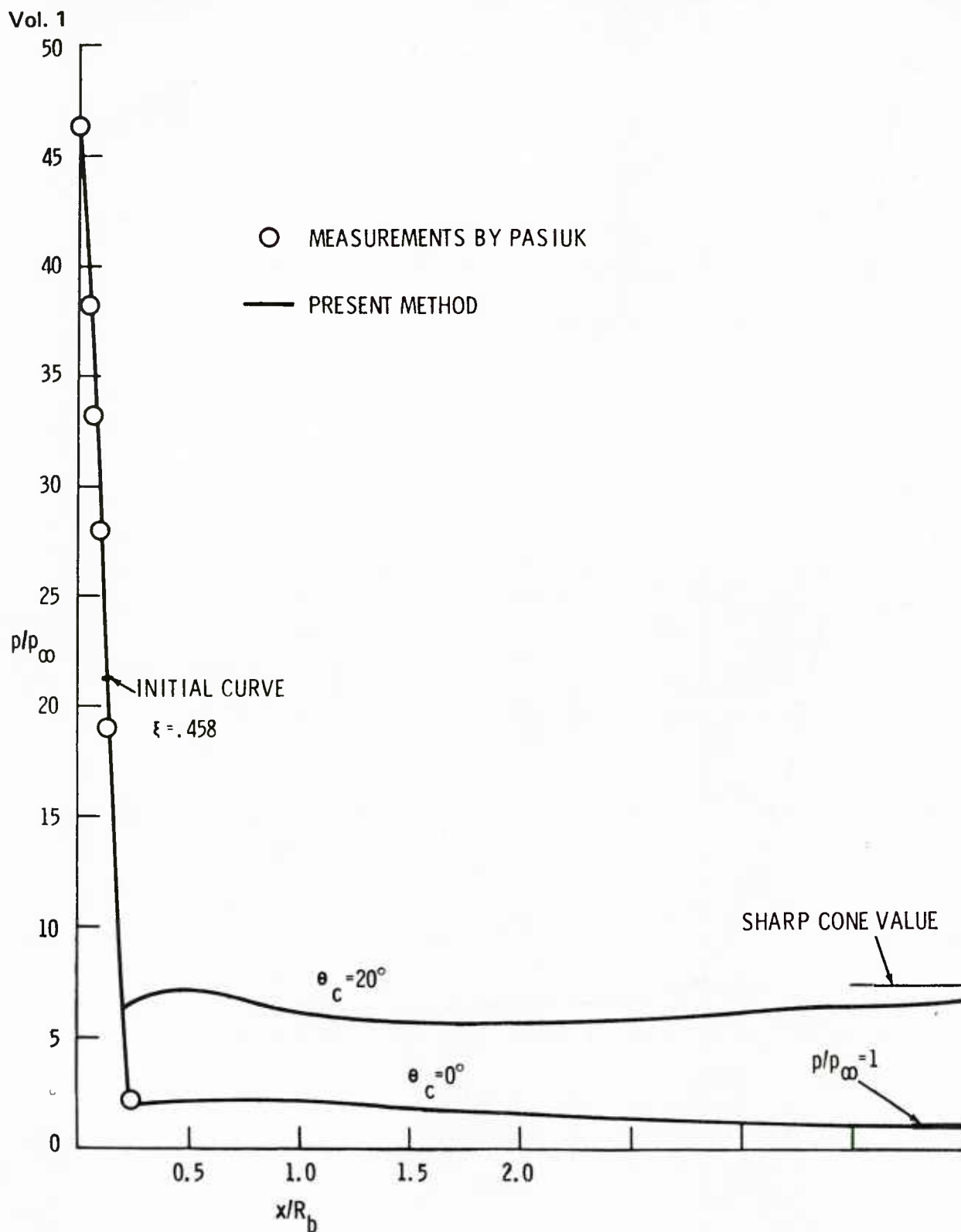


(U) FIG. 6 PRESSURE ON A SPHERE-CONE AND A SPHERE-CYLINDER AT  $M_\infty = 4$



(U) FIG. 7 Pressure on a Sphere-Cone and a Sphere-Cylinder  
at  $M_\infty = 10$





(U) FIG. 8 Pressure on a Spheroid-Cone and a Spheroid-Cylinder  
of Bluntness 4 at  $M_\infty = 5.98$

DUDLEY KNOX LIBRARY - RESEARCH REPORTS



5 6853 01000495 5

U126777

Not releasable to foreign nationals.  
Shelved numerically in the vault. d